

ABSTRACT

Title of Document: FAILURE MECHANICS OF FUNCTIONAL NANOSTRUCTURES IN ADVANCED TECHNOLOGIES

Zheng Jia, Doctor of Philosophy, 2014

Directed By: Associate Professor Teng Li,
Department of Mechanical Engineering

The past decade has seen a surge of interest in developing novel functional nanostructures to enable advanced technologies, such as flexible electronics and high performance lithium-ion batteries. Examples of such functional nanostructures include organic/inorganic multi-layer thin films in flexible electronics and nano-sized silicon/tin-based anodes in lithium/sodium ion batteries. Widespread implementation of these advanced technologies with novel functional nanostructures in the future will broadly impact human's daily life. However, grand challenges for developing robust novel functional nanostructures still exist. During operating cycles, these functional nanostructures undergo large deformation and high stresses, which may cause fracture and pulverization of the nanostructures, thereby leading to degradation and mechanical failure of the flexible devices or battery cells. Therefore, enhancing mechanical durability of the novel functional nanostructures in a mechanically demanding environment remains

a significant challenge to the nanostructure design.

This dissertation aims to shed lights on capturing the characteristics of the failure mechanisms of some novel functional nanostructures by theoretical and computational mechanics approach, The novel functional nanostructures investigated in my thesis includes inorganic/organic multilayer nanostructures, polyimide-supported brittle ITO films, substrate-supported ductile metal films and nanobead/nanowall/nanowire/nanoparticle electrodes in high-performance batteries. More importantly, we also explore possible solutions to effectively enhance the mechanical durability of these functional nanostructures.

Failure Mechanics of Functional Nanostructures in Advanced Technologies

By

Zheng Jia

Dissertation submitted to the Faculty of the Graduate School of the
University of Maryland, College Park, in partial fulfillment
of the requirements for the degree of
Doctor of Philosophy

2014

Advisory Committee:

Associate Professor Teng Li, Chair/Advisor

Professor Hugh A. Bruck

Associate Professor Chunsheng Wang, Dean's Representative

Associate Professor Peter W. Chung

Assistant Professor Liangbing Hu

© Copyright by

Zheng Jia

2014

Acknowledgements

I wish to first express my deepest gratitude to my supervisor, Professor Teng Li. This dissertation thesis would not have been possible without his trust and encouragement. He guided me into research with enormous patience especially in the first year of my PhD study. His vast knowledge in mechanics, enthusiasm for researches and rigorous scrutiny into details have been the constant driving force for my progresses. Teng is always supportive on my career development. Just to mention a few examples: Teng is always willing to spend a lot of time to help me improve my presentation skills through our regular meetings; I cannot forget those “torture processes” I experienced in mock presentations before my conference talks and dissertation defense. It is also so unforgettable that Teng tried to seize every opportunity to help me develop my career as a scholar: He helped me apply for distinguished fellowships, from campus level to national level; He constantly introduced me to other professors and researchers during conferences to build up my reputation in academia; He got a lot of great collaboration opportunities for me to enrich my researches and he also generously sent me to Prof. Zhigang Suo’s group in Harvard to let me branch into new exciting research fields. Teng is also a great teacher. I was in his continuum mechanics course and was deeply impressed by his fabulous lecturing style and deep understanding of materials. I feel so lucky to have Teng as my PhD supervisor. He is an excellent teacher and spectacular researcher with great personality. In my research career, my supervisor sets the role model and target.

I am also deeply grateful to Prof. Zhigang Suo at Harvard who generously hosted me as a visiting student in his research group in Spring 2014. I enjoyed all times discussing with Zhigang, in his office or in his class. He extended my knowledge to mechanics of soft materials. Zhigang is truly friendly and inspiring. I always appreciate his willingness to spend a lot of time discussing my research projects and interests. It was a great pleasure to visit and work in his group.

I also wish to bring my deep gratitude to my committee members, Professor Liangbing Hu, Professor Chunsheng Wang, Professor Abhijit Dasgupta and Professor Hugh Bruck for their valuable suggestions and comments during various stages of my researches. I have vastly benefitted from lectures given by Prof. Abhijit Dasgupta and Prof. Hugh Bruck. I also learned a lot about batteries and electrochemistry from the discussions with Prof. Chunsheng Wang. Our fruitful collaborations on Li-ion batteries with Prof. Liangbing Hu have been greatly deepened my understanding on mechanics in batteries and the collaboration experience itself has been really pleasant and fruitful.

I was fortunate to have many other wonderful collaborators, Prof. Zhihong Nie, Prof. Yuhuang Wang, Dr. Hongli Zhu, Dr. Xiaogang Han, Mr. Jiayu Wan at University of Maryland, Prof. Yue Qi from Michigan State University and Prof. Jun Lou, Dr. Cheng Peng from Rice University. Dr. Cheng Peng is a great researcher and also a great friend; it's always pleased to talk to him. All the collaborators have helped to shape my research. Their comments and feedbacks have been very valuable.

The research group of Teng is a wonderful family. Every person in our group is easy-going and willing to help each other. I thank all these great friends, Dr. Zhao Zhang, Dr. Andrew Fox, Shuze Zhu, Yinjun Huang and Jian Cheng. I am so glad to be immersed in such a friendly and relaxed atmosphere. Special thanks also go to my friends at Harvard: Dr. Lihua Jin, Yecheng Wang, Jianguo Li, Zhengjin Wang, Jingda Tang and so on. They made my visit at Harvard really joyful and unforgettable. Also not forgetting to my friends Dr. Guoqiang Jian, Dr. Cheng Pang, Dr. Guanggang Qu, Dr. Guojie Cao, Dr. Weiwei Sun, Li Shi, Qiang Huang, Zhixi Zhan, Hao Tang. In the past five years, they have been always there for me.

Deepest love is due to my beloved parents for their continuous support during my PhD study. I heartily appreciate my fiancée, Qian Zhang. Without her support and encouragement, my thesis would never have been accomplished.

Table of Contents

Acknowledgements	ii
Table of Contents	v
Chapter 1. Introduction	1
1.1. Background and Motivation	1
1.1.1. Flexible Electronics	1
1.1.2. Lithium/Sodium-ion Batteries	5
1.2. Scope and Goals of the thesis research	9
Chapter 2. Brittle Cracking of Inorganic/organic Multi-layered Structures in Flexible Electronics	11
2.1. Failure Mechanics of Organic-inorganic Multilayer Permeation Barriers in Flexible Electronics	11
2.1.1. Introduction.....	11
2.1.2. Computational Model	17
2.1.3. Driving Forces for Interfacial Delamination and Channel Cracking in a Multilayer Permeation Barrier under Tension	20
2.1.4. Effect of a Protective Coating on the Durability of a Multilayer Permeation Barrier	24
2.1.5. Discussion	30
2.1.6. Summary	34
2.2. Fracture Mechanics in Indium Tin Oxide-based Multilayer Electrodes	35
2.2.1. Introduction.....	35
2.2.2. Experimental Design and Tests of ITO-based Multilayer Electrodes	38
2.2.3. Mechanics Modelling and Results	44
2.2.4. Summary	52
Chapter 3. Brittle Cracking of Polyimide Substrate Supported ITO Thin Films	54
3.1. Mechanics Modeling of Tensile Cracking in Indium Tin Oxide Thin Films on Polyimide Substrates	54
3.1.1. Introduction.....	54
3.1.2. Experimental Results and Discussion	57
3.1.3. Mechanics Model and Results	63
3.1.4. Summary	72
3.2. a Map of Buckling-driven Failure Modes of Substrate-supported Thin Brittle Films	73
3.2.1. Introduction.....	73
3.2.2. In Situ Experimental Observation of Buckling-driven Failure of Substrate Supported Thin Brittle Films	74
3.2.3. a Map of Buckling-driven Failure Modes of Substrate-supported Thin Brittle Films	75

3.2.4. <i>Effect of Substrate Stiffness on the Map of Buckling-driven Failure Modes</i> ...	79
3.2.5. <i>Summary</i>	82
Chapter 4. Ductile Failure of Substrate-supported Metal Layers under Biaxial In-plane Loading	84
4.1. Necking Limit of Substrate-supported Metal Layers under Biaxial In-plane Loading	84
4.1.1. <i>Introduction</i>	84
4.1.2. <i>Mechanics Model</i>	87
4.1.3. <i>Results and Discussion</i>	96
4.1.4. <i>Summary</i>	107
Chapter 5. Novel-Design of Si-based Nanostructures as Anodes for Lithium-ion Batteries	108
5.1. Mechanics Modeling of Non-cracking Si Beads-string Lithium-ion Battery Electrodes	108
5.1.1. <i>Introduction</i>	108
5.1.2. <i>In Situ Observation of Lithiation of Si beads-string electrodes</i>	109
5.1.3. <i>Mechanics Modeling of Si Beads-string Electrodes under Lithiation</i>	112
5.1.4. <i>Summary</i>	122
5.2. Silicon Nanowalls for Lithium-Ion Batteries Fabricated using Nanoimprint Lithography	123
5.2.1. <i>Introduction</i>	123
5.2.2. <i>Nanowall Fabrication and Anode Characterization</i>	127
5.2.3. <i>Mechanics Modeling on Stress Evolution in Nanowall Anodes</i>	135
5.2.4. <i>Summary</i>	139
Chapter 6. Stress Development and Its Effect on Lithiation Kinetics and Fracture In Silicon-based Anodes in Lithium-ion Batteries	140
6.1. Stress-Modulated Driving Force for Lithiation Reaction in Hollow Nano-Anodes	140
6.1.1. <i>Introduction</i>	140
6.1.2. <i>Lithiation-induced stress field in a hollow nanowire</i>	143
6.1.3. <i>Effect of stress on driving force for lithiation</i>	157
6.1.4. <i>Summary</i>	163
6.2. Stress Generation during Two-Step Electrochemical Lithiation of Amorphous Silicon	164
6.2.1. <i>Introduction</i>	164
6.2.2. <i>FEM Model of Two-phase Lithiation</i>	167
6.2.3. <i>Evolution of Stress Field during Two-phase Lithiation of α-Si Particle</i>	169
6.2.4. <i>Effect of Two-step Mechanism on Lithiation Kinetics</i>	182
6.2.5. <i>Reaction-induced fracture during two-phase lithiation of solid α-Si particle</i>	186
6.2.6. <i>Summary</i>	187
Chapter 7. Mechanics on Tin Anodes in Sodium-Ion Batteries	189

7.1. Tin Anode for Sodium-Ion Batteries Using Natural Wood Fiber as a Mechanical Buffer and Electrolyte Reservoir	189
7.1.1. Introduction.....	189
7.1.2. Fabrication of Tin-based Anodes and Chemo-electrical Performance of the Anodes	191
7.1.3. Mechanics Modeling on Wrinkling-induced Stress Releasing in Cellulose-supported Tin Anodes	200
7.1.4. Summary	205
Chapter 8. Conclusions and Outlook	207
8.1. Summary and Concluding Remarks	207
8.2. Outlook and Future Work.....	211
Bibliography	214

List of Tables

Table 2.1. Critical strains of ITO-based multilayer electrodes. The value range of critical strain in each structure was determined from at least three electro-mechanical tests.	43
Table 2.2 Normalized critical strains for failure modes (a): channel cracking in the top ITO layer and failure mode (b): channel cracking in both ITO and Al ₂ O ₃ layers for various crack densities.	49

List of Figures

Figure 1.1. (a) Flexible rollable displays. (b) skin-like sensors. (c) printable solar cell. (d) flexible electronic paper.....	2
Figure 1.2. (a) Multilayer Structures. (b) Device islands on substrate.	2
Figure 1.3. (a) Schematics of lithium-ion batteries. (b) Schematics of lithiation-induced fracture and pulverization ³²	6
Figure 2.1 Scanning electron microscope image of the cross section of an organic-inorganic multilayer permeation barrier (Courtesy of Vitex Sys. Inc.)	13
Figure 2.2. Moisture can permeate through various defects in a permeation barrier. (a) pin-holes in an as-made barrier; (b) a channel crack in the oxide layer of a barrier; and (c) delamination along the oxide-organic interface in a barrier.	14
Figure 2.3. Schematic of (a) the computational model considering (b) both the channel crack in the oxide layer and the concomitant oxide-organic interfacial delamination.	19
Figure 2.4. (a) Normalized driving force of interfacial delamination along the tensile direction as a function of normalized delamination width; (b) Normalized driving force of oxide cracking and interfacial delamination perpendicular to the tensile direction as a function of normalized steady-state delamination width.....	21
Figure 2.5. Normalized effective driving force for channel cracking as a function of normalized interfacial toughness.	24
Figure 2.6. The normalized driving force for a tunnel crack in the top oxide layer of a permeation barrier with a protective coating of thickness h_p , as a function of the stiffness of the protective coating E_p	26
Figure 2.7. Normalized driving force as a function of normalized delamination length..	28
Figure 2.8. Effective driving force as a function of normalized interfacial toughness for various stiffness of the protective coating. Here $h_p/h = 1$	30
Figure 2.9. Dash and dotted lines with markers plot the normalized driving force for oxide layer cracking as a function of E_p , for $h_p/h = 1$ and 10, and $d_{po}/h = 0.1$ and 2, respectively. Curves in Figure 2.6 are included for comparison (dash line and solid lines with markers).	32
Figure 2.10. Impact of the coating-oxide interfacial delamination on (a) the driving force for oxide-organic interfacial delamination along the tensile direction and on (b) the driving force for both oxide layer cracking and oxide-organic interfacial delamination perpendicular to the tensile directions. Here $h_p/h = 1$. The corresponding curves in Figure	

2.7 are included for comparison (dash line and dash lines with markers).....	33
Figure 2.11. Schematics of five structural designs of ITO-based multilayer electrodes. The thicknesses of PET, Al ₂ O ₃ , ITO, PMMA, and S1813 are 127 μm, 60 nm, 80 nm, 100 nm and 1 μm, respectively. A 5 nm Cr layer is coated between adjacent layers to increase interlayer adhesion (not shown for visual clarity).	39
Figure 2.12. In situ observation of multilayer structures in different strain levels: (a) Structure 1, (b) Structure 2, and (c) Structure 3 are at the strain of ~4%; and (d) Structure 1, (e) Structure 2 and (f) Structure 3 are at the strain of ~13%. The white scale bar in each figure is 30 μm in length.....	41
Figure 2.13. (a) Cracks density and (b) normalized change in electrical resistance as the function of strain in different ITO-based multilayer electrodes.	42
Table 2.1. Critical strains of ITO-based multilayer electrodes. The value range of critical strain in each structure was determined from at least three electro-mechanical tests.	43
Figure 2.14. (a) The elastic energy reduction associated with the steady state channel cracking propagation in the multilayer can be computed by subtracting the elastic energy stored in a slice of the multilayer structure of unit thickness far behind the crack front (Slice 1) from that far ahead of the crack front (Slice 2). (b) Schematics of models of Slice 1 and Slice 2 used in finite element simulations.....	48
Table 2.2 Normalized critical strains for failure modes (a): channel cracking in the top ITO layer and failure mode (b): channel cracking in both ITO and Al ₂ O ₃ layers for various crack densities.....	49
Figure 2.15. Normalized driving force for cracking propagation in Structures 1 to 5 as a function of crack density.....	52
Figure 3.1. Crack initiation and propagation during in situ tensile test. A crack tip was found near the top edge of the blue rectangle box in (a) strain=3.68% and this crack propagated downward and advanced outside of the same blue rectangle box in (b) strain=4.70%. Similar phenomena is also shown in the red rectangle box in (b) strain=4.70% and (c) strain=5.85%. The dust in the right corner is used as the reference for in situ observation.	58
Figure 3.2. (a-e). Snap shots of polyimide-supported ITO film under increasing tensile strain. Note the onset of channel crack initiation at 1.59 % tensile strain (b) and the increasing crack density as the tensile strain increases. No appreciable increase of crack density when tensile strain increases from 4.70% to 5.85% (d-e), indicating the saturation of channel cracking in the ITO film. (f). ITO fragments near the sample rupture location. Note the obvious delamination along the ITO/polyimide interface. Here ITO film thickness is 80 nm.....	59

Figure 3.3. The crack density and the variation of electrical resistance of an 80 nm thick ITO film deposited on polyimide as a function of the applied strain. R_0 denotes the electrical resistance of the unloaded ITO thin film. 62

Figure 3.4. Crack density as a function of applied strain for ITO thin films with thickness of 80nm and 200nm, respectively. Two samples were tested for each film thickness. 63

Figure 3.5. (a) Schematics of the simulation model. (b) Unit cell used in finite element simulation. (c) The traction-displacement laws used to model the ITO/polymer interface. 64

Figure 3.6. The crack density vs. applied strain curves from the best-fit simulations and experiments, for ITO film thickness of 80 nm and 200nm, respectively. 69

Figure 3.7. (a) The variation of the tensile stress in the 80 nm thick ITO thin film as a function of the relative location in a unit cell model, at various applied strains. For the horizontal axis, 0 denotes the center of the ITO fragment and 1 denotes the right edge of the ITO fragment (i.e., the channel crack surface). (b) The delamination length normalized by the ITO fragment width as a function of applied strain, for both 80 nm and 200 nm thick ITO thin films, respectively. 70

Figure 3.8. (a) Scanning electron microscope image of a thin brittle ITO film (100nm thick) on a thick polyimide substrate (75 μm thick) under uniaxial tension. The long strips along vertical directions result from tensile fracture of the ITO film and are then subject to Poisson's compression perpendicular to tension direction. Some ITO strips buckle away from the substrate and eventually crack at the crest along the direction roughly parallel to the applied tension. (Inset shows perspective view of buckling-driven film cracking in a different sample.) (b) In another polyimide-supported ITO film (80nm thick), Poisson's compression in the ITO strips only leads to film delamination, without film cracking. Note that the widths of interfacial delamination in (b) are much longer than those in (a). 75

Figure 3.9. (a). Solid lines plot Ad_{cr}/h as a function of b/h , for various values of Γ . Dashed line plots Af_{cr}/h as a function of b/h . Inset shows a schematic of the model. (b). A map delineates three buckling-driven failure modes in the parameter space of interfacial adhesion energy and initial interfacial defect size, namely, A) buckling-driven delamination followed by film cracking, B) Buckling-driven film cracking without delamination and C) Buckling-driven delamination without film cracking. 77

Figure 3.10. (a-d). The map of buckling-driven failure modes (same as those defined in Fig. 2b) in the parameter space of interfacial adhesion energy and initial interfacial defect size, for various substrate stiffness. Each mark indicates a finite element simulation case, with triangles denoting Mode A, disks denoting Mode B and squares denoting Mode C. The boundary lines between different failure modes are estimated from the simulation

results.....	82
Figure 4.1. Schematics of necking band in substrate-supported metal film.....	92
Figure 4.2. Critical necking strain ε of a freestanding layer as a function of orientation angle of the necking band θ when the layer is under three different tension modes. Here the hardening exponent of the layer $N = 0.2$. (a) Under equi-biaxial tension, necking instability could occur in any orientation at a critical necking strain $\varepsilon = (1 + 3N)/6 \cong 0.27$; (b) Under plane-strain tension, the minimum critical necking strain $\varepsilon = N = 0.2$, and necking instability occurs along the direction perpendicular the applied tension (i.e., $\theta = 0^\circ$); (c) Under uniaxial tension, however, the minimum critical necking strain $\varepsilon = 0.31$, and necking instability occurs along a direction of $\theta = 39^\circ$	98
Figure 4.3. Necking limit curves showing strains at the onset of necking as a function of $S = KshsKfhf$ in (a) metal film with $Nf = 0.02$ supported by metal substrate with $Ns = 0.2$ and (c) metal film with $Nf = 0.1$ supported by metal substrate with $Ns = 0.5$ subject to loading modes from uniaxial tension to equi-biaxial tension. (b),(d) Corresponding necking band orientation angle ψ in negative- ρ range.....	99
Figure 4.4. Necking band orientation angle in a substrate supported metal layer as a function of S for various hardening index $N = 0.02, 0.1, 0.2$	105
Figure 4.5. Necking limit of a substrate-supported layer as a function of S under (a) uniaxial tension, (b) plane-strain tension, and (c) equi-biaxial tension, for $N=0.02, 0.1$ and 0.2 , respectively. Note that $S=0$ corresponds to the limiting case of a freestanding layer.....	106
Figure 4.6. orientation angle as a function of S under uniaxial-tension loading mode for $N = 0.02, N = 0.1$ and $N = 0.2$	106
Figure 4.7. Critical S as a function of loading ratio ρ for $N = 0.02, N = 0.1$ and $N = 0.2$	107
Figure 5.1. Microstructural evolution of Si-CNT heterostructures upon lithiation propagation. a,e, Schematic drawings show two different nucleation models with the free sliding and fixed interfaces. b-d, Microstructural evolution of CNT@ α -Si core-shell structure upon lithiation. f,g, Microstructural evolution of f-CNT@ α -Si beads-string structure upon lithiation. h, Microstructural evolution of f-CNT@ α -Si upon lithiation (0V, $t = 15s$) shows that Li^+ propagated in two pathways: along both the α -Si surface and CNT/Si interface in the radial direction. i, Schematic drawing indicates a two pathways diffusion mechanism of Li^+ on f-CNT@ α -Si beads-string structure.....	111
Figure 5.2. Mechanical response and cracking due to morphology change. a, Formation of cracks on partially lithiated α -Si shell of CNT@ α -Si core-shell structure (0V, $t = 720s$). b, A fully lithiated f-CNT@ α -Si beads-string structure without cracks (-3V, $t = 540s$). .	112

Figure 5.3. Simulations of the lithiation and lithiation-induced stress in a-c, CNT@ α -Si core-shell structure and d-f, f-CNT@ α -Si beads-string structure..... 117

Figure 5.4. Snapshots of f-CNT@a-Si bead under lithiation. Here the inner surface of Si bead is free (no mechanical constraint from CNT). Li⁺ can only diffuse from the outer surface of the Si bead. Note that the Si bead fractures under lithiation..... 120

Figure 5.5. Snapshots of f-CNT@a-Si bead under lithiation. Here the inner surface of Si bead is free (no mechanical constraint from CNT). Li⁺ can diffuse from both the inner and outer surfaces of the Si bead. Note that the Si bead fractures under lithiation. 121

Figure 5.6. Snapshots of f-CNT@a-Si bead under lithiation. Here the inner surface of Si bead is perfectly bonded to the f-CNT. Li⁺ can only diffuse from the outer surface of the Si bead. Note that the strong mechanical constraint from the f-CNT can avert the fracture of Si bead under lithiation..... 122

Figure 5.7. Outline of NIL process for Si nanowall anode on an SS substrate (the SS substrate is not shown in this figure) 128

Figure 5.8. (a). SEM images of large area and uniformly distributed Si nanowall structure, (b) Zoomed-in SEM images of (a) (c). SEM image to showing the dimensions of the Si nanowalls (d). Energy dispersed X-ray spectroscopy of Si nanowall/substrate, with peaks of Si, Cr and Fe 130

Figure 5.9. (a). Electrochemical cycling performance of Si nanowall anode (b). Voltage profile of 1st, 10th, 20th and 40th cycle of Si nanowall (c). EIS plot of the battery before cycling (blue) and after 40 cycles (red) (d). Rate performance of the Si nanowall half cell. 133

Figure 5.10 (a) and (b) SEM images at different magnifications of the Si nanowall anode after cycling. A residual Cr layer from the mask is observed on top of the nanowall. (c) High magnification SEM of Si nanowalls after cycling shows porous structure with an average pore size of ~30 nm 134

Figure.5.11 Lithiation/delithiation-induced mean stresses in the nanowall. (a) Schematic of the simulation model. The origin of the coordinate system is defined with origin at the centroid of bottom surface. (b) and (c) show the mean stress distribution within the mid-plane of the nanowall ($z = 0$) and outer surface of nanowall ($z = h/2$) during lithiation half cycle, respectively, with extent of lithiation described by $x_{average} = 1$. (d) and (e) are the counterparts of (b) and (c) during delithiation half cycle, respectively 138

Figure 6.1. (a) Left: cross-section of a pristine hollow cylindrical silicon nanowire with an initial inner radius R_i and an initial outer radius R_o is considered to be the reference state. A material point (labeled by the red dot) is at a radius R . Right: in the lithiation

state at time t , the lithiation front is located at a radius of $A(t)$, the outer surface is now at a radius $r_O(t)$, and the material point labeled by R in the reference state moves to a new location at a radius $r(t)$. (b) Cross-section of a pristine solid cylindrical silicon nanowire of a radius R_S , with the same volume of the hollow silicon nanowire defined in (a). 143

Figure 6.2. Finite element simulation results on lithiation-induced stress field in a hollow silicon nanowire with a traction-free inner surface (a-c), with a fixed inner surface (d-f) and in a solid silicon nanowire (g-i). In hollow silicon nanowire, distributions of radial stress σ_r (a, d), hoop stress σ_θ (b, e) and axial stress σ_z (c, f) are shown for various reaction front positions (depicted by a dashed line) of $A/R_S=1.04$ (blue curve), $A/R_S=0.86$ (green curve) and $A/R_S=0.58$ (red curve). In solid silicon nanowire, distributions of radial stress σ_r (g), hoop stress σ_θ (h) and axial stress σ_z (i) are shown for reaction front positions (depicted by a dashed line) of $A/R_S=0.9$ (blue curve), $A/R_S=0.6$ (green curve) and $A/R_S=0.3$ (red curve). 146

Figure 6.3. Theoretical mechanics model results on lithiation-induced stress field in a hollow silicon nanowire with a traction-free inner surface (a-c) and with a fixed inner surface (d-f). Distributions of radial stress σ_r (a, d), hoop stress σ_θ (b, e) and axial stress σ_z (c, f) are shown for various reaction front positions (depicted by a dashed line) of $A/R_S=1.04$ (blue curve), $A/R_S=0.86$ (green curve) and $A/R_S=0.58$ (red curve). 155

Figure 6.4. Finite element simulation results on stress-modulated driving force for lithiation as a function of the lithiation front position A/R_S , for (a) a solid silicon nanowire and (b-d) hollow silicon nanowires with normalized inner radius of (b) $R_I/R_S=0.25$, (c) $R_I/R_S=0.5$ and (d) $R_I/R_S=0.75$, respectively. Blue lines in (b-d) represent the case of a hollow nanowire with a traction-free inner surface and red lines represent the case of a hollow nanowire with a fixed inner surface. 161

Figure 6.5. Theoretical mechanics model results on stress-modulated driving force for lithiation as a function of the lithiation front position A/R_S , for (a) a solid silicon nanowire and (b-d) hollow silicon nanowires with normalized inner radius of (b) $R_I/R_S=0.25$, (c) $R_I/R_S=0.5$ and (d) $R_I/R_S=0.75$, respectively. Blue lines in (b-d) represent the case of a hollow nanowire with a traction-free inner surface and red lines represent the case of a hollow nanowire with a fixed inner surface. 163

Figure 6.6. Schematic illustration of lithiation of Si NPs during the two-step lithiation. (a-c) In the first step of lithiation, the lithiation advances by a two-phase mechanism with a migrating amorphous-amorphous interface between α -Si phase and $Li_{2.5}Si$ phase. The interface exists until the α -Si phase is fully consumed, leading to a phase of $Li_{2.5}Si$. (c-d) In the second step of lithiation, the $Li_{2.5}Si$ phase is further lithiated to $Li_{3.75}Si$ phase without a visible interface. 167

Figure 6.7. Stress evolution of α -Si particle during two-step lithiation. (a)Radial

distribution of normalized lithium concentration C . The first step of lithiation advances via a two-phase mechanism, with an atomically sharp α -Si/Li_{2.5}Si interface propagating towards the center of the particle as indicated by the black arrow. In the second step of lithiation, the lithium concentration distribution within the particle is assumed to be uniform and ramps from 0.67 (Li_{2.5}Si) to 1 (Li_{3.75}Si). (b-d) stress ($\sigma_{\text{von-mises}}$, σ_r , σ_θ) distribution in the first step of lithiation. (d-f) stress distribution in the second step of lithiation. 170

Figure 6.8. Evolution of hoop stress at the surface layer of the particle undergoing (a) two-step lithiation of α -Si. To understand the stress releasing occurring in the second step of lithiation, two control simulations with two hypothetical lithiation mechanisms are carried out: (b) one-step and two-phase lithiation; (c) two-step lithiaiton with concentration-independent stiffness of Li_xSi phase. 174

Figure 6.9. Theoretical results of an α -Si particle undergoing two-step lithiation. (a) Hoop stress evolution at the particle surface ($R = B$) as a function of state of charge (SOC). The plastic yielding during the first step and the linear decreasing of hoop stress owing to stiffness softening during the second step are captured by the theoretical model. Snapshots (i-iv) illustrate the lithiation state at various SOC. The Von-Mises stress, hoop stress and radial stress distribution in the whole particle are plotted at (b) the start of second step ($SOC = 0.67$) and (c) end of second step ($SOC = 1$) 178

Figure 6.10. Stress evolution of hollow α -Si particle supported by inner rigid core during two-step lithiation. (a) Schematic of the hollow particle, with R_I being the inner radius, R_O the outer radius and R the distance from an element to the center. All dimension are defined in reference configuration (b) Representative Li profiles C along the radial direction are plotted as a function of $(R-R_I)/H$. (c-d) stress ($\sigma_{\text{von-mises}}$, σ_r , σ_θ) distribution in the first step of lithiation. (e-f) stress distribution in the second step of lithiation. Hoop stress is partially released because of the compression induced by the inner hard core. 181

Figure 6.11. Evolution of hoop stress at the surface layer of the hollow α -Si particle undergoing (a) two-step lithiation and (b) one-step two-phase lithiation. Direct comparison reveals that second step of lithiation partially releases the high tensile stress at surface layer which is built up in the first step. 182

Figure 6.12. Stress-modulated energy barrier for migration of lithiation front is shown with various lithiation front position in (a) solid α -Si (blue dots) and c-Si (red dots) particles and (b) hollow ones. Theoretical results are also shown to benchmark the FEM calculations 185

Figure 7.1. (a) Hierarchical structure of wood fiber. (b) Soft wood fiber substrates effectively release sodiation generated stresses by structural wrinkling. The thickness of Sn is 50 nm and the fiber diameter is $\sim 25 \mu\text{m}$. (c) Dual pathways for ion transport. The hierarchical and mesoporous structure of the fiber plays an important role as an

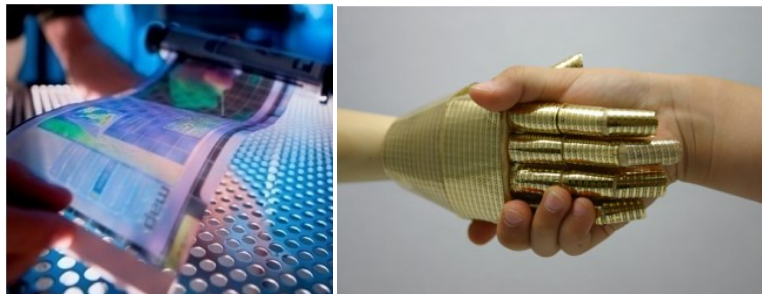
electrolyte reservoir.....	193
Figure 7.2. Electrochemical performance of the Sn anodes. (a) Galvanostatic charge/discharge voltage profiles of Sn@WF at the 1 st , 2 nd , 100 th , and 400 th cycle at a rate of C/10. (b) Cycling performance of Sn@WF, Al ₂ O ₃ coated fiber, and Cu current collector at a rate of C/10. The inset illustrates the structure of the wood fiber and Al ₂ O ₃ coated fiber.....	196
Figure 7.3. Sn@WF (a,c) before and (b,d) after 400 cycles at a rate of C/10. Sn on Cu current collector (e) before and (f) after 400 cycles. SEI formation and Sn volume expansion are clearly observed.	198
Figure 7.4. Chemomechanical modeling of the hoop stresses in Sn@WF at the fully sodiated (a) and desodiated (c) states. Color contours denote the hoop stress ($\sigma_{\theta\theta}$) level. The associated distributions of hoop stress normalized by yield stress versus location along film thickness are presented in (b) and (d). The hoop stress distributions for the Sn on a stiff substrate (Al ₂ O ₃ or Cu) are denoted by the dashed line for comparison. The stress level comparison reveals that the wrinkling of Sn@WF effectively releases the sodiation/desodiation induced mechanical stresses.	204

Chapter 1. Introduction

1.1. Background and Motivation

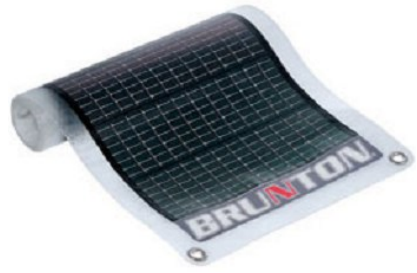
1.1.1. Flexible Electronics

The past decade has seen a wealth of research on flexible electronics, an emerging technology with an array of applications including flexible rollable display (Fig. 1.1a), skin-like sensors (Fig. 1.1b), printable solar cells (Fig. 1.1c) and flexible electronic paper (Fig. 1.1d) ¹⁻⁴. The study of flexible electronics is the culmination of the materials science, electronics, mechanics, and manufacturing fields toward the creation of electronic circuits fabricated on flexible substrates. Flexible electronics have the potential to outperform their traditional rigid counterparts in terms of flexibility, light weight, low cost and large area.



(a)

(b)



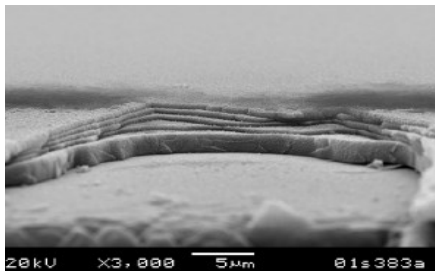
(c)



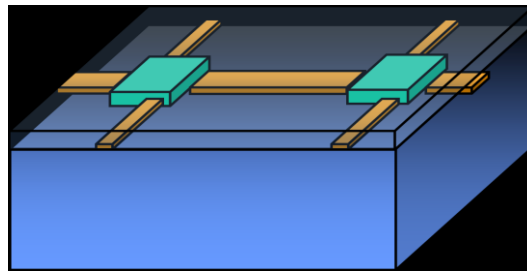
(d)

Figure 1.1. (a) Flexible rollable displays. (b) skin-like sensors. (c) printable solar cell. (d) flexible electronic paper

The new attractive attributes of flexible electronics result from the new building blocks (shown in Fig. 1.2) and new material combinations (e.g. inorganic/organic multilayer).



(a)



(b)

Figure 1.2. (a) Multilayer Structures. (b) Device islands on substrate.

However, these new building blocks and new material combinations also pose new mechanics challenge for robust design of flexible electronics. In the past two decades, fracture mechanics of thin brittle films on rigid substrates has been a focal topic in the discipline of solid mechanics. Existing studies have largely originated from the context of traditional microelectronics⁵⁻¹², thus focused on film-substrate structures with comparable stiffness and subject to small strains (~1%). Nevertheless, for flexible devices, the large difference in stiffness of the constituent materials of permeation barriers

(typically, the Young's modulus of inorganic material like ITO or aluminum oxide is more than 100 times higher than that of polyimide material) and the large mechanical deformation (up to 10%) they undergo cause the material response of inorganic/organic material combinations different from that of brittle films on rigid substrates. Therefore the rich but complicate failure behaviors of inorganic/organic hybrids that have not yet been clearly described in existing studies require new efforts to decipher its underpinning mechanism. On the research front of the fracture of thin brittle films on compliant substrates, Cotterell and Chen¹³ investigated the buckling and cracking of thin films on compliant substrate under compression; Ambrico and Begley¹⁴ explored the role of substrate compliance on channel cracking in a brittle film and found that on a compliant substrate the channel crack in the brittle film reaches steady-state propagation at a length much greater than the film thickness. Mei et al.¹⁵ investigated the effect of interfacial delamination on channel cracking of a brittle thin film on an elastic substrate, and showed that interfacial delamination not only increases the fracture driving force for channel crack growth, but also adds further to the fracture resistance by requiring additional energy for the interfacial fracture. These studies mainly focused on the fracture of film-on-substrate *bi-layer* structures, which shed important lights on but cannot fully capture the fracture characteristics of the *multilayer* organic-inorganic multilayer structures. For example, the channel cracking of an oxide layer in a multilayer permeation barrier can be constrained by the presence of adjacent stiff oxide films. Such a constraint is, in turn, mediated by the

thickness of the compliant organic layer in between two oxide films. Cordero et al.¹⁶ studied the critical strains for various configurations of channel cracks in an inorganic-organic-inorganic tri-layer permeation barrier on a polymer substrate and showed that the barrier can sustain the largest strain when the organic layer is of some intermediate thicknesses. However, co-evolving failure mechanisms in multilayer structures, namely, film cracking and interfacial delamination, are still at large and require systematic computational modeling.

Furthermore, in flexible electronics, substrate-supported metal layers are being developed as structural elements and functional components in modern technologies, with the promise of enhanced mechanical performance in comparison with freestanding metal layers. For example, thin metal films deposited on polymer substrates are often used as deformable interconnects in flexible electronic devices that are often subject to large stretches, bends and twists. Polymer-coated metal layers have been shown to be able to undergo significant plastic deformation before rupture, thus hold potential to serve as robust deformable metal conductors in flexible electronics. Most existing theoretical studies assume plane strain condition of the bilayer deformation. In practice, substrate-supported metal layers are often subject to large and complicated in-plane loading. For example, the electronic sensitive skins covering the elbow of a robot experience large biaxial stretches. Therefore, the understanding of necking instability of substrate-supported metal layers under arbitrary biaxial in-plane loading, however, is

poorly studied so far.

1.1.2. Lithium/Sodium-ion Batteries

Rechargeable lithium ion batteries are very crucial to portable electronic devices for their high specific capacity, low self-discharging rate, low weight and low cost. Typically, a lithium-ion battery comprises of an anode (negative electrode), a cathode (positive electrode) and lithium-ion conducting electrolyte (Fig. 1.3a) ¹⁷. On charging, lithium ions are extracted from the cathode and inserted into the anode, while reversed during discharging process. Compared with other available anode materials, such as graphite and metals, silicon is the most promising candidate for the lithium ion batteries because of its highest known theoretical charge capacity (ca. 4200mAh/g), more than ten times that of graphite anodes (around 372mAh/g). In addition, silicon is the second most abundant element in the world and thus inexpensive. Many types of Si-based anodes have been fabricated under laboratory conditions ¹⁸⁻³¹. However, wide applications of silicon-based anodes are still limited by the huge volume change (order of 400%) associated with the insertion and extraction of lithium ions. Such a massive volume change would cause fracture and pulverization of the electrode (Fig. 1.3b), thereby leading to capacity fading and failure of the battery cell after several charging\recharging cycles.

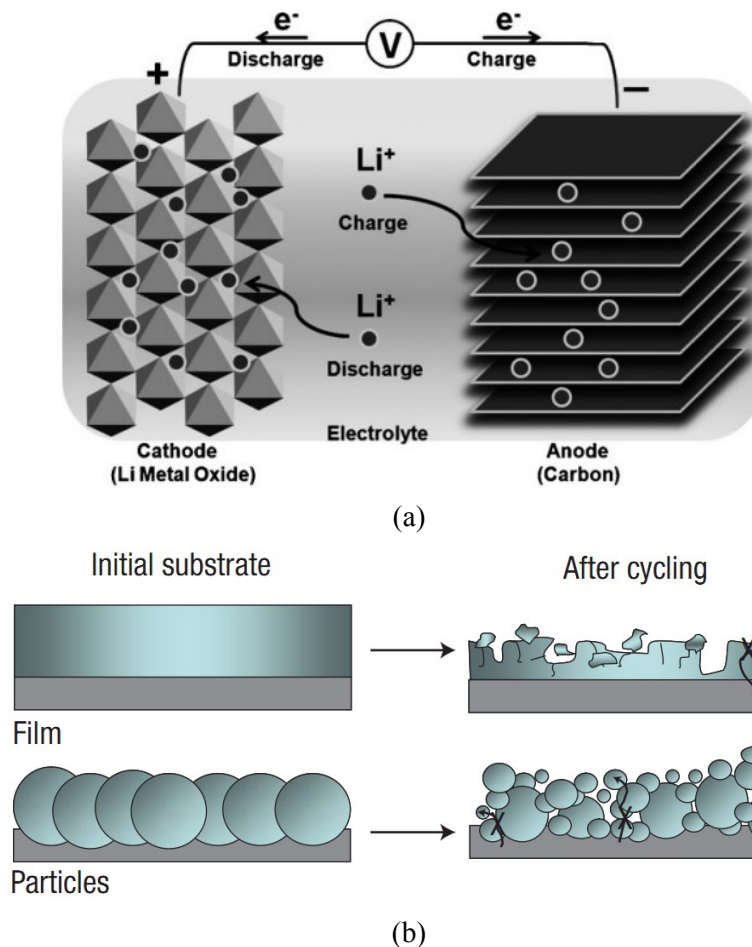


Figure 1.3. (a) Schematics of lithium-ion batteries. (b) Schematics of lithiation-induced fracture and pulverization³².

To circumvent the mechanical failure induced by large volume change, researchers have developed nano-structured Si-based anodes using nanowires³², core-shell nanowires³³, nano-silicon sponges³⁴, virus-enabled nano-anodes³⁵. Compared to bulk forms, nano-sized Si anode exhibits higher yield strength and fracture strength and is better capable of accommodating massive volume expansions, thus it is much less susceptible to failure induced by large volume change than their bulk counterparts. It has been reported that most of abovementioned nanostructured Si electrodes can provide capacity of 2000-3000mAh/g with 100 cycles. Nevertheless, the fundamental understanding of

lithiation-induced stress and failure mechanisms of such nanostructured Si electrodes still remains opaque. To decipher the underpinning science, theoretical formulations of mechanical failure in nano-anodes were established, such as bi-layer thin film model³⁶, core-shell model³⁷ and diffusion induced stress model³⁸. The results reveal that anode has a flow-tolerant critical size below which the mechanical failure can be avoided. However, plastic flow was also observed in silicon thin film anodes during lithium insertion and extraction through in situ observation of stress evolution³⁹. This observation reveals that irreversible deformation exists during electrochemical reaction in silicon anodes, which cannot be addressed by aforementioned mechanics theory. The plasticity effect on the mechanical performance of nanostructured Si anodes still need to be further explored. It has been reported that in nanostructured silicon anodes, lithiation reaction is a reaction rate-limiting process rather than a diffusion-limiting process, which is characterized by a moving sharp lithiation reaction boundary separating a fully lithiated Si phase and a pristine pure Si phase. Moreover, lithiation-induced fracture process has not been explicitly considered in existing studies. Therefore, comprehensive mechanics modeling integrating coevolving lithiation and plasticity deformation, moving sharp lithiation reaction boundary and lithiation-induced fracture is crucial to the understanding of underpinning failure mechanisms of nanostructured Si electrodes.

Besides energy storage technologies used in portable electronics and electronic vehicles, grid scale storage is also a crucial component of an energy landscape that incorporates a

wide variety of renewable energy sources. As discussed above, Li-ion batteries and other electrochemical storage methods are considered among the most promising technologies for energy storage due to their high energy density and cyclability^{32, 40, 41}. Grid scale storage requires a low cost, safe, and environmentally benign battery system. Na is an earth abundant material and therefore Na-ion batteries fulfill these requirements better than Li-ion batteries. Widespread implementation of Na-ion batteries is limited by several factors: (1) slow Na ion diffusion kinetics, (2) large volume changes and structural pulverization during charging/discharging, and (3) difficulty in maintaining a stable solid electrolyte interphase (SEI).⁴² These challenges are related to the large size of the Na ion, which makes it impossible to simply adopt the knowledge and strategies developed for high performance Li-ion batteries. Several cathode materials and electrolyte systems have been studied for Na-ion batteries, including bi-layered $\text{Na}_2\text{V}_2\text{O}_5$, P2 $\text{Na}_{0.66}\text{Fe}_{0.5}\text{Mn}_{0.5}\text{O}_2$, and fluorinated ethylene carbonate (FEC) as an electrolyte additive⁴³⁻⁵¹. Anode materials that have been investigated include metal oxides and alloys, hard carbon, and nano-composites^{46, 52, 53}. Sn is a promising anode material because it alloys with Na at a high specific capacity of 847 mAh/g when $\text{Na}_{15}\text{Sn}_4$ is formed. Studies of Sn film and nanostructured anodes were reported; the cycle life, however, is limited to 20 cycles due to pulverization⁵⁴⁻⁵⁶. The pulverization is primarily due to a 420% volume expansion associated with the formation of $\text{Na}_{15}\text{Sn}_4$ ⁵⁷. Recently developed Sn nanoforests and SnO_2 @graphene nanocomposites improve cycling performance but lack the

processability and cycling performance required for low cost grid scale storage^{58, 59}.

Further studies on developing high-performance tin-based anode is needed.

1.2. Scope and Goals of the thesis research

Aiming to understand the yet unexplored mechanisms that govern the mechanical durability of novel functional nanostructures in flexible electronics and lithium/sodium-ion batteries, the proposed research will be carried out through a coherent research framework integrating theoretical mechanics analysis, mechanics modeling and collaborative experiments. The rest of the thesis is organized as follows. Chapter 2 studies the inorganic film cracking and interfacial delamination in multi-layer nanostructures in flexible electronics and offers a simple but effective strategy to improve the mechanical durability of the multilayer nanostructures. Chapter 3 conducts mechanics modeling to simulate the brittle tensile cracking process of polymer-supported ITO thin films. At high tensile strain level, the underpinning science of buckling in ITO stripe induced by large lateral contraction due to Poisson's effect is also explored. Chapter 4 presents a comprehensive investigation to decipher the ductile failure and necking retardation mechanisms in two representative material structures, namely, a metal layer supported by a stiff plastic substrate, and a metal layer supported by a compliant elastomer substrate, respectively. Chapter 5 provides understanding of the mechanical

failure mechanisms of novel silicon anodes designs such as core-shell Si anodes, beads-string Si anodes and Si nanowalls by modeling the lithiation process and concomitant mechanical deformation. Chapter 6 investigates the lithiation-induced stress evolution in solid/hollow nanowire under one-stage or two stage lithiation mechanism. The contribution of stresses to lithiation kinetics and fracture behavior is also discussed. Chapter 7 introduce a novel nature-inspired design of cellulose-supported anodes for sodium-ion battery which possesses excellent electrochemical performance. Mechanics modeling reveals the origin of its excellent battery performance.

Chapter 2. Brittle Cracking of Inorganic/organic Multi-layered Structures in Flexible Electronics

2.1. Failure Mechanics of Organic-inorganic Multilayer Permeation Barriers in Flexible Electronics

2.1.1. Introduction

The past decade has seen a wealth of research on flexible electronics, an emerging technology with an array of promising applications, such as paper-like displays and organic light emitting diodes (OLEDs). Flexible electronics are attractive for their large deformability, low weight, large surface areas, and low cost. Organic materials (e.g., polymers), used for both active device layers and structural substrates, make these attributes possible. For example, the emissive electroluminescent layer of OLEDs is composed of a thin film of organic compounds; and flexible devices are often fabricated on thin polymer substrates. The functional organic materials used in flexible devices are extremely vulnerable to moisture⁶⁰⁻⁶⁴, thus result in a rather limited device lifetime — a grand challenge to the future success of flexible electronics technology. A natural choice for long-lasting flexible devices is to protect them with permeation barriers. Multilayer organic-inorganic permeation barriers are emerging as a promising solution to the stringent barrier requirement of flexible electronics⁶⁵. The mechanical failure of the multilayer permeation barriers under large deformation, however, could be fatal to the

barrier performance⁶⁵. So far, little attention, if any^{16, 66}, has been given to the failure mechanics of multilayer organic-inorganic permeation barriers. To address this largely unexplored issue, we study two co-evolving tensile failure mechanisms of the multilayer permeation barriers, namely, channel crack and interfacial delamination, through systematic computational modeling. Emerging from our study is a simple but effective design to enhance the durability of multilayer permeation barriers by applying a thin protective coating.

Designing a permeation barrier to allow a reasonable service life of flexible devices is remarkably challenging. For example, to guarantee a service life of about one year for OLEDs, the water vapor permeation rate (WVPR) of the barriers should be no more than 10^{-6} g/m²/day⁶⁷. In contrast, the WVPR requirements for current electronic devices (e.g., LCD displays) range from 10^0 g/m²/day to 10^{-2} g/m²/day, while the best traditional barriers can only achieve a WVPR of 10^{-3} g/m²/day, still over three orders of magnitude greater than the design criteria for OLEDs. Furthermore, the large and repeated deformation that flexible devices undergo also requires that the permeation barriers be rugged.

Organic materials (e.g., polymers) are often rugged but highly permeable to moisture, while inorganic materials (e.g., ceramics and glass) are almost impermeable to moisture but extremely fragile. Thus, neither by itself is an effective permeation barrier for flexible electronics. Such a conundrum has led to the design of multilayer barrier coatings

consisting of alternating thin films of inorganic and organic materials, with the hope to capitalize on both the impermeability of the inorganic layers and the ruggedness of the organic layers⁶⁶⁻⁶⁸. For example, a multilayer barrier made of a stack of alternating layers of polyacrylate and Al₂O₃ has been demonstrated to have a WVPR of about 2×10⁻⁶ g/m²/day at ambient conditions (e.g., Figure 2.1). It has been proposed that the organic layers “decouple” the pin-hole defects in neighboring Al₂O₃ layers, resulting in long and meandering moisture diffusion paths, thus significantly impeding the moisture permeation through the barrier⁶⁹. Such a promising barrier performance, however, was achieved in the as-made barriers that are not subject to large mechanical deformation.

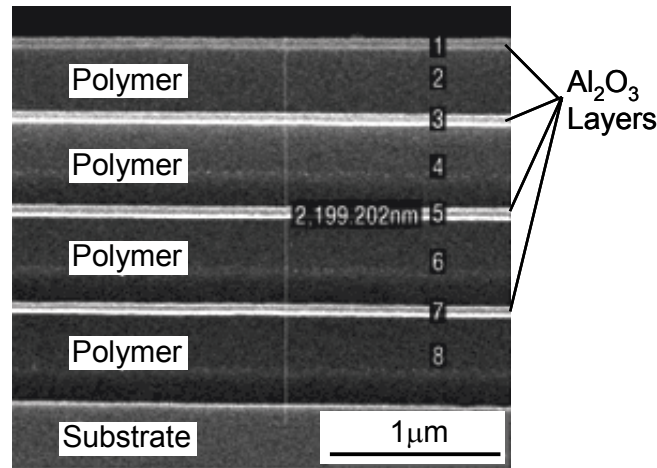


Figure 2.1 Scanning electron microscope image of the cross section of an organic-inorganic multilayer permeation barrier (Courtesy of Vitex Sys. Inc.)

Given the stringent barrier requirements for flexible electronics, any mechanical failure in the brittle oxide films of the multilayer barriers would be fatal for the barrier performance.

While the organic layers in multilayer barriers are compliant and can recover from large strains, the oxide layers are brittle and fracture at small strains. Typical fracture modes

include channel cracks in the oxide layers and delamination along the oxide-organic layer interfaces. Moisture permeates through an as-made multilayer barrier mainly via the pin-hole defects in the oxide layers (Figure 2.2a) ⁶⁹. By contrast, a channel crack in the oxide layer can substantially increase moisture permeation through the barrier by opening *a line source of moisture* (Figure 2.2b), rather than the point source from the initial pin-holes. The situation becomes even worse when oxide-organic layer interfacial delamination accompanies the channel crack propagation, because the moisture wicking along the delaminated interface results in *an area source of moisture* at the delamination site, as illustrated in Figure 2.2c. Therefore, fracture-induced defects (i.e., channel cracks and interfacial delamination) are expected to drastically accelerate moisture permeation through the barrier, and hence are fatal to the flexible devices. As a result, to study the barrier performance under large mechanical deformation, it is imperative to investigate the failure mechanism of the organic-inorganic hybrid layered structures.

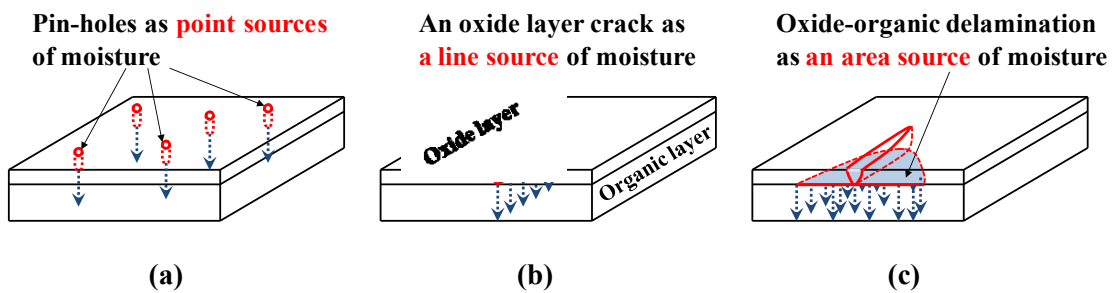


Figure 2.2. Moisture can permeate through various defects in a permeation barrier. (a) pin-holes in an as-made barrier; (b) a channel crack in the oxide layer of a barrier; and (c) delamination along the oxide-organic interface in a barrier.

Fracture mechanics of thin brittle films on rigid substrates has been a focal topic in the discipline of solid mechanics in the past two decades. Existing studies have largely originated from the context of traditional microelectronics⁵⁻¹⁰, thus focused on film-substrate structures with comparable stiffness and subject to small strains (~1%). For flexible devices, the large difference in stiffness of the constituent materials of permeation barriers (e.g., the Young's modulus of Al₂O₃ is more than 100 times higher than that of polyacrylate) and the large mechanical deformation they undergo leads to rich but complicate failure behaviors that have not yet been clearly described in existing studies. On the research front of the fracture of thin brittle films on compliant substrates, Cotterell and Chen¹³ investigated the buckling and cracking of thin films on compliant substrate under compression; Ambrico and Begley¹⁴ explored the role of substrate compliance on channel cracking in a brittle film and found that on a compliant substrate the channel crack in the brittle film reaches steady-state propagation at a length much greater than the film thickness. Mei et al.¹⁵ investigated the effect of interfacial delamination on channel cracking of a brittle thin film on an elastic substrate, and showed that interfacial delamination not only increases the fracture driving force for channel crack growth, but also adds further to the fracture resistance by requiring additional energy for the interfacial fracture. These studies mainly focused on the fracture of film-on-substrate *bi-layer* structures, which shed important lights on but cannot fully capture the fracture characteristics of the *multilayer* organic-inorganic permeation barriers. For example,

the channel cracking of an oxide layer in a multilayer permeation barrier can be constrained by the presence of adjacent stiff oxide films. Such a constraint is, in turn, mediated by the thickness of the compliant organic layer in between two oxide films. Cordero et al.¹⁶ studied the critical strains for various configurations of channel cracks in an inorganic-organic-inorganic tri-layer permeation barrier on a polymer substrate and showed that the barrier can sustain the largest strain when the organic layer is of some intermediate thicknesses. In that study, however, the organic-inorganic interfaces were assumed to remain perfectly bonded as channel crack propagates, thus no interfacial delamination was considered.

When a multilayer permeation barrier is under large deformation, it is highly possible that the oxide-organic layer interfacial delamination and the channel cracking of the oxide film facilitate each other and thus co-evolve. On one hand, as the delaminated oxide film becomes freestanding, it induces a larger driving force for channel crack propagation. On the other hand, the channel crack exerts more concentrated traction on the interface at the delamination front, promoting further delamination. The co-evolution of interfacial delamination and necking fracture of a thin Cu film on a compliant polyimide substrate under large tensile deformation has been predicted in computational modeling⁷⁰ and further observed in recent experiments^{71, 72}. The co-evolution of delamination and buckling of a compressive film on a substrate has also been studied earlier.

Aiming to understand the yet unexplored mechanisms that govern the mechanical durability of multilayer organic-inorganic permeation barriers, we study the co-evolving channel cracking and interfacial delamination in such barriers under tension, through computational modeling.

2.1.2. Computational Model

It has been shown that ¹⁶, if the organic layers are thicker than the oxide layers in a multilayer permeation barrier, channel cracking in the top oxide layer requires the least driving force when compared with other tensile failure modes (e.g., parallel channel cracking in multiple oxide layers, or channel cracking across the entire thickness of the coating). In the real design of multilayer permeation barriers (e.g., Figure 2.1), the organic layers are often much thicker (e.g., 5~7 times) than the oxide layers. Therefore, it is reasonable to assume the dominating tensile failure mode of a real barrier to be the channel cracking in the top oxide layer with possible interfacial delamination originating from the channel root. Since other oxide layers except the top one remains intact in this dominating failure mode, and the oxide layers are more than 100 times stiffer than the organic layers, it is justified to assume that the constraint from other layers of the barrier to the channel cracking and interfacial delamination of the top oxide layer is mainly due to the oxide layer next to the top one, while the contribution from other layers below, be it oxide or polymer, is negligible. Above said, we model a tri-layer barrier (two oxide layers sandwiching an organic layer) perfectly bonded to a thick polymer substrate, and

analyze the tensile failure of this structure using the finite element code ABAQUS.

Figure 2.3 illustrates the fracture of a blanket tri-layer barrier on a polymer substrate subject to uniaxial tension. Under sufficiently large tension, cracks initiate from built-in imperfections (e.g., pinholes, edges or corners) in the oxide layer and further propagate to form channel cracks. The stress concentration near the channel root can be severe enough to cause interfacial delamination. As to be shown later, under tension, the driving force for interfacial delamination decreases as the delamination advances in the tensile direction. As a result, the interfacial delamination eventually stops advancing in the tensile direction when such a driving force becomes smaller than the oxide-organic interfacial toughness. On the other hand, the channel crack continues propagating in the direction perpendicular to the applied tension and so does the concomitant interfacial delamination near the root of the channel crack front.

The detailed shape and deformation state near the front of the channel crack and the concomitant interfacial delamination can be rather complicated, and thus hard to predict. By contrast, far ahead and far behind the cracking and delamination front, the structure can be taken to deform under the plane strain conditions. To compute the driving force for interfacial delamination in the tensile direction, we simulate a slice of material of unit thickness far behind the cracking and delamination front and calculate the energy release rate at the delaminating front in the tensile direction using contour integral available in ABAQUS. Taking all materials in the structure to be linearly elastic, the driving force for

both the channel cracking and the interfacial delamination to propagate in the direction perpendicular to the applied tension can be calculated by the elastic energy stored in a slice of material of unit thickness far ahead of the fracture front minus the elastic energy stored in a slice of material of unit thickness far behind the fracture front.

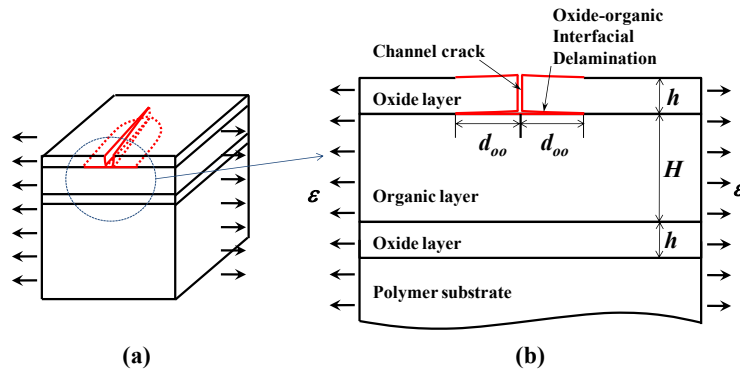


Figure 2.3. Schematic of (a) the computational model considering (b) both the channel crack in the oxide layer and the concomitant oxide-organic interfacial delamination.

In the simulation model, the two oxide layers are films of thickness h , the organic layer between two oxide layers is a film of thickness H , and the polymer substrate is a block of thickness $1000h$ and length $1000h$. The horizontal displacement is set to be zero along the centerline of the laminate, and set to be u along both sides of the laminate. The quantity $\epsilon = u/500h$ will be called the applied strain. Far behind the channel front, the width of the oxide-organic interfacial delamination originated from the channel root is d_{oo} at each side. In simulations, we fix the ratio $H/h=5$ but vary the ratio d_{oo}/h to study its effect on the driving force for delamination. In the region near the tip of the interfacial delamination, both the oxide film and the organic layer are densely meshed into four-node quadrilateral plane strain concentric-circle elements. The portion outside of this

region are meshed with triangle plane strain elements of matching sizes near the regions and coarser elements far away from the regions to reduce the computation time. In the simulations, the Young's modulus and the Poisson's ratio of the oxide layer are $E_{oxide} = 300 \text{ GPa}$ and $\nu_{oxide} = 0.3$, respectively, and those of the organic layer are $E_{organic} = 2 \text{ GPa}$ and $\nu_{organic} = 0.3$, respectively. The Young's modulus and the Poisson's ratio of the substrate are taken to be the same as that of the organic layer, respectively. These values are representative of an Al_2O_3 /polyacrylate multilayer permeation barrier on a polyethylene terephthalate substrate.

2.1.3. Driving Forces for Interfacial Delamination and Channel Cracking in a Multilayer Permeation Barrier under Tension

The driving force for interfacial delamination *in the tensile direction* far behind the channel front (e.g., inset of Figure 2.4a) can be represented by the energy release rate at the delamination front. Dimensional considerations lead to this energy release rate taking the form

$$G_d = f\left(\frac{d_{oo}}{h}, \frac{E_{organic}}{E_{oxide}}, \frac{H}{h}\right) E_{oxide}^* \varepsilon^2 h, \quad (2.1)$$

where $E_{oxide}^* = E_{oxide} / (1 - \nu_{oxide}^2)$ is the plane strain modulus of the oxide. The dimensionless function f denotes the normalized driving force of interfacial delamination and can be calculated numerically by contour integral using finite element method.

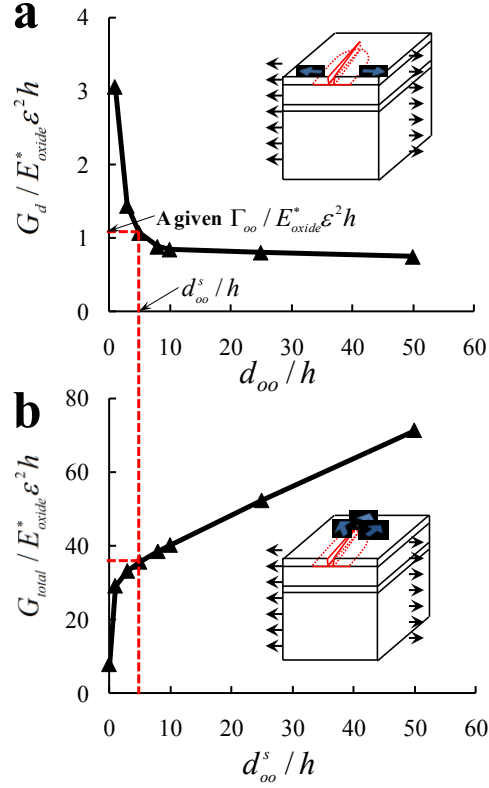


Figure 2.4. (a) Normalized driving force of interfacial delamination along the tensile direction as a function of normalized delamination width; (b) Normalized driving force of oxide cracking and interfacial delamination perpendicular to the tensile direction as a function of normalized steady-state delamination width.

Figure 2.4a plots normalized driving force of interfacial delamination $G_d / E_{oxide}^* \epsilon^2 h$ as a function of normalized delamination width d_{oo} / h . When the delamination width is small (e.g., $d_{oo} / h < 1$), the stress concentration near the channel crack root leads to a significantly large driving force of interfacial delamination. As the delamination width increases, the driving force of interfacial delamination drops considerably when $d_{oo} / h < 10$ and then gradually reaches a plateau when $d_{oo} / h > 10$. The initiation and propagation of the interfacial delamination is governed by the competition between driving force G_d and oxide-organic interfacial toughness Γ_{oo} . Figure 2.4a indicates that,

for a modest oxide-organic interfacial toughness, delamination can initiate at the channel crack root. As the delamination advances along the interface in the tensile direction, the driving force decreases. The delamination eventually stops propagating at a width, d_{oo}^s , where the driving force drops to the value of the interfacial toughness, i.e., $G_d = \Gamma_{oo}$.

We next compute the total driving force G_{total} for both the channel cracking and the interfacial delamination to propagate *in the direction perpendicular to the applied tension* (e.g., inset of Figure 2.4b). G_{total} takes a form similar to Eq. (2.1) but with a different dimensionless function f . As discussed in section 2.1.2, the stress state and deformation characteristics near the channel cracking front and the concomitant interfacial delamination are rather complicated. Assuming the structure deforms elastically, G_{total} can be calculated by comparing the elastic energy stored in a slice of material of unit thickness far ahead of the fracture front and that stored in a slice of material of unit thickness far behind the fracture front. We consider the steady-state fracture process where far behind the channel cracking front the oxide-organic interfacial delamination reaches a constant width of d_{oo}^s . Figure 2.4b plots $G_{total} / E_{oxide}^* \epsilon^2 h$ as a function of the normalized steady-state delamination width d_{oo}^s / h . In the case of perfect bonding between the oxide layer and the organic layer (e.g., no interfacial delamination, $d_{oo}^s / h = 0$), G_{total} corresponds to the driving force for pure channel cracking, which agrees with previous study^{15, 16}. Once interfacial delamination occurs and advances, G_{total} increase significantly. This can be explained by the considerable elastic energy

released from the delaminated portion of the oxide layer in the wake of the channel cracking due to the loss of substrate constraint. For example, G_{total} triples for $d_{oo}^s/h=1$ and increases nearly six times for $d_{oo}^s/h=25$. By contrast, if there is no interfacial delamination, only a narrow region in the oxide layer along the channel crack surface can be relaxed, leading to a modest elastic energy release. The condition for steady-state channel cracking and interfacial delamination can be described as

$$G_{total} \geq \Gamma_{oxide} + 2\Gamma_{oo}d_{oo}^s/h \quad (2.2)$$

where Γ_{oxide} is the cohesive fracture toughness of the oxide layer, and the second term on the right denotes the energy required for the interfacial delamination accompanying per unit area advance of the channel crack.

For a given oxide-organic interfacial toughness Γ_{oo} , one can determine the corresponding steady-state delamination width d_{oo}^s (e.g., Figure 2.4a), from which one can further obtain G_{total} (e.g., Figure 2.4b). In this sense, both d_{oo}^s and G_{total} are functions of Γ_{oo} . By moving the term of $2\Gamma_{oo}d_{oo}^s/h$ in Eq. 2.2 to the left-hand side, an effective driving force for steady-state channel cracking of the oxide layer can be defined as

$$G_{eff} = G_{total} - 2\Gamma_{oo}d_{oo}^s/h \quad (2.3)$$

and thus the condition for steady-state channel cracking can be given by

$$G_{eff} \geq \Gamma_{oxide} \quad (2.4)$$

in which the right-hand side denotes the resistance that is independent of the interfacial property, and the left-hand side represents the driving force that is a function of the

oxide-organic interfacial toughness.

Figure 2.5 plots the normalized effective driving force for channel cracking G_{eff}/G_0 as a function of normalized interfacial toughness $\Gamma_{oo}/E_{oxide}^*\epsilon^2h$. Here G_0 is the driving force for channel cracking without oxide-organic interfacial delamination, i.e., $G_0 = G_{total}(d_{oo}^s = 0)$ as in Figure 2.4b. The smaller the oxide-organic interfacial toughness, the larger the steady-state delamination width, and therefore, the larger the effective driving force for channel cracking of the oxide layer.

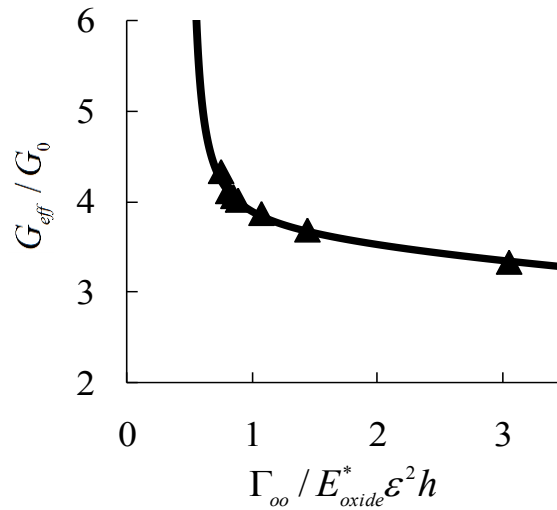


Figure 2.5. Normalized effective driving force for channel cracking as a function of normalized interfacial toughness.

2.1.4. Effect of a Protective Coating on the Durability of a Multilayer Permeation Barrier

The results in Section 2.1.3 show that the tensile failure of the organic-inorganic multilayer permeation barriers is driven by the elastic energy release due to the channel

cracking of the top oxide layer and the delamination along the oxide-organic interface. To enhance the mechanical durability of the multilayer permeation barriers under tension, we propose to add a thin deformable protective coating (e.g., a polymeric material) on the surface of the top oxide layer in the permeation barrier. The polymeric coating can sustain large tensile deformation without rupture, therefore can offer additional mechanical constraint that leads to a reduced driving force for the channel cracking and interfacial delamination in the permeation barriers. In this section, we quantify the reduction of these driving forces as a function of the stiffness and thickness of the protective coating. Here we assume a perfect bonding between the protective coating and the top oxide layer, i.e., no coating-oxide delamination. The effect of possible delamination along the coating-oxide interface will be discussed in next section.

When a multilayer permeation barrier with a thin protective coating is under tension, the cracks may initiate from pre-existing imperfections in the top oxide layer and then tunnel through. Due to the mechanical constraint of the protective coating, the elastic energy released by such a tunnel crack is less than that by a channel crack in a bare permeation barrier without protective coating.

Figure 2.6 plots the normalized driving force $G_0^p / E_{oxide}^* \varepsilon^2 h$ for a tunnel crack in the top oxide layer of a permeation barrier with a protective coating of thickness h_p , as a function of the stiffness of the protective coating E_p . Here it is assumed that no oxide-organic interfacial delamination occurs. For comparison, the normalized driving force for a

channel crack in the top oxide layer of a bare permeation barrier without oxide-organic interfacial delamination $G_0 / E_{oxide}^* \epsilon^2 h$ is also included (the dash line). There is a nearly four-fold decrease in the driving force of oxide layer cracking when a protective coating is applied. Such a drastic decrease in fracture driving force also shows weak dependence on the stiffness and thickness of the protective coating. For example, a very compliant protective coating (e.g., $E_p = 2$ MPa) of the same thickness of the oxide layer can lead to a similar reduction of crack driving force comparable to that due to a stiff and thick protective coating (e.g., with a stiffness of 20 GPa and a thickness ten times of the oxide layer).

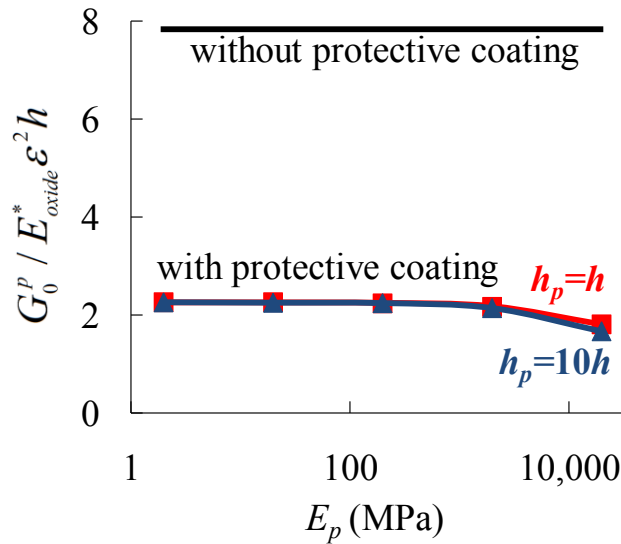


Figure 2.6. The normalized driving force for a tunnel crack in the top oxide layer of a permeation barrier with a protective coating of thickness h_p , as a function of the stiffness of the protective coating E_p .

We now consider the case where delamination along the oxide-organic interface can emanate from the root of a tunnel crack in the top oxide layer of a permeation barrier with protective coating. In such a case, the protective coating is expected to constrain the

opening of the tunnel crack, thus leading to a limited relaxation of the elastic energy in the debonded portion of the oxide layer and organic layer, therefore resulting in a decrease in the driving forces for both interfacial delamination and tunnel cracking.

The driving force for the oxide-organic interfacial delamination in the tensile direction far behind the channel front now takes the form

$$G_d^p = f_p \left(\frac{d_{oo}}{h}, \frac{E_{organic}}{E_{oxide}}, \frac{E_p}{E_{oxide}}, \frac{H}{h}, \frac{h_p}{h} \right) E_{oxide}^* \varepsilon^2 h \quad (2.5)$$

Figure 2.7a plots the normalized driving force for interfacial delamination $G_d^p / E_{oxide}^* \varepsilon^2 h$ as a function of the steady-state delamination width d_{oo}^s / h , for various stiffness of the protective coating (i.e., $E_p = 2$ MPa, 20 MPa, 200MPa, 2GPa and 20GPa, which are representative of polymers ranging from very compliant elastomers to stiff plastics). Here the thickness of the protective coating is taken to be the same as that of the oxide layer, i.e., $h_p/h = 1$. When compared with the case of no protective coating (i.e., Figure 2.4a), Figure 2.7a clearly shows that, a thin ($h_p/h = 1$) and compliant (e.g., $E_p = 2$ MPa) protective coating can significantly reduce the driving force for the oxide-organic interfacial delamination. For example, when $d_{oo}^s / h \leq 10$, the reduction of the delamination driving force is approximately three-fold if a protective layer is applied. When $d_{oo}^s / h \geq 25$, the protective layer reduces the delamination driving force to nearly zero. Furthermore, this reduction of the delamination driving force remains nearly independent of the protective coating stiffness, unless a very stiff polymer coating (e.g., $E_p = 20$ GPa) is applied, which leads to an even more substantial reduction of the

delamination driving force.

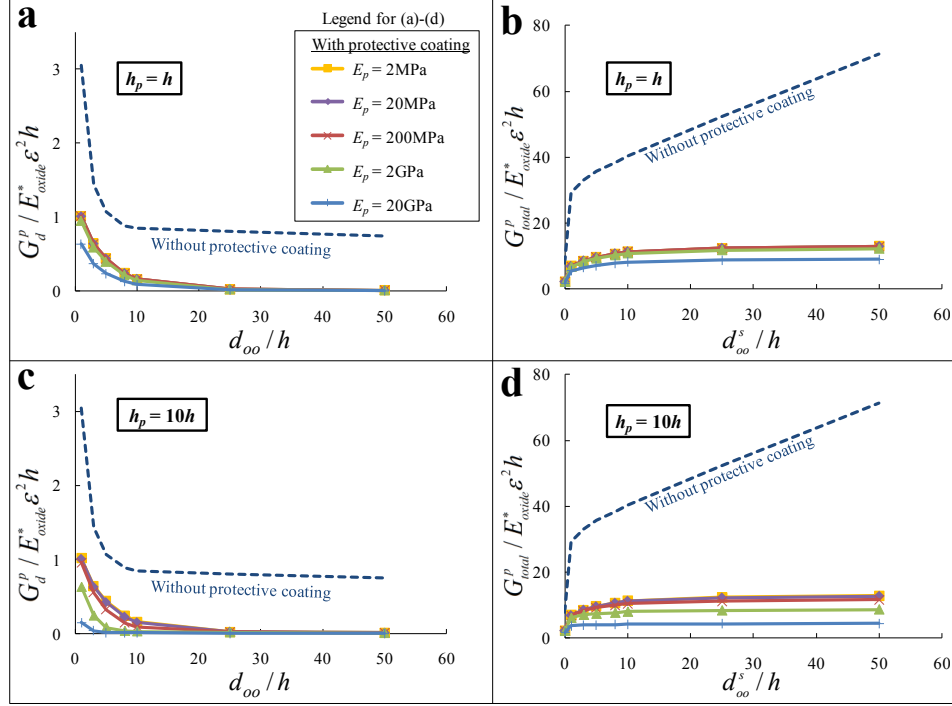


Figure 2.7. Normalized driving force as a function of normalized delamination length.

When a protective coating is applied, the total driving force G_{total}^p for both the tunnel cracking and the interfacial delamination to propagate in the direction perpendicular to the applied tension takes a form similar to Eq. (2.5) but with a different dimensionless function f_p . G_{total}^p can be computed and is plotted as a function of the normalized steady-state delamination width d_{oo}^s / h , as shown in Figure 2.7b. When compared with the case of no protective coating (i.e., Figure 2.4b), Figure 2.7b also clearly shows substantial reduction of the total driving force G_{total}^p . For example, when $d_{oo}^s / h \leq 10$, the reduction of G_{total}^p is more than four-fold, if a protective coating is applied. When $d_{oo}^s / h \geq 25$, $G_{total}^p / E_{oxide}^* \epsilon^2 h$ reaches a plateau of ~ 12.8 . By contrast, if there is no

protective coating (e.g., Figure 2.4b), the total driving force increases approximately linearly with d_{oo}/h when $d_{oo}^s/h \geq 25$. Figure 2.7b also shows a dependence of the reduction of G_{total}^p on the stiffness of the protective coating similar to that in Figure 2.7a. Figure 2.7c and 2.7d further plot $G_d^p/E_{oxide}^* \varepsilon^2 h$ and $G_{total}^p/E_{oxide}^* \varepsilon^2 h$ as functions of d_{oo}^s/h for the case of $h_p/h = 10$, respectively. A thicker protective coating can result in more substantial reduction of $G_d^p/E_{oxide}^* \varepsilon^2 h$ and $G_{total}^p/E_{oxide}^* \varepsilon^2 h$. The dependence of the reduction of fracture driving force on protective coating stiffness is also stronger when a thicker protective coating is applied.

Following the similar procedure in Section 2.1.3, an effective driving force for steady-state tunnel cracking of the oxide layer can be defined as

$$G_{eff}^p = G_{total}^p - 2\Gamma_{oo} d_{oo}^s / h, \quad (2.6)$$

which takes into account of the effects of both the oxide-organic delamination and that of the protective coating. Figure 2.8 plots $G_{eff}^p/E_{oxide}^* \varepsilon^2 h$ as a function of normalized interfacial toughness $\Gamma_{oo}/E_{oxide}^* \varepsilon^2 h$. Here $h_p/h = 1$. Figure 2.8 clearly shows that, for a given oxide-organic interfacial toughness, the effective driving force for oxide layer cracking can be considerably reduced when a thin and compliant protective coating is applied on the top of the oxide layer. Such a reduction of effective driving force for oxide layer cracking is nearly independent of stiffness of the protective coating when $E_p \leq 2$ GPa. A very stiff plastic protective coating (e.g., $E_p = 20$ GPa) can further reduce the effective cracking driving force modestly.

The results in this section reveal a simple but effective design strategy to improve the durability of the organic-inorganic multilayer permeation barriers in flexible electronics. Well bonded to the surface of the top oxide layer, even a thin and compliant protective coating (e.g., an elastomeric layer with a thickness comparable to that of the oxide layer) can considerably reduce the driving forces for the tunnel cracking of the top oxide layer and the oxide-organic interfacial delamination. In other words, a multilayer permeation barrier with protective coating can sustain larger elongations before fracture than a bare multilayer permeation barrier.

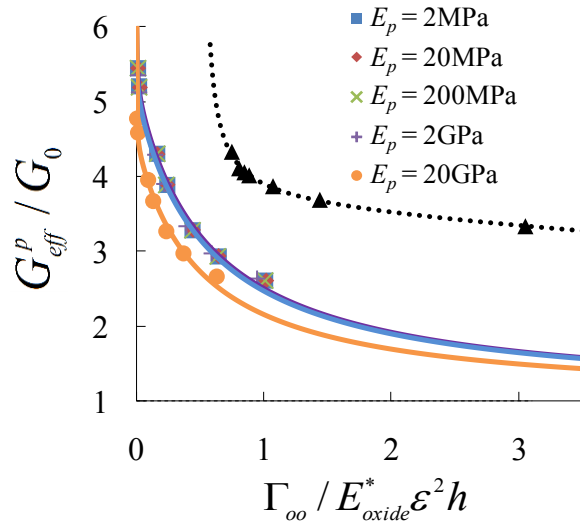


Figure 2.8. Effective driving force as a function of normalized interfacial toughness for various stiffness of the protective coating. Here $h_p/h = 1$.

2.1.5. Discussion

The reduction of the fracture driving forces reported in Section 2.1.4 results from the constraint of the protective coating to the elastic energy release in the wake of oxide layer tunnel cracking and oxide-organic interfacial delamination. If the adhesion between the

protective coating and the top oxide layer is not sufficiently strong, the stress concentration due to the tunnel cracking near the coating-oxide interface may cause delamination. As a result, the mechanical constraint of the protective coating to the top oxide layer is weakened, leading to less reduction of the driving force for oxide layer tunnel cracking and oxide-organic interfacial delamination.

To study the impact of possible delamination along the interface between the protective coating and the top oxide layer, we simulate two cases: (1) delamination occurs only along the coating-oxide interface; (2) delaminations occur along both the coating-oxide interface and the oxide-organic interface.

The simulation results for case 1 are presented in Figure 2.9, which plots the normalized driving force for oxide layer cracking as a function of the normalized stiffness of the protective coating E_p , for two protective coating thickness, $h_p/h = 1$ and 10, and two coating-oxide delamination length, $d_{po}/h = 0.1$ and 2, respectively. The driving force for the oxide layer tunnel cracking without coating-oxide and oxide-organic interfacial delaminations, as well as that for the oxide layer channel cracking without oxide-organic interfacial delamination (i.e., Figure 2.6), are included for comparison. If the protective coating is stiff and relatively thick (e.g., $E_p = 20$ GPa and $h_p/h = 10$), the reduction of the driving force for oxide layer cracking decreases from nearly four-fold (from Figure 2.6) to nearly two-fold, if a delamination of length $d_{po} = 2h$ occurs along the coating-oxide interface. If the protective coating is too compliant (e.g., $E_p = 20$ MPa), a small

delamination (e.g., $d_{po}/h = 0.1$) along the coating-oxide interface can lead to a driving force for oxide layer cracking comparable to that in a permeation barrier without protective coating.

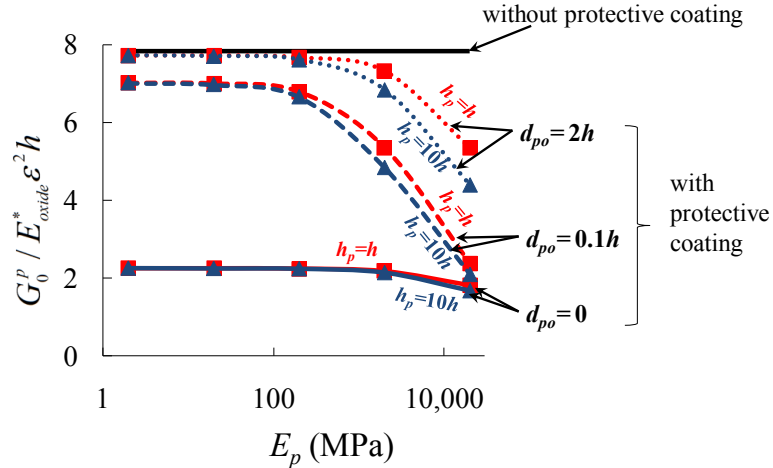


Figure 2.9. Dash and dotted lines with markers plot the normalized driving force for oxide layer cracking as a function of E_p , for $h_p/h = 1$ and 10 , and $d_{po}/h = 0.1$ and 2 , respectively. Curves in Figure 2.6 are included for comparison (dash line and solid lines with markers).

The simulation results for case 2 are presented in Figure 2.10, and compared with the results in Figures 2.7a and 2.7b. In case 2, a delamination of length $d_{po} = h$ along the coating-oxide interface is prescribed. In comparison with Figure 2.4a, Figure 2.10a plots the normalized driving force for oxide-organic interfacial delamination in the tensile direction as a function of d_{oo}^s / h . For a compliant protective coating (e.g., $E_p \leq 200$ MPa), a short delamination along the coating-oxide interface results in an elevated driving force for oxide-organic interfacial delamination comparable to that of a bare permeation barrier. In other words, a compliant protective coating debonded from the oxide layer can only provide negligible mechanical constraint to the elastic energy release in the wake of oxide tunnel cracking. For a stiff protective coating (e.g., $E_p = 20$ GPa), a short delamination

along the coating-oxide interface leads to a modest increase in the driving force for oxide-organic interfacial delamination when d_{oo}^s/h is small. Such an increase gradually diminishes when $d_{oo}^s/h \geq 25$. In comparison with Figure 2.4b, Figure 2.10b plots the normalized total driving force for both the tunnel cracking and the interfacial delamination to propagate in the direction perpendicular to the applied tension as a function of d_{oo}^s/h . A short delamination along the coating-oxide interface induces a loss of mechanical constraint of a compliant protective coating similar to that shown in Figure 2.10a. When a stiff protective coating is applied, the loss of mechanical constraint is partial and remains to be approximately constant as d_{oo}^s/h increases.

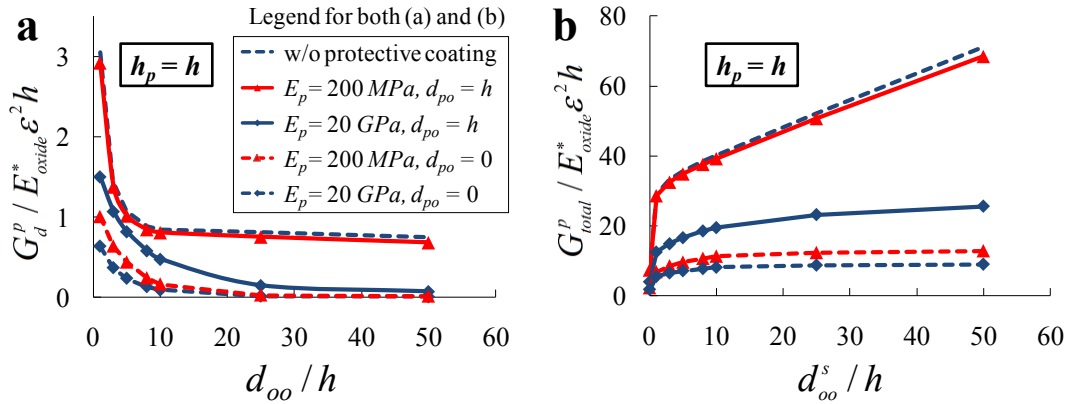


Figure 2.10. Impact of the coating-oxide interfacial delamination on (a) the driving force for oxide-organic interfacial delamination along the tensile direction and on (b) the driving force for both oxide layer cracking and oxide-organic interfacial delamination perpendicular to the tensile directions. Here $h_p/h = 1$. The corresponding curves in Figure 2.7 are included for comparison (dash line and dash lines with markers).

The above simulation results show that, delamination along the coating-oxide interface is detrimental for a compliant protective coating, causing nearly the loss of its mechanical constraint. On the other hand, a stiff protective coating can tolerate short delamination

along the coating-oxide interface by providing partial mechanical constraint to the failure of the permeation barrier. The results in Figures 2.9 and 2.10 can offer quantitative guidelines for the material selection and interface adhesion control of the protective coating.

2.1.6. Summary

We perform comprehensive computational modeling to study the tensile failure of organic-inorganic multilayer permeation barriers in flexible electronics. Major findings of the present study are recapped as follows:

1. Two failure mechanisms that are fatal for the barrier performance, namely, cracking of the top oxide layer and delamination along the oxide-organic interface, are shown to facilitate each other, and thus to co-evolve.
2. The driving force for the oxide-organic delamination along the tensile direction and that for the oxide layer cracking and the concomitant oxide-organic delamination perpendicular to the tensile direction are quantitatively determined, from which an effective driving force for the oxide layer cracking is defined and shown to decrease as the oxide-organic interfacial adhesion increases. This suggests that a strong interlayer adhesion is crucial for the mechanical durability of the multilayer hybrid permeation barriers.
3. Emerging from the above results is a structural design strategy to enhance the durability of the multilayer permeation barriers, that is, by well bonding a protective

coating onto the surface of the oxide layer. We show that a thin, compliant and well bonded protective coating can offer effective mechanical constraint to the permeation deformation and thus substantially decrease the effective oxide cracking driving force by several folds.

4. Further studies show that strong adhesion between the protective coating and the top oxide layer is crucial for the coating performance. Delamination along the coating-oxide interface can result in partial or nearly total loss of the mechanical constraint from the protective coating, depending on the stiffness of the coating.

The results from the present study are expected to offer mechanistic understanding of the failure mechanics of the multilayer hybrid permeation barriers in flexible electronics. The simple but effective strategy of applying a protective coating can potentially improve the mechanical durability of the permeation barriers. While the results from this study can provide quantitative guidance for the material selection and structural optimization of the permeation barriers, further experimental investigation are needed to validate abovementioned research findings.

2.2. Fracture Mechanics in Indium Tin Oxide-based Multilayer Electrodes¹

2.2.1. Introduction

¹ *Experimental results in section 2.2 were obtained by Dr. Cheng Peng and Prof. Jun Lou from department of materials science and nanoengineering, Rice University.*

Indium Tin Oxide (ITO) is one of the most widely used transparent conducting oxides in applications such as electronic displays and solar cells. The low resistivity and high transmittance of ITO have led to the recent explorations of polymer-supported ITO films as the transparent electrodes in flexible electronics. Flexible devices are often subject to repeated large deformation. While compliant polymer substrates can sustain large strain, brittle ITO films often fracture at a small strain. The cracking of ITO electrodes leads to loss of electrical conductance, posing crucial challenge to the reliability of flexible devices. As an effort to address this challenge, a multilayer structural design of ITO-based electrodes with enhanced electro-mechanical durability is reported here. In particular, in situ electro-mechanical experiments done by our collaborators and our coherent mechanics modeling reveal that, a top protective polymeric coating above and an intermediate polymeric layer below the ITO electrode can effectively reduce the driving force for cracking of the ITO electrode. The findings suggest a feasible solution to durable transparent electrodes for flexible electronics.

The multilayer structural design of ITO-based electrodes in the present study is inspired by the recent progress in designing high performance permeation barriers for flexible electronics. While flexible electronics is being developed toward an array of promising applications (e.g., paper like displays and sensitive electronic skins, etc) ^{1, 16, 73, 74}, the service life of flexible devices is limited due to the vulnerability of functional organic layers in flexible devices to the attack of environmental water vapor and oxygen. High

performance permeation barriers are desired to achieve long-lasting flexible electronics devices. However, designing such permeation barriers to allow a reasonable service life of flexible devices is rather challenging, given the design criteria over three orders of magnitude more stringent than that of traditional barriers in terms of water vapor permeation rate and the large deformation of the flexible devices. Recently, organic-inorganic multilayer permeation barriers (e.g., alternating layers of polyacrylate and Al_2O_3) are emerging as a promising solution to the stringent barrier requirement of flexible electronics. In such multilayer permeation barriers, the inorganic layer serves as the barrier for water vapor and oxygen and the organic layers decouple the defects (e.g., pinholes) in the as-made inorganic layers and thus yield a remarkably elongated diffusion path for water and oxygen molecules. Modeling study of the failure mechanics of multilayer permeation barriers shows that the organic layers can also increase the critical fracture strain of the inorganic layers¹⁶. A recent study further reveals that a compliant protective coating on the top inorganic layer in a multilayer permeation barrier can further enhance the mechanical durability of the permeation barriers⁷⁵.

Motivated by the progress in the abovementioned multilayer permeation barriers, our collaborators design and fabricate ITO-based multilayer electrodes with enhanced electro-mechanical durability. The failure mechanics of the ITO-based multilayer electrodes are investigated through both in situ electro-mechanical experiments of the electrodes and coherently devised mechanics modeling. So far, existing studies on

inorganic/organic multilayer permeation barriers for flexible electronics are mainly based on modeling and no systematic experimental study of their failure mechanics has been reported. In this sense, results from the present paper could also potentially lead to a better understanding of the failure mechanisms of multilayer permeation barriers.

2.2.2. Experimental Design and Tests of ITO-based Multilayer Electrodes

Five different structures of ITO-based multilayer electrodes are designed and fabricated, and schematics of the cross-section view of these five structures are showed in Figure 2.11. The polyethylene terephthalate (PET, 127 μm thick) in well-cut dog-bone shape (gauge length and width are 7 mm and 3 mm, respectively) is employed as the substrate. The PET substrate is first coated by an Al_2O_3 (60 nm thick) layer using e-beam evaporation method (Sharon E-Beam Evaporator). In Structure 1, an ITO layer (80 nm thick) is further coated directly on top of the Al_2O_3 layer, using e-beam evaporation method. In Structure 2, an intermediate polymeric layer of polymethyl methacrylate (PMMA, 495A2 from MicroChem Corp.) is first coated onto the surface of the Al_2O_3 layer by spin coating method with the speed of 1000 rms for 30 seconds, and the resulting thickness of PMMA is about 100 nm. An ITO layer (80 nm thick) is then coated on top of the PMMA layer. In Structure 3, S1813 (Shipley Microposit S1813 photoresist) is used as intermediate polymeric layer between the Al_2O_3 and ITO layers and is spin coated with the speed of 3000 rms for 30 seconds with a resulting thickness about 1 μm . In Structures 4 and 5, a layer of PMMA (100 nm thick) and S1813 (1 μm thick) is spin coated on top

of the ITO layer of Structure 3, respectively, serving as a top protective coating. The thicknesses of various layers in these five structure designs are determined by an atomic force microscope (Digital Instrument Nanoscope IIIA), using the contact mode. To ensure the well bonding in between layers in all five designs, a 5 nm thick Cr layer (not shown in Figure 1 for visual clarity) is coated between adjacent layers by e-beam evaporation method.

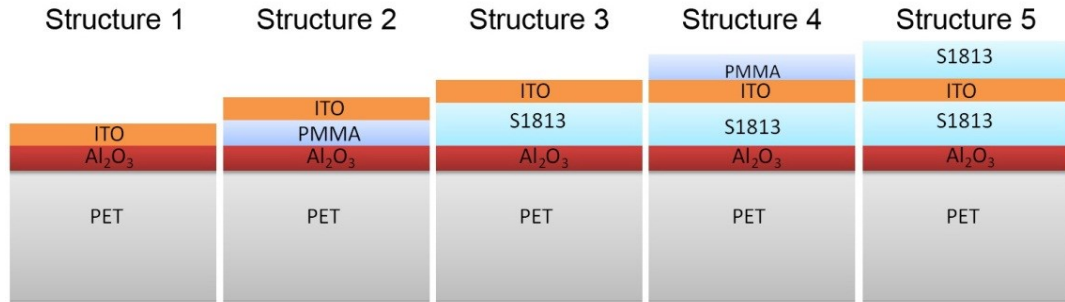


Figure 2.11. Schematics of five structural designs of ITO-based multilayer electrodes. The thicknesses of PET, Al₂O₃, ITO, PMMA, and S1813 are 127 μm, 60 nm, 80 nm, 100 nm and 1 μm, respectively. A 5 nm Cr layer is coated between adjacent layers to increase interlayer adhesion (not shown for visual clarity).

To characterize the channel cracks initiation and propagation of the ITO layers in different multilayer electrode structures, *in situ* uni-axial tensile tests are performed inside a SEM chamber. The *in situ* tensile tests are of particular importance to correlate crack initiation and propagation process with the applied tensile strain, and to avoid the unloading-induced partial or full closure of cracks in the ITO layer in *ex situ* tests.

The channel crack initiation and propagation process in the ITO layer in Structures 1, 2 and 3 are quite similar: ITO layers are very smooth, without any appreciable cracks before loading; as the tensile strain increases to a threshold value, small channel cracks

start to initiate at the edges of sample and then grow along the sample width direction, perpendicular to the tensile loading direction. Figure 2.12 shows a series of snapshots of these multilayer electrodes during tensile loading. Some interesting phenomena are found as following. First, the channel crack distribution in the ITO film is quite uniform along the sample length direction (also the loading direction), which suggests that the rather uniform elongation of the PET substrate. Second, as the strain level increases, the number of channel cracks in the same structure would increase, e.g., the number is only 4 in Figure 2.12(b) but 8 in Figure 2.12(e). Finally, at the same strain level, the number of cracks is affected by the existence and thickness of the intermediate polymer layer: the number of cracks can be reduced after inserting a thin polymer layer in Structure 2, compared to Structure 1 (Figure 2.12(a) and (b), and Figure 2.12(d) and (e)), even the thickness of the polymer is on the same order of Al_2O_3 barrier and ITO function layer (100 nm PMMA, 60 nm Al_2O_3 and 80 nm ITO); and the number of cracks can be further reduced if the polymer thickness is increased in Structure 3 (1 μm S1813), compared to Structure 2 (Figure 2.12(b) and (c), and Figure 2.12(e) and (f)). It is worth noting that, when Structure 1 is subject to severe tension, some ITO strips (demarcated by two neighboring channel cracks) delaminate and buckle away from the substrate (e.g., Figure 2.12(d)), driven by the compressive stress in the ITO film due to the Poisson's effect. Severe bending due to buckling results in high tensile stress near the top surface of the

buckled crest of the ITO strip, which eventually leads to the ITO cracking at the crest along the direction roughly parallel to the applied tension

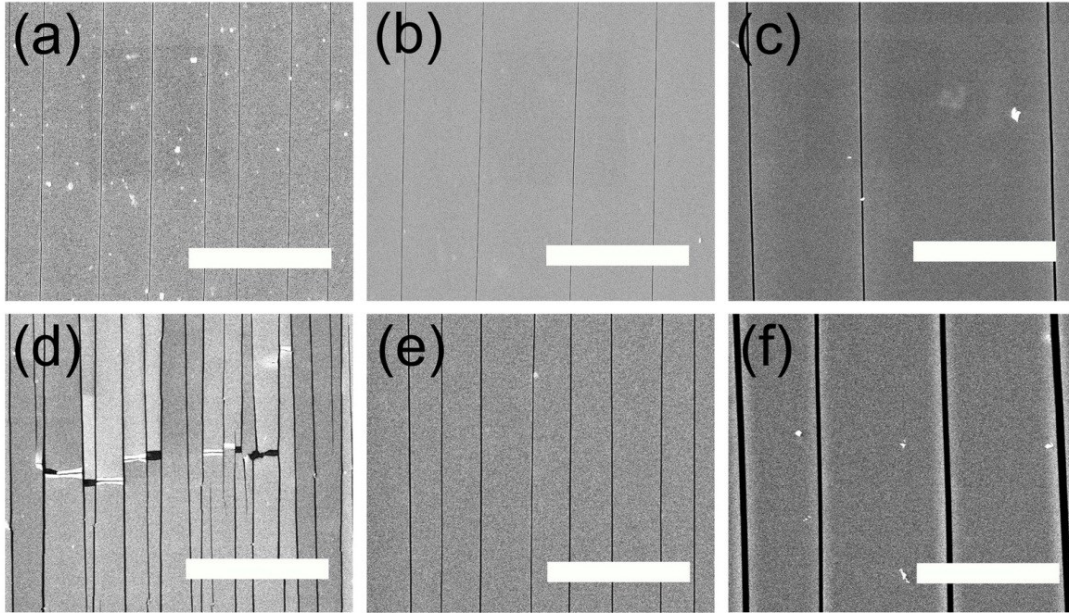


Figure 2.12. In situ observation of multilayer structures in different strain levels: (a) Structure 1, (b) Structure 2, and (c) Structure 3 are at the strain of $\sim 4\%$; and (d) Structure 1, (e) Structure 2 and (f) Structure 3 are at the strain of $\sim 13\%$. The white scale bar in each figure is $30\ \mu\text{m}$ in length.

To quantitatively describe the channel cracking under applied tensile strain, we define crack density as the number of channel cracks per unit length in the tensile loading direction. The crack density as a function of the applied tensile strain in Structures 1 to 3 is shown in Figure 2.13(a). For each structure, the crack density first increases significantly as the applied strain increases, and then gradually saturates at certain value. The sample without any intermediate polymeric layer (Structure 1) has the highest value of saturating crack density, while the sample with the thicker S1813 intermediate polymeric layer has the lowest value of saturating crack density (Structure 3). Both

qualitative observation and quantitative results of the evolution of crack density at various applied strains indicate that the intermediate PMMA layer in Structure 2 can effectively reduce the crack density when compared with that in Structure 1, and the crack density can be further reduced when a thicker and stiffer intermediate polymeric layer is used (Structure 3).

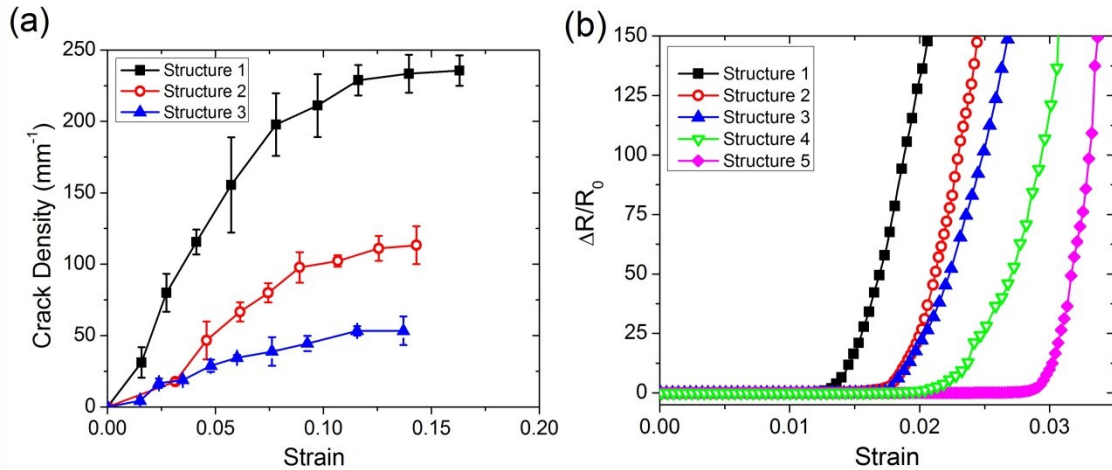


Figure 2.13. (a) Cracks density and (b) normalized change in electrical resistance as the function of strain in different ITO-based multilayer electrodes.

In real applications of flexible electronics, the strain level should be less than that for the initiation of channel cracks in functional layers, and that strain level is always less than 3% in ITO-based electrodes. Other than mechanical failure, conductive failure, defined as the dramatic increase in electrical resistance during deformation, is also employed to evaluate the electro-mechanical quality of electrodes in a more direct and effective way.

Figure 2.13(b) plots the normalized change in electrical resistance as a function of the applied tensile strain. For each multilayer electrode, the electrical resistance of the ITO

thin film remains nearly unchanged when the applied tensile strain is relatively small. In other words, the ITO thin film remains electrically conductive when subject to a modest elongation. As the applied tensile strain further increases, the electrical resistance first rises gradually, and then shoots up dramatically, leading to the conductive failure. The critical strain of an ITO-based multilayer electrode is defined as the strain when the normalized change in electrical resistance starts to shoot up dramatically, and the value ranges of critical strain for all the electrodes are listed in Table 2.1. It is found that the value of critical strain in Structure 1 is the smallest. More importantly, the critical strain is affected by the existence of the intermediate layer: the value of critical strain is increased after inserting the intermediate polymeric layer (PMMA or S1813) in Structure 2 or 3. However, not like the crack density, the thickness of the intermediate polymeric layer seems to play little role in the critical strain: there is nearly no difference of critical strains between Structure 2 and 3.

Table 2.1. Critical strains of ITO-based multilayer electrodes. The value range of critical strain in each structure was determined from at least three electro-mechanical tests.

Structure number	1	2	3	4	5
Critical strain (%)	1.0-1.3	1.7-1.9	1.7-1.9	2.1-2.3	2.5-2.8

The above results clearly show that the intermediate polymeric layer can reduce the density of channel cracks in high strain level (>4%) and increase the electrical stability in low strain level (<3%). It has been previously shown that the mechanical durability of the top oxide layer in a multilayer structure can be enhanced by applying a thin protective

coating onto the surface of the top oxide⁷⁵. In this work, we coat a polymeric layer (thin PMMA or thick S1813) on top of the ITO thin film (Structures 4 and 5), aiming to increase the electro-mechanical properties during the tensile loading. The results in Figure 2.13(b) clearly show that the critical strain has been increased after the protective coating, and this is a clear evidence for the improvement of electro-mechanical quality in multilayer structures. In particular, the critical strain of Structure 5 is even higher than that of Structure 4, indicating that a thicker polymeric layer offers more mechanical constraint, which leads to a reduced driving force for the channel cracking of ITO layer.

2.2.3. Mechanics Modelling and Results

To understand the dependence of the critical strains of ITO electrodes (as in Table 2.1 and Figure 2.3(b)) on the multilayer structural design, we next establish a mechanics model to compute the driving force for steady state channel/tunnel cracking of the ITO electrodes in Structures 1 to 5. Results from our mechanics modeling offer a mechanistic understanding of the role of intermediate and top protective polymeric layers on the improvement of electro-mechanical durability of ITO electrodes.

We first figure out the dominating failure modes of ITO-based multilayer electrodes. It has been shown that¹⁶, for a multilayer structure such as Structures 2 to 5 under tension, if the intermediate polymeric layer is thicker than the ITO layer, channel cracking of the top ITO layer in Structures 2 and 3 (or tunnel cracking of the ITO layer in Structures 4 and 5) requires the least driving force when compared with other tensile-cracking failure

modes, such as tunnel cracking of the intermediate polymeric layer or channel cracking of ITO/polymer/ Al_2O_3 as a whole. In our multilayer design of Structures 2 to 5, both PMMA and S1813 layers are thicker than the ITO layer. Therefore, channel/tunnel cracking of the ITO layers is expected to be the dominating failure mode in Structures 2 to 5, which agrees with our experimental observation.

For Structure 1, however, the ITO layer directly lies on the Al_2O_3 layer without any intermediate polymeric layer in between. Under tension, there may exist two possible failure modes of Structure 1. In failure mode (a), channel cracks occur only in the top ITO layer while the Al_2O_3 layer remains intact, while in failure mode (b), channel cracks cut through the whole thickness of both ITO and Al_2O_3 layers. To determine dominating failure mode of Structure 1, we next compute the critical fracture strains corresponding to the above two failure modes, the lower of which determines the dominating failure mode.

Taking all materials in the multilayer structure to be linearly elastic, the steady state channel cracking propagation is driven by the associated reduction of elastic energy in the multilayer due to crack opening. This elastic energy reduction can be computed by subtracting the elastic energy stored in a slice of the multilayer structure of unit thickness far behind the crack front (Slice 1) from that far ahead of the crack front (Slice 2), as illustrated in Figure 2.14(a). When the thickness of the intermediate polymeric layer in Figure 2.14(a) vanishes, it corresponds to Structure 1. Assuming a uniform spacing s

between neighboring channel cracks (i.e., $1/s$ is the crack density), dimensional analysis leads to the following form of the elastic energy reduction in Structure 1

$$U = E'_{ITO} \varepsilon^2 h_{ITO}^2 f \left(\frac{h_{ITO}}{h_{Al_2O_3}}, \frac{E_{ITO}}{E_{Al_2O_3}}, \frac{h_{ITO}}{s} \right) \quad (2.7)$$

where $E'_{ITO} = E_{ITO} / (1 - \nu_{ITO}^2)$ is the plane strain Young's Modulus of ITO, ε is the applied tensile strain. h_{ITO} ($h_{Al_2O_3}$) and E_{ITO} ($E_{Al_2O_3}$) are the thickness and Young's Modulus of ITO (Al_2O_3), respectively, and ν_{ITO} is the Poisson's ratio of ITO. The dimensionless function f denotes the normalized energy released rate of ITO film cracking and can be calculated numerically using finite element method. For clarity, the dimensionless functions f for failure modes (a) and (b) are designated as f_a and f_b , respectively. For failure mode (a), channel cracks will propagate in the ITO layer if the associated reduction of elastic energy U_a exceeds the fracture toughness of ITO, Γ_{ITO} , times the thickness of the ITO layer. Therefore the critical condition can be given as

$$U_a = \Gamma_{ITO} h_{ITO} \quad (2.8)$$

A combination of Eqs. (2.7) and (2.8) gives the normalized critical applied strain ε_a for crack propagation in the ITO layer

$$\frac{\varepsilon_a}{\sqrt{\Gamma_{ITO} / E'_{ITO} h_{ITO}}} = \sqrt{\frac{1}{f_a}} \quad (2.9)$$

For failure mode (b), cracks channel through the whole thickness of ITO and Al_2O_3 layers, therefore, the associated reduction of elastic energy is

$$U_b = \Gamma_{ITO} h_{ITO} + \Gamma_{Al_2O_3} h_{Al_2O_3}, \quad (2.10)$$

where $\Gamma_{Al_2O_3}$ is the fracture toughness of Al_2O_3 . A combination of Eqs. (2.7) and (2.10) gives the critical strain ε_b for channel cracking propagation in both ITO and Al_2O_3

$$\frac{\varepsilon_b}{\sqrt{(\Gamma_{ITO} h_{ITO} + \Gamma_{Al_2O_3} h_{Al_2O_3})/E'_{ITO} h_{ITO}^2}} = \sqrt{\frac{1}{f_a}} \quad (2.11)$$

In our specimens, $h_{Al_2O_3} = 0.75h_{ITO}$. For simplicity, the fracture toughnesses of ITO and Al_2O_3 are taken to be identical, i.e., $\Gamma_{ITO} = \Gamma_{Al_2O_3}$. Equation (2.11) can then be reorganized as

$$\frac{\varepsilon_b}{\sqrt{\Gamma_{ITO}/E'_{ITO} h_{ITO}}} = \sqrt{\frac{1.75}{f_b}} \quad (2.12)$$

Dimensionless functions f_a and f_b are calculated by normalizing the elastic energy reduction U associated with channel crack propagation. As aforementioned, this elastic energy reduction can be computed by subtracting the elastic energy stored in a slice of the multilayer structure of unit thickness far behind the crack front (Slice 1) from that far ahead of the crack front (Slice 2), as illustrated in Figure 2.14(a). The elastic energy stored in Slice 1 and Slice 2 can be directly calculated using finite element code ABAQUS. Schematics of models used in finite element calculation for Slices 1 and 2 are given in Figure 2.14(b). The width s of the model is defined by the inverse of crack density. Taking advantage of symmetry, only half of the slice is modeled and symmetric boundary condition is set for the left edge of the model (in Slice 1, the ITO portion of the

left edge is set free to simulate the free channel crack surface); a horizontal displacement $u/2$ is set along the right edge of the model. Therefore, the quantity u/s defines the applied strain. In the finite element calculations, the Young's moduli of ITO, Al_2O_3 and PET are set to be 200 GPa, 300 GPa and 2 GPa, respectively, and their Poisson's ratios are 0.3, 0.3 and 0.4, respectively. The thickness of the PET substrate is set to be $625h_{\text{ITO}}$. The whole model is meshed with the second-order eight-node quadrilateral elements, with densified mesh in the region near the crack tip. The elastic energy stored in Slice 1 and Slice 2 can be readily calculated.

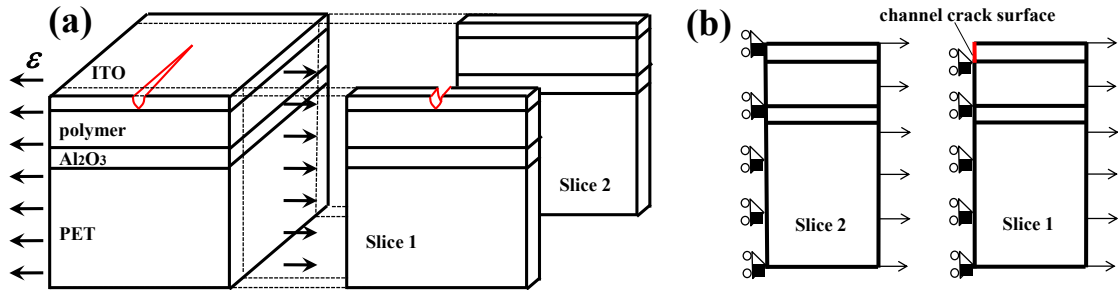


Figure 2.14. (a) The elastic energy reduction associated with the steady state channel cracking propagation in the multilayer can be computed by subtracting the elastic energy stored in a slice of the multilayer structure of unit thickness far behind the crack front (Slice 1) from that far ahead of the crack front (Slice 2). (b) Schematics of models of Slice 1 and Slice 2 used in finite element simulations.

Table 2.2 lists the calculated normalized critical strains for failure modes (a) and (b) for three different crack densities. For all crack densities considered, the critical strains for failure mode (b) is always lower than those for failure mode (a). In other words, for Structure 1, the dominating failure mode is the channel cracking through the whole thickness of ITO and Al_2O_3 layers. This can be understood as follows. For failure mode

(a), the opening of the channel cracks in the top ITO layer is constrained by the underlying Al₂O₃ layer. For failure mode (b), the opening of the channel cracks cutting through both ITO and Al₂O₃ layers is subject to the constraint of the underlying PET substrate. Given the huge difference in the Young's moduli of Al₂O₃ and PET, the mechanical constraint of the Al₂O₃ layer in failure mode (a) is much stronger than that of the PET substrate in failure mode (b). Consequently, under tension, Structure 1 is vulnerable to channel cracking through the whole thickness of ITO and Al₂O₃ layers.

Table 2.2 Normalized critical strains for failure modes (a): channel cracking in the top ITO layer and failure mode (b): channel cracking in both ITO and Al₂O₃ layers for various crack densities.

	Crack density =10 mm ⁻¹	30 mm ⁻¹	100 mm ⁻¹
$\frac{\varepsilon_a}{\sqrt{\Gamma_{ITO}/E'_{ITO}h_{ITO}}}$	0.518	0.528	0.532
$\frac{\varepsilon_b}{\sqrt{\Gamma_{ITO}/E'_{ITO}h_{ITO}}}$	0.197	0.208	0.226

We next compute the driving forces for the steady state channel/tunnel cracking in Structures 1 to 5. The comparison of such driving forces provides mechanistic understanding of the dependence of the measured critical strains of ITO electrodes on the multilayer structural design. The driving forces of cracking for Structures 1 to 5 are defined as

$$G_i = \frac{U_i}{h_i} = \frac{E'_{ITO} \varepsilon_{app}^2 h_{IT}^2 f_i}{h_i} \quad i = 1, \dots, 5 \quad (2.13)$$

where U_i is the associated reduction of elastic energy due to crack propagation in Structure i as defined in Eq. (2.7), h_i is the total thickness of the cracked layers ($h_i = 1.75h_{ITO}$ for Structure 1 and $h_i = h_{ITO}$ for Structures 2 to 5). The values of the dimensionless function f_i are computed using finite element method. Here, PMMA and S1813 are modeled as linear elastic materials with Young's modulus of 2 GPa and 7 GPa, respectively, and Poisson's ratio of 0.4 for both.

Figure 2.15 plots normalized driving force for cracking propagation $G_i / E'_{ITO} \varepsilon_{app}^2 h_{ITO}$ in Structures 1 to 5 as a function of crack density. In the range of crack density we study (i.e., $10 \text{ mm}^{-1} \sim 100 \text{ mm}^{-1}$), $G_1 > G_2 > G_3 > G_4 > G_5$. In other words, for a given fracture toughness of the ITO layer, Structure 1 has the lowest critical strain to lose electronic conductance of the ITO electrode while Structure 5 has the highest critical strain. Such a prediction of the dependence of critical strain on the structural design agrees with the experimental measurements as shown in Table 2.1 and Figure 2.13(b). Such dependence can be further understood as follows. In Structures 2 and 3, the deformable intermediate polymeric layer prevents the channel cracks in the ITO layer from penetrating into the Al_2O_3 layer. In turn, the intact stiff Al_2O_3 can offer relatively strong mechanical constraint to the ITO cracking. By contrast, the Al_2O_3 layer in Structure 1 fractures with the ITO layer. As a result, there is a more than two-fold decrease of crack driving force in Structures 2 and 3 from that in Structure 1, for a given crack density. Since the S1813

intermediate layer in Structure 3 is stiffer and thicker than the PMMA intermediate layer in Structure 2, the overall mechanical constraint on the ITO cracking in Structure 3 is slightly stronger than that in Structure 2. Therefore, $G_2 > G_3$. For Structures 4 and 5, the top protective polymeric layer further constrains the cracking opening displacement of the ITO layer (turning channel cracking into tunnel cracking), which results in an about four-fold decrease of the crack driving force from Structures 2 and 3, for a given crack density. When compared with Structure 1, the overall reduction of the crack driving force in Structure 5 is more than ten-fold. In other words, a thin, compliant and well-bonded top protective layer and an intermediate polymeric layer can effectively enhance the electro-mechanical durability of the ITO-based multilayer electrodes. The above results agree with those in a recent study of the mechanical durability of inorganic/organic multilayer permeation barriers for flexible electronics. The slight decrease of the crack driving force as the increase of crack density as shown in Figure 2.15 can be explained by the partial mitigation of the stress level in the uncracked portions of the ITO layer due to channel/tunnel crack propagation. More crack propagation (i.e., higher crack density) leads to further reduction of the effective stress level in the ITO layer, and thus the slight decrease of the crack driving force. Experimental results in Table 2.1 show that the critical failure strains of Structure 5 are higher than those of Structure 4, while the modeling results in Figure 5 show that the driving force for cracking in Structures 5 is only slightly lower than that of Structure 4. For Structures 2 and 3, the experimental

results on critical failure strains are nearly identical, but the modeling results in Figure 2.15 predict a 10~20% difference in their driving forces for cracking. These discrepancies between the experimental and modeling results may be attributed to the assumption of well-bonded interfaces in the multilayer electrodes in our models. In reality, interfacial delamination may occur between the ITO layer and the polymeric layers, which leads to an increased driving force for cracking of the ITO layer ⁷⁵.

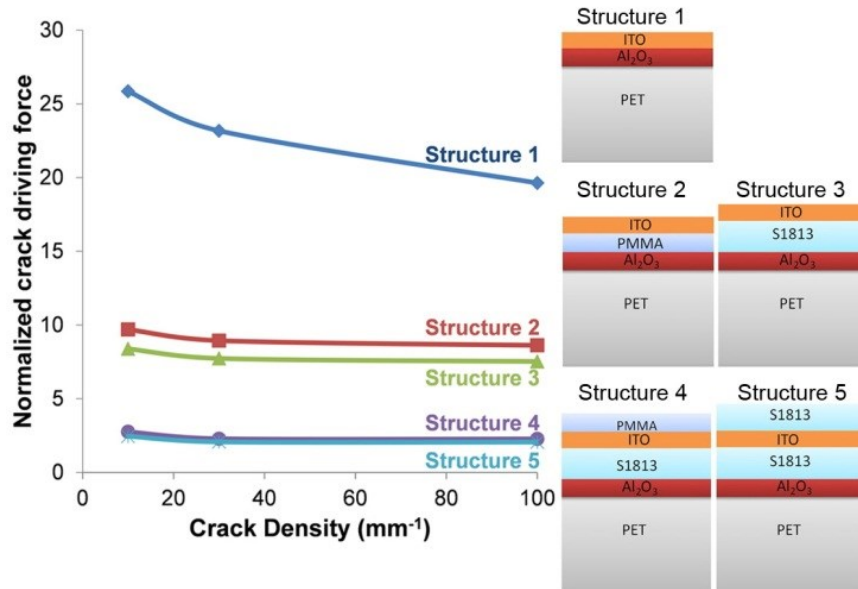


Figure 2.15. Normalized driving force for cracking propagation in Structures 1 to 5 as a function of crack density.

2.2.4. Summary

In summary, we perform a coherent study integrating *in situ* electro-mechanical experiments and mechanics modeling to investigate the failure mechanics of five structural designs of ITO-based multilayer electrodes under tension. While the experimental results show that a top protective polymeric coating above and an

intermediate polymeric layer below the ITO layer can effectively enhance the electro-mechanical durability of the ITO-based multilayer electrodes, the mechanics modeling suggests that this enhanced durability is due to the reduction of driving force for ITO cracking up to ten folds. The findings in this work can provide quantitative guidance for the material selection and structural optimization of organic-inorganic multilayer structures with high mechanical durability.

Chapter 3. Brittle Cracking of Polyimide Substrate Supported ITO Thin Films

3.1. Mechanics Modeling of Tensile Cracking in Indium Tin Oxide Thin Films on Polyimide Substrates²

3.1.1. Introduction

Flexible electronics, e.g., paper like displays, printable thin-film solar cells, and skin-like smart prostheses, are attracting enormous interests due to their large deformability, light weight, large surface areas, and low cost^{76, 77}. The desirable attributes of flexible electronics result from new choices of building block materials (e.g., organic/inorganic hybrids) and manufacturing method (e.g., roll-to-roll printing). For example, ITO thin films on polymer substrates are widely used as transparent conductors and interconnects in flexible displays. While compliant polymer substrates can sustain large strain, ITO thin films are brittle and often fracture at small strain. The cracking of ITO conductors and interconnects leads to loss of electrical conductance, posing crucial challenge to the reliability of flexible devices. In this section, we report a coherent study integrating *in situ* electro-mechanical experiments and mechanics modeling to decipher the failure mechanics of ITO thin films on polyimide substrates under tension. *In situ* tensile tests inside a scanning electron microscope (SEM) (done by our collaborators in Rice university) reveal real time details of crack initiation and propagation, crack density evolution, and associated resistance variations in thin ITO conductors on polyimide

² Experimental results shown in section 3.1 were obtained by Dr. Cheng Peng and Prof. Jun Lou from Department of Materials Science and NanoEngineering, Rice University.

substrates. Our mechanics model offers quantitative determination of critical mechanical properties (ITO cohesive toughness, fracture stress, and ITO/polyimide interfacial toughness) from the experimental data and explains the thickness dependence of crack density evolution in ITO conductors.

Fracture of thin brittle films on rigid substrates (e.g., Si) has been a focused topic in the discipline of materials science and mechanics in the past two decades, largely originated from the context of microelectronics⁹⁻¹¹. These studies shed important lights on but cannot fully capture the characteristics of the fracture mechanisms of thin brittle films (e.g., ITO) on polymer substrates used in flexible electronics. For example, ITO is more than two orders of magnitude stiffer than typical polymers (e.g., polyimide), while electronic materials in microelectronics have comparable stiffness. Furthermore, flexible devices are often subject to deformation (up to 10%) much larger than that traditional microelectronic devices typically undergo ($< 1\%$). These two distinctions cause the material response of ITO thin films on polymer substrates different from that of brittle films on rigid substrates, which therefore requires new efforts to describe its characteristics. A growing literature exists on the rupture of thin metal films on polymer substrates⁷⁸⁻⁸¹. Metal film necking and metal/polymer interfacial delamination have been shown as the major fracture mechanisms. Unlike the ductile failure of thin metal films on polymer substrates as a result of diffusive necking, the fracture of brittle ITO thin films on polymer substrates results from channel cracking, which in turn often interplays with

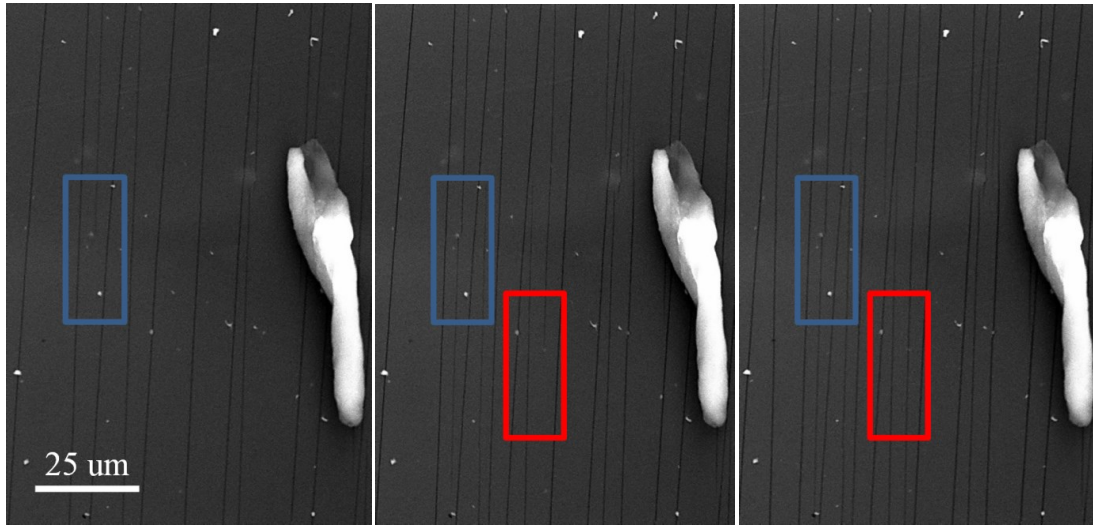
the delamination along the ITO/polymer interface. Existing studies on the brittle fracture of ITO thin films on polymer substrates under tension include the fragmentation tests in which the crack density evolution as a function of the applied strain is monitored^{82,83}. The cohesive toughness of the ITO films and the adhesive toughness of the ITO/polymer interface can be estimated based on the experimental data from fragmentation tests⁸⁴. The variation of electrical resistance due to ITO cracking has also been studied^{85,86}. Other mechanics models investigate the effect of the large film/substrate stiffness ratio on the cracking of thin brittle films on compliant substrates.

In this section, our collaborators perform *in situ* mechanical and electrical tests of ITO thin films deposited on polyimide substrates inside SEM, in which both the evolution of the crack density in ITO thin films and the resulting variation of the electrical resistance of the ITO thin films are monitored real time as a function of applied tensile strain. Simultaneous *in situ* mechanical and electrical tests are of particular importance to correlate crack initiation and propagation with its resistance change, and to avoid the unloading-induced partial or full closure of cracks in the ITO thin film in *ex situ* tests. We further conduct mechanics modeling to simulate the tensile failure process of ITO thin films on polymer substrates, and apply the model to the experimental data to compute the critical but hard-to-measure properties, such as the cohesive toughness and fracture strength of the ITO thin films and the adhesive toughness of the ITO/polyimide interface. The mechanics modeling suggests that the saturation of crack density in ITO thin films

results from the decrease of the tensile stress in ITO below its fracture strength as the ITO/polyimide interfacial delamination advances, which agrees with experimental observation.

3.1.2. Experimental Results and Discussion

From *in situ* SEM observation, the unloaded ITO thin films were smooth, without any appreciable cracks. As the tensile strain increased to a threshold value (e.g., 1.59% for 80nm thick ITO films), small channel cracks started to initiate at certain locations in the ITO film and then grew along the sample width direction (perpendicular to the tensile load direction). Figure 3.1 illustrates the typical process of crack initiation and propagation as the tensile load increases. Here the ITO film thickness is 80nm. For example, a crack tip was found near the top edge of the blue rectangle box in Figure 3.1a at the tensile strain of 3.68% and this crack propagated downward and advanced outside of the same blue rectangle box at the tensile strain of 4.70% (Figure 3.2b). Meanwhile, a channel crack not existing in the view of Figure 3.1a propagated upward with its tip slightly above the top edge of the blue rectangle box in Figure 3.1b. Similar crack propagation is also evident when comparing the red rectangle box in Figure 3.1b and 3.1c, as the tensile strain increased from 4.70% to 5.85%



(a) strain=3.68%

(b) strain=4.70%

(c) strain=5.85%

Figure 3.1. Crack initiation and propagation during in situ tensile test. A crack tip was found near the top edge of the blue rectangle box in (a) strain=3.68% and this crack propagated downward and advanced outside of the same blue rectangle box in (b) strain=4.70%. Similar phenomena is also shown in the red rectangle box in (b) strain=4.70% and (c) strain=5.85%. The dust in the right corner is used as the reference for in situ observation.

Figure 3.2 shows a series of snap shots of the polyimide-supported ITO film to illustrate the increasing number of cracks in the film as the tensile load increases. Here the ITO film thickness is 80nm. At small tensile strain (e.g., 0.55%, Fig. 2a), the ITO film remained intact. Above a threshold tensile strain for crack initiation (1.59%, Figure 3.2b), channel cracks started to emerge in the view. As the tensile strain increased (e.g, Figure 3.2c-e), more channel cracks initiated and propagated through the sample width. It was found that the channel crack distribution in the ITO film is quite uniform along the sample length direction (also the tensile load direction), suggesting the rather uniform elongation of the polyimide substrate. The sample was further stretched until the

polyimide substrate ruptured into two halves. Figure 3.2f shows the ITO fragments near the sample rupture location. Note the obvious delamination along the ITO/polyimide interface near the edges of the ITO fragments.

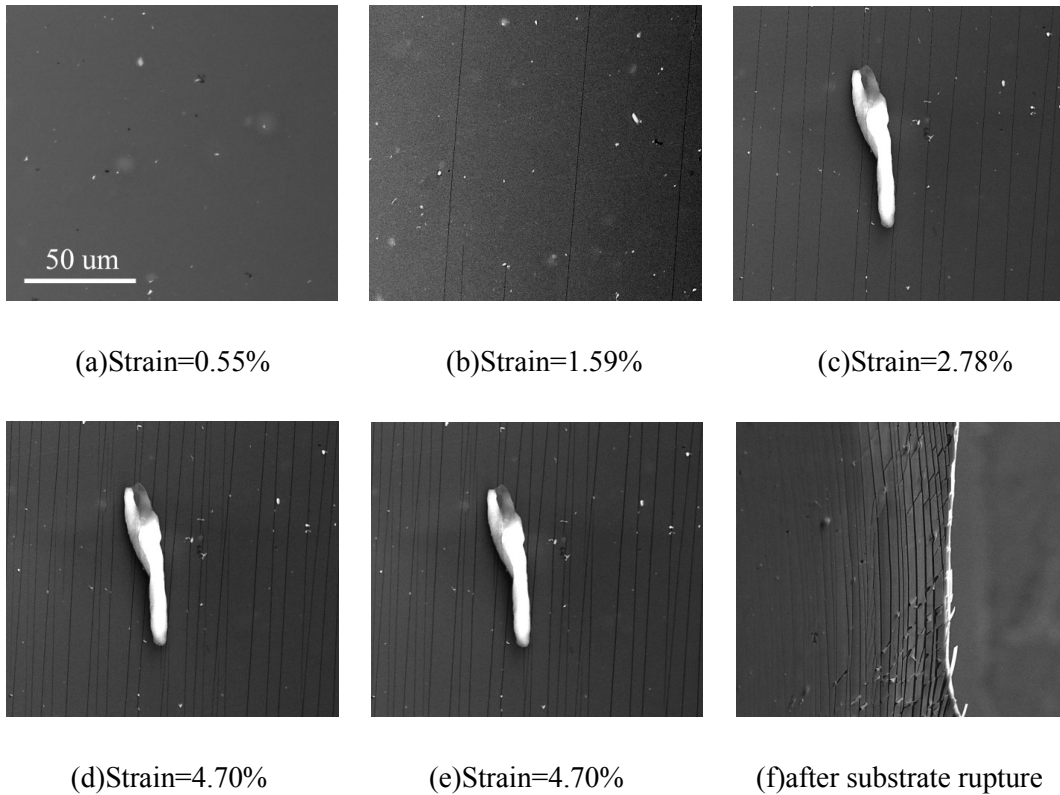


Figure 3.2. (a-e). Snap shots of polyimide-supported ITO film under increasing tensile strain. Note the onset of channel crack initiation at 1.59 % tensile strain (b) and the increasing crack density as the tensile strain increases. No appreciable increase of crack density when tensile strain increases from 4.70% to 5.85% (d-e), indicating the saturation of channel cracking in the ITO film. (f). ITO fragments near the sample rupture location. Note the obvious delamination along the ITO/polyimide interface. Here ITO film thickness is 80 nm.

To quantitatively characterize the ITO cracking under tensile strain, we define the *crack density* as the number of channel cracks in ITO film per unit length in the tensile load direction. In all data reported hereafter, the crack density of the samples is calculated as

the average of crack density values obtained from at least three SEM images of the cracked ITO thin film in different random locations. Figure 3.3 plots the crack density in an 80 nm thick ITO film on a polyimide substrate as well as the resulting resistance variation of the ITO thin film as a function of the applied tensile strain. As shown in Figure 3.3, once the onset of crack initiation starts, the crack density first increases significantly as the tensile strain increases, and then gradually saturates at about 130 mm^{-1} as the tensile strain approaches to 5.85%. Also evident in Figure 3.3, the electrical resistance of the ITO thin film remains nearly unchanged when the applied tensile strain is relatively small. For example, when compared with the as-fabricated ITO film, there is less than 2.5 times increase in resistance for a tensile strain less than 3%. In other words, the ITO thin film remains electrically conductive when subject to a modest elongation. As the applied tensile strain further increases, the ITO electrical resistance first rises gradually, and then shoots up dramatically as the tensile strain approaches the value at which the crack density saturates. Such a correlation between the evolution of crack density and the change in electrical resistance in the ITO thin film under tension can be explained as follows. At the onset of crack initiation, many channel cracks start to nucleate but have not fully propagate through the whole sample width. As a result, the electrical conductance of the partially cracked ITO film remains nearly unchanged as a current can percolate through the whole ITO conductor. As the applied tensile strain increases modestly, the short channel cracks nucleated in the ITO thin film start to

advance through the width of the samples, but the opening displacement of these channel cracks is relatively small, as evident by the rather thin crack lines in the SEM images (e.g., Figure 3.2b, c). When the crack opening is small, the local irregularity of the macroscopically straight channel cracks (e.g., the zigzag grain boundaries in the ITO thin film) may keep the ITO fragments in contact at certain locations in the wake of the channel cracks, and it is also likely that at certain locations the channel cracks have not fully developed to reach the ITO/polyimide interface thus the ITO thin film is not completely fragmentized. As a result, the ITO thin film remains conductive and its electrical resistance only increases modestly. As the applied strain further increases, channel cracks in the ITO thin film are fully developed, resulting in larger cracking opening (as shown by the thicker cracking lines in Figure 3.2d~f). Our further measurements of the total crack length and crack opening in the ITO thin film as a function of the applied strain further confirm the above explanation. That is, the total crack length increases drastically at small strains (corresponding to channel crack initiation) and such increases in total crack length diminish significantly (corresponding to the fully developed channel cracks) when the applied strain is beyond about 4% (at which the ITO resistance starts to increase dramatically). Further increase of the ITO resistance is shown to be consistent with the continuously increasing crack opening.

Also as evident in Figure 3.2f and further predicted in the simulations, the ITO fragments partially delaminate from the polyimide substrate. Consequently, the conductance of the

ITO thin film is nearly cut off. As to be further explained later, the interfacial delamination mitigates the tensile stress transferred from the substrate to the ITO film, therefore prevents further initiation of channel cracks, resulting in the saturation of the crack density.

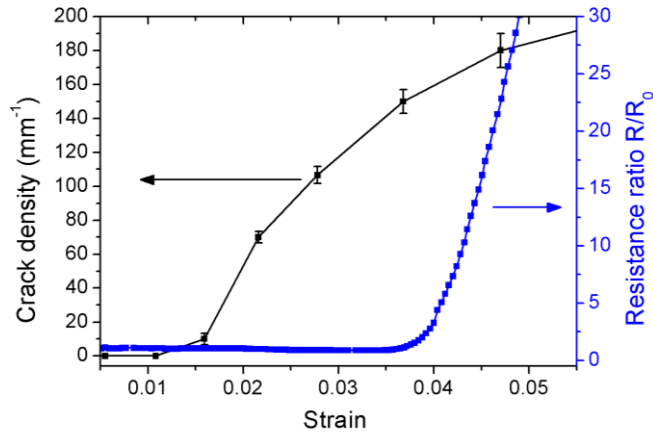


Figure 3.3. The crack density and the variation of electrical resistance of an 80 nm thick ITO film deposited on polyimide as a function of the applied strain. R_0 denotes the electrical resistance of the unloaded ITO thin film.

Figure 3.4 plots the crack density in the ITO thin films as a function of applied tensile strain for film thickness of 200 nm and 80 nm, respectively. For each thickness, two samples were tested. It was found that the crack initiation in a thicker ITO film occurs at relatively smaller applied tensile strain than that for a thinner ITO film. However, the saturated crack density of the thicker ITO film is lower than that of the thinner ITO film. Assuming a brittle nature of ITO film fracture, the critical tensile strain to initiate cracking in an ITO thin film scales inversely with the square root of the length of the largest pre-existing defects in the film. For a thicker ITO film, it is more likely to have

larger initial defects (e.g., voids, missing grains, or embrittled grain boundary during deposition), and therefore entails a relatively lower onset strain of crack initiation. The thickness dependence of the crack density will be explained in detail later through a fracture mechanics analysis.

3.1.3. Mechanics Model and Results

We next establish a mechanics model to use the *in situ* experimental data of ITO crack density evolution to compute the critical but hard-to-measure properties of the ITO/polymer laminates, such as the cohesive toughness and fracture strength of the ITO films and the adhesive toughness of the ITO/polyimide interface. We also offer a mechanistic understanding of the thickness dependence of the saturated ITO crack density.

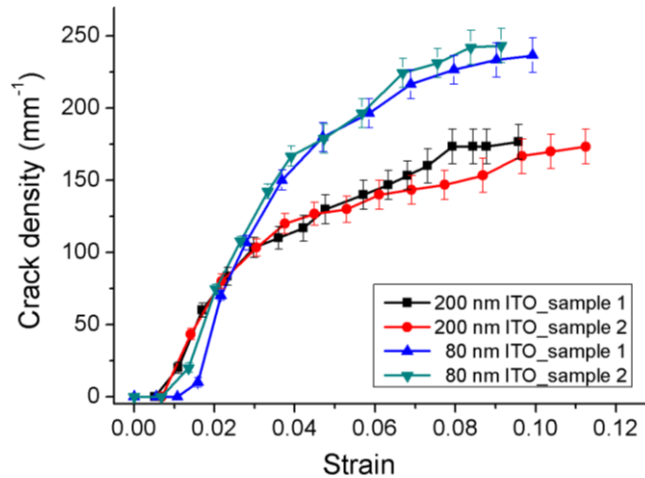


Figure 3.4. Crack density as a function of applied strain for ITO thin films with thickness of 80nm and 200nm, respectively. Two samples were tested for each film thickness.

A. Simulation model

Figure 3.5 depicts the finite element simulation model. Under tension, a thin blanket ITO film on a polymer substrate is subject to channel cracking (Figure 3.5a). For simplification, we assume the channel cracks in ITO are uniformly spaced (i.e., the crack density is given by $1/s$, where s is the width of ITO fragments). The ITO/polymer laminate is taken to deform under the plane strain conditions. Taking advantage of symmetry we model only a unit cell of the laminate, consisting of a half of the ITO stripe between two neighboring channel cracks and the substrate underneath (Figure 3.5b). In the simulation model, the film is a layer with thickness h , and the substrate is a block with thickness $1000h$ and length $s/2$. Symmetric boundary condition is set for the left edge of the unit cell and a horizontal displacement u is set along substrate portion of the right edge of the unit cell. The quantity $2u/s$ defines the applied strain.

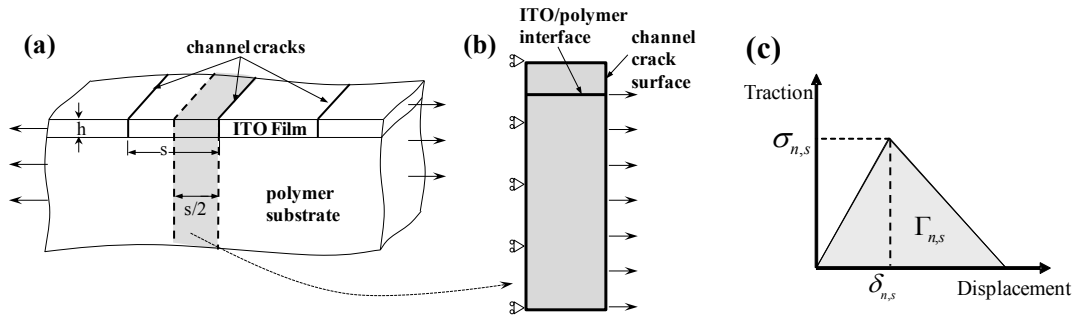


Figure 3.5. (a) Schematics of the simulation model. (b) Unit cell used in finite element simulation. (c) The traction-displacement laws used to model the ITO/polymer interface.

Both the ITO film and the polymer substrate are modeled as linear elastic materials with Young's modulus of 140 GPa and 2GPa, respectively, and Poisson's ratio of 0.3 and 0.4, respectively. The linear elastic assumption is reasonable for the ITO film but has some

limitations for the polymer substrate whose impact on modeling results will be discussed in detail later in this section.

The channel cracks lead to stress concentration in the substrate near the channel roots, which could be severe enough to cause delamination along the ITO/polymer interface, as also evident in the *in situ* experiments. To simulate the cracking-induced interfacial delamination, the ITO/polymer interface is modeled as an array of nonlinear springs, which is characterized by a tensile and a shear traction-displacement law, with six parameters: interfacial tensile strength σ_n and shear strength σ_s , critical opening displacement δ_n and sliding displacement δ_s , and the areas under the traction-displacement curves Γ_n and Γ_s (i.e., the normal and shear adhesion energy of the ITO/polymer interface, respectively), as illustrated in Figure 3.5c. We assume that $\sigma_n = \sigma_s$, $\delta_n = \delta_s$ and $\Gamma_n = \Gamma_s$. In all simulations, $\sigma_n = 500\text{MPa}$ and $\delta_n = 0.5\text{nm}$. The interfacial toughness Γ_n is varied to fit the crack density vs. applied strain curve from *in situ* experiments. The ITO/polymer interface is meshed with four-node cohesive elements sharing nodes with the neighboring elements in the film and the substrate. The viscous regularization option in finite element codes ABAQUS is used for the cohesive elements to enhance the computation convergence.

B. Modeling strategy and results

When a freestanding ITO thin film is subject to tension, it fractures by a *single* channel crack running through its width. Supported by a polymer substrate, the tensile fracture of

the ITO thin film involves the initiation and propagation of *multiple* channel cracks, and the subsequent increase and saturation of the crack density as the applied tension increases, as observed in experiments. The increase of crack density is due to the transfer of tensile load from the polymer substrate to the ITO film through the interface. The brittle nature of the channel cracks in ITO thin film leads to severe stress concentration in the substrate near the channel roots that can cause delamination along the ITO/polymer interface. As the delamination initiates and propagates along the interface, the tensile load transferred from the polymer substrate to the ITO film decreases. If the delamination length is sufficiently large, the maximum tensile stress in the ITO film drops below the ITO fracture strength. As a result, no further channel cracks can be initiated in the ITO film. In other words, the crack density in the ITO film saturates.

1. ITO/polyimide interfacial toughness and ITO fracture strength

Based on such an understanding, we apply the following modeling strategy in the simulations. For a given crack density vs. applied strain curve from *in situ* experiments (e.g., Figure 3.4), the crack density corresponding to the channel crack onset strain (e.g., 10/mm at 1.59% for 80 nm thick ITO film) defines a FEM simulation model with width of 50 μ m (e.g., Figure 3.5b). An ITO/polymer interfacial toughness (i.e., Γ_n) is assigned for the traction-displacement law of the interface. This unit cell model is stretched to the channel crack onset strain. The maximum tensile stress in the ITO, which occurs at the ITO portion of the left edge of the unit cell, is obtained. Given the brittle nature of the fracture of the ITO thin film, such a tensile stress indicates the ITO fracture strength,

above which channel cracking occurs. A series of FEM unit cell models are then built with widths corresponding to the crack density values in the same experimental curve. Each simulation model is then stretched to a certain applied strain at which the maximum tensile stress in the ITO thin film reaches the ITO fracture strength determined from the first simulation model (i.e., right before next channel crack initiates). Although the subsequent crack initiation is not simulated directly, the modeling strategy adopted here can still reasonably capture the underlying failure mechanism, given that the brittle nature of the crack initiation and propagation (e.g., as shown in Figure 3.1). The corresponding crack density vs. applied strain curve based on the above simulations is then plotted together with that from the *in situ* experiment for comparison. The value of Γ_n in the traction-displacement law of the ITO/polyimide interface is then varied, and the above simulation procedure is repeated until the best fit between the simulation and experiment curves is reached. The corresponding value of Γ_n and maximum tensile stress in the ITO thin film are defined as the ITO/polyimide interfacial toughness and the ITO fracture strength, respectively.

Figure 3.6 plots the crack density vs. applied strain curves from the best-fit simulations and experiments, for ITO film thickness of 80 nm and 200nm, respectively. The ITO/polyimide interfacial toughness and the ITO fracture strength obtained from the best fit simulations are 9.5J/m^2 and 2.4GPa for 80 nm thick ITO film, and 10.8J/m^2 and 1.7GPa for 200 nm thick ITO film, respectively. As shown in Figure 3.6, the simulation

curves can fit the experiment curves quite well until a certain applied strain. When the applied strain further increases, the maximum tensile stress in the ITO film cannot reach the ITO fracture strength, therefore no further channel crack can be initiated. In this sense, the simulation model underestimates the saturated crack density. Such a discrepancy in saturated crack density between the modeling and the experiment results can be attributed to the assumption of elastic behavior of the polymer substrate. In reality, the polymer substrate yields and deforms plastically if the applied tensile strain exceeds a critical value. The linear elastic assumption for the polymer leads to an overestimated tensile stress in the substrate. As a result, under a given applied tension, the length of the delamination along the ITO/polymer interface is also overestimated due to the increased stress concentration at the delaminating front. Consequently, the tensile stress transferred to the ITO thin film is underestimated, leading to a prediction of saturated crack density lower than that measured in the *in situ* experiments. Nonetheless, those predicted values from the simulations offer estimates of the lower bounds of the ITO/polyimide interfacial toughness and ITO fracture strength, which agree with the results from other recent experiments.

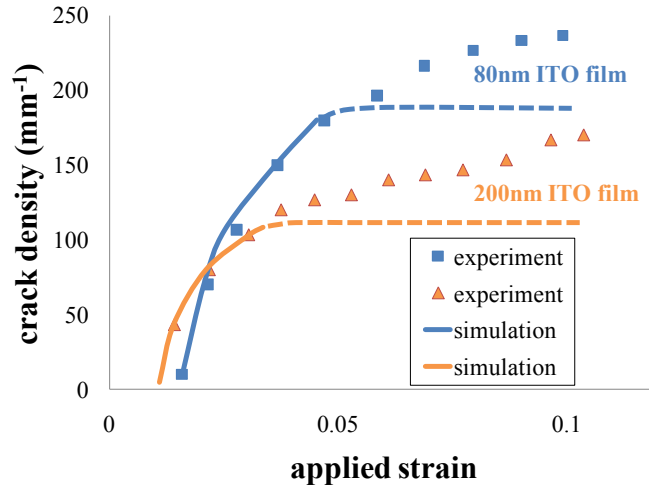


Figure 3.6. The crack density vs. applied strain curves from the best-fit simulations and experiments, for ITO film thickness of 80 nm and 200nm, respectively.

Figure 3.7a plots the variation of the tensile stress in the 80 nm thick ITO thin film as a function of the relative location in a unit cell model, at various applied strains. When the applied strain is small, the distribution of the tensile stress is rather uniform in majority part of the ITO thin film except the portion near the channel crack. As the applied strain increases, interfacial delamination initiates and propagates. As a result, the tensile stress transferred to the ITO thin film is reduced, leading to a rather non-uniform distribution of the tensile stress in the ITO thin film, with the highest level at the center of the ITO fragment and gradually diminishing to zero in the delaminated portion. Figure 3.7b further plots the delamination length normalized by the ITO fragment width as a function of applied strain, for both 80 nm and 200 nm thick ITO films, respectively, which clearly shows the advance of interfacial delamination, and therefore the underlying mechanism for the saturation of crack density in polymer-supported ITO thin films under tension.

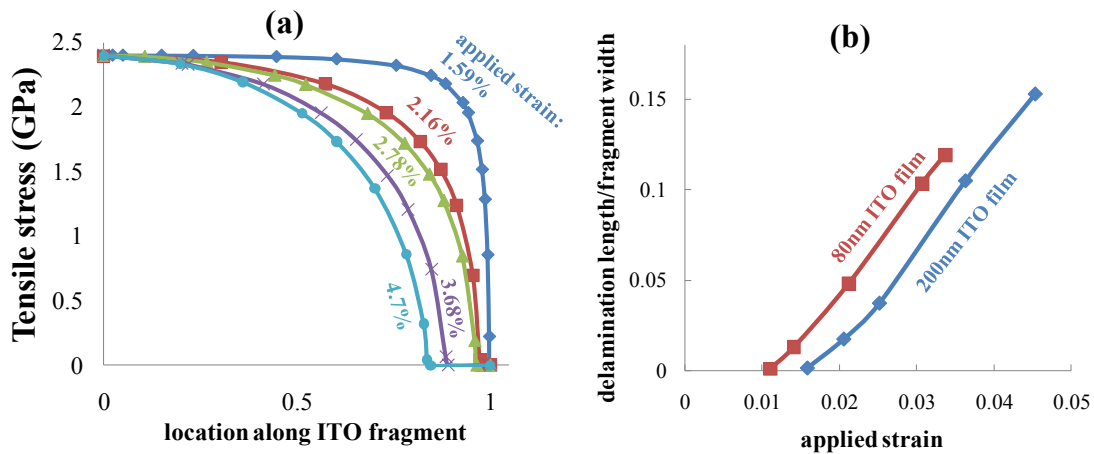


Figure 3.7. (a) The variation of the tensile stress in the 80 nm thick ITO thin film as a function of the relative location in a unit cell model, at various applied strains. For the horizontal axis, 0 denotes the center of the ITO fragment and 1 denotes the right edge of the ITO fragment (i.e., the channel crack surface). (b) The delamination length normalized by the ITO fragment width as a function of applied strain, for both 80 nm and 200 nm thick ITO thin films, respectively.

2. ITO cohesive toughness

Given the brittle nature of the ITO thin film fracture, the cohesive toughness of the ITO thin film is defined as the energy required for propagating channel crack to generate new crack surface of unit area. The detailed shape and deformation state near the channel crack front can be rather complicated, and hard to predict. By contrast, far ahead and far behind the channel crack front, the structure can be taken to deform under the plane strain conditions. Since both ITO and polymer are assumed to be linearly elastic at the channel crack onset strain, the driving force for the channel cracking can be calculated by the elastic energy stored in a slice of ITO/polymer laminate of unit thickness far ahead of the channel crack front minus the elastic energy stored in a slice of ITO/polymer laminate of unit thickness far behind the channel crack front. In the simulation, the widths of these two slices of ITO/polymer laminate are set to be the reciprocal of the crack density

corresponding to the crack onset strain in the *in situ* experiment. The slice far ahead of the channel crack front has a continuous ITO thin film, while the slice far behind has a channel crack in the middle of the ITO thin film. Each slice is subject to an applied strain equal to the crack onset strain, and the resulting strain energy is calculated in ABAQUS. Applying the above simulation strategy to the experiment results, we obtain a cohesive toughness of 42.0J/m^2 for ITO films with thickness of 80nm and 40.4J/m^2 for ITO films with thickness of 200nm. These values roughly agree with the results from other recent studies⁸⁴.

3. Mechanistic understanding of thickness dependence of saturated crack density in ITO film

The thickness dependence of the saturated crack density in polymer supported brittle films has been observed in previous studies⁸⁷. A few mechanics models have been considered to explain such thickness dependence⁸⁸. A consideration of the force balance of an ITO fragment at the saturation limit gives $\tau = 2h_{ITO}\sigma/s_{cr}$, where τ is the interfacial shear stress, h_{ITO} is the ITO film thickness, σ is the tensile stress in ITO film and s_{cr} is a length close to the ITO fragment width at the saturation limit (i.e., $1/s_{cr}$ approximately denotes the saturated crack density). A fracture mechanics based dimensional consideration leads to $\sigma \propto \sqrt{\Gamma_{ITO}/h_{ITO}}$, where Γ_{ITO} is the cohesive toughness of the ITO film. Given that the same fabrication conditions in depositing ITO films of different thickness on the same polymer substrate, it is reasonable to assume similar interfacial properties in different samples (e.g., as evident by the similar

interfacial toughness values predicted above). In other words, the interfacial shear stress τ remains to be constant. The above analysis yields that the thickness dependence of the saturated crack density takes the form of $\sqrt{\Gamma_{ITO}h_{ITO}}/s_{cr} \approx \text{constant}$. Using the ITO cohesive toughness obtained in Section 3.1.3.B2 and the saturated crack density data from *in situ* experiments, the value of $\sqrt{\Gamma_{ITO}h_{ITO}}/s_{cr}$ for $h_{ITO}=80$ nm agrees with that for 200nm within about 10%. This good agreement confirms the above mechanics understanding of the thickness dependence of the saturated crack density in polyimide supported ITO thin films.

3.1.4. Summary

In summary, we reported a coherent study integrating *in situ* electro-mechanical experiments and mechanics modeling to decipher the failure mechanics of ITO thin films on polyimide substrates under tension. Our *in situ* tensile tests inside SEM reveal real time details of crack initiation and propagation, crack density evolution, and associated electrical resistance variations in thin ITO conductors on polyimide substrates. The corresponding mechanics model offers quantitative determination of critical mechanical properties (ITO cohesive toughness, fracture stress, and ITO/polyimide interfacial toughness) from the experimental data and explains the experimentally observed thickness dependence of crack density evolution in ITO conductors. While the understanding from the two dimensional model used in this paper sheds light on the governing failure mechanisms of the ITO/polymer structure (i.e., ITO channel cracking

vs. ITO/polymer interfacial delamination), further studies such as three dimensional modeling are necessary to capture the detailed interplay of these two governing failure mechanisms.

3.2. a Map of Buckling-driven Failure Modes of Substrate-supported Thin Brittle Films

3.2.1. Introduction

Substrate-supported thin films have found widespread applications in microelectronics and flexible electronics technology⁸⁹. For example, thin indium tin oxide (ITO) films deposited on a polymer substrate are often used as transparent conductors and interconnect in flexible devices. As flexible electronic devices frequently experience large deformation, the mechanical failure of such thin films (e.g., ITO) poses significant challenge to the device reliability⁹⁰. A common failure mechanism of substrate-supported thin films is compression-induced buckling or wrinkling. The compression in the film may result from residual stress (e.g., due to film/substrate thermal mismatch or from film growth), or from the Poisson's effect when the film/substrate laminate is subject to uniaxial tension. Well bonded to a rather compliant substrate (e.g., an elastomer), a thin film under compression can wrinkle coherently with the underlying substrate⁹¹⁻⁹⁴; on a relatively stiff substrate, however, a thin brittle film under compression may partially

delaminate from the substrate and buckle to mitigate the compression. In turn, the film buckling drives further growth of delamination. Buckling-driven delamination of thin films on substrates has been extensively studied^{15, 95-100}. Recent experiments on substrate-supported thin brittle films in the context of flexible electronics reveal the *buckling-driven cracking* of the thin brittle films (e.g. Figure 3.8a), a different buckling-driven failure mode that is much less studied^{13, 101, 102}. In practice, the buckling-driven cracking of ITO films is more detrimental than the buckling-driven delamination of ITO films, as ITO film cracking cuts off the electrical conductance while a delaminated ITO strip can still carry electric currents. A question that remains unanswered is: what governs various buckling-driven failure modes in substrate-supported thin brittle films? To address this unsolved issue, this paper delineates a theoretical analysis and carries out numerical simulations to quantitatively determine key parameters that govern the buckling-driven failure modes in a substrate-supported thin brittle film.

3.2.2. In Situ Experimental Observation of Buckling-driven Failure of Substrate Supported Thin Brittle Films

As shown in Figure 3.8a, a thin ITO film on a polyimide substrate is subject to uniaxial tension. Channel cracks initiate and propagate in the brittle ITO film along the direction perpendicular to the tension. Upon further tension, some ITO strips (demarcated by two neighboring channel cracks) delaminate and buckle away from the substrate, driven by

the film compression due to Poisson's effect. The buckled portion of ITO film eventually cracks at the crest along the direction roughly parallel to the applied tension. By contrast, in another polyimide-supported ITO film that is subject to uniaxial tension, the similar ITO strips are found to only delaminate and buckle under Poisson compression, without film cracking (Figure 3.8b). The length of the delaminated portion of the ITO film in the latter case is found to be much longer than that in the buckling-driven cracking case.

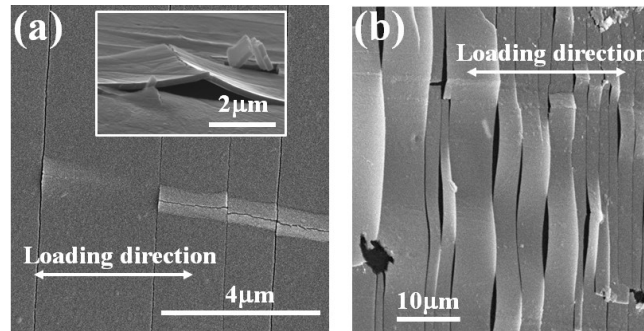


Figure 3.8. (a) Scanning electron microscope image of a thin brittle ITO film (100nm thick) on a thick polyimide substrate (75 μm thick) under uniaxial tension. The long strips along vertical directions result from tensile fracture of the ITO film and are then subject to Poisson's compression perpendicular to tension direction. Some ITO strips buckle away from the substrate and eventually crack at the crest along the direction roughly parallel to the applied tension. (Inset shows perspective view of buckling-driven film cracking in a different sample.) (b) In another polyimide-supported ITO film (80nm thick), Poisson's compression in the ITO strips only leads to film delamination, without film cracking. Note that the widths of interfacial delamination in (b) are much longer than those in (a).

3.2.3. *a Map of Buckling-driven Failure Modes of Substrate-supported Thin Brittle Films*

In the following, we delineate a theoretical model to decipher the dominant buckling-driven failure mode for a given film/substrate structure subject to film compression. A thin brittle film of thickness h on an infinitely thick elastic substrate of width B is subject to film compression ε_f . An initial imperfection is introduced as a

delamination of width $2b$ at the center location of the interface. When ε_f exceeds the critical Euler buckling strain $\varepsilon_{cr} = -\pi^2 h^2 / (12b^2)$, the delaminated portion of the film buckles with an out-of-plane amplitude profile of $w(x) = (A/2)[1 + \cos(\pi x/b)]$, where A is the peak amplitude of the buckled portion (see inset of Figure 3.9a).

The out-of-plane film buckling provides a driving force for further growth of delamination, which increases as the buckling amplitude increases. We next determine a critical buckling amplitude A_d^{cr} , above which the initial interfacial delamination starts to advance. The total potential energy of the system is given by $U_{total} = U_{unbuckled} + U_{buckled}^m + U_{buckled}^b - (B - 2b)\Gamma$, where $U_{unbuckled}$ is the strain energy of the film portion still bonded to the substrate, $U_{buckled}^m$ and $U_{buckled}^b$ are the membrane energy and bending energy of the buckled portion of the film, respectively, and Γ is the film/substrate interfacial adhesion energy. Here in the theoretical model we assume the substrate is rigid, thus the substrate strain energy is not included in U_{total} (the effect of substrate stiffness will be studied later through numerical simulations). The unbuckled portion of the film is only subject to membrane compression ε_f , so $U_{unbuckled} = (B - 2b)h(E_f' \varepsilon_f^2 / 2)$, where E_f' is the plane strain Young's Modulus of the film. For the buckled portion of the film, $U_{buckled}^m = bhE_f' \varepsilon_x^2$, where $\varepsilon_x = \varepsilon_f + (\pi A / 4b)^2$ (the latter term denotes the contribution of bending to the non-linear membrane strain in the buckled portion of the film), and $U_{buckled}^b = \int_{-b}^b (E_f' h^3 / 24) \left(\frac{d^2 w}{dx^2} \right)^2 dx = E_f' \pi^4 A^2 h^3 / 96b^3$. Energy minimization of U_{total} with respect to A and b gives a critical buckling

amplitude

$$\frac{A_d^{cr}}{h} = \sqrt{\frac{8}{3} \left(\sqrt{1 + \frac{9\Gamma}{2E_f' h} \left(\frac{2b}{\pi h}\right)^4} - 1 \right)}, \quad (3.1)$$

above which the initial delamination starts to advance. Figure 3.9a plots A_d^{cr}/h as a function of b/h , for various values of Γ (solid lines). Here, $E_f' = 132\text{GPa}$, which is representative for ITO. A_d^{cr} increases monotonically as Γ or b increases. That is, a stronger interfacial adhesion or a longer initial interfacial defect makes the film more resistant to further interfacial delamination.

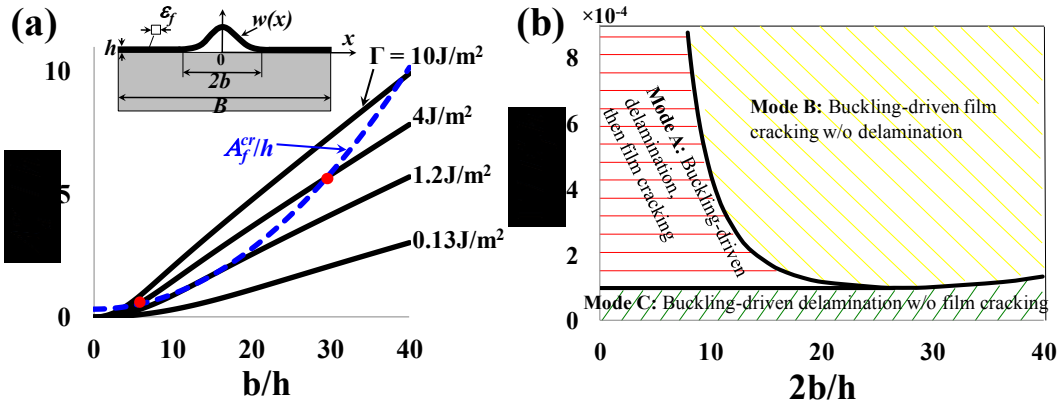


Figure 3.9. (a). Solid lines plot A_d^{cr}/h as a function of b/h , for various values of Γ . Dashed line plots A_f^{cr}/h as a function of b/h . Inset shows a schematic of the model. (b). A map delineates three buckling-driven failure modes in the parameter space of interfacial adhesion energy and initial interfacial defect size, namely, A) buckling-driven delamination followed by film cracking, B) Buckling-driven film cracking without delamination and C) Buckling-driven delamination without film cracking.

We next determine the critical buckling amplitude above which fracture occurs at the crest of the buckled portion of the film. The total strain in the buckled portion of the film consists of the contribution from the compressive membrane strain ($= -\pi^2 h^2 / (12b^2)$),

and that from the bending strain, which varies from tensile to compressive across the film thickness and is linearly proportional to film curvature $\frac{d^2w}{dx^2}$. Therefore, if the film buckles severely, the strain at the top surface of the buckled crest, given by $\frac{\pi^2 h^2}{4b^2} \left(\frac{A}{h} - \frac{1}{3}\right)$, may become tensile and exceed the fracture strain of the brittle film material, causing film cracking at the crest. The above argument gives a critical buckling amplitude, above which buckling-driven cracking of the film occurs,

$$\frac{A_f^{cr}}{h} = \frac{1}{3} + \left(\frac{2b}{\pi h}\right)^2 \frac{\sigma_f}{E_f'} , \quad (3.2)$$

where σ_f is the fracture strength of the brittle film material. The dashed line in figure 3.9a plots A_f^{cr}/h as a function of b/h , for the case of $\sigma_f = 2GPa$ and $E_f' = 132GPa$ (representative for ITO). A_f^{cr} increases monotonically as b increases. The comparison of the two critical buckling amplitudes defined in Eqs. (3.1) and (3.2) determines the dominant buckling-driven failure mode of a given film/substrate structure (e.g., E_f' , σ_f , and Γ) with an interfacial delamination of width $2b$ under sufficient film compression. That is, if $A_d^{cr} < A_f^{cr}$, buckling-driven delamination occurs; while if $A_f^{cr} < A_d^{cr}$, buckling-driven film cracking occurs.

As shown in figure 3.9a, there exists a critical value of interfacial adhesion energy Γ ($\approx 1.2J/m^2$), below which $A_d^{cr} < A_f^{cr}$ for all value of b/h . In other words, if the interface is weak (e.g., $\Gamma < 1.2J/m^2$), large compression in the film always leads to further advance of initial delamination, which mitigates the film compression in the buckled portion. Therefore, no buckling-driven film cracking occurs. For a given $\Gamma > 1.2J/m^2$,

the A_f^{cr} vs. b/h curve intersects the A_d^{cr} vs. b/h curve at two points. For example, the two curves intersect at $b/h = 5.6$ and 29.4 for $\Gamma = 4J/m^2$. When $b/h < 5.6$, $A_d^{cr} < A_f^{cr}$. As a result, under sufficient film compression, the initial delamination starts to advance until $b/h = 5.6$, after which $A_d^{cr} \geq A_f^{cr}$. In other words, the failure mode is buckling-driven delamination first, followed by film cracking. When $5.6 < b/h < 29.4$, $A_f^{cr} < A_d^{cr}$. As a result, the buckled portion of the film always cracks at the crest before any further advance of the initial delamination. When $b/h > 29.4$, $A_d^{cr} < A_f^{cr}$, which means the initial delamination always advance under sufficient film compression but no film cracking can occur. The above comparison between A_d^{cr} and A_f^{cr} delineates three possible buckling-driven failure modes: A). Buckling-driven delamination followed by film cracking, B). Buckling-driven film cracking without delamination, and C). Buckling-driven delamination without film cracking. Figure 3.9b plots a map of these three failure modes in the parameter space of interfacial adhesion energy and initial interfacial defect size.

3.2.4. Effect of Substrate Stiffness on the Map of Buckling-driven Failure Modes

To investigate the effect of substrate stiffness on the buckling-driven failure modes of substrate-supported thin brittle films, we perform finite element modeling to simulate the full process of buckling-driven failure. The film/substrate laminate is assumed to deform under plane strain condition (e.g., inset of Fig. 3.9a). In the simulation model, the film is a layer with thickness of h and the substrate is a block with thickness of $50h$ and width of

$B = 200h$. Both the film and the substrate are modeled as linear elastic materials. The Young's Modulus and the Poisson's ratio of the film are 120GPa and 0.3, respectively. The Young's Modulus of the substrate varies from 2GPa to 20GPa, with a Poisson's ratio of 0.4. The film is densely meshed with four-node plane strain elements with element size of $0.1h$. The substrate is also meshed with four-node plane strain elements with matching element size near the interface and coarse elements far away from the interface. The film compression is introduced as a thermal mismatch strain. To help initiate film buckling, an initial interfacial delamination of various widths is prescribed at the center location of the interface, and an inverse V-notch with height of $0.02h$ and half width of $0.4h$ is introduced at the center of the bottom surface of the delaminated film. The simulations are carried out using finite element code ABAQUS v6.9. To simulate the buckling-induced delamination, the bonded portion of the interface is modeled with cohesive elements, whose traction-displacement laws are varied to define an interfacial adhesion energy ranging from $0.5J/m^2$ to $10J/m^2$. The bonded interface is meshed with four-node cohesive elements sharing nodes with the neighboring elements in the film and the substrate. To simulate the brittle fracture at the crest of the buckled film, extended finite element method (XFEM) is employed to enrich the film elements along the centerline of the film. Maximum principal stress criterion for crack initiation is used with the film strength set to be 2GPa. Viscous regularization option in ABAQUS is used for both the cohesive elements and the XFEM enrichment to enhance computation

convergence.

Figure 3.10 plots the map of buckling-driven failure modes in the parameter space of interfacial adhesion energy and initial imperfection size, for various Young's Moduli of the substrate E_s . Emerging from the simulation results are the same three failure modes as revealed from the theoretical analysis (i.e., Figure 3.9b). Simulation results show that, as the substrate becomes more compliant, Modes A and B become more dominant in the parameter space explored. That is, buckling-driven film cracking is more likely to occur. The effect of substrate stiffness can be understood as follows. As the substrate becomes more compliant, the deformation of the film near the edges of delamination front is less constrained. In other words, the substrate can more easily deform locally to accommodate out-of-plane buckling of the film, which on one hand leads to increasing buckling amplitude, and on the other hand results in decreasing driving force for further advance of delamination. In figure 3.9a, there exists a critical interfacial adhesion energy (indicated by the horizontal boundary between Mode A and Mode C), below which no film cracking occurs (i.e., Mode C), no matter what the size of initial delamination is. By contrast, as shown in figure 3.10, if the size of initial delamination is too small, Mode A or B dominates, which eventually leads to film cracking, no matter how weak the interfacial adhesion is. That is, to avoid buckling-driven cracking of a brittle film supported by a rather compliant substrate, a long initial interfacial delamination and a weak interfacial adhesion are desired to allow Mode C to occur. For example, in figure

3.8a, $2b/h \approx 6.4$, while in figure 3.8b, $2b/h \approx 174$. Taking $E_s = 2\text{GPa}$, a representative stiffness for polyimide, figure 3.10d suggests buckling-driven film cracking after delamination advance (Mode A) in Fig. 3.8a and buckling-driven delamination without film cracking (Mode C) in Fig. 3.8b, assuming a weak interfacial adhesion. In this sense, the model prediction agrees well with experimental observations.

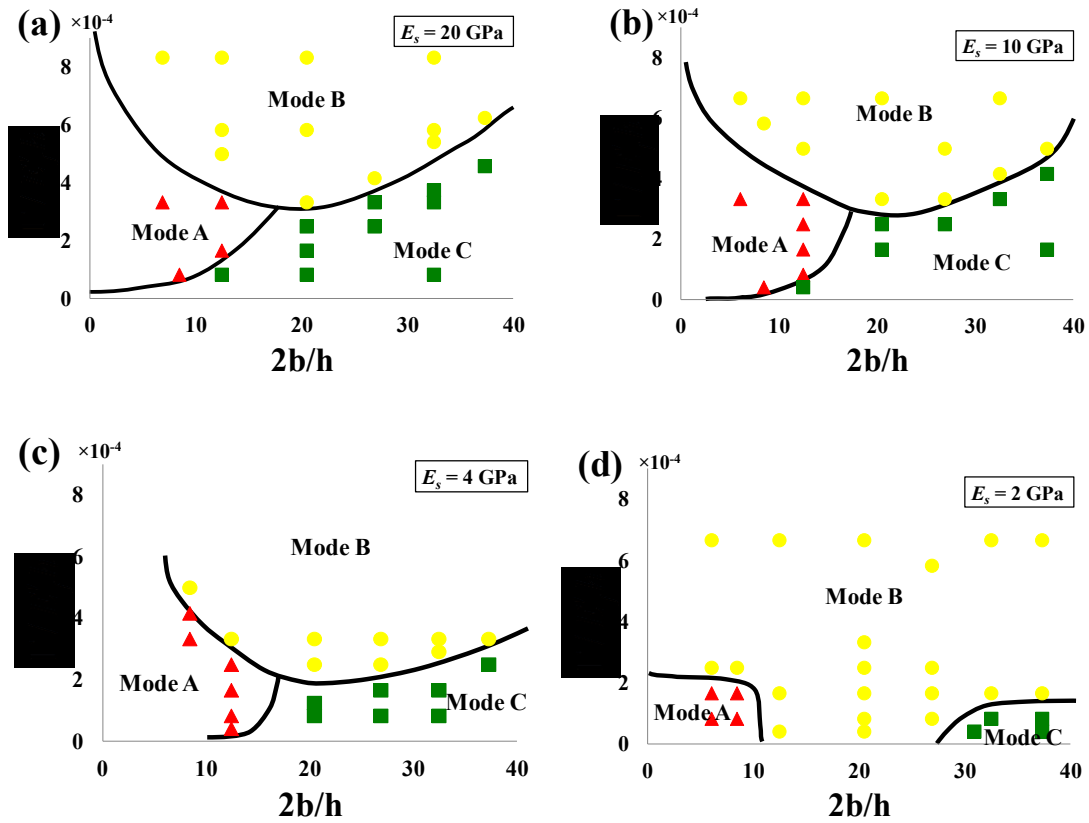


Figure 3.10. (a-d). The map of buckling-driven failure modes (same as those defined in Fig. 2b) in the parameter space of interfacial adhesion energy and initial interfacial defect size, for various substrate stiffness. Each mark indicates a finite element simulation case, with triangles denoting Mode A, disks denoting Mode B and squares denoting Mode C. The boundary lines between different failure modes are estimated from the simulation results.

3.2.5. Summary

In summary, through theoretical analysis and numerical modeling, we identify three

buckling-driven failure modes in substrate-supported thin brittle films, two of which eventually leads to film cracking and the third involves only buckling-driven delamination without film cracking. These three failure modes are mapped out in the parameter space of interfacial adhesion energy and initial interfacial defect size. As the substrate becomes more compliant, the failure modes leading to film cracking becomes more dominant against the delamination-only failure mode. Interestingly emerging from the results is that, a thin brittle film strongly bonded on a substrate is indeed more prone to buckling-driven cracking, a more detrimental failure mode for transparent ITO conductors widely used in displays and flexible electronics. In this sense, the present study offers guidelines on optimal material selection and adhesion control in designing functional thin brittle films in microelectronics and flexible electronics devices.

Chapter 4. Ductile Failure of Substrate-supported Metal Layers under Biaxial In-plane Loading

4.1. Necking Limit of Substrate-supported Metal Layers under Biaxial In-plane Loading

4.1.1. Introduction

Substrate-supported metal layers are being developed as structural elements and functional components in modern technologies, with the promise of enhanced mechanical performance in comparison with freestanding metal layers. For example, thin metal films deposited on polymer substrates are often used as deformable conductors and interconnects in flexible electronic devices that are often subject to large stretches, bends and twists¹⁰³⁻¹¹³. Polymer-coated metal layers have been shown to be able to undergo significant plastic deformation before rupture, thus hold potential as energy absorbing structural elements subject to high intensity impulsive loads.

Ductile failure of metal layers under in-plane loading often initiates from strain localization, such as the onset of necking instability. Localized strain in the necked region promotes the increase of stress triaxiality, which in turn causes microscopic damage and eventually leads to ductile fracture near the neck. The onset of necking instability in a material occurs when the geometric softening prevails over material hardening, as attributed to Considere¹¹⁴. When a substrate-supported metal layer is under in-plane loading, the necking limit strain of the metal/substrate bilayer depends on the effective

incremental modulus of the bilayer. Under tension, polymers neck but the incipient strain localization often gives way to stable neck propagation along the length of the polymer layer. In other words, polymers often harden more than metals. Furthermore, many elastomers can sustain substantial stretch without suffering from necking instability, that is, these elastomers stiffen so steeply that their incremental modulus remains constant or even increases modestly upon tension. By contrast, the incremental modulus of a metal layer decreases monotonically with stretching. Consequently, under tension, a polymer/metal or elastomer/metal bilayer has a greater effective incremental modulus than a single freestanding metal layer. As a result, onset of necking instability in such substrate-supported metal layers are expected to occur at higher strains¹¹⁵⁻¹¹⁷. Uniaxial tensile experiments have shown that a freestanding thin metal film usually ruptures at a small strain $\sim 1\%$ ¹¹⁸⁻¹²³. By contrast, polymer-supported thin metal films can sustain tensile strains up to 50% before rupture^{108, 110, 124-130}. It is predicted that the substrate constraint to the necking development in the metal layer disappears when the metal layer debonds from the substrate^{70, 117}, which has been recently verified by the experimental observation of interfacial delamination in the later stage of the tensile fracture process of a thin Cu film on a polyimide substrate¹⁰⁸. Necking in a single freestanding metal layer can also be retarded under dynamic stretching due to inertia effect¹³¹⁻¹³⁷. The interaction of the substrate and inertia effects on necking retardation has also been investigated^{115,}

138-142

In practice, substrate-supported metal layers are often subject to large and complicated in-plane loading. For example, the electronic sensitive skins covering the elbow of a robot experience large biaxial stretches. The understanding of necking instability of substrate-supported metal layers under arbitrary biaxial in-plane loading, however, is poorly studied so far. Most existing theoretical studies assume plane strain condition of the bilayer deformation. Xue and Hutchinson (2008) investigated the necking retardation of elastomer-supported metal layers under biaxial loading, but the biaxial loading ratio in that study is limited to be in the positive regime. As to be shown later in the present paper, in the positive loading ratio regime, the necking band always occurs in the direction perpendicular to that of the greater tensile load. By contrast, most reported tensile experiments of substrate-supported metal layers are uniaxial tests. As commonly observed in such uniaxial tensile experiments, the incipient necking bands often occur along a slanted direction in between the two loading directions. For example, Fig. 1a shows the necking bands in a thin Cu film (100 nm thick) supported by a polyimide substrate (100 μ m thick) occur along a direction about 60° away from the uniaxial loading direction. So far, the quantitative correlation between the critical necking limit strain as well as the necking band orientation and the material properties and thickness ratio of a metal/substrate bilayer in the full range of biaxial in-plane loading ratio still remains unclear.

This section presents a comprehensive investigation to decipher the above quantitative

correlation in two representative material structures, namely, a metal layer supported by a stiff plastic substrate, and a metal layer supported by a compliant elastomer substrate, respectively. In particular, it is shown that a metal layer supported by a sufficiently stiff and thick elastomer substrate is immune from necking instability. This further motivates the investigation of the enhanced energy absorption of elastomer-supported metal layers in comparison with that of an all-metal layer with the same mass.

4.1.2. Mechanics Model

A. Constitutive relations

Necking instability occurs at strains sufficiently large so that the elasticity of the metal layer can be neglected. In this study, we describe the constitutive relation of metal using the finite strain J_2 deformation theory of plasticity developed by Hill¹⁴³ and Hutchinson and Neale¹⁴⁴, as recapped below. With reference to Cartesian base vectors coaxial with the principal stress axes, we have

$$\bar{\sigma}_{ij} = L_{ijkl} \dot{\epsilon}_{kl} + \dot{p} \delta_{ij} \quad (4.1)$$

where $\bar{\sigma}_{ij}$ is the Jaumann rate of the Cauchy stress, $\dot{\epsilon}_{ij}$ is the Eulerian strain rate, \dot{p} is the hydrostatic part of the stress rate, and δ_{ij} is the Kronecker delta. The instantaneous moduli L_{ijkl} are assumed to satisfy the indicial symmetries

$$L_{ijkl} = L_{jikl} = L_{ijlk} = L_{klij} \quad (4.2)$$

Let σ_{ij} be the Cauchy stress, s_{ij} be the deviatoric stress and $\sigma_e = \sqrt{3s_{ij}s_{ij}/2}$ be the effective stress; then the instantaneous moduli can be given as

$$L_{ijkl} = \frac{2}{3}E_s \left[\frac{1}{2}(\delta_{ik}\delta_{jl} + \delta_{jk}\delta_{il}) - \frac{1}{3}\delta_{ij}\delta_{kl} \right] - (E_s - E_t) \frac{s_{ij}s_{kl}}{\sigma_e^2} + Q_{ijkl} \quad (4.3)$$

where E_s and E_t are the secant modulus and tangent modulus of the uniaxial true stress-Eulerian strain curve at σ_e , respectively. For Q_{ijkl} , the last term in (4.3), its only non-zero components in principal axes are the “shearing” terms, such as

$$Q_{1212} = \frac{1}{3}E_s [(\varepsilon_1 - \varepsilon_2) \coth(\varepsilon_1 - \varepsilon_2) - 1] \quad (4.4)$$

Notice that in (4.4), $\varepsilon_1 = \varepsilon_{11}$ and $\varepsilon_2 = \varepsilon_{22}$, as the Cartesian base vectors are coaxial with the principal Eulerian strains.

In view of the above remarks, by using the definition of L_{ijkl} and the incompressibility condition $\dot{\varepsilon}_{kk} = 0$, the constitutive law (4.1) can be expressed as

$$\bar{\sigma}_{ij} = \frac{2}{3}E_s \dot{\varepsilon}_{ij} - (E_s - E_t) \frac{s_{ij}s_{kl}}{\sigma_e^2} \dot{\varepsilon}_{kl} + Q_{ijkl} \dot{\varepsilon}_{kl} + \dot{p} \delta_{ij} \quad (4.5)$$

In the localized necking band analysis, plane stress condition is assumed. Before necking instability occurs, the only two non-vanishing stress components are $\sigma_{11} = \sigma_1$ and $\sigma_{22} = \sigma_2$ ($\sigma_{33} = 0$). Taking advantage of the plane stress condition $\bar{\sigma}_{33} = 0$ and the incompressibility condition, the hydrostatic stress rate \dot{p} can be solved as

$$\dot{p} = \left(\frac{2}{3}E_s \dot{\varepsilon}_{11} + \frac{2}{3}E_s \dot{\varepsilon}_{22} \right) + (E_s - E_t) \frac{s_{33}}{\sigma_e^2} [\sigma_{11} \dot{\varepsilon}_{11} + \sigma_{22} \dot{\varepsilon}_{22}] \quad (4.6)$$

Substituting (4.6) into (4.1), the constitutive relation (4.1) can be reduced to

$$\bar{\sigma}_1 = L_{11} \dot{\varepsilon}_1 + L_{12} \dot{\varepsilon}_2 \quad (4.7)$$

$$\bar{\sigma}_2 = L_{21} \dot{\varepsilon}_1 + L_{22} \dot{\varepsilon}_2 \quad (4.8)$$

$$\bar{\sigma}_{12} = 2L_s \dot{\varepsilon}_{12} \quad (4.9)$$

where the instantaneous moduli $L_{ij}(i, j = 1, 2)$ are given by

$$L_{11} = \frac{4}{3}E_s - (E_s - E_t) \left(\frac{\sigma_1}{\sigma_e} \right)^2 \quad (4.10)$$

$$L_{22} = \frac{4}{3}E_s - (E_s - E_t) \left(\frac{\sigma_2}{\sigma_e} \right)^2 \quad (4.11)$$

$$L_{12} = L_{21} = \frac{2}{3}E_s - (E_s - E_t) \frac{\sigma_1 \sigma_2}{\sigma_e^2} \quad (4.12)$$

$$L_s = \frac{1}{3}E_s(\varepsilon_1 - \varepsilon_2) \coth(\varepsilon_1 - \varepsilon_2) = \frac{1}{3}E_s(\varepsilon_1 - \varepsilon_2) \frac{e^{2\varepsilon_1} + e^{2\varepsilon_2}}{e^{2\varepsilon_1} - e^{2\varepsilon_2}} \quad (4.13)$$

J_2 deformation theory gives the relation between the principal Eulerian strain and the principal deviatoric stress as follows

$$\varepsilon_i = \mu s_i, \quad (4.14)$$

where μ can be obtained from the uniaxial tension curve and is a function of the effective stress $\sigma_e = \sqrt{3s_i s_i / 2}$ and the effective strain $\varepsilon_e = \sqrt{2\varepsilon_i \varepsilon_i / 3}$. Therefore, equation (4.14) can be rewritten as

$$\mu = \frac{3}{2} \frac{\varepsilon_e}{\sigma_e} = \frac{3}{2E_s} \quad (4.15)$$

Imposing proportional straining path

$$\frac{\varepsilon_2}{\varepsilon_1} = \rho = \text{constant} \quad (4.16)$$

to the structure, we then have

$$\sigma_1 = \frac{2E_s}{3}(2 + \rho)\varepsilon_1 \quad (4.17)$$

$$\sigma_2 = \frac{2E_s}{3}(1 + 2\rho)\varepsilon_1 \quad (4.18)$$

$$\sigma_e = \frac{2E_s}{3} \sqrt{3(1 + \rho + \rho^2)} \varepsilon_1 \quad (4.19)$$

For a material with a power-law hardening $\sigma_e = K\varepsilon_e^N$ in the plastic range, the secant

modulus and tangent modulus can be given by

$$E_s = K\varepsilon_e^{N-1} \quad (4.20)$$

$$E_t = NK\varepsilon_e^{N-1}, \quad (4.21)$$

respectively, where

$$\varepsilon_e = 2\sqrt{\frac{1+\rho+\rho^2}{3}}\varepsilon_1 \quad (4.22)$$

The above constitutive relation is also adopted in this study to describe the stress-strain behavior of the stiff plastic substrate.

The elastomer substrate in this study is described as incompressible neo-Hookean materials, whose strain energy density W is given by

$$W = \frac{E}{6}(\lambda_1^2 + \lambda_2^2 + \lambda_3^2 - 3) \quad (4.23)$$

where E is Young's modulus at zero strain, λ_i ($i = 1,2,3$) are the principal stretches.

The incompressibility implies a constraint that $\lambda_1\lambda_2\lambda_3 = 1$. As a result of the plane stress condition $\sigma_{33} = 0$, we have

$$\sigma_1 \equiv \sigma_{11} = \frac{E}{3}(\lambda_1^2 - \lambda_3^2) = \frac{E}{3}[e^{2\varepsilon_1} - e^{-2(\varepsilon_1+\varepsilon_2)}] \quad (4.24)$$

$$\sigma_2 \equiv \sigma_{22} = \frac{E}{3}(\lambda_2^2 - \lambda_3^2) = \frac{E}{3}[e^{2\varepsilon_2} - e^{-2(\varepsilon_1+\varepsilon_2)}] \quad (4.25)$$

All shear stress components vanish given the proportional loading path. Following Biot (1965), the rate form of constitutive relation for Neo-Hookean material can be given as follows

$$\bar{\sigma}_{11} = \frac{4E}{9} \lambda_1^2 \dot{\varepsilon}_1 - \frac{2E}{9} \lambda_2^2 \dot{\varepsilon}_2 - \frac{2E}{9} \lambda_3^2 \dot{\varepsilon}_3 + \dot{p} \quad (4.26)$$

$$\bar{\sigma}_{22} = -\frac{2E}{9} \lambda_1^2 \dot{\varepsilon}_1 + \frac{4E}{9} \lambda_2^2 \dot{\varepsilon}_2 - \frac{2E}{9} \lambda_3^2 \dot{\varepsilon}_3 + \dot{p} \quad (4.27)$$

$$\bar{\sigma}_{33} = -\frac{2E}{9} \lambda_1^2 \dot{\varepsilon}_1 - \frac{2E}{9} \lambda_2^2 \dot{\varepsilon}_2 + \frac{4E}{9} \lambda_3^2 \dot{\varepsilon}_3 + \dot{p} \quad (4.28)$$

$$\bar{\sigma}_{12} = \frac{E}{3} (\lambda_1^2 + \lambda_2^2) \dot{\varepsilon}_{12} \quad (4.29)$$

Take advantage of the plane stress condition $\bar{\sigma}_{33} = 0$, the hydrostatic stress rate \dot{p} can be explicitly solved as

$$\dot{p} = \frac{2E}{9} \lambda_1^2 \dot{\varepsilon}_1 + \frac{2E}{9} \lambda_2^2 \dot{\varepsilon}_2 - \frac{4E}{9} \lambda_3^2 \dot{\varepsilon}_3 \quad (4.30)$$

Substitute (4.30) into (4.26) and (4.27) and consider the incompressibility $\dot{\varepsilon}_1 + \dot{\varepsilon}_2 + \dot{\varepsilon}_3 = 0$, the rate-form constitutive relation for the neo-Hookean material can be written in a more compact way similar to (4.7-4.9) as follows

$$\bar{\sigma}_1 = \hat{L}_{11} \dot{\varepsilon}_1 + \hat{L}_{12} \dot{\varepsilon}_2 \quad (4.31)$$

$$\bar{\sigma}_2 = \hat{L}_{21} \dot{\varepsilon}_1 + \hat{L}_{22} \dot{\varepsilon}_2 \quad (4.32)$$

$$\bar{\sigma}_{12} = 2\hat{L}_s \dot{\varepsilon}_{12} \quad (4.33)$$

where the explicit form of instantaneous moduli \hat{L}_{ij} ($i, j = 1, 2$) is given by

$$\hat{L}_{11} = \frac{2E}{3} [\lambda_1^2 + \lambda_3^2] = \frac{2E}{3} [e^{2\varepsilon_1} + e^{-2(\varepsilon_1 + \varepsilon_2)}] \quad (4.34)$$

$$\hat{L}_{22} = \frac{2E}{3} [\lambda_2^2 + \lambda_3^2] = \frac{2E}{3} [e^{2\varepsilon_2} + e^{-2(\varepsilon_1 + \varepsilon_2)}] \quad (4.35)$$

$$\hat{L}_{12} = \hat{L}_{21} = \frac{2E}{3} \lambda_3^2 = \frac{2E}{3} e^{-2(\varepsilon_1 + \varepsilon_2)} \quad (4.36)$$

$$\hat{L}_s = \frac{E}{6} (\lambda_1^2 + \lambda_2^2) = \frac{E}{6} (e^{2\varepsilon_1} + e^{2\varepsilon_2}) \quad (4.37)$$

B. Localized necking analysis for a substrate-supported metal layer under in-plane loading

Consider a flat metal layer of uniform initial thickness h perfectly adhered to a substrate of uniform initial thickness H (Fig. 4.1b). The metal/substrate bilayer is subject to a homogeneous strain field with in-plane strains $\varepsilon_{11} = \varepsilon_1$, $\varepsilon_{22} = \varepsilon_2$ and all other $\varepsilon_{ij} = 0$. Therefore, the stress field is also homogeneous with $\sigma_{11} = \sigma_1$, $\sigma_{22} = \sigma_2$ and all other $\sigma_{ij} = 0$ before necking instability occurs. Under a proportional loading path (i.e., $\frac{\varepsilon_2}{\varepsilon_1} = \rho$), the bilayer first deforms homogeneously, and above a critical strain level, homogeneous deformation gives way to strain localization in the form of localized plastic deformation in a narrow band which is referred as the necking band while the deformation remains homogeneous elsewhere. The necking band sets in with its in-plane normal direction \mathbf{n} making an angle θ to x_1 direction (Fig. 4.1c).

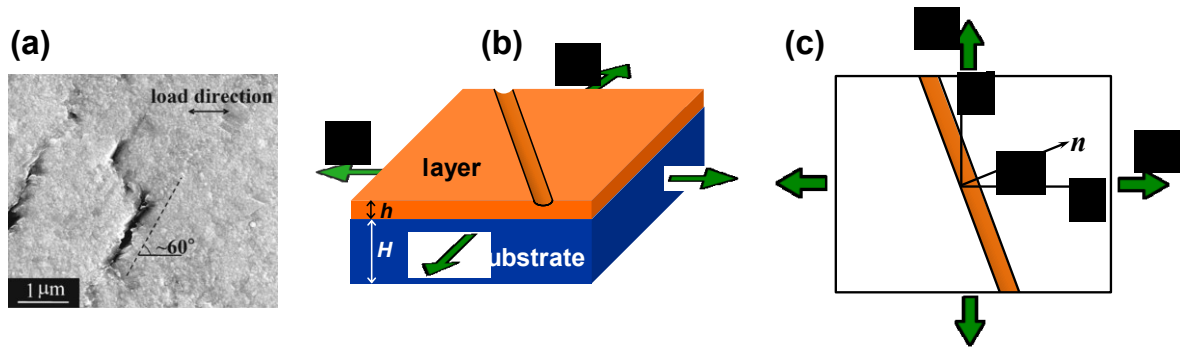


Figure 4.1. Schematics of necking band in substrate-supported metal film

The bifurcation analysis of a freestanding metal sheet (Hill, 1975; Rice, 1976; Neale and Hutchinson, 1978) is adapted to study the necking limit of a substrate-supported metal layer. We assume the plastic flow field within the necking band varies across the band along its normal direction, i.e.,

$$v_i = F_i(n_1 x_1 + n_2 x_2) \quad i = 1, 2 \quad (4.38)$$

where v_i denotes the differences between the velocity components inside and outside the necking band, and $n_1 = \cos \theta$ and $n_2 = \sin \theta$ are the components of the unit normal to the necking band (Fig. 4.1c). Then the velocity gradients within the necking band can be written as

$$v_{i,j} = F'_i n_j \equiv f_i n_j \quad i, j = 1, 2 \quad (4.39)$$

Accordingly, the strain rate field inside the necking band is given by

$$\dot{\epsilon}_{ij} = \frac{1}{2}(v_{i,j} + v_{j,i}) \quad i, j = 1, 2 \quad (4.40)$$

Incompressibility of plastic deformation gives that $\dot{\epsilon}_{33} = -(\dot{\epsilon}_{11} + \dot{\epsilon}_{22})$.

At the onset of necking, equilibrium across the necking band and its underlying substrate part requires that the nominal traction rates \dot{T}_i on the necking band boundaries be continuous. Thus,

$$\Delta \dot{T}_j^m h + \Delta \dot{T}_j^s H = n_i \dot{t}_{ij}^m h + n_i \dot{t}_{ij}^s H = 0 \quad (4.41)$$

where \dot{t}_{ij} is the difference between the nominal stress rate components inside and outside the necking band. Superscripts m and s denote the metal layer and the substrate, respectively. \dot{t}_{ij} can be related to the Jaumann rate of the Cauchy stress $\bar{\sigma}_{ij}$ through

$$\dot{t}_{ij} = \bar{\sigma}_{ij} + \sigma_{ik} v_{j,k} - (\sigma_{ik} \dot{\epsilon}_{jk} + \sigma_{jk} \dot{\epsilon}_{ik}) \quad (4.42)$$

Substituting (4.42) and the constitutive relations presented in Section A into the equilibrium equation (4.41), a set of linear homogeneous equations in f_1 and f_2 can be

obtained as follows,

$$\begin{bmatrix} g_{11} & g_{12} \\ g_{21} & g_{22} \end{bmatrix} \begin{bmatrix} f_1 \\ f_2 \end{bmatrix} = \begin{bmatrix} 0 \\ 0 \end{bmatrix} \quad (4.43)$$

where

$$g_{11} = \left\{ n_1^2 (L_{11}^m - \sigma_1^m) + n_2^2 \left[L_s^m + \frac{1}{2} (\sigma_2^m - \sigma_1^m) \right] \right\} h + \left\{ n_1^2 (L_{11}^s - \sigma_1^s) + n_2^2 \left[L_s^s + \frac{1}{2} (\sigma_2^s - \sigma_1^s) \right] \right\} H \quad (4.44)$$

$$g_{12} = g_{21} = n_1 n_2 \left[L_{12}^m + L_s^m - \frac{1}{2} (\sigma_1^m + \sigma_2^m) \right] h + n_1 n_2 \left[L_{12}^s + L_s^s - \frac{1}{2} (\sigma_1^s + \sigma_2^s) \right] H \quad (4.45)$$

$$g_{22} = \left\{ n_1^2 \left[L_s^m + \frac{1}{2} (\sigma_1^m - \sigma_2^m) \right] + n_2^2 (L_{22}^m - \sigma_2^m) \right\} h + \left\{ n_1^2 \left[L_s^s + \frac{1}{2} (\sigma_1^s - \sigma_2^s) \right] + n_2^2 (L_{22}^s - \sigma_2^s) \right\} H. \quad (4.46)$$

The condition for the onset of necking instability is met if non-trivial solution of f_1 and f_2 exists to satisfy (4.43). That is,

$$\det \begin{bmatrix} g_{11} & g_{12} \\ g_{21} & g_{22} \end{bmatrix} = 0 \quad (4.47)$$

For a metal layer with a power-law hardening $\sigma_e = K_m \varepsilon_e^{N_m}$ supported by a plastic substrate with a power-law hardening $\sigma_e = K_s \varepsilon_e^{N_s}$, (4.47) becomes

$$\left\{ \left\{ \cos^2 \psi \left[4 - (1 - N_f) \frac{(2+\rho)^2}{(1+\rho+\rho^2)} - 2(2+\rho)\varepsilon_1 \right] + \sin^2 \psi \left[(1-\rho) \frac{2}{e^{2(1-\rho)\varepsilon_1-1}} \varepsilon_1 \right] \right\} + S \left\{ \cos^2 \psi \left[4 - (1 - N_s) \frac{(2+\rho)^2}{(1+\rho+\rho^2)} - 2(2+\rho)\varepsilon_1 \right] + \sin^2 \psi \left[(1-\rho) \frac{2}{e^{2(1-\rho)\varepsilon_1-1}} \varepsilon_1 \right] \right\} \left(\frac{2\sqrt{1+\rho+\rho^2}\varepsilon_1}{\sqrt{3}} \right)^{N_s-N_f} \right\} * \left\{ \left\{ \cos^2 \psi \left[(1-\rho) \frac{2e^{2(1-\rho)\varepsilon_1}}{e^{2(1-\rho)\varepsilon_1-1}} \varepsilon_1 \right] + \sin^2 \psi \left[4 - (1 - N_f) \frac{(1+2\rho)^2}{(1+\rho+\rho^2)} - 2(1+2\rho)\varepsilon_1 \right] \right\} + S \left\{ \cos^2 \psi \left[(1-\rho) \frac{2e^{2(1-\rho)\varepsilon_1}}{e^{2(1-\rho)\varepsilon_1-1}} \varepsilon_1 \right] + \sin^2 \psi \left[4 - (1 - N_f) \frac{(1+2\rho)^2}{(1+\rho+\rho^2)} - 2(1+2\rho)\varepsilon_1 \right] \right\} \right\}$$

$$\begin{aligned}
& \rho) \frac{2e^{2(1-\rho)\varepsilon_1}}{e^{2(1-\rho)\varepsilon_1-1}} \varepsilon_1 \Big] + \\
& \sin^2 \psi \left[4 - (1 - N_s) \frac{(1+2\rho)^2}{(1+\rho+\rho^2)} - 2(1 + 2\rho)\varepsilon_1 \right] \left(\frac{2\sqrt{1+\rho+\rho^2}\varepsilon_1}{\sqrt{3}} \right)^{N_s-N_f} \Big\} - \\
& \cos^2 \psi \sin^2 \psi \left\{ \left[2 - (1 - N_f) \frac{(1+2\rho)(2+\rho)}{1+\rho+\rho^2} + (1 - \rho) \frac{e^{2(1-\rho)\varepsilon_1+1}}{e^{2(1-\rho)\varepsilon_1-1}} \varepsilon_1 - 3(1 + \rho)\varepsilon_1 \right] + \right. \\
& \quad S \left[2 - (1 - N_s) \frac{(1+2\rho)(2+\rho)}{1+\rho+\rho^2} + (1 - \rho) \frac{e^{2(1-\rho)\varepsilon_1+1}}{e^{2(1-\rho)\varepsilon_1-1}} \varepsilon_1 - \right. \\
& \quad \left. \left. 3(1 + \rho)\varepsilon_1 \right] \left(\frac{2\sqrt{1+\rho+\rho^2}\varepsilon_1}{\sqrt{3}} \right)^{N_s-N_f} \right\}^2 = 0 \tag{4.48}
\end{aligned}$$

where dimensionless group $S = \frac{K_s H}{K_m h}$.

For a given value of $\rho = \frac{\varepsilon_2}{\varepsilon_1}$, critical strains ε_1 can be solved numerically from (4.48) in the permissible range of orientation angle θ (between 0° and 90°). The lowest critical strain and the corresponding angle define the critical necking limit strain and the necking band orientation of a plastic-supported metal layer under a biaxial loading ratio ρ , respectively.

For a power law metal layer supported by a neo-Hookean elastomer substrate, (4.47) becomes

$$\begin{aligned}
& \left\{ \cos^2 \theta \left[4 - (1 - N) \frac{(2+\rho)^2}{(1+\rho+\rho^2)} - 2(2 + \rho)\varepsilon_1 \right] + \right. \\
& \sin^2 \theta \left[(1 - \rho) \frac{2}{e^{2(1-\rho)\varepsilon_1-1}} \varepsilon_1 \right] \left. \right\} \left(\frac{2\sqrt{1+\rho+\rho^2}\varepsilon_1}{\sqrt{3}} \right)^{N-1} + S \{ \cos^2 \theta [e^{2\varepsilon_1} + 3e^{-2(1+\rho)\varepsilon_1}] + \\
& \sin^2 \theta e^{2\rho\varepsilon_1} \} * \left\{ \cos^2 \theta \left[(1 - \rho) \frac{2e^{2(1-\rho)\varepsilon_1}}{e^{2(1-\rho)\varepsilon_1-1}} \varepsilon_1 \right] + \sin^2 \theta \left[4 - (1 - N) \frac{(1+2\rho)^2}{(1+\rho+\rho^2)} - \right. \right.
\end{aligned}$$

$$\begin{aligned}
& 2(1 + 2\rho)\varepsilon_1 \left] \left(\frac{2\sqrt{1+\rho+\rho^2}\varepsilon_1}{\sqrt{3}} \right)^{N-1} + S \{ \cos^2 \theta e^{2\varepsilon_1} + \sin^2 \theta [e^{2\rho\varepsilon_1} + 3e^{-2(1+\rho)\varepsilon_1}] \} \right\} - \\
& \cos^2 \theta \sin^2 \theta \left\{ \left[2 - (1 - N) \frac{(1+2\rho)(2+\rho)}{1+\rho+\rho^2} + (1 - \rho) \frac{e^{2(1-\rho)\varepsilon_1} + 1}{e^{2(1-\rho)\varepsilon_1} - 1} \varepsilon_1 - \right. \right. \\
& \left. \left. 3(1 + \rho)\varepsilon_1 \right] \left(\frac{2\sqrt{1+\rho+\rho^2}\varepsilon_1}{\sqrt{3}} \right)^{N-1} + 3Se^{-2(1+\rho)\varepsilon_1} \right\}^2 = 0
\end{aligned} \tag{4.49}$$

where dimensionless group $S = \frac{EH}{K_m h}$ and N is the hardening index of the metal.

Similarly, the critical necking limit strain and necking band orientation of the elastomer-supported metal layer under a biaxial loading ratio ρ can be defined as the lowest possible critical strain satisfying (4.49) and its corresponding angle θ , respectively.

4.1.3. Results and Discussion

A. Necking limit of freestanding metal layers under biaxial in-plane loading

We first present the representative results of necking instability analysis of freestanding metal layers as a demonstration of the dependence of necking limit strain and necking band orientation on biaxial in-plane loading.

The governing equation of the necking limit of a freestanding metal layer can be readily obtained by reducing (4.48) or (4.49) using $S = 0$. Figure 4.2 plots the critical strain of the onset of necking instability in a freestanding metal layer as a function of necking band orientation angle θ , for three representative in-plane loading conditions, i.e.,

equibiaxial tension ($\rho = 1$), plane-strain tension ($\rho = 0$) and uniaxial tension $\rho = -1/2$.

Under equibiaxial tension, the critical necking condition (4.48) reduces to

$$S(e^{2\varepsilon_1} + 3e^{-4\varepsilon_1}) - (1 + 3N - 6\varepsilon_1)(2\varepsilon_1)^{N-1} = 0, \quad (4.50)$$

which agrees with the results in Xue and Hutchinson (2006). Note that such a condition is independent of the necking band orientation angle θ (Fig. 4.2a). In other words, under equibiaxial tension, necking instability could occur in any orientation if the applied loading reaches the necking limit strain determined by (4.50). For a freestanding metal layer, i.e., $S = 0$, (4.50) further reduces to

$$\varepsilon_1 = \frac{1+3N}{6}. \quad (4.51)$$

This means that the necking limit strain of a freestanding metal layer with power-law hardening under equibiaxial tension depends only on its hardening index.

Under plane-strain tension, the lowest critical strain of the onset of necking instability in a freestanding metal layer always occurs when $\theta = 0$, as shown in Fig. 4.2b. That is, necking band always appears along the direction perpendicular to the plane-strain tension direction. The critical necking limit strain reduces to the well-known Considere criterion

$$\varepsilon_1 = N. \quad (4.52)$$

By contrast, as shown in Fig. 4.2c, under uniaxial tension, the lowest critical strain of the onset of necking instability in a freestanding metal layer occurs at a finite value of θ . That is, necking band appears along a slanted direction to the uniaxial tension direction.

For example, for a hardening index of $N = 0.2$, the necking limit strain under uniaxial tension is 0.31, with a necking band orientation angle of about 39° .

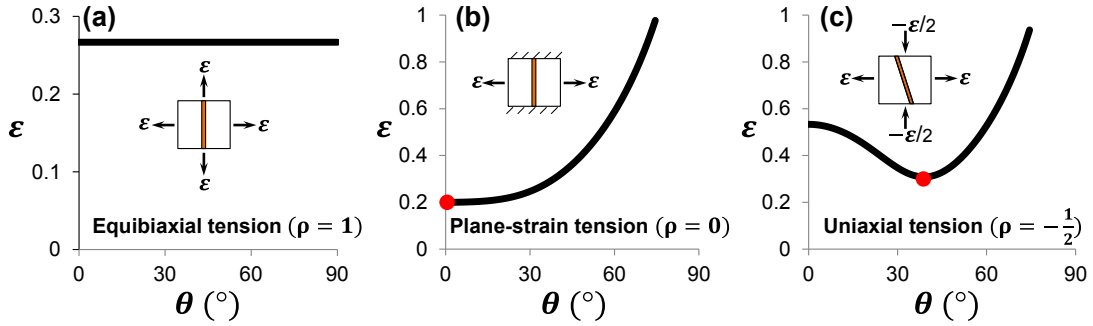


Figure 4.2. Critical necking strain ϵ of a freestanding layer as a function of orientation angle of the necking band θ when the layer is under three different tension modes. Here the hardening exponent of the layer $N = 0.2$. (a) Under equi-biaxial tension, necking instability could occur in any orientation at a critical necking strain $\epsilon = (1 + 3N)/6 \cong 0.27$; (b) Under plane-strain tension, the minimum critical necking strain $\epsilon = N = 0.2$, and necking instability occurs along the direction perpendicular the applied tension (i.e., $\theta = 0^\circ$); (c) Under uniaxial tension, however, the minimum critical necking strain $\epsilon = 0.31$, and necking instability occurs along a direction of $\theta = 39^\circ$.

B. Necking limit of plastic-supported metal layers under biaxial in-plane loading

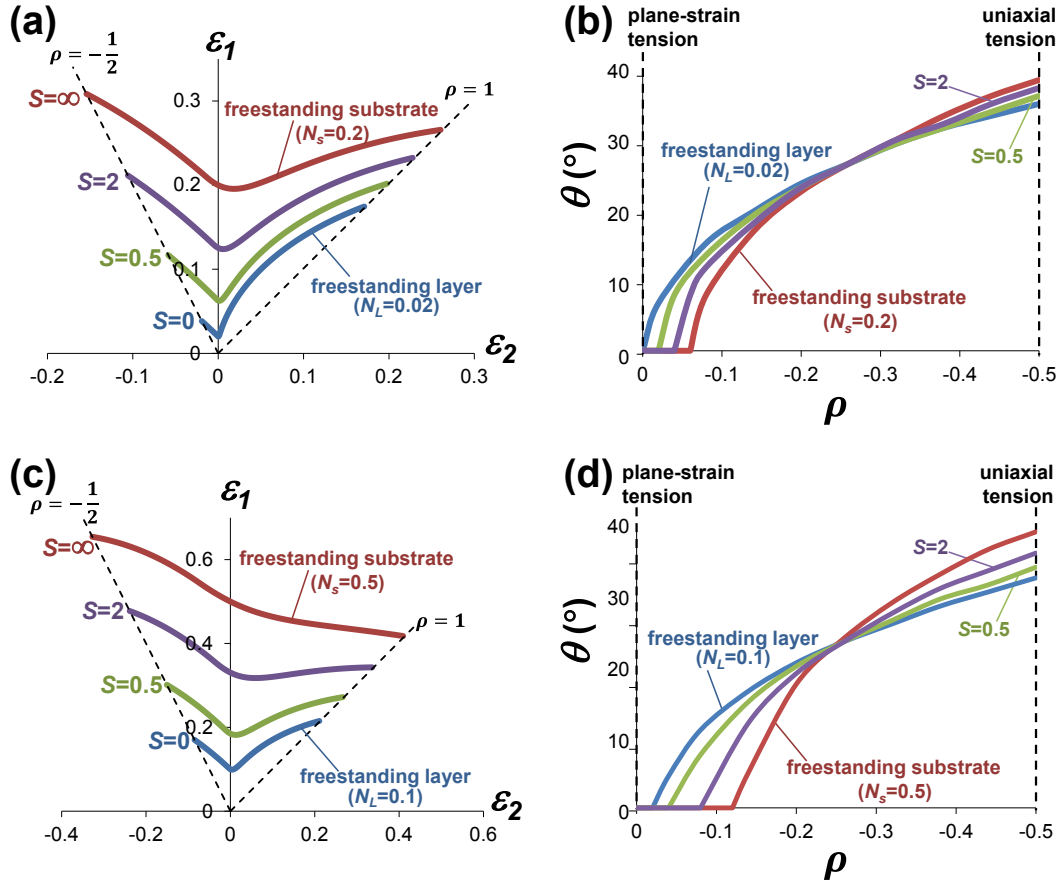


Figure 4.3. Necking limit curves showing strains at the onset of necking as a function of $S = \frac{K_s h_s}{K_f h_f}$ in (a) metal film with $N_f = 0.02$ supported by metal substrate with $N_s = 0.2$ and (c) metal film with $N_f = 0.1$ supported by metal substrate with $N_s = 0.5$ subject to loading modes from uniaxial tension to equi-biaxial tension. (b),(d) Corresponding necking band orientation angle ψ in negative- ρ range.

The necking limit of a plastic/metal bilayer depends on four parameters: the loading ratio ρ ($=\varepsilon_2/\varepsilon_1$), the hardening indices of the metal N_f and of the substrate N_s , and a dimensionless group $S = \frac{K_s H}{K_m h}$. Figures 4.3a and 4.3c plot the combinations of the two in-plane strain components ε_1 and ε_2 at the onset of the necking instability of a plastic-supported metal layer, for two different combinations of N_f and N_s . The necking limit diagrams such as those shown in Figs. 4.3a, c and later in Figs. 4.4a, c, e, are

analogous to the “forming limit diagram” as referred to as in the sheet metal forming industry¹⁴⁵⁻¹⁵¹, and can serve as guidelines in designing functional substrate-supported metal layers of certain desirable deformability.

Figure 4.3a shows four necking limit curves corresponding to $S = 0, 0.5, 2$ and ∞ . Here, $N_m = 0.02$ and $N_s = 0.2$. $S = 0$ and $S = \infty$ serve as two limiting cases and all other cases with a positive and finite S sit between these two limiting cases. The extent to which necking is retarded by the metal substrate increases with increasing thickness-stiffness ratio S , indicating that larger S leads to larger critical necking strain. As shown in Fig. 4.3a, necking retardation already becomes significant when $S = 0.5$ and necking strain is about the average the two limiting cases when $S = 2$. Since the thickness-stiffness ratio S is linear proportional to the thickness ratio $\frac{H}{h}$ between substrate and film, it can be arbitrarily large by solely controlling the thickness of the substrate given a metal film. Therefore, necking in the metal film can be retarded significantly by choosing thick and stiff metal substrate with higher hardening index; however, the necking limit cannot exceed that of the freestanding substrate in which $S = \infty$. The critical orientation angle ψ minimizing the critical necking strains are plotted in Fig. 4.3b for negative loading ratios varying from plane-strain tension ($\rho = 0$) to uniaxial tension ($\rho = -0.5$) with various thickness-stiffness ratio S . In biaxial tension modes ($\rho \geq 0$), zero-orientation angle $\theta = 0^\circ$ always minimize the critical necking strain. In the range with non-positive loading ratio shown in Fig. 4.3b, all curves start

from (0,0) which indicates that necking band always orients perpendicular to loading direction under plane-strain straining. For free-standing film with small hardening index $N = 0.02$, any non-zero loading ratio ρ corresponds to a non-zero necking band orientation angle. However, interestingly, for free-standing substrate with large hardening index $N = 0.2$, necking band orientation angle remains zero until the loading ratio ρ becomes smaller than a critical value (-0.06 for $N = 0.2$). For metal-metal bilayer with $S = 0.5$ or 2 , the necking band orientation angle deviates from zero angle at a loading ratio between 0 and -0.6. Fig. 4.3b clearly shows that larger thickness-stiffness ratio leads to small critical value at which necking band orientation angle becomes non-zero. Similar results for metal film with hardening index $N = 0.1$ well bonded to metal substrate with hardening index $N = 0.5$ are shown in Fig. 4.3c and Fig. 4.3d for various thickness-stiffness ratio S . In Fig. 4.3d, different from free-standing film with $N = 0.02$, the necking band orientation angle in free-standing film with $N = 0.1$ remains zero until the loading ratio ρ becomes smaller than -0.04 .

As discussed above, for metal-metal bilayers (with $N_s > N_f$) which are described by thickness-stiffness ratios $S = \frac{K_s H}{K_f h}$, the necking limit curve of free-standing film ($S = 0$) and that of free-standing substrate ($S = \infty$) serve as the lower and upper limit, respectively. Near the upper limiting case, i.e. $S \rightarrow \infty$, the necking strain of metal film is infinitely close to that of free-standing metal substrate ($N_s > N_f$). Why does the necking strain never go beyond the necking limit of free-standing substrate in metal-metal bilayer?

Once the theoretical necking strain of free-standing metal substrate is reached, the substrate would neck and cannot provide constraint on film anymore thereby, the film necks simultaneously. Consequently, metal substrate with large hardening index ($N_s > N_f$) does retard the necking formation in the metal film but eventually necking instability would occur and fail the metal film by strain localization in the necking band.

Figure 4.4 presents the necking limit curves for metal films with different hardening index of 0.02 (Fig. 4.4a), 0.1 (Fig. 4.4c) and 0.2 (Fig. 4.4e) with various thickness-stiffness ratios $S = \frac{EH}{Kh}$ which describes the effect or constraint on the film from the underlying elastomer substrate. The extent to which the necking strain is retarded after adding the elastomer substrate increases as S increases. In Fig. 4.4a, critical necking strain of the metal film with $N_f = 0.02$ is almost doubled when $S = 0.4$, and tripled when $S = 0.6$. Interestingly, for the case of $S = 0.6$, the necking limit curve terminates before reaching the line representing uniaxial tension with $\rho = -0.5$. It indicates that for proportional straining states with loading ratios close to -0.5 , no necking limit exists which implies that the metal-elastomer could be theoretically stretched to very large strain without forming a neck. When $S = 0.9$, for straining state near plane-strain tension with ρ around 0, the necking strain is significantly increased compared with the free-standing metal film; while for straining state near uniaxial tension or equi-biaxial tension, no necking limit exists. For $S > 1$, in all range of loading ratio from -0.5 to 1, necking limit vanishes, which means the constraint from the substrate

is strong enough to prevent the formation of single necking in the metal film. Compared with metal substrate, it is well known that substrate made of elastomer characterized by Neo-Hookean constitutive law would never fail by necking. It indicates that, in metal-elastomer bilayer, there is no upper limit of necking limit set by the elastomer substrate, which is in contrast to the upper limit imposed by the metal substrate in metal-metal bilayer. This is the reason why, with large thickness-stiffness ratios (roughly $S > 1$), elastomer-supported metal film is immune to failure of necking. However, we need to be very cautious in making assessment of metal-elastomer bilayer using necking analysis. Necking analysis can show that for large S elastomer substrate could keep its metal film away from necking but it does not mean the bilayer is immortal under stretching because it may also fail by surface instability mode of the film or fracture of elastomer substrate. As noted above, in biaxial tension range ($\rho \geq 0$), neck in metal-elastomer bilayer is perpendicular to the maximum principal strain, i.e. $\theta = 0^\circ$. In negative ρ range, Fig.4b presents orientation angle as a function of loading ratio ρ for different S . Elastomer helps stable necking band in the perpendicular direction to the maximum principal strain when loading ratio ρ close to 0. For example, in bilayer with $S = 0.6$, the orientation angle remains zero until the loading ratio ρ becomes smaller than -0.02, while when $S = 0$ the orientation angle becomes non-zero once ρ becomes negative. Similar necking limit curves and orientation angle curves for $N = 0.1$ and $N = 0.2$ are shown in Fig. 4.4c,d and Fig. 4.4e,f, respectively.

The critical necking strains in metal-elastomer bilayer under uniaxial tension ($\rho = -0.5$), plane-strain tension ($\rho = 0$) and equi-biaxial tension ($\rho = 1$) are plotted in Fig. 4.5. the critical necking strain increases as thickness-stiffness ratio increases, indicating thick and stiff elastomer substrate could retard film necking effectively. As shown in Fig. 4.5, all critical strain vs. S curves terminate at a certain value of S (indicated by vertical dash lines in Fig. 4.5a) beyond which no necking limit exists. Fig. 4.6 presents orientation angle as a function of S under uniaxial-tension loading mode for $N = 0.02$, $N = 0.1$ and $N = 0.2$. Results illustrate that higher hardening index N of metal film and larger thickness-stiffness ratio tends to make the orientation angle more slanted. The orientation angle predicted by necking analysis is within the range of 35° to 45° , which roughly agrees with existing experimental observations.

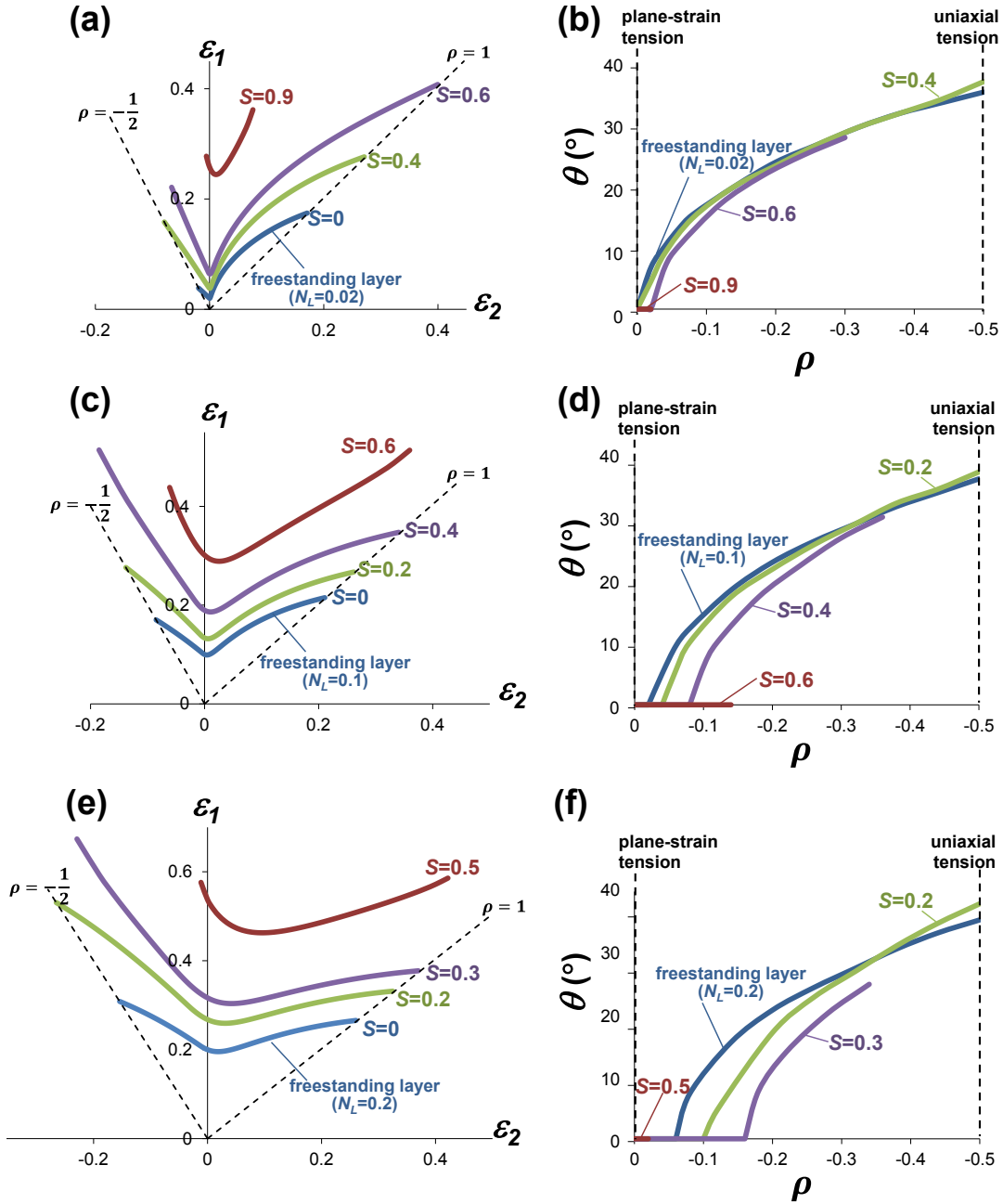


Figure 4.4. Necking band orientation angle in a substrate supported metal layer as a function of S for various hardening index $N = 0.02, 0.1, 0.2$.

As abovementioned, in Fig. 4.5, each curve characterized by a loading ratio ρ ($-0.5, 0$ or 1) and a hardening index N terminates at a certain value of S above which no film necking is expected. Besides there three special loading modes, for any loading ratio ρ

between -0.5 and 1, a critical S can be determined for a given hardening index N . Results are presented in Fig. 4.7 for hardening index $N = 0.02, 0.1$ and 0.2 . The highest critical value S among all loading modes for each hardening index N is indicated by the dash line and it serves as a design guide line that by choosing elastomer substrate with S larger than this highest critical value, no necking will occur in metal film over the whole range of loading ratios from -0.5 to 1 .

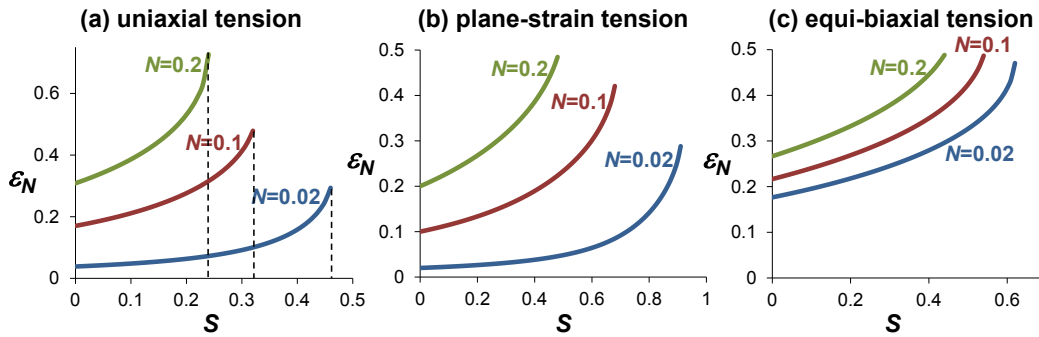


Figure 4.5. Necking limit of a substrate-supported layer as a function of S under (a) uniaxial tension, (b) plane-strain tension, and (c) equi-biaxial tension, for $N=0.02, 0.1$ and 0.2 , respectively. Note that $S=0$ corresponds to the limiting case of a freestanding layer.

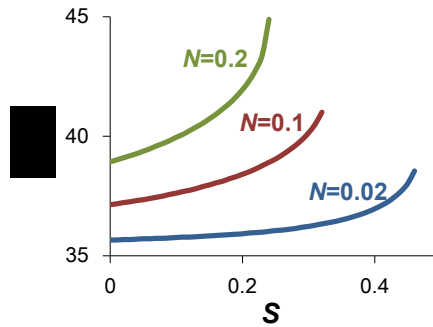


Figure 4.6. orientation angle as a function of S under uniaxial-tension loading mode for $N = 0.02, N = 0.1$ and $N = 0.2$.

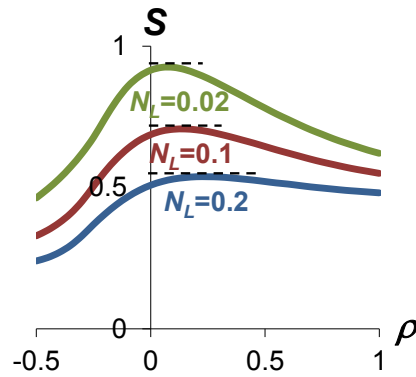


Figure 4.7. Critical S as a function of loading ratio ρ for $N = 0.02$, $N = 0.1$ and $N = 0.2$.

4.1.4. Summary

This chapter presents a comprehensive investigation to decipher the quantitative correlation in two representative material structures, namely, a metal layer supported by a stiff plastic substrate, and a metal layer supported by a compliant elastomer substrate, respectively. The results dictate that a substrate can help to retard the necking band formation. In particular, it is shown that a metal layer supported by a sufficiently stiff and thick elastomer substrate is immune from necking instability. This study offers quantitative understanding of necking retardation in substrate-supported metal film under arbitrary biaxial loading.

Chapter 5. Novel-Design of Si-based Nanostructures as Anodes for Lithium-ion Batteries

5.1. Mechanics Modeling of Non-cracking Si Beads-string Lithium-ion Battery Electrodes³

5.1.1. Introduction

Inspired by the pioneering work of Cui et al.³², intensive effort has been recently focused on silicon nanomaterials as a potential anode material for high capacity lithium ion batteries¹⁵²⁻¹⁵⁶. Nanostructured materials were found to shorten electronic and ionic transport paths and enable strain relaxation to prevent Si fracture induced capability loss. *In-situ* TEM studies of the detailed lithiation processes of single Si particles have provided direct evidence that silicon nanoparticles below a critical size are immune from cracking¹⁵⁴. However, retaining the electrical connectivity for silicon nanoparticles in an electrochemically demanding environment remains a greater challenge to electrode design. Even if Si particles do not crack, electrodes made of Si particles can easily detach from the current collector or from other conducting phase, resulting in undesirable capacity fade. Both experiments and modeling have shown that capacity does fade due to the loss of electric contacts between particles without particle fracture; on the other hand,

³ Experiments shown in Section 5.1 were done by Prof. Yuhuang Wang's and Prof. John Cumings's research groups in University of Maryland-College Park. The DFT calculation was done by Prof. Yue Qi from General Motors Research.

capacity can remain the same if the fractured pieces are still electrically connected. To maintain electrical connectivity in Si electrode, our collaborators demonstrate the synthesis of electrically wired silicon beads on covalently carboxyl-functionalized CNT (*f*-CNT) strings. This beads-string structure affords advantageous features unattainable in conventional coaxial morphology where Si is coated on CNTs uniformly over the entire surface. Both theoretical modeling and comparative *in situ* TEM studies reveal remarkably improved structural durability of this novel beads-string structure during lithiation/delithiation.

5.1.2. *In Situ Observation of Lithiation of Si beads-string electrodes*

The surface chemistry of CNTs plays a vital role in controlling the growth of α -Si on the CNTs. For *f*-CNTs, the functional bands serve as nucleation centers, from which the growth of α -Si starts and extends axially away in both directions, leading to a beads-string structure with discrete ellipsoidal α -Si beads threaded on the nanotube (Fig. 5.1e). In contrast, for pristine, unfunctionalized CNTs, a uniform, continuous α -Si coating is typically formed (Fig. 5.1a). This is attributed to uniform nucleation on the nearly defect-free and atomically smooth surface of a pristine CNT.

Upon lithiation, the α -Si shell or beads show two phase structures as light and dark contrasts in *in situ* TEM images (Fig. 5.1), which can be readily identified as unreacted silicon (dark) and fully-lithiated silicon (light), both being amorphous. The light/dark interface in TEM observations represents the α -Li₁₅Si₄/ α -Si interface. The rotational

symmetry of the beads is retained in the lithiated structure, which results from the isotropic propagation of lithiation reaction front in the α -Si beads. Note this lithiation mode of α -Si is in stark contrast with that of crystalline Si, in which anisotropic reaction rate in crystalline Si can lead to faceted or asymmetric nanostructures after lithiation^{156, 157}.

Figure 5.1 compares the morphology evolution of the beads-string structure with that of the core-shell structure. Lithium quickly diffuses through the surface of α -Si along axial direction, followed by lithiation reaction front propagating from the outer surface of α -Si radially toward the CNT at the center. As a result, a tapered lithiation front is formed in the α -Si during the lithiation process. Besides the surface reaction, another lithiation front also propagates outwards from the CNT/Si interface toward the outer surface (Figure 5.1h,i). This new pathway was not observed with the core-shell structures grown on relatively defect-free CNTs.

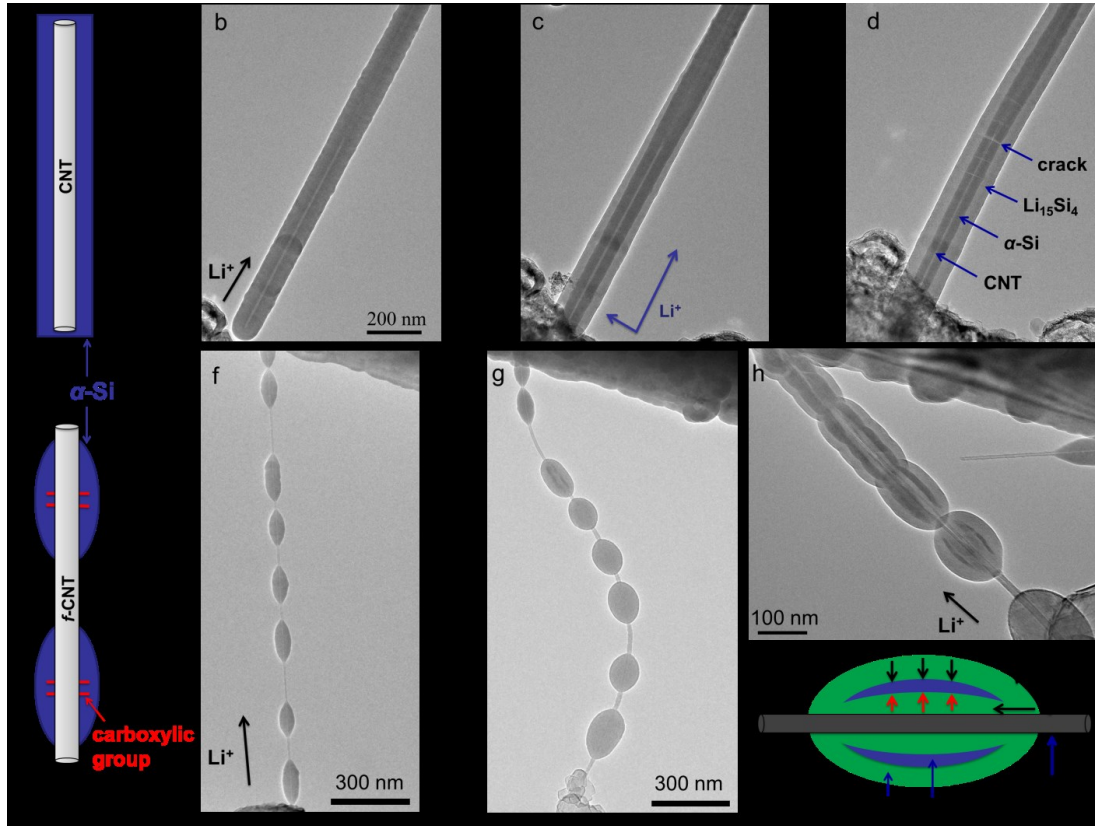


Figure 5.1. Microstructural evolution of Si-CNT heterostructures upon lithiation propagation. a,e, Schematic drawings show two different nucleation models with the free sliding and fixed interfaces. b-d, Microstructural evolution of CNT@ α -Si core-shell structure upon lithiation. f,g, Microstructural evolution of f-CNT@ α -Si beads-string structure upon lithiation. h, Microstructural evolution of f-CNT@ α -Si upon lithiation (0V, $t = 15$ s) shows that Li^+ propagated in two pathways: along both the α -Si surface and CNT/Si interface in the radial direction. i, Schematic drawing indicates a two pathways diffusion mechanism of Li^+ on f-CNT@ α -Si beads-string structure.

The above different lithiation morphology leads to distinct deformation and failure behaviors of the Si phase in these two nanostructured electrodes. As evident in Fig. 5.1d and Fig. 5.2a, upon further lithiation of the CNT@ α -Si core-shell heterostructure, the un lithiated portion of the α -Si shell tends to crack along radial direction. Even by slow and gentle lithiation of comparable structures at a minimum bias (0 V) with respect to lithium metal, the α -Si shell failed to avert the formation of these cracks (Fig. 5.2a). The

fragmentation of the α -Si shell under lithiation can severely degrade the cycle stability of the CNT@ α -Si electrodes. By contrast, all *f*-CNT@ α -Si beads-string electrodes tested in our *in situ* experiments sustained significant lithiation-induced deformation without appreciable fracture, suggesting a highly robust non-cracking nanostructure design of anodes for lithium ion batteries.

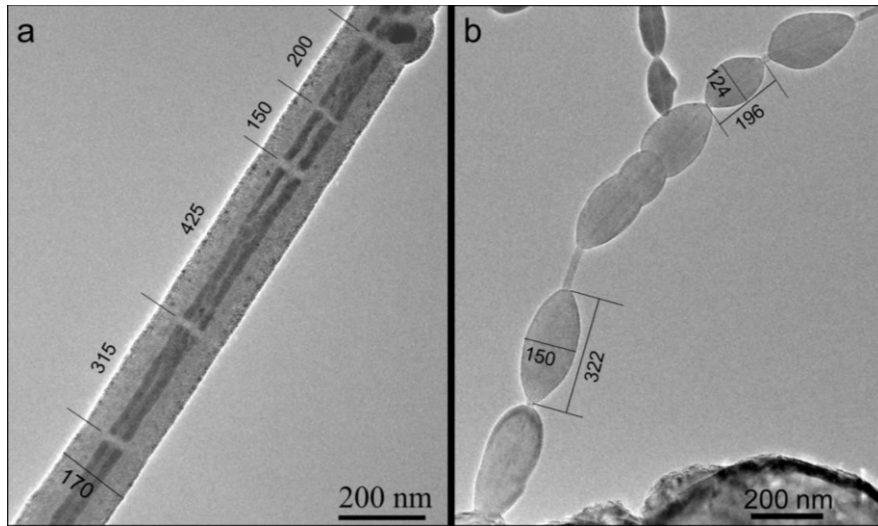


Figure 5.2. Mechanical response and cracking due to morphology change. a, Formation of cracks on partially lithiated α -Si shell of CNT@ α -Si core-shell structure (0V, $t = 720$ s). b, A fully lithiated *f*-CNT@ α -Si beads-string structure without cracks (-3V, $t = 540$ s).

Distinct deformation and failure behaviors of beads-string electrodes are attributed to the significantly improved bonding strength of the CNT/ Si interfaces.

5.1.3. Mechanics Modeling of Si Beads-string Electrodes under Lithiation

A. Mechanics Simulation

To understand the fracture of CNT@ α -Si core-shell nanostructure and the crack-averting feature of the *f*-CNT@ α -Si beads-string nanostructure observed in experiments from a mechanics point of view, we model the lithiation process and the associated mechanics

deformation/stress in these two nanostructures. We describe Li^+ diffusion in Si by classic diffusion equation and set Li^+ diffusivity to be concentration dependent: $D = D_0(1/(1 - c) - 4c)$, where c is the normalized Li^+ concentration (e.g., $c = 1$ denotes fully lithiated stage and $c=0$ denotes pristine stage)¹⁵⁸, and D_0 is a diffusivity constant and chosen to be $10^{-18}\text{m}^2/\text{s}$ in order to give a realistic velocity of the lithiation reaction front.

Such a concentration dependent diffusivity can capture the lithiation reaction as a rate-limiting step and thus allows for the formation of a moving sharp lithiation reaction boundary separating a fully lithiated Si phase ($c = 1$) and a pristine α -Si phase ($c = 0$). Lithiation process involves deformation of Si due to lithium insertion. The abovementioned nonlinear diffusion model and the lithiation-induced deformation and stress are solved by the finite element codes ABAQUS through a fully-coupled implicit analysis. In the finite element model, we adopt an isotropic linear elastic model to describe pristine α -Si and lithiated Si, with both Young's modulus and Poisson's ratio varying linearly with Li^+ concentration from 80 GPa and 0.24 (for pristine Si, $c = 0$) to 12 GPa and 0.22 (for fully lithiated Si, $c = 1$), respectively. The linear elasticity assumption of lithiated Si could lead to overestimated stress level in Si, as in reality the lithiated phase behind the reaction front often undergoes the structural relaxation by plastic deformation. We found that even at an overestimated stress level, the $f\text{-CNT}@ \alpha\text{-Si}$ beads-string nanostructure still can sustain the huge lithiation-induced volume change without fracture (Fig. 5.3). In this sense, the linear elasticity assumption for Si only

results in quantitative difference in stress prediction, but the underlying mechanistic understanding of the different deformation and failure behaviors of the two nanostructures under lithiation remains valid. To capture the possible cracking in Si during lithiation, cohesive zone elements are implemented at locations that are most susceptible to cracking (along the center line in radial direction in both FEM models). In these cohesive zone elements, the cohesion strength and the toughness of Si are set to be 3GPa and $12.5\text{J}/\text{m}^2$, respectively. Viscosity stabilization of the deformation of cohesive zone elements is employed to improve FEM numerical convergence. For the CNT@ α -Si core-shell nanostructure, the inner surface of the α -Si shell is set to be free. To satisfy the deformation compatibility, kinematic constraints are applied at the two ends of the α -Si shell to ensure the same axial displacement during lithiation. For the f -CNT@ α -Si beads-string nanostructure, the f -CNT is modeled as a thin layer of linearly elastic elements with a Young's Modulus of 300GPa and the f -CNT/ α -Si interface is assumed to be perfectly bonded.

B. Mechanics Modeling of f -CNT@ α -Si beads-string nanostructure and CNT@ α -Si core-shell nanostructure under lithiation

The fracture mechanism of core-shell structures and the crack-averting feature of beads-string structures can be further understood by modeling the lithiation process and concomitant mechanical deformation in these two nanostructures. As discussed in section 5.1.3.B, to model the evolving lithiated/pristine Si interface, we adopt an isotropic diffusivity of Li^+ in Si with a non-linear dependence on Li-concentration in our model.

The diffusion-induced stress is calculated simultaneously through a coupled chemomechanical model as the distribution of Li^+ concentration evolves. Because of the rotational symmetry of both nanostructures, we can model only half of their cross-section along the axial direction.

The simulation clearly captures the lithiation process of the $\text{CNT}@a\text{-Si}$ core-shell nanostructure observed in TEM (Fig. 5.3a-c). For the $\text{CNT}@a\text{-Si}$ core-shell nanostructure, the inner surface of the $a\text{-Si}$ shell is set to be free, as suggested by the rather weak interface with the CNT. Li^+ can diffuse into the $a\text{-Si}$ shell only from its outer surface, as shown in the experiments. Figures 5.3b and 5.3c show five sequential snapshots of the lithiation process of the $\text{CNT}@a\text{-Si}$ core-shell nanostructure, with color shades representing normalized Li^+ concentration (e.g., $c=1$ denotes fully lithiated and $c=0$ unlithiated) and the stress component in axial direction (that can potentially initiate cracking), respectively. The reaction front emerges as a rather sharp interface separating the fully lithiated Si phase in the wake and the unlithiated $a\text{-Si}$ shell ahead. As lithiation progresses, the sharp reaction front propagates radially toward the center of the $a\text{-Si}$ shell. The lithiation-induced volume expansion leads to compressive stress in the axial direction in the Li-rich phase of the $a\text{-Si}$ shell, which is balanced by the axial tensile stress in the unlithiated $a\text{-Si}$ shell. As the lithiation front sweeps from the outer surface into the $a\text{-Si}$ shell, the axial tensile stress in the unlithiated $a\text{-Si}$ shell increases monotonically. Once the axial tensile stress exceeds the cohesion strength of $a\text{-Si}$, crack

initiates from the free inner surface of the α -Si shell and propagates along radial direction (Fig. 5.3c). The radial crack propagation is arrested near the reaction front due to the compressive stress in the fully lithiated phase, agreeing well with experimental observation.

For the f -CNT@ α -Si beads-string nanostructure, the inner surface of the α -Si shell is covalently bonded to a CNT of high stiffness, giving the strong interface between α -Si and functionalized CNT surface. The simulation (Fig. 5.3e, 5.3f) well captures the evolution of both morphology and reaction front of the α -Si beaded, as observed at different lithiation degrees. We find that even though the unlithiated phase of the α -Si bead is under tension, the magnitude of the tensile stress is effectively mitigated due to the strong mechanical constraint of the chemical tailored Si-C interface. As a result, the axial tensile stress in the α -Si bead is never high enough to initiate cracks in the unlithiated Si. Without the strong interfacial bonding, Li diffusion along the inner surface of the α -Si bead still helps mitigate the axial tensile stress, but cannot sufficiently avert the cracking of the unlithiated phase (See next section). By contrast, if the CNT/ α -Si interface is strong enough, the α -Si bead can survive full lithiation without cracking, even if Li diffusion only occurs from the outer surface of the bead, as experimentally observed.

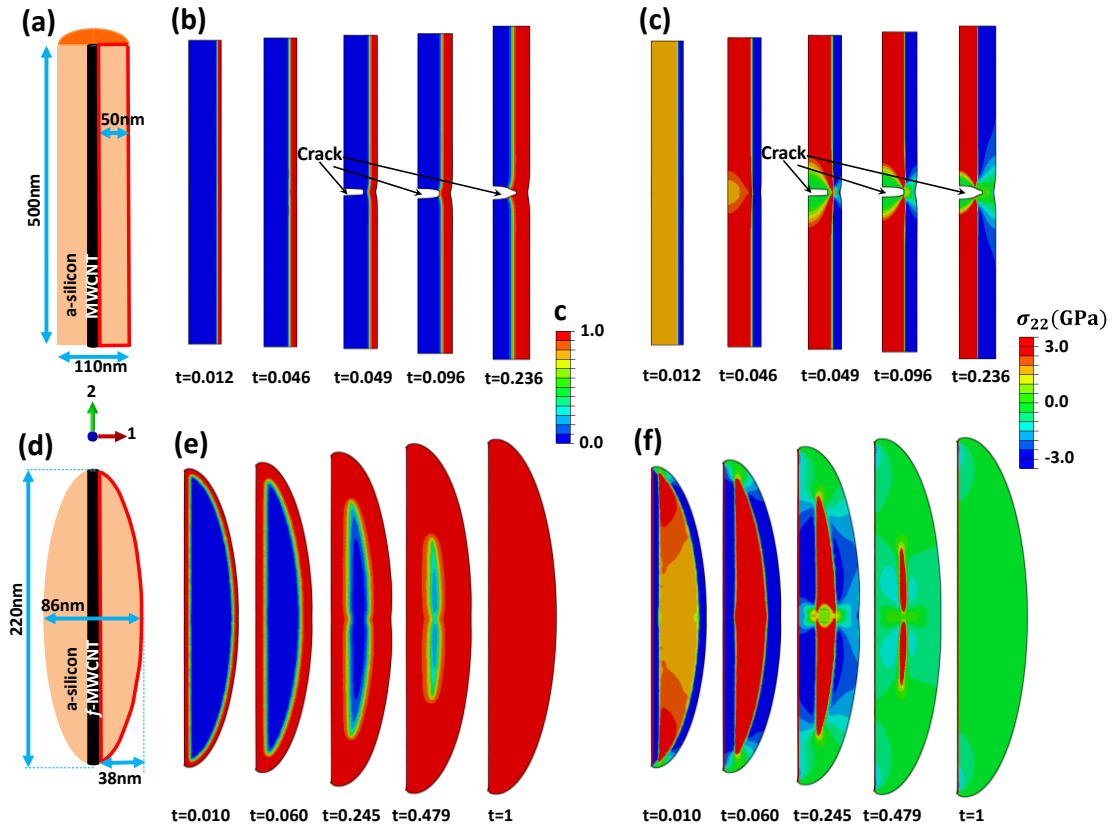


Figure 5.3. Simulations of the lithiation and lithiation-induced stress in a-c, CNT@ α -Si core-shell structure and d-f, f -CNT@ α -Si beads-string structure.

C. Key underpinning mechanism of non-cracking f -CNT@ α -Si beads-string nanostructure under lithiation

To decipher the key underpinning mechanism that f -CNT@ α -Si beads-string nanostructures can sustain huge volume increase during lithiation without fracture, we perform the following further simulations.

First, using the same FEM model as depicted in Fig. 5.3d and similar simulation strategy described above, we set the inner surface of the α -Si bead to be free and allow the diffusion of Li^+ only from the outer surface of the α -Si bead. In other words, these boundary conditions correspond to the case that the deformation of α -Si bead is not constrained by the CNT and there is no fast Li^+ diffusion path along the CNT surface.

Figure 5.4 plots the sequential snapshots (as counterparts of Figs. 5.3e and 5.3f) of the lithiation process of the f -CNT@ α -Si beads-string nanostructure under the above boundary conditions. Without Li^+ diffusion along the bead inner surface, the Li^+ concentration in the α -Si bead assumes a profile similar with that in the α -Si shell as shown in Fig. 5.3b, with a sharp reaction front moving radially toward the bead inner surface. The stress in the lithiated phase is compressive and that in the pristine phase is tensile. Without the mechanical constraint from the CNT, the tensile stress in the pristine Si phase increases significantly until it reaches the cohesion strength of Si. Cracking then initiates and propagates in the unlithiated Si, which eventually is arrested near the reaction front, similar with the cracking process shown in Fig. 5.3b and 5.3c.

Next, we set the inner surface of the α -Si bead to be free but allow the diffusion of Li^+ from both the inner and outer surfaces of the α -Si bead. As shown in Fig. 5.5, such a boundary condition leads to a Li^+ concentration profile and stress distribution similar with those in Figs. 5.3e and 5.3f, respectively. Without the strong interfacial bonding of the f -CNT, however, the tensile stress in the unlithiated phase of Si can become high enough in later stages of lithiation to initiate cracking inside the Si bead.

Finally, we let the inner surface of the α -Si shell perfectly bonded to a CNT of high stiffness but only allow the diffusion of Li^+ from the outer surface of the α -Si bead. In other words, these boundary conditions correspond to the case that the deformation of α -Si bead is constrained by the CNT but there is no fast Li^+ diffusion path along the CNT

surface. As shown in Fig. 5.6, even though the resulting Li^+ concentration profile and stress distribution are similar with those in Figs. 5.4a and 5.4b, respectively, the strong mechanical constraint from the *f*-CNT can avert crack initiation in the Si bead. Upon full lithiation, the stress in the Si bead decreases to a negligible level, comparable to that as shown in the last panel of Fig. 5.3f.

The above further simulations clearly reveal that the strong mechanical constraint from the *f*-CNT is the key underpinning mechanism of non-cracking *f*-CNT@ α -Si beads-string nanostructure under lithiation, while the fast lithiation from the inner surface of the Si bead helps mitigate lithiation-induced stress but cannot sufficiently avert cracking occurrence.

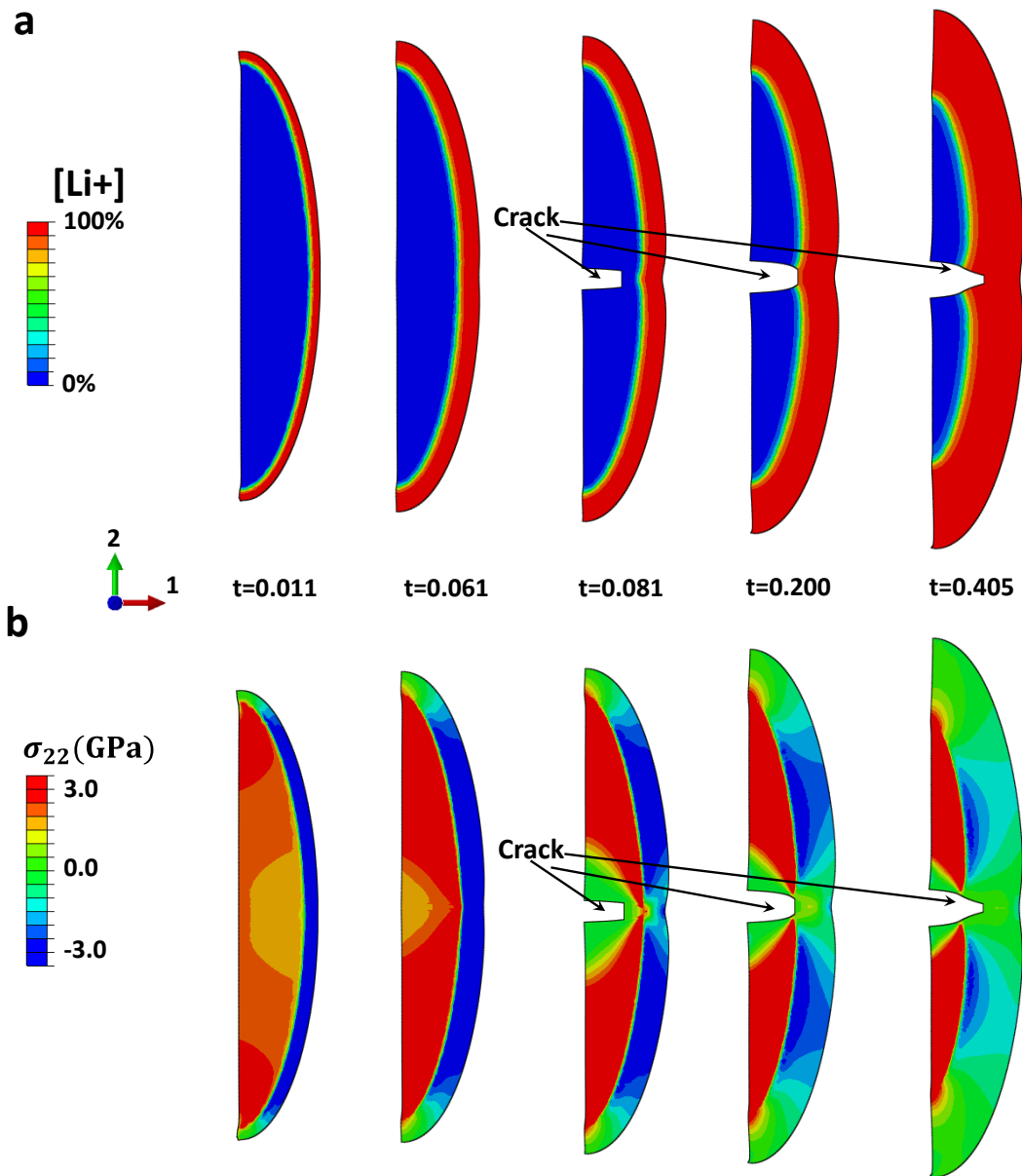


Figure 5.4. Snapshots of f-CNT@a-Si bead under lithiation. Here the inner surface of Si bead is free (no mechanical constraint from CNT). Li⁺ can only diffuse from the outer surface of the Si bead. Note that the Si bead fractures under lithiation.

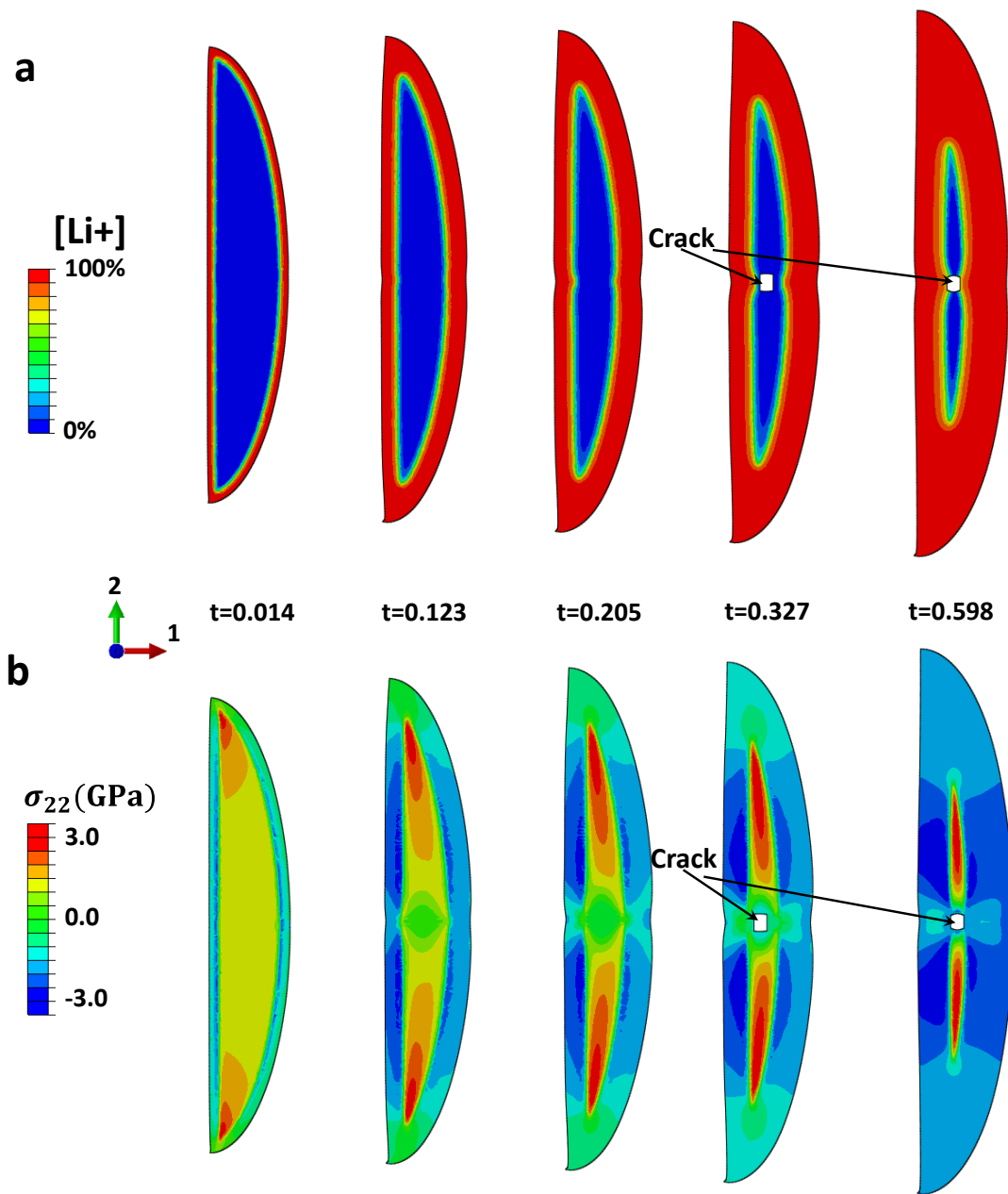


Figure 5.5. Snapshots of f-CNT@a-Si bead under lithiation. Here the inner surface of Si bead is free (no mechanical constraint from CNT). Li+ can diffuse from both the inner and outer surfaces of the Si bead. Note that the Si bead fractures under lithiation.

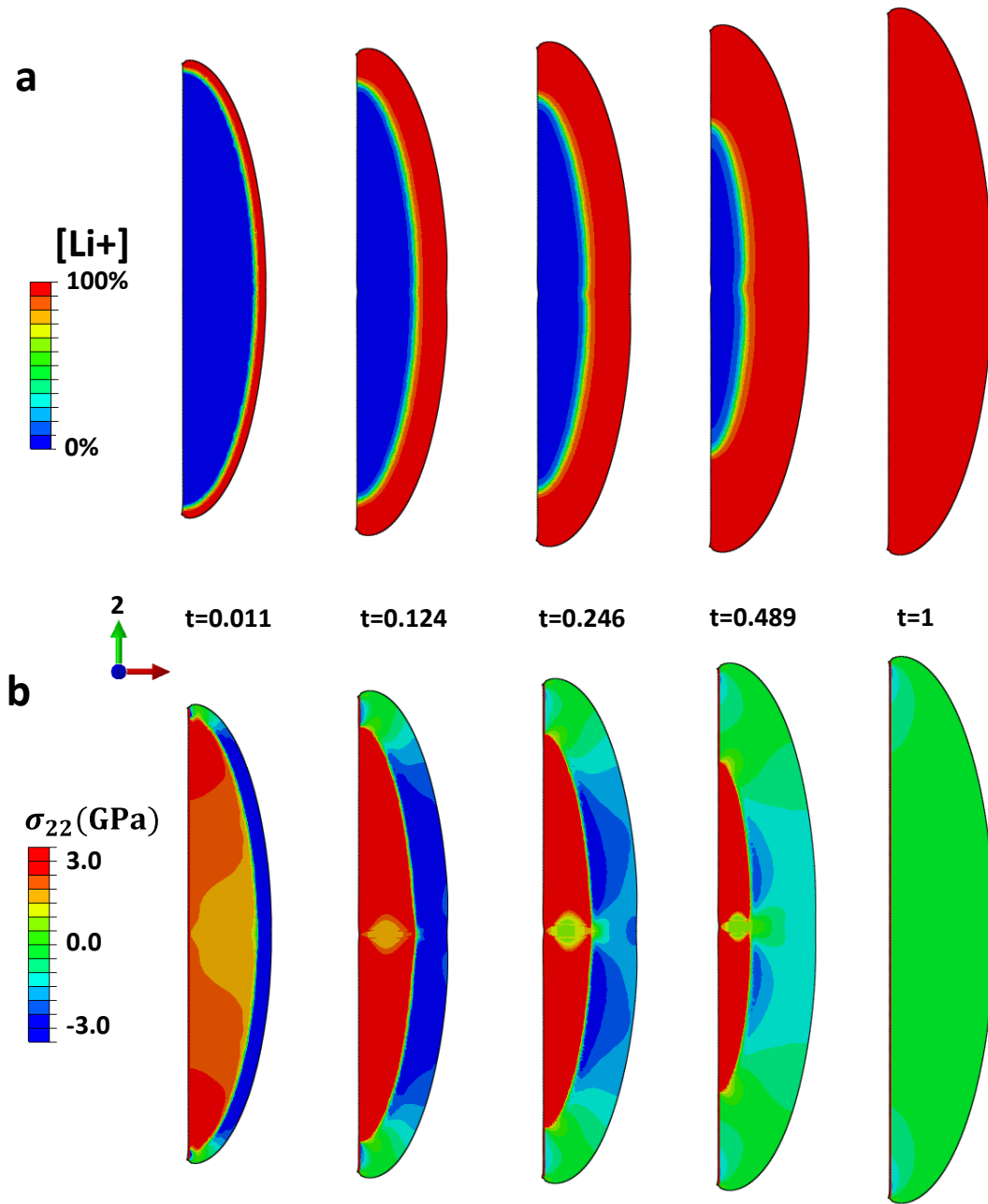


Figure 5.6. Snapshots of f-CNT@ α -Si bead under lithiation. Here the inner surface of Si bead is perfectly bonded to the f-CNT. Li⁺ can only diffuse from the outer surface of the Si bead. Note that the strong mechanical constraint from the f-CNT can avert the fracture of Si bead under lithiation.

5.1.4. Summary

In summary, f-CNT@ α -Si beads-string heterostructures with chemically tailored

carbon-silicon interface were synthesized based on a fundamental understanding of carbon surface chemistry and Si nucleation on covalently modified CNT surfaces. *In situ* TEM studies of lithiation propagation reveal that these novel heterostructures can accommodate huge volume change during lithiation and delithiation without appreciable mechanical failure. By contrast, CNT@ α -Si core-shell nanostructures fracture upon lithiation. FEM studies suggest that the strong Si-C interface made possible by the carboxylic functional bands on CNTs plays key roles in enabling non-cracking *f*-CNT@ α -Si beads-string heterostructures. These findings thus provide important new insights in the synthesis of high performance Si electrodes for lithium ion batteries.

5.2. Silicon Nanowalls for Lithium-Ion Batteries Fabricated using Nanoimprint Lithography⁴

5.2.1. Introduction

Lithium (Li) ion batteries are one of the most important electrochemical energy storage devices and are widely used in portable electronics. For future Li ion battery powered electronic vehicles, however, electrode materials with higher energy/power density and longer cycle life are needed^{32, 41, 159-161}. Silicon (Si), as a Li ion battery anode material,

⁴ *Experiments in section 5.2 were done by Mr. Jiayu Wan and Prof. Liangbing Hu from Department of Materials Science, University of Maryland-College Park and Dr. Alex Kaplan and Prof. Jay Guo from University of Michigan-Ann Arbor.*

has a theoretical specific capacity of 4200 mAh/g, 10 times higher than a conventional graphite anode in commercial batteries. Additionally, Si is an earth abundant and environmentally friendly material with a mature manufacturing process in solar cells and semiconductors industrial that could enable mass production for batteries. Enthusiasm aside, there are significant challenges to use Si as an anode for Li ion batteries³². A large volume expansion (up to 400%) and contraction during lithiation and delithiation could result in pulverization of the Si anode. The cracked Si loses contact with the current collector, reducing accessible capacity over time. This significant volume change also affects the stability of the solid electrolyte interface (SEI), when the Si anode surface fluctuates during cycling. Recently successful demonstration of using Si nanowires as anodes in Li ion batteries to mitigate pulverization and enhance cycle life³² has led to a surge of interests in developing high performance Si nanostructures and Si nanocomposites anodes for Li ion batteries, including Si-C nanocomposite,¹⁶²⁻¹⁶⁶ Si nanotube,¹⁵² and three dimensional (3-D) Si nanoparticles³⁴ et al. were reported. In order to understand the mechanism of Si as an anode material, fundamental studies on its electrochemical,^{167, 168} nanomechanics,¹⁶⁹⁻¹⁷¹ and transport properties have been reported. A problem of a low first Coulombic Efficiency (QE), however, still exists in the reported nanostructures.

The highly irreversible capacity of the first cycle is often attributed to side reactions, SEI formation, cracking, and separation of electrode materials from collector¹⁷².

Nanostructured materials such as nanowires and nanoparticles, can easily release the mechanical strain during charging; reducing the potential for pulverization during the first cycle. However, the large surface area of these nanostructures results in a greater amount of side reactions occurring at the anode-electrolyte interface. The formation of the SEI layer consumes Li ions, contributing to an irreversible consumption of Li. The reduction of surface oxide layers on Si, which could form when the Si anode is exposed to air during electrode preparation, also leads to irreversible consumption of Li. Thus, the large Si surface area of existing nanostructures plays a major role in the low first QE of those nanostructured Si anodes.

We propose a two-dimensional (2-D) nanowall structure that can effectively address the issues associated with lower dimensional Si nanostructures. A schematic image of nanowalls is shown in Figure 5.7h. Each nanowall possesses sub-micron scale length and height, and can be as thin as 50 nanometers. The nanowall structure maintains the advantages of existing nanostructures: stress during volume expansion is largely released, and direct electrical contact with current collector for easy electron transport is maintained. Most importantly, the nanowall structure has approximately 50% less specific surface area than nanowires of similar dimensions. Thus, the first QE is expected to be higher for nanowall structures than for one dimensional (1-D) nanostructured anodes in Li-ion batteries. Recently, He et al. created Cu/Si nanorods that form a wall like structure. Although their anode shows a unique mechanical deformation during large

volume expansion, it does not perform a high first QE. Their “wall” is composed of nanorod at the first cycle, so that the surface area is not reduced.

Here, for the first time we created a periodic, amorphous Si (a-Si) nanowall structure via nanoimprint lithography (NIL) ¹⁷³ and investigated its electrochemical and mechanical properties as anodes in Li ion batteries. We demonstrate that a high QE can be achieved for the first cycle due to the lower specific surface area of the nanowall electrode compared with lower dimensional Si nanostructures, such as Si nanowires.

NIL can be used to generate high-resolution feature sizes at tens of nanometers scale over large areas. Recently, structures have been fabricated for applications in fields such as photonics, transparent metal electrodes solar cells and sensors, to name a few. To fabricate the nanowall structure, a typical thermal imprint process begins by placing a pre-patterned mold directly in contact with a resist-coated substrate. High temperature and pressure are then applied to reflow the resist into the mold, creating a mirror image of the pre-patterned features in the resist. Using these features to create a mask, we can then transfer nano-scale patterns into Si and create high aspect-ratio Si nano-structures with depths in the micron range. This is done with deep reactive ion etching (DRIE), specifically utilizing a cycled "Bosch" process, which has been used in the past to create nanostructures with aspect ratios greater than 50:1.

As shown in Figure 5.7 each Si nanowall is 900 nm high, 600 nm long and 50 nm thick. Perpendicular to the wall surface, the structure has a 220nm period, with a space between

each wall 170 nm. Along the wall length direction, the periodicity is 700 nm with 100 nm spacing between walls. A discontinuous nanowall pattern rather than a continuous grating is proposed here to allow each nanowall to "breathe", relaxing the stress resulting from lithiation/delithiation induced volume expansion/contraction. Cycling results show that our Si nanowall anodes created by NIL achieve a high 1st QE (85%), high stability (40 cycles) and a good rate performance (1000 mAh/g at 2C). This paper not only demonstrates a new method to improve battery performance, but also opens new opportunities of nanowall structures for other applications due to their unique mechanical, electronic and optical properties. The NIL fabricated nanowalls can also be potentially utilized for other applications such as 3-D batteries.¹⁷⁴

5.2.2. Nanowall Fabrication and Anode Characterization

To fabricate a Si nanowall anode sample, 20 nm Cr (ESPI metals) and 900 nm Si (Materion corporation, 99.999%) are first deposited on top of a stainless steel (SS) spacer by e-beam evaporation (Temescal BJD-1800). The layer of Cr is used to enhance the binding of a-Si to the substrate. Energy dispersive X-ray spectroscopy (EDS) results show the purity of the a-Si is 97%. The nanoimprint patterning process (Figure 5.7), begins by spinning imprint resist (mr-I 8030, Microchem) is spun onto the sample and imprinted with a 220 nm period silsesquioxane (SSQ) mold in a NX2000 Nanoimprinter (Nanonex, NJ) (Figure 5.7a). Directional evaporation of Ti onto resist is used to increase the effective linewidth of the resist structure, decreasing the width of the opening down to

approximately 50nm, the desired width of our walls (Figure 5.7b). After reactive ion etching (RIE) with an oxygen plasma to remove residual resist (Figure 5.7c), Cr is deposited and a liftoff process is performed to generate a 220 nm Cr grating with 50 nm linewidth (Figure 5.7d). In order to create a disconnected wall structure, a subsequent imprint is then performed with a 700nm period mold perpendicular to the 220 nm period Cr grating (Figure 5.7e). After the residual layer of resist is removed, RIE is again used to remove the Cr grating in the portion of area exposed by the 700nm resist pattern (approximately 100 nm in width) (Figure 5.7f). The final Cr pattern is then used as a mask for DRIE to create the nanowalls (Figure 5.7g).

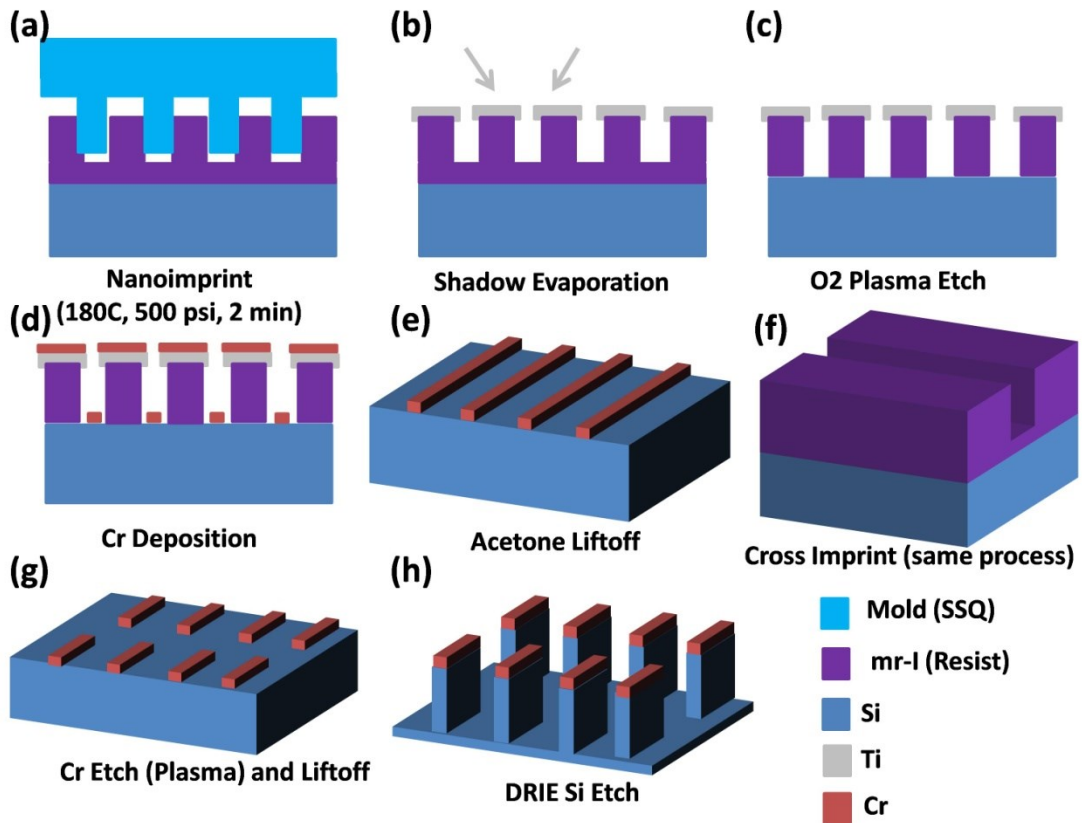


Figure 5.7. Outline of NIL process for Si nanowall anode on an SS substrate (the SS substrate is not shown in this figure)

We characterized the morphology and composition of the prepared Si nanowall structure with scanning electron microscope (SEM) equipped with a Bruker EDS detector. The highly uniform size and lateral distribution of the Si nanowall array is shown in Figure 5.8a. Figure 5.8b shows a tilted view displaying the 3D feature of the Si nanowall structure. In Figure 5.8c (top view), the length and thickness of the nanowalls are measured to be about 600 nm and 50 nm, respectively. The space in between nanowalls is designed to accommodate volume expansion during charge/discharge. It is apparent that from Figure 5.8b and 5.8c that there is some edge roughness associate with each nanowall. This edge roughness is generated during fabrication due to the roughness of the shadow evaporation, which masks the Cr deposition. There is also so-called "scalping" which occurs during the DRIE Bosch process on the sidewalls of the nanostructure. Figure 5.8d show the EDS analysis of one prepared Si nanowall sample. We confirmed our composition of the whole electrode by Figure 5.8d, showing three elements of Si, Fe and Cr which correspond to nanowalls, the substrate and binding layer (also residual Cr mask), respectively.

The top down nanoimprint technique ensures that Si nanowalls are in direct electronic contact with the current collector, and have a suitable specific surface area that allows for fast charge/discharge, while reducing the amount of SEI formation that contributes to a low first QE. The small thickness of the nanowalls (50 nm in our experiment) allows for a short diffusion path of Li ions, increasing the potential for high power applications. The

large openings on all four sides of the nanowalls can effectively release the stress of volume expansion/shrinking during charge and discharge, allowing a stable cycling performance of the nanowall electrode.

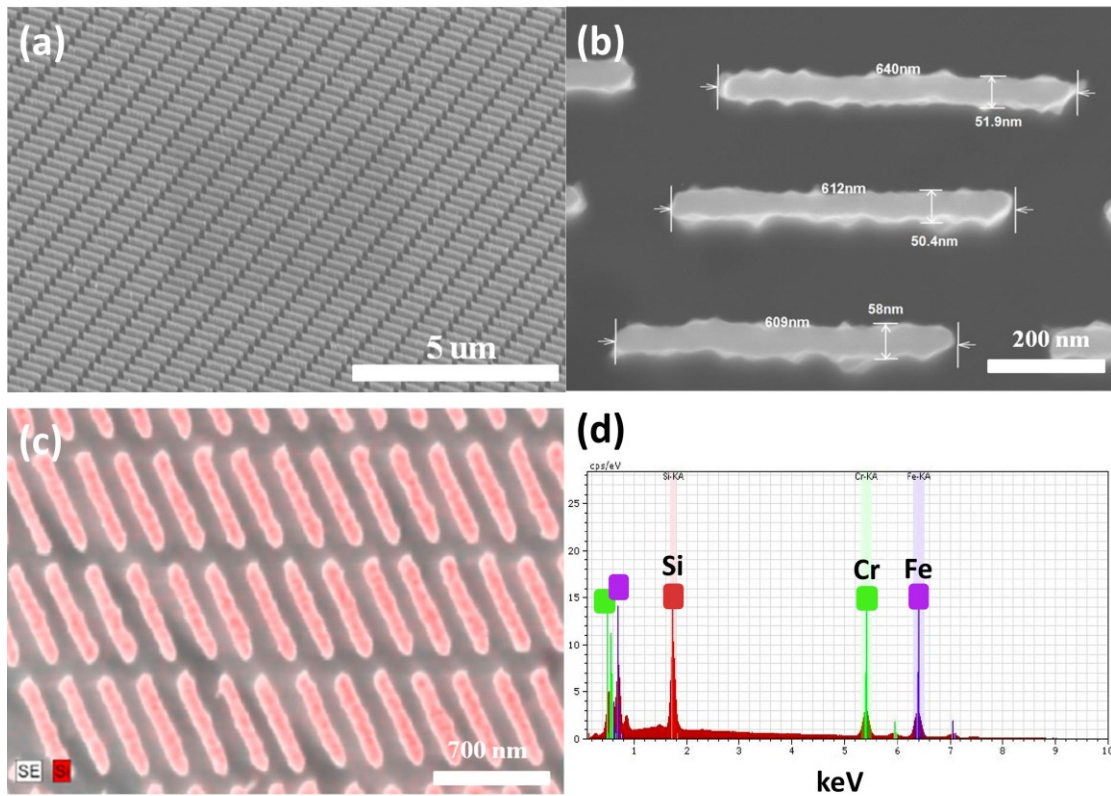


Figure 5.8. (a). SEM images of large area and uniformly distributed Si nanowall structure, (b) Zoomed-in SEM images of (a) (c). SEM image to showing the dimensions of the Si nanowalls (d). Energy dispersed X-ray spectroscopy of Si nanowall/substrate, with peaks of Si, Cr and Fe

After fabrication, the samples were dried in a 100 °C vacuum oven overnight and then directly assembled into coin cells. Electrochemical measurements were performed using a Biologic VMP3 electrochemical station, and the cycling and electrochemical impedance

spectroscopy (EIS) results are presented in Figure 5.9. Figure 5.9a shows the cycling performance and Coulombic efficiency of Si nanowall at the rate of 840 mA/g for 40 cycles. The first charge and discharge capacity of the Si nanowall is 2324 mAh/g and 1993 mAh/g, respectively, corresponding to a first QE of 85%. This initial QE of Si nanowall anodes still have room for improvement by increasing the large scale uniformity of the nanowalls or by using surface modification. The Si nanowall demonstrates stable cycling performance, retaining a discharge capacity of 1801mAh/g after 40 cycles, 90% of the initial value. The capacity retention is highlighted in Figure 5.10b, which plots the charge and discharge voltage profiles of the 1st, 10th, 20th and 40th cycles. The capacity suffers almost no losses during the first twenty cycles. The typical voltage profile of amorphous Si (a-Si) is seen, with lithiation of a-Si begins at approximately 0.4V vs. Li/Li⁺. Figure 5.9c shows the EIS data of the Si nanowall half cells. Both EIS data before and after cycling were taken at fully delithiated state. The EIS results before cycling and after 40 cycles are shown by the blue and red curves, respectively. Bulk resistance of the cell is equal to the first intersection of the EIS curve with the real impedance axis. From the inset, we observed that the initial bulk resistance of 8 ohms (before cycling test) increases to 10 ohms after 40 cycles, indicating the formation of SEI layer. The diameter of the semicircle represents the charge transfer resistance (R_{ct}) of the cell. We observed the charge transfer resistance of the Si nanowall decreases after cycling. Examination of the nanowall structures after cycling in SEM

helps to explain this phenomenon (Figure 5.10). After 40 cycles, the individual nanowalls have become more porous (Figure 5.10b). As the cycling progresses, the increasing porosity of the Si exposes more surface area to the electrolyte, increasing the charge transfer process and reducing R_{ct} . This is confirmed by the rate performance data in Figure 5.9d.

To determine the rate performance, the half cells were cycled at charge/discharge rates ranging from $C/5$ to $2C$. Charging at higher rates reduces the capacity of batteries as the Li insertion reaction is limited by diffusion/reaction at interface. The formation of a porous structure during cycling increased the surface area of the electrode, increasing the capacity of the high rate cycles. Comparing the capacity of $1C$ battery at cycles 15-25 and 35-45 shows an increase of 200mAh/g for later cycles. The capacity of the battery at $2C$ is about 1000mAh/g , 3 times higher than the capacity of conventional graphite electrodes.

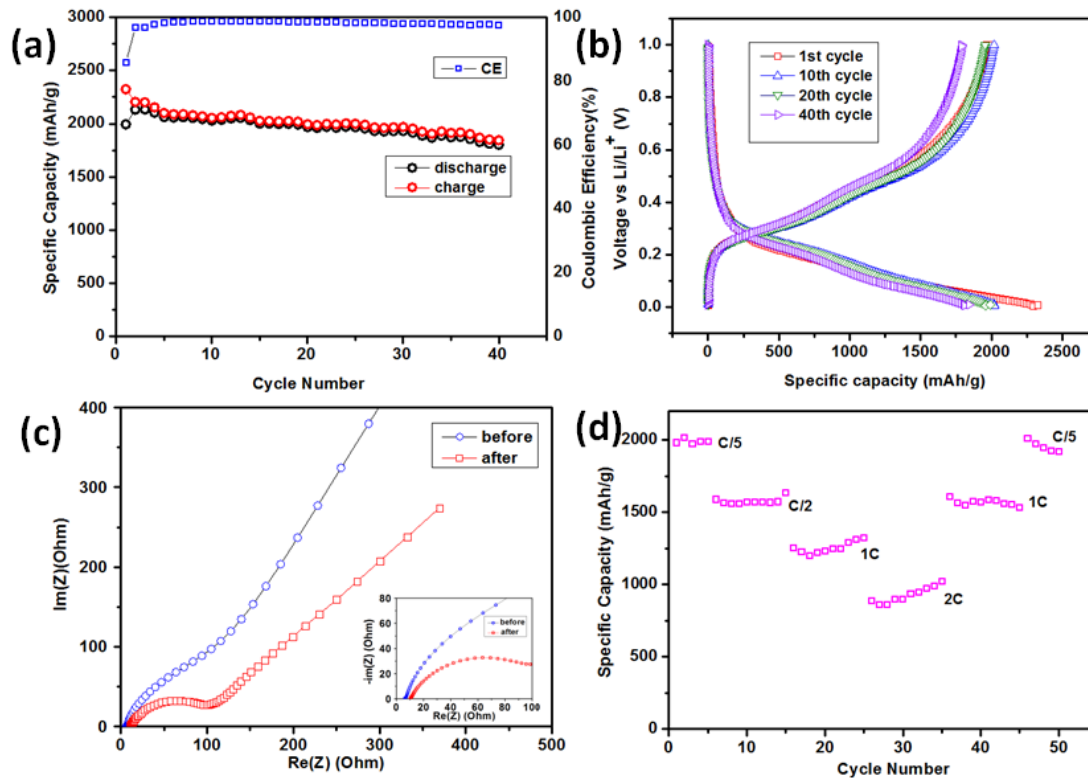


Figure 5.9. (a). Electrochemical cycling performance of Si nanowall anode (b). Voltage profile of 1st, 10th, 20th and 40th cycle of Si nanowall (c). EIS plot of the battery before cycling (blue) and after 40 cycles (red) (d). Rate performance of the Si nanowall half cell.

The half cells were disassembled in a glove box in the delithiated state, and the residual electrolyte and SEI were washed away to expose the Si nanowalls. The morphology of the electrode was examined by SEM as shown in Figure 5.10. From Figure 5.10a we see that the Si nanowalls retain their wall structure and remain attached to the substrate, indicating good structural stability and binding. The cracked surface on top of the nanowall is a residual layer of Cr left over from nanowall fabrication. The cracking and distortion of this layer suggest large volume changes and stresses during cycling. The space between each nanowall is largely reduced, indicating a significant volume change of the Si nanowall structure by lithiation. Figure 5.10b shows the porous structure of the

Si nanowall after cycling. Both the sides and top of the nanowall have become porous. We also observed a slight twisting of the nanowalls after 40 cycles in both Figure 5.10a and 5.10b. Overall, Si nanowalls can withstand significant volume changes associated with lithiation and delithiation. A higher magnification image of the porous structure on Si sidewall is shown in Figure 5.10c. It seems from this image that the porous structure formed many nano-channels in the Si sidewalls, allowing Li^+ ions diffuse further inside. However, during the formation of the porous structure, active material will detach from the walls, resulting in a slight capacity reduction.

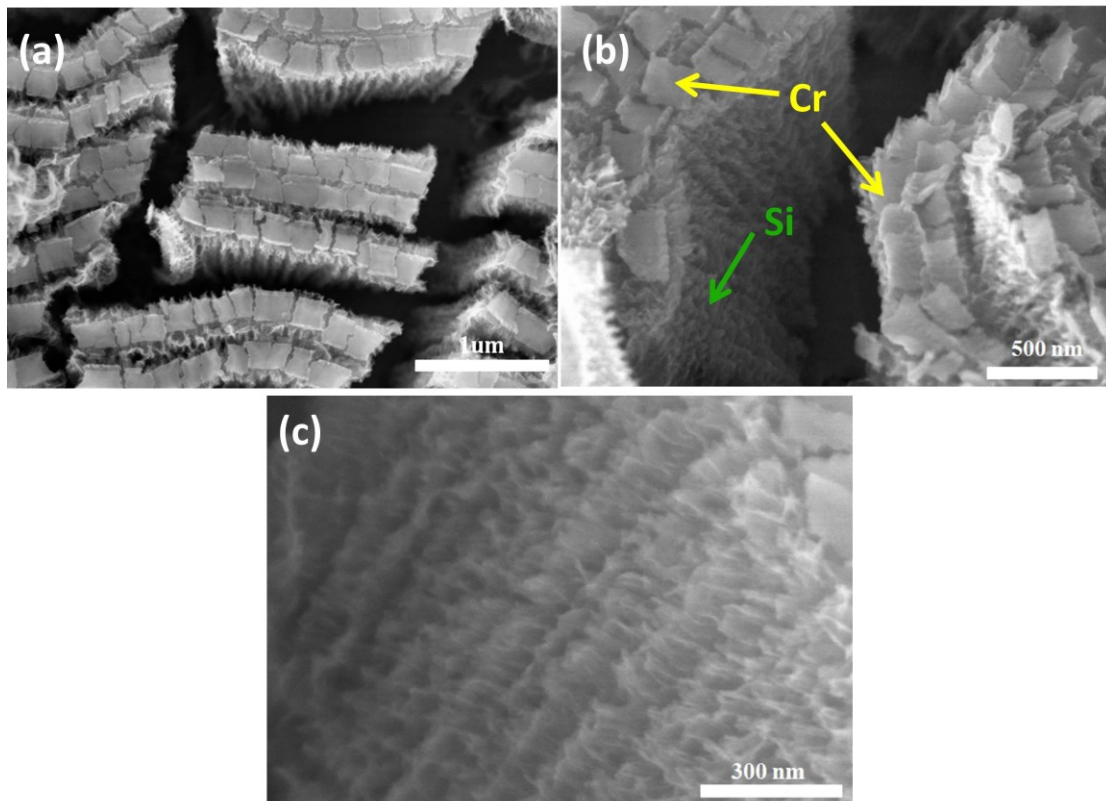


Figure 5.10 (a) and (b) SEM images at different magnifications of the Si nanowall anode after cycling. A residual Cr layer from the mask is observed on top of the nanowall. (c) High magnification SEM of Si nanowalls after cycling shows porous structure with an average pore size of ~ 30 nm

As shown in Figure 5.10a and 5.10b the nanowall structure thickens and develops a very rough surface morphology after 40 cycles, indicating pore formation at both surface and interior of the nanowall. The formation of such a porous structure is attributed to the hydrostatic tensile stress in the nanowall induced by lithiation and delithiation, as revealed by mechanics modeling in the following.

5.2.3. Mechanics Modeling on Stress Evolution in Nanowall Anodes

During lithiation and delithiation, Li ions insert into and extract from the nanowall, inducing large and cyclic deformation of the Si. As to be shown later, the stress associated with the large deformation in the nanowall is highly non-uniform (e.g., stress level varies with positions in the nanowall) and tri-axial. If the Li concentration is sufficiently large, the associated stress can be high enough to cause the plastic flow of the lithiated Si. A cavity in a solid can unstably grow in size by atom diffusion away from the cavity surface driven by sufficiently high hydrostatic stress (defined as the mean stress $\sigma_m = \frac{\sigma_{11} + \sigma_{22} + \sigma_{33}}{3}$). Therefore, if the lithiation/delithiation-induced mean stress in the Si is high enough, defects in the nanowall (e.g., voids) could grow unstably, leading to a porous structure. The underlying energetics can be explained by a simple model. The free energy of a lithiated Si with an incipient spherical void of radius R under a mean stress σ_m applied to the void is given $G(R) = 4\pi R^2\gamma - \frac{4}{3}\pi R^3\sigma_m$, where γ is the surface energy of lithiated silicon. Under lithiation/delithiation-induced stresses, the incipient void tends to grow or shrink to minimize the free energy G , from which one determines a critical

void size $R_c = 2\gamma/\sigma_m$. That is, a void with $R < R_c$ shrinks and thus may heal spontaneously while a void with $R > R_c$ unstably grows into a pore of large size. Next, we calculate lithiation/delithiation-induced stresses in the Si nanowall, so that the critical void size in different regions of the nanowall can be estimated, which in turn help decipher the formation of the porous structure after lithiation/delithiation cycles as observed in the experiments.

We simulate the concurrent Li diffusion and mechanical deformation during initial lithiation and following delithiation of the amorphous Si nanowall using finite element package ABAQUS 6.10 (see Supporting Information for model details). The extent of lithiation is described by the average Li/Si atomic ratio $x_{average}$, defined as the ratio of Li atoms in the nanowall. For example, $x_{average} = 1$ means that on average one Si atom takes one Li atom in the nanowall. We assume the extent of volume expansion has a linear relationship with lithium content in Li_xSi .³⁵ From our experiment, $x_{average}$ reaches 2 at the end of the lithiation cycle, resulting in a 200% volume expansion of the nanowall. Simulation results reveal that the mean stress level in the nanowall increases with the extent of lithiation and nearly saturates as $x_{average}$ approaches 1. The distribution of the mean stress at two representative planes of the nanowall, i.e., the mid-plane ($z = 0$) and the outer surface ($z = h/2$, where h is the nanowall thickness), are shown in Figure 5.11b and 5.11c, respectively. Here $x_{average} = 1$. The regions labeled by A through G undergo a significant tensile mean stress ranging from 150 to 600

MPa. As mentioned above, the tensile mean stress state acts as the driving force for the nucleation and growth of nano-pores. For example, during lithiation nano-pore formation is likely to occur in the middle part of nanowall (regions A, B and E) and near the bottom corners (regions C, D, F and G).

Moreover, simulation results show that during lithiation the area under significant tensile mean stress at the mid-plane of the nanowall (regions A to D shown in Figure 5.11b) is much larger than that at the outer surface (regions E to G shown in Figure 5.11c). The mean stress level at the mid-plane is also even higher than that at the outer surface, indicating that interior of the nanowall is more susceptible to pore formation during lithiation.

In the following delithiation half cycle shown in Figures 5.11d and 5.11e, the regions experiencing a significant tensile mean stress of 150MPa to 1GPa are labeled by a through k. Comparison between mean stress distributions at the mid-plane and outer surface reveals that, during delithiation, pores are more likely to nucleate and grow near the nanowall outer surface, opposite to the trend during the lithiation half cycle. It is interesting to note that the associated mean stress distribution is reversed with the transition from lithiation to delithiation: those regions initially under tensile mean stress are now mainly under compression and vice versa. This trend is clearly shown in Figure 5.11d and 5.11e: the regions labeled by a through k are geometrically complementary to those hydrostatically tensile regions denoted by A through G in Figures 5.11b and 5.11d.

Therefore, nearly all of the nanowall experiences a significant tensile mean stress at certain stage during a lithiation/delithiation cycle. As a result, pores are likely to form throughout the entire nanowall after many cycles. This prediction is confirmed by the experimentally-observed homogeneous pore distribution in the nanowall structure observed in experiments (Figure 5.10).

The simulation results of significant tensile mean stress in the nanowall can be used to derive the critical void size R_c for pore formation. For simplicity, we assume the surface energy γ of lithiated silicon is independent of lithium concentration with a value of $1\text{J}/\text{m}^2$.¹⁹ The values of R_c values corresponding to regions under tensile stress during lithiation and delithiation are analyzed. The critical radii in all regions ranges from 2nm~13.3nm. Such an estimate agrees with experimental observation: the radii of the pores in the nanowall after 40 lithiation/delithiation cycles are much greater than 13.3nm (Figure 5.10c), indicating that voids greater than the critical size grow into larger pores under significant tensile mean stress.

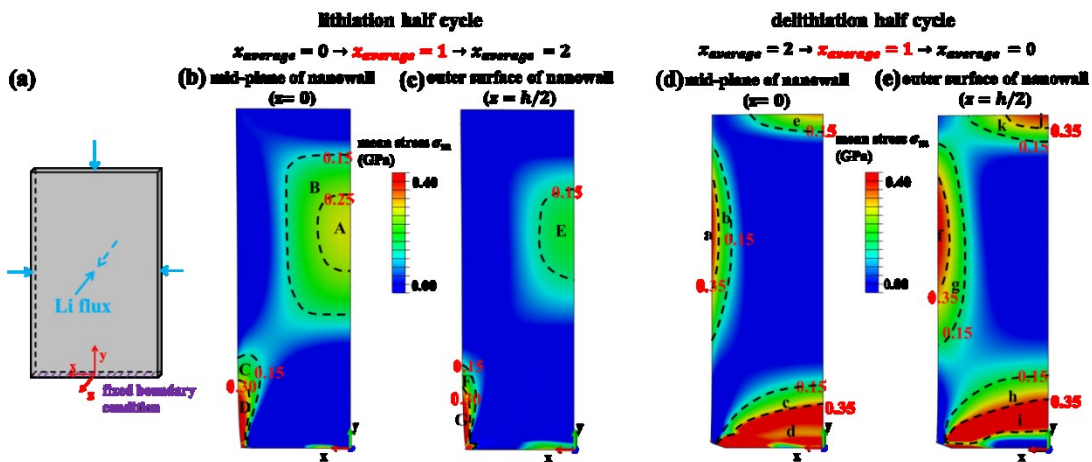


Figure.5.11 Lithiation/delithiation-induced mean stresses in the nanowall. (a) Schematic of

the simulation model. The origin of the coordinate system is defined with origin at the centroid of bottom surface. (b) and (c) show the mean stress distribution within the mid-plane of the nanowall ($z = 0$) and outer surface of nanowall ($z = h/2$) during lithiation half cycle, respectively, with extent of lithiation described by $x_{average} = 1$. (d) and (e) are the counterparts of (b) and (c) during delithiation half cycle, respectively

5.2.4. Summary

In summary, we designed a novel 2D a-Si nanowall structure as anode for Li ion batteries that exhibits excellent electrochemical properties. The lower specific surface area of the nanowall structure compared to 1D/0D nanostructures leads to a high 1st QE. A high specific capacity of ~ 2100 mAh/g is obtained at C/5 and remains stable for over 40 cycles. Porous structures form throughout the nanowall after cycles, which is attributed to the complementary distributions of the tensile mean stress in the nanowall induced by lithiation and delithiation. While this novel nanowall structure is promising in its excellent electrochemical properties, further fundamental studies could reveal desirable electronic and optical properties as well.

Chapter 6. Stress Development and Its Effect on Lithiation Kinetics and Fracture In Silicon-based Anodes in Lithium-ion Batteries

6.1. Stress-Modulated Driving Force for Lithiation Reaction in Hollow Nano-Anodes

6.1.1. Introduction

There has been a surge of interests in developing next-generation lithium-ion batteries with high specific capacity^{33, 41, 159, 175, 176}. Silicon is emerging as the most promising anode material due to its high specific capacity which is about ten times that of current graphite-based anodes^{177, 178}. The high theoretical capacity of silicon stems from the fact that one silicon atom can host up to 3.75 lithium atoms upon fully lithiation¹⁷⁹. However, on the other hand, insertion of large amount of lithium atoms causes excessive volume change (~300%) and large mechanical stresses, which may eventually fracture the silicon anodes and lead to huge irreversible capacity fading^{32, 154, 169}. Therefore, mechanical failures induced by the large volumetric expansion during lithiation are the key issue that hinders the mass application of silicon as anodes for next-generation lithium-ion batteries. To mitigate the mechanical failures of silicon-based anodes, intensive research efforts have been focused on developing nanostructured anodes including nanowires^{32, 180}, nano-sized thin film¹⁸¹, nanoporous structures^{34, 182}, nano-sized beaded-string structure¹⁸³, nano-walls¹⁸⁴ and nano-islands^{185, 186}. Lithiation-induced stress, deformation and mechanical failure in these novel silicon nanostructures are widely studied through

experimental characterization¹⁸⁷⁻¹⁸⁹ and chemo-mechanical modeling^{36, 171, 190-195}. As shown in these studies, shape optimization, mechanical constraint and size control help release excessive lithiation-induced stresses and thus avoid pulverization of anodes and active materials in nano-structured silicon anodes^{36, 183, 190, 196}.

Lithiation kinetics in such silicon nanostructured anodes has also been studied recently^{191, 197, 198}. Experimental evidences have accumulated that the lithiation of crystalline silicon advances by the movement of an atomically-sharp reaction front^{171, 180, 198, 199}, which separates an unlithiated pristine silicon phase and a fully lithiated silicon phase (as shown by the schematics of Figure 1(b)). Therefore, the lithiation of silicon is a two-phase reaction^{200, 201} and it indicates that the lithiation process is controlled by the reaction between lithium and silicon at the reaction front, rather than the diffusion of lithium through the lithiated silicon phase^{171, 191}. Experimental measurements of reaction velocity in solid silicon particles reveal that the reaction front usually slows down as it progresses into the solid particles¹⁹⁷. Existing studies have shown that lithiation-induced stress field could affect the driving force of lithiation^{188, 189, 193, 202, 203}. A theoretical model is recently developed to account for simultaneous lithiation and the associated stress field evolution^{191, 196}. Interestingly, the model predicts that the evolving stress field across the reaction front acts as an energy barrier and retards the lithiation reaction. Therefore, it is expected that the contribution of stresses to the driving force for Li-Si reaction results in the observed slowing of reaction front in solid particle silicon anodes

Recently, hollow nanostructured silicon anodes attract attentions since they have more free space to accommodate the large volume expansion due to lithium insertion and thus possess excellent cycling performance^{34, 162, 204-207}. It is noteworthy that lithiation of hollow silicon nanowires also shows similar slowing or even halting of the reaction front¹⁸³. Although the observed slowing or halting of reaction front in hollow silicon anodes can also be attributed to the negative contribution of lithiation-induced stress, a quantitative understanding is still lacking to fully decipher the lithiation-induced stress field and its influence on reaction rate in hollow silicon nano-anodes. What remain elusive include, for example: How does the hollow nature of silicon nano-anodes alter the role of mechanical stresses in retarding lithiation reaction? How does the slowing of reaction front in hollow silicon anodes differ from that in solid ones? Is hollow nanostructure a good anode design from lithiation kinetics standpoints? Quantitative answers to these questions are crucial for advancing the design of high-performance silicon-based hollow anodes.

In this paper, we present a finite element based chemo-mechanical modeling method as well as a theoretical model to quantitatively determine the stress field in hollow silicon nanowire anodes as the lithiation reaction proceeds. The driving force for the movement of the sharp lithiation reaction front is then identified based on the stress distribution across the sharp reaction front. The lithiation process is fully specified by the current

position of the lithiation front and the lithiation-induced volume expansion of the fully lithiated silicon. Our calculation reveals that, compared with solid silicon anodes, hollow silicon anodes suffer less stress-induced reduction of driving force for lithiation, therefore could act as a better anode structural design for next-generation high performance lithium-ion batteries.

6.1.2. Lithiation-induced stress field in a hollow nanowire

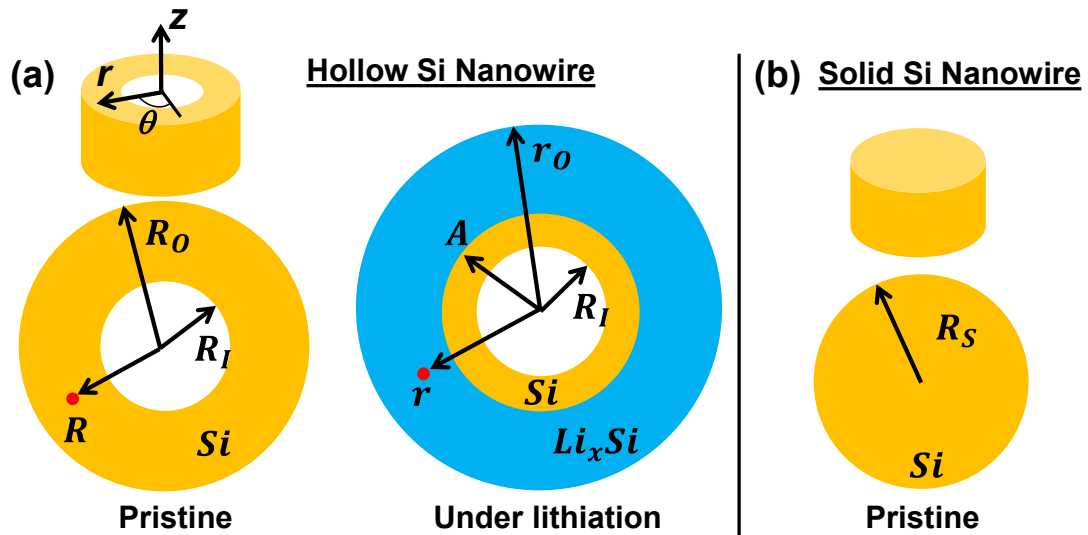


Figure 6.1. (a) Left: cross-section of a pristine hollow cylindrical silicon nanowire with an initial inner radius R_I and an initial outer radius R_O is considered to be the reference state. A material point (labeled by the red dot) is at a radius R . Right: in the lithiation state at time t , the lithiation front is located at a radius of $A(t)$, the outer surface is now at a radius $r_o(t)$, and the material point labeled by R in the reference state moves to a new location at a radius $r(t)$. (b) Cross-section of a pristine solid cylindrical silicon nanowire of a radius R_S , with the same volume of the hollow silicon nanowire defined in (a).

We consider the lithiation process of a hollow cylindrical amorphous silicon nanowire anode with an inner radius R_I and outer radius R_O at the pristine reference state, whose cross-section view is illustrated in Figure 6.1(a). Recent experiments indicate that the

reaction rate of amorphous silicon at the lithiation front is isotropic, without obvious preferential directions¹⁸³. Therefore, as lithiation advances, velocity of the reaction front is the same everywhere along the front and thus the lithiation front sweeps through the hollow silicon nanowire with a cylindrical shape of radius $A(t)$ (Figure 6.1(a)). Here, $A(t)$ decreases with time as the reaction front propagates from the outer surface of silicon nanowire to its inner surface. During this process, lithiated silicon expands in volume to accommodate the lithium insertion. Therefore, a material element characterized by initial radius R in the reference state is deformed and moves to a new position with radius $r(t)$ after this material element is lithiated. In particular, the outer surface with a radius R_0 in the reference state is pushed out to be the current outer surface with a radius r_o . During the lithiation process, stress field arises and evolves in response to the volume change caused by lithium insertion.

A. Chemo-mechanical simulations

To solve the lithiation-induced stress field in the silicon nanowire, the concurrent lithiation reaction and deformation of the silicon nanowire along its cross-section are simulated using finite element code ABAQUS. In order to mimic the inward movement of the reaction front, the cross section of the silicon nanowire is evenly divided into N (an integer) annuluses and these annuluses are lithiated one by one from outer surface toward inner core of the silicon nanowire. Experimental evidence has accumulated that the reaction front is atomically sharp with thickness of ~ 1 nm¹⁹⁹. In the simulation, the

thickness of the reaction front is defined by the thickness of each annulus, which is set to be 2 nm to compromise between simulation expense and modeling fidelity. The lithiation of each annulus is modeled by prescribing a volume change of 400% (i.e., fully lithiated). The pristine silicon is modeled to be linearly elastic with a Young's modulus of 160 GPa and a Poisson's ratio of 0.24¹⁷¹. The fully lithiated silicon phase is taken to be elastic-perfectly plastic with a Young's modulus of 40 GPa, a Poisson's ratio of 0.22 and a yielding stress of 1.5 GPa^{39,171}. Recent experiments reveal that a hollow cylindrical silicon anode with the deformation of its inner surface largely constrained demonstrates a better durability during lithiation compared with its counterpart with its inner surface free to deform. To study such a boundary effect on the lithiation-induced stress field, we perform chemo-mechanical simulations with two types of boundary conditions of the inner surface of the hollow silicon nanowire: traction-free and fixed. In all simulations, the outer surface of the silicon nanowire is traction-free, simulating the lithiation of the silicon nanowire without external lateral constraint as suggested in *in situ* experiments. To clarify how the hollow geometry affects the lithiation process, we compare the lithiation of hollow silicon nanowires with different inner radii but same volume with that of a solid silicon nanowire of the same volume, i.e., $R_O^2 - R_I^2 = R_S^2$ (Figure 6.1). To facilitate the comparison among various lithiation stages, in all results reported hereinafter, all stress components are plotted as a function of radial location in the reference configuration (i.e., pristine state) and all length dimensions are normalized by

R_S .

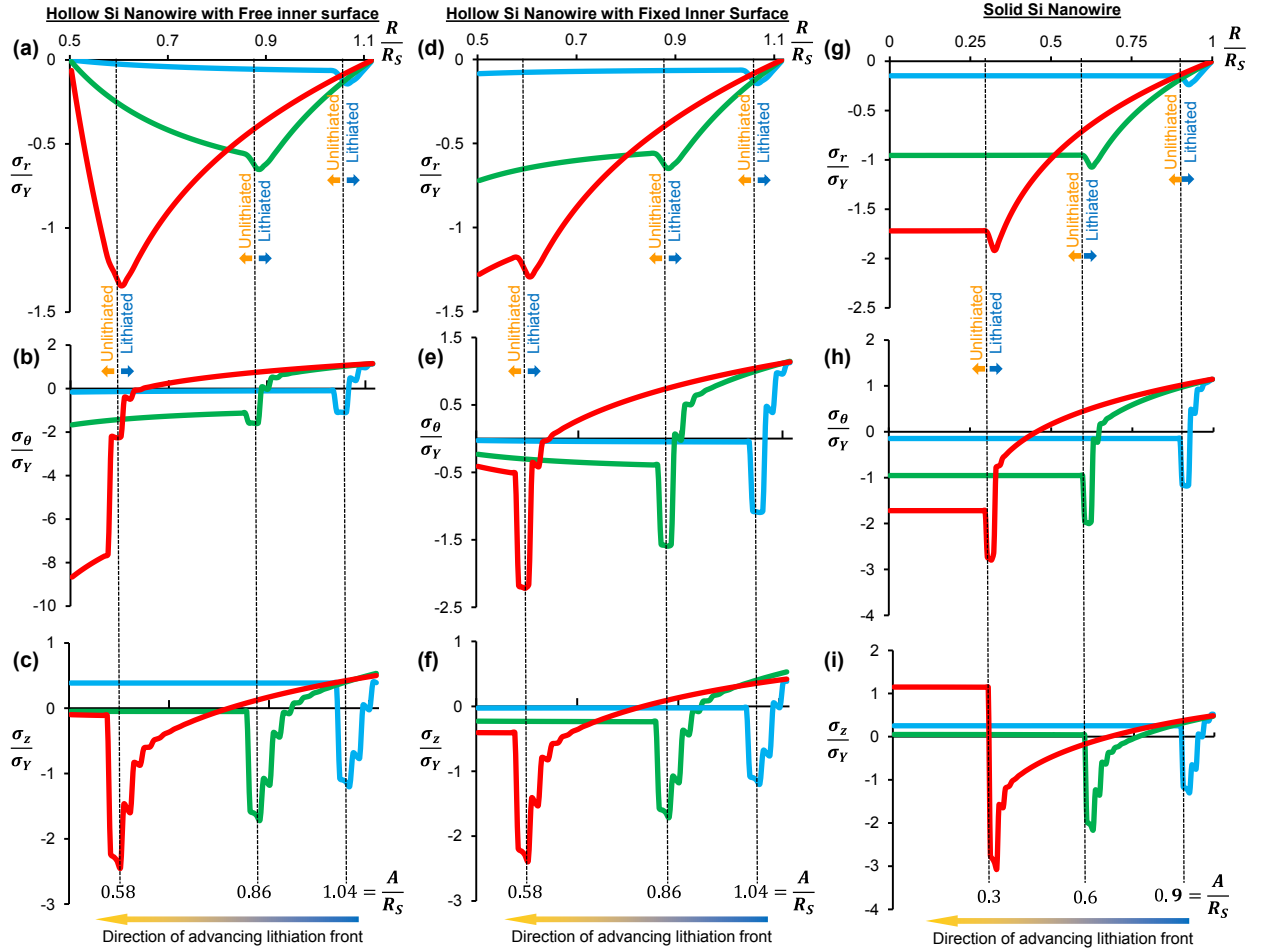


Figure 6.2. Finite element simulation results on lithiation-induced stress field in a hollow silicon nanowire with a traction-free inner surface (a-c), with a fixed inner surface (d-f) and in a solid silicon nanowire (g-i). In hollow silicon nanowire, distributions of radial stress σ_r (a, d), hoop stress σ_θ (b, e) and axial stress σ_z (c, f) are shown for various reaction front positions (depicted by a dashed line) of $A/R_S=1.04$ (blue curve), $A/R_S=0.86$ (green curve) and $A/R_S=0.58$ (red curve). In solid silicon nanowire, distributions of radial stress σ_r (g), hoop stress σ_θ (h) and axial stress σ_z (i) are shown for reaction front positions (depicted by a dashed line) of $A/R_S=0.9$ (blue curve), $A/R_S=0.6$ (green curve) and $A/R_S=0.3$ (red curve).

Figure 6.2 plots the finite element simulation results on the distribution of three stress components (i.e., radial stress σ_r , hoop stress σ_θ , and axial stress σ_z , all normalized by the yield stress of fully lithiated silicon σ_y) along the radial direction of the hollow

silicon nanowire, for three stages of lithiation process with the reaction front being at $\frac{A}{R_S} = 1.04, 0.86, \text{ and } 0.58$, respectively. The inner and outer radii of the hollow silicon nanowire is 50 nm and 111.8 nm respectively, with a corresponding solid nanowire of radius $R_S = 100$ nm. Figure 6.2 shows tri-axial nature of the lithiation-induced stress field in various stages. When the inner surface of the hollow silicon nanowire is free (Figure 6.2 (a-c)), it is shown that that compressive stresses accumulate in the unlithiated pristine silicon core along both radial and hoop directions with radial stress vanishing at the inner surface due to the traction-free boundary condition. The unlithiated core experiences increasing compressive radial/hoop stresses as lithiation advances. Axial stress σ_z is constant in the unlithiated silicon core, being tensile at the early stage of lithiation, gradually decreasing to be zero as lithiation advances. In Figure 6.2(b) and 6.2(c), a discontinuity in hoop stress σ_θ and axial stress σ_z exists across the lithiation front due to the abrupt change of material properties from pristine silicon phase to fully lithiated phase ($Li_{3.75}Si$). At the reaction front, the constraint from the inner unlithiated core acts against the lithiation-induced volume expansion of the $Li_{3.75}Si$ phase. As a result, the $Li_{3.75}Si$ phase at the reaction front is under compressive stresses σ_θ and σ_z ; and the resulting von Mises stress readily exceeds the yielding strength, causing yielding of the fully lithiated silicon phase on the reaction front. In the outer lithiated shell, due to the “pushing-out” effect, the $Li_{3.75}Si$ phase undergoes elastic unloading and the hoop stress σ_θ gradually becomes tensile inside the lithiated shell and eventually reaches σ_Y

at the external surface of the anode, which may induce fracture nucleating at the nanowire surface as reported for solid crystalline nanopillar in literature. When the inner surface of the hollow silicon nanowire is fixed (Figure 6.2 (d-f)), the constraint at its inner surface strongly affects the stress distribution within the unlithiated silicon core by setting a non-trivial compressive radial stress σ_r at the inner surface of hollow nanowire but effectively reducing the compressive hoop stress σ_θ . On the other hand, the stress distribution in the lithiated shell is rather close to that in a hollow nanowire with a free inner surface. Distributions of stress components in solid nanowire with various reaction front positions are shown in Figure 6.2 (g-i), the inner unlithiated core experiences in-plane hydrostatic compression with constant distribution of radial stress σ_r and hoop stress σ_θ ($\sigma_r = \sigma_\theta$). It is noted that

B. A theoretical mechanics model

As an effort to validate the simulated results shown above, in this section we present a theoretical mechanics model of the lithiation-induced stress field in a hollow silicon nanowire. Zhao et al. recently established a theoretical formulation of concurrent reaction and plasticity to investigate the lithiation of a hollow nanowire with its outer surface confined by a rigid solid-electrolyte interphase layer. In their theoretical model, the diffusion of lithium in silicon is assumed to be fast enough to allow for a uniform distribution of lithium, and as a result, lithiation front is not involved in the model and the lithiation process is fully specified by the lithiation-induced uniform volume expansion of

the silicon. To further clarify the underpinning mechanism of lithiation-induced stresses associated with the evolving sharp lithiation front, here we present a theoretical formulation considering both concurrent movement of reaction front and volume expansion induced by lithium insertion at the reaction front.

i). Stress distribution in the lithiated silicon shell ($A < r \leq r_0$)

In the current configuration at time t , consider a shell of silicon between the lithiation front A and radius r (Figure 6.1(a), right panel), which results from the lithiation and deformation of a pristine silicon shell between radii A and R in the reference state (Figure 6.1(a), left panel). Elongation of the silicon nanowire along its axial direction is expected to be negligible, thus the lithiated silicon in its cross section is assumed to deform under plane-strain conditions. Therefore, we have,

$$r^2 - A^2 = \beta(R^2 - A^2) \quad (6.1)$$

where β is the volume expansion ratio defined by the volume of the lithiated silicon $Li_{3.75}Si$ over that of the pristine silicon. Equation (6.1) relates the current coordinate $r(R, t)$ of a material point to its initial coordinate R and the current position of lithiation front $A(t)$, and can be re-organized as

$$r = \sqrt{A^2 + \beta(R^2 - A^2)} \quad (6.2)$$

Equation (6.2) determines the current configuration of the lithiated nanowire, where A acts as the only variable. Therefore, the current position of lithiation front $A(t)$ fully specifies the lithiation kinetics of the silicon nanowire anode.

The deformation kinematics of the silicon nanowire can be described by the deformation gradient tensor $\underline{\mathbf{F}}$ as follows:

$$\underline{\mathbf{F}} = \begin{bmatrix} \lambda_r & 0 & 0 \\ 0 & \lambda_\theta & 0 \\ 0 & 0 & \lambda_z \end{bmatrix} \quad (6.3)$$

where hoop stretch $\lambda_\theta = r/R$ and axial stretch $\lambda_z = 1$ (plane-strain conditions). It is worth noting that during lithiation elastic strains are trivial compared with the large plastic and volumetric strains and thus are neglected. Therefore, the total deformation gradient tensor $\underline{\mathbf{F}}$ can be decomposed into a volumetric part and a plastic part as $\underline{\mathbf{F}} = \underline{\mathbf{F}}_v \underline{\mathbf{F}}_p$. The volume change of lithiated silicon is given by $\det(\underline{\mathbf{F}}) = \det(\underline{\mathbf{F}}_v) \det(\underline{\mathbf{F}}_p) = \det(\underline{\mathbf{F}}_v) = \beta$, entirely a result of lithiation-induced volume change, i.e., $\lambda_r \lambda_\theta \lambda_z = \beta$. The radial stretch is then calculated as $\lambda_r = \frac{R}{r} \beta$. Moreover, the lithiation-induced volume expansion is intrinsically isotropic and takes the following form:

$$\underline{\mathbf{F}}_v = \begin{bmatrix} \lambda_v & 0 & 0 \\ 0 & \lambda_v & 0 \\ 0 & 0 & \lambda_v \end{bmatrix} \quad (6.4)$$

As abovementioned, $\det(\underline{\mathbf{F}}_v) = \beta$ and therefore $\lambda_v = \beta^{1/3}$. The deformation gradient tensor corresponding to plasticity is then given by

$$\underline{\mathbf{F}}_p = \underline{\mathbf{F}} \underline{\mathbf{F}}_v^{-1} = \begin{bmatrix} \lambda_r^p & 0 & 0 \\ 0 & \lambda_\theta^p & 0 \\ 0 & 0 & \lambda_z^p \end{bmatrix} = \begin{bmatrix} \frac{R}{r} \beta^{2/3} & 0 & 0 \\ 0 & \frac{r}{R} \beta^{-1/3} & 0 \\ 0 & 0 & \beta^{-1/3} \end{bmatrix} \quad (6.5)$$

Given the relation between true strain and stretch ratio, the increment of true strain can be solved as

$$\delta \varepsilon_r^p = 2(\beta - 1)A\delta A/r^2 \quad (6.6.1)$$

$$\delta \varepsilon_\theta^p = (1 - \beta)A\delta A/r^2 \quad (6.6.2)$$

$$\delta \varepsilon_z^p = 0 \quad (6.6.3)$$

Equations (6.6.1-3) indicate that the deformation geometry of the lithiated silicon shell is fully evolved by the inward movement of the lithiation front ($\delta A < 0$). The increment of equivalent plastic strain is obtained as

$$\delta \varepsilon_{eq}^p = \sqrt{\frac{2}{3} \delta \varepsilon_{ij}^p \delta \varepsilon_{ij}^p} = \frac{2}{\sqrt{3}} \frac{A|(1-\beta)\delta A|}{r^2} = \frac{2}{\sqrt{3}} \frac{(1-\beta)A\delta A}{r^2} \quad (6.7)$$

The lithiated silicon is taken to be perfectly rigid plastic. According to the J_2 flow rule, the deviatoric stress components are solved as

$$s_r = \frac{2}{3} \frac{\sigma_Y}{\delta \varepsilon_{eq}^p} \delta \varepsilon_r^p = -\frac{\sigma_Y}{\sqrt{3}} \quad (6.8.1)$$

$$s_\theta = \frac{\sigma_Y}{\sqrt{3}} \quad (6.8.2)$$

$$s_z = 0 \quad (6.8.3)$$

where σ_Y is the yielding stress of fully lithiated silicon $Li_{3.75}Si$. Therefore, we have

$$\sigma_r - \sigma_\theta = s_r - s_\theta = -\frac{2}{\sqrt{3}} \sigma_Y \quad (6.9)$$

The equilibrium equation defined in the current configuration requires

$$\frac{\partial \sigma_r(r,t)}{\partial r} + 2 \frac{\sigma_r(r,t) - \sigma_\theta(r,t)}{r} = 0 \quad (6.10)$$

where the boundary condition at the silicon nanowire surface $r = r_0$ is traction-free, i.e., $\sigma_r(r_0, t) = 0$. Plugging (6.9) into (6.10) and integrating over r give the radial stress in the lithiated shell ($A \leq r \leq r_0$):

$$\sigma_r = \frac{2}{\sqrt{3}} \sigma_Y \log\left(\frac{r}{r_0}\right), \quad (A < r \leq r_0) \quad (6.11)$$

The hoop stress σ_θ inside the lithiated shell is then determined by Eq. (6.9)

$$\sigma_\theta = \frac{2}{\sqrt{3}}\sigma_Y + \frac{2}{\sqrt{3}}\sigma_Y \log\left(\frac{r}{r_0}\right), \quad (A < r \leq r_0) \quad (6.12)$$

Therefore, at the outer surface of the silicon nanowire $r = r_0$, the hoop stress $\sigma_\theta(r_0, t) = \frac{2}{\sqrt{3}}\sigma_Y > 0$ (tensile), which agrees with the experimentally observed cracks at the outer surface of the lithiated Si anodes²⁰⁸. The axial stress is obtained from Eqs. (6.8.3), (6.11) and (6.12),

$$\sigma_z = \frac{1}{\sqrt{3}}\sigma_Y + \frac{2}{\sqrt{3}}\sigma_Y \log\left(\frac{r}{r_0}\right), \quad (A < r \leq r_0) \quad (6.13)$$

ii). *Stresses on the lithiation front ($r = A$)*

For a material element right on the lithiation front characterized by $r = A$, lateral expansion (along axial and hoop directions) is strongly constrained by the inner unlithiated core. As a result, all stretch components can be written as

$$\lambda_r = \beta, \lambda_\theta = \lambda_\psi = 1. \quad (6.14)$$

The plastic stretches at the lithiation reaction front are then given as

$$\lambda_r^p = \lambda_r \beta^{-1/3} = \beta^{2/3} \quad (6.15.1)$$

$$\lambda_\theta^p = \lambda_\theta = \beta^{-1/3} \quad (6.15.2)$$

On the lithiation front $r = A$, silicon reacts with lithium and eventually forms fully lithiated phase, $Li_{3.75}Si$. The associated volume expansion ratio β ramps from 1 (pristine state) to 4 (fully lithiated state) as the lithium concentration accumulates. Therefore, given a lithiation front at A , change of β evolves the plastic deformation at reaction front. Then, the increments of true strains are derived as

$$\delta \varepsilon_r^p = \frac{2 \delta \beta}{3 \beta} \quad (6.16.1)$$

$$\delta \varepsilon_\theta^p = \delta \varepsilon_\phi^p = -\frac{1 \delta \beta}{3 \beta} \quad (6.16.2)$$

The equivalent plastic strain is

$$\delta \varepsilon_{eq}^p = \sqrt{\frac{2}{3} \delta \varepsilon_{ij}^p \delta \varepsilon_{ij}^p} = \frac{2 \delta \beta}{3 \beta} \quad (6.17)$$

Therefore, the deviatoric stresses are

$$s_r = \frac{2}{3} \frac{\sigma_Y}{\delta \varepsilon_{eq}^p} \delta \varepsilon_r^p = \frac{2}{3} \sigma_Y \quad (6.18.1)$$

$$s_\theta = s_\phi = s_z = -\frac{1}{3} \sigma_Y \quad (6.18.2)$$

Radial stress σ_r is continuous across the lithiation front, therefore, at the lithiation front $r = A$,

$$\sigma_r = \frac{2}{\sqrt{3}} \sigma_Y \log \left(\frac{A}{r_0} \right) \quad (6.19)$$

Equations (6.18.1) and (6.18.2) indicate that $\sigma_r - \sigma_\theta = \sigma_Y$ and $\sigma_r = \sigma_\theta$, and we have

$$\sigma_\theta = -\sigma_Y + \frac{2}{\sqrt{3}} \sigma_Y \log \left(\frac{A}{r_0} \right) \quad (6.20)$$

$$\sigma_z = -\sigma_Y + \frac{2}{\sqrt{3}} \sigma_Y \log \left(\frac{A}{r_0} \right) \quad (6.21)$$

iii). *Stress distribution in the remaining unlithiated hollow silicon shell ($R_I \leq r < A$)*

The unlithiated hollow silicon part ($R_I \leq r < A$) is an annulus between radii R_I and A and subjected to a radial compression $\frac{2}{\sqrt{3}} \sigma_Y \log \left(\frac{r_0}{A} \right)$ at the lithiation reaction front. As discussed above, the inner surface of the remaining unlithiated silicon is either under fixed boundary condition (if the hollow nanowire is bonded to an inner constraint) or traction-free (if the hollow nanowire is free-standing). The stress field in the pristine unlithiated silicon can be obtained by solving a Lamé problem. For the traction-free

inner surface, the stress field ($R_I \leq r < A$) is given as

$$\sigma_r = \frac{2}{\sqrt{3}} \sigma_Y \log \left(\frac{A}{r_0} \right) \frac{A^2}{A^2 - R_I^2} \left(1 - \frac{R_I^2}{r^2} \right), \quad (R_I \leq r < A) \quad (6.22.1)$$

$$\sigma_\theta = \frac{2}{\sqrt{3}} \sigma_Y \log \left(\frac{A}{r_0} \right) \frac{A^2}{A^2 - R_I^2} \left(1 + \frac{R_I^2}{r^2} \right), \quad (R_I \leq r < A) \quad (6.22.2)$$

$$\sigma_z = \frac{4\mu}{\sqrt{3}} \sigma_Y \log \left(\frac{A}{r_0} \right) \frac{A^2}{A^2 - R_I^2}, \quad (R_I \leq r < A) \quad (6.22.3)$$

Similarly, fixed boundary condition at the inner surface gives a stress field ($R_I \leq r < A$)

as follows

$$\sigma_r = \frac{2}{\sqrt{3}} \sigma_Y \log \left(\frac{A}{r_0} \right) \left[\frac{1}{\frac{r^2}{A^2} + \frac{1}{(1-2\nu)R_I^2}} + \frac{1}{\frac{1}{r^2} + 1} \right], \quad (R_I \leq r < A) \quad (6.23.1)$$

$$\sigma_\theta = \frac{2}{\sqrt{3}} \sigma_Y \log \left(\frac{A}{r_0} \right) \left[-\frac{1}{\frac{r^2}{A^2} + \frac{1}{(1-2\nu)R_I^2}} + \frac{1}{\frac{1}{r^2} + 1} \right], \quad (R_I \leq r < A) \quad (6.23.2)$$

$$\sigma_z = \frac{4\nu}{\sqrt{3}} \sigma_Y \log \left(\frac{A}{r_0} \right) \frac{1}{\frac{(1-2\nu)R_I^2}{A^2} + 1}, \quad (R_I \leq r < A) \quad (6.23.3)$$

where ν is the Poisson's ratio of pristine amorphous silicon.

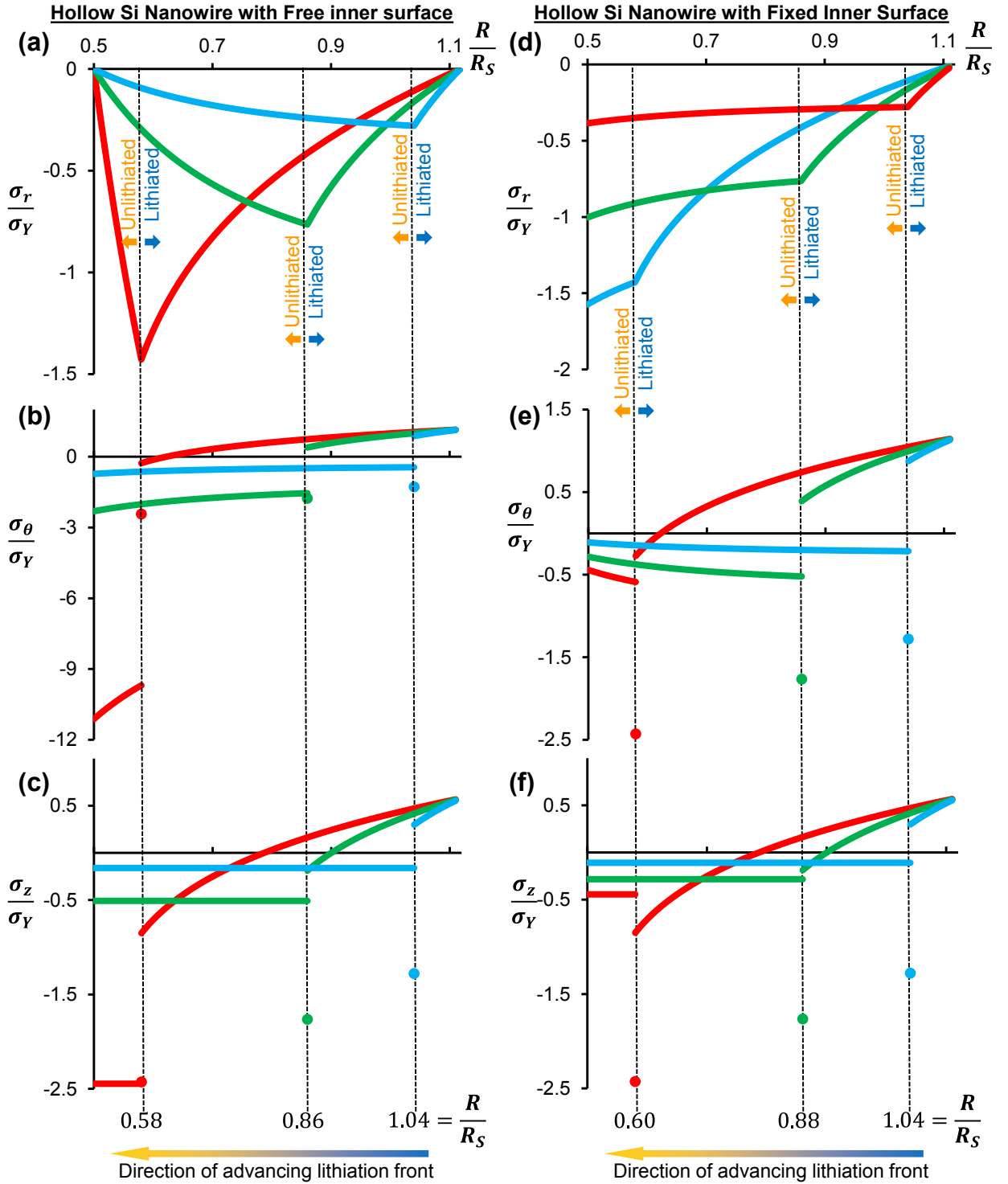


Figure 6.3. Theoretical mechanics model results on lithiation-induced stress field in a hollow silicon nanowire with a traction-free inner surface (a-c) and with a fixed inner surface (d-f). Distributions of radial stress σ_r (a, d), hoop stress σ_θ (b, e) and axial stress σ_z (c, f) are shown for various reaction front positions (depicted by a dashed line) of $A/R_S=1.04$ (blue curve), $A/R_S=0.86$ (green curve) and $A/R_S=0.58$ (red curve).

Figure 6.3 plots the theoretical mechanics model results on the distribution of radial stress σ_r , hoop stress σ_θ , and axial stress σ_z , along the radial direction of the hollow silicon nanowire, for three stages of lithiation process with the reaction front being at $A/R_S = 1.04, 0.86,$ and $0.58,$ respectively. The same geometric parameters of the hollow silicon nanowire and its solid counterpart as in finite element simulations (e.g., in Figure 6.2) are used here. For the case of silicon nanowire with a free inner surface, distribution of radial stress σ_r (Figure 6.3(a)) and hoop stress σ_θ (Figure 6.3(b)) agree reasonably well with the prediction from finite element simulations (Figure 6.2(a) and (b), respectively). The jump of hoop stress between a material point on the lithiation front and its neighboring material point in the fully lithiated shell results from neglecting the trivial elastic deformation in the lithiated phase. Moreover, the distribution of axial stress σ_z outside the unlithiated core (Figure 6.2(c), e.g., on the right of each dashed line) also well reproduces the finite element simulation results presented in Figure 6.2(c). However, the theoretical mechanics model predicts an increasing compressive axial stress inside the unlithiated core (Fig. 6.2(c), e.g., on the left of each dashed line) as the lithiation advances. This is different from the prediction from finite element simulation as shown in Fig. 6.2(c). Such a discrepancy might result from the assumption of plane-strain conditions adopted in the theoretical mechanics model, which could indeed constrain the modest axial elongation of the silicon nanowire under lithiation.

For the case of silicon nanowire with a fixed inner surface, the theoretical mechanics

model results (Fig. 6.3(d-f)) match remarkably well with those obtained by finite element simulations (Fig. 6.2 (d-f)). In such a case, the fixed inner surface constrains the free expansion of the silicon nanowire in its axial direction, which in turn makes the assumption of plane-strain conditions reasonable and accurate.

Both finite element simulations and theoretical mechanics model capture the interplay between the concurrent reaction and plasticity during lithiation of the silicon nanowire and reveal the three dimensional nature of the resulting stress field in the nanowire. In particular, we show that the resulting stress and deformation fields in the hollow silicon nanowire can be fully determined once the position of the lithiation front is given. Recent studies show that reaction kinetics is dictated by the stress field within the unlithiated core and right on the reaction front. As shown above, since the stress field within the unlithiated core is highly affected by the boundary conditions at the inner surface of the hollow silicon nanowire, it is expected that such boundary conditions would significantly influence the lithiation kinetics of the silicon nanowire. In next section, we report detailed study of the effect of the lithiation-induced stress on the driving force for lithiation reaction.

6.1.3. Effect of stress on driving force for lithiation

The reaction at lithiation front advances by transforming lithium and silicon into a lithiated phase, as described by the chemical reaction equation, $Li + \frac{1}{x}Si = \frac{1}{x}Li_xSi$. The driving force for such a reaction to proceed represents the net change of the free energy

associated with the reaction, which can be given by

$$\Delta G = \Delta G_{intrinsic} - e\Phi + \Delta G_{stress} \quad (6.24)$$

where $\Delta G_{intrinsic}$ represents the free energy change due to lithiation reaction without any applied voltage and stress, which intrinsically takes a negative value (i.e., energetically favorable). For example, $\Delta G_{intrinsic} = -0.18eV$ for $Li_{2.1}Si$; $-e\Phi$ denotes the external work done by the applied voltage Φ ; and ΔG_{mech} represents the contribution of mechanical stress on the driving force for lithiation reaction. A negative ΔG drives the reaction while a positive one stalls the reaction. Moreover, a more negative ΔG represents a higher driving force and a more positive ΔG denotes more resistance to lithiation.

The contribution of lithiation-induced stresses to the lithiation driving force can be computed by

$$\Delta G_{stress} = \frac{1}{x} (\sigma_m^{Si} \Omega^{Si} - \sigma_m^{Li_xSi} \Omega^{Li_xSi}) \quad (6.25)$$

where Ω^{Si} and Ω^{Li_xSi} represent the atomic volumes of Si and Li_xSi , respectively (note that $\Omega^{Li_xSi} = \beta \Omega^{Si}$); σ_m^{Si} and $\sigma_m^{Li_xSi}$ denote the mean stress (i.e., $\frac{1}{3}(\sigma_r + \sigma_\theta + \sigma_z)$) in the remaining unlithiated silicon and the mean stress on the lithiation front, respectively.

Figure 6.4 plots ΔG_{stress} as a function of the lithiation front position A/R_S , for a solid silicon nanowire and hollow silicon nanowires of the same volume as the solid one but with various inner radii, using the finite element simulation results of lithiation-induced

stresses (e.g., as in Figure 6.2).

For a solid silicon nanowire, ΔG_{stress} is always positive and monotonically increases as the reaction advances (Fig. 6.4(a)). For example, $\Delta G_{stress} \approx 0.81$ eV when $A/R_S = 0.03$ (very close to fully lithiation), which is significantly higher than the intrinsic driving force for lithiation reaction $\Delta G_{intrinsic}$. In other words, lithiation-induced stress could potentially severely retard or even halt the lithiation reaction in a solid silicon nanowire.

For a hollow silicon nanowire, (e.g., Fig. 6.4(c) for the one corresponding to Fig. 6.2), at the initial stage of lithiation reaction, ΔG_{stress} is positive and increase monotonically with a slope modestly lower than that for a solid nanowire as the reaction advances. There is negligible difference between the two cases of boundary conditions at the inner surface of the nanowire. However, in later stage of lithiation reaction, the change of ΔG_{stress} as the reaction proceeds further shows distinct trends for the two cases of boundary conditions at the inner surface of the nanowire. With a fixed inner surface of the nanowire, ΔG_{stress} continues increase monotonically, in a rather linear fashion. For example, $\Delta G_{stress} \approx 0.38$ eV when $A/R_S = 0.53$ (very close to fully lithiation, reaching the last virtual annulus in simulation). By contrast, with a free inner surface, ΔG_{stress} reaches its peak value of ~ 0.28 eV at an intermediate lithiation stage ($A/R_S = 0.67$), and then decreases monotonically as the reaction advances toward the inner surface, becoming negative (~ -0.1 eV) as approaching full lithiation. The above

results suggest: (a) At the initial stage of lithiation reaction, the resistance due to lithiation-induced stress is relatively lower for hollow silicon nanowires when compared with a solid one; and (b) At the later stage of lithiation reaction, a free inner surface of hollow silicon nanowires can indeed facilitates the lithiation reaction by increasing the driving force. For (b), as shown in Fig. 6.2, at the later stage of lithiation reaction, the level of the three principal stress components, thus the level of mean stress on the lithiation front $\sigma_m^{Li_xSi}$ is comparable for both cases of boundary conditions at the inner surface. On the other hand, the compressive hoop stress σ_θ in the remaining unlithiated silicon of the nanowire with a free inner surface reaches a level ($\sigma_\theta/\sigma_Y \approx -8$) substantially higher than not only the other two principal stress components, but also the hoop stress on the lithiation front ($\sigma_\theta/\sigma_Y \approx -2$). As a result, the mean stress in the unlithiated silicon σ_m^{Si} becomes so negative that the first term in Eq. (6.25) overbalances the second term, leading to a negative ΔG_{stress} .

Further comparison among hollow nanowires with the same volume but different inner radii (Fig. 6.4(b-d)) show that a hollow nanowire anode with a larger inner radius experiences lower stress-induced resistance to lithiation reaction at its early stage, regardless the boundary conditions at the inner surface, and could have even higher driving force for lithiation reaction toward its final stage if the inner surface of the nanowire is free.

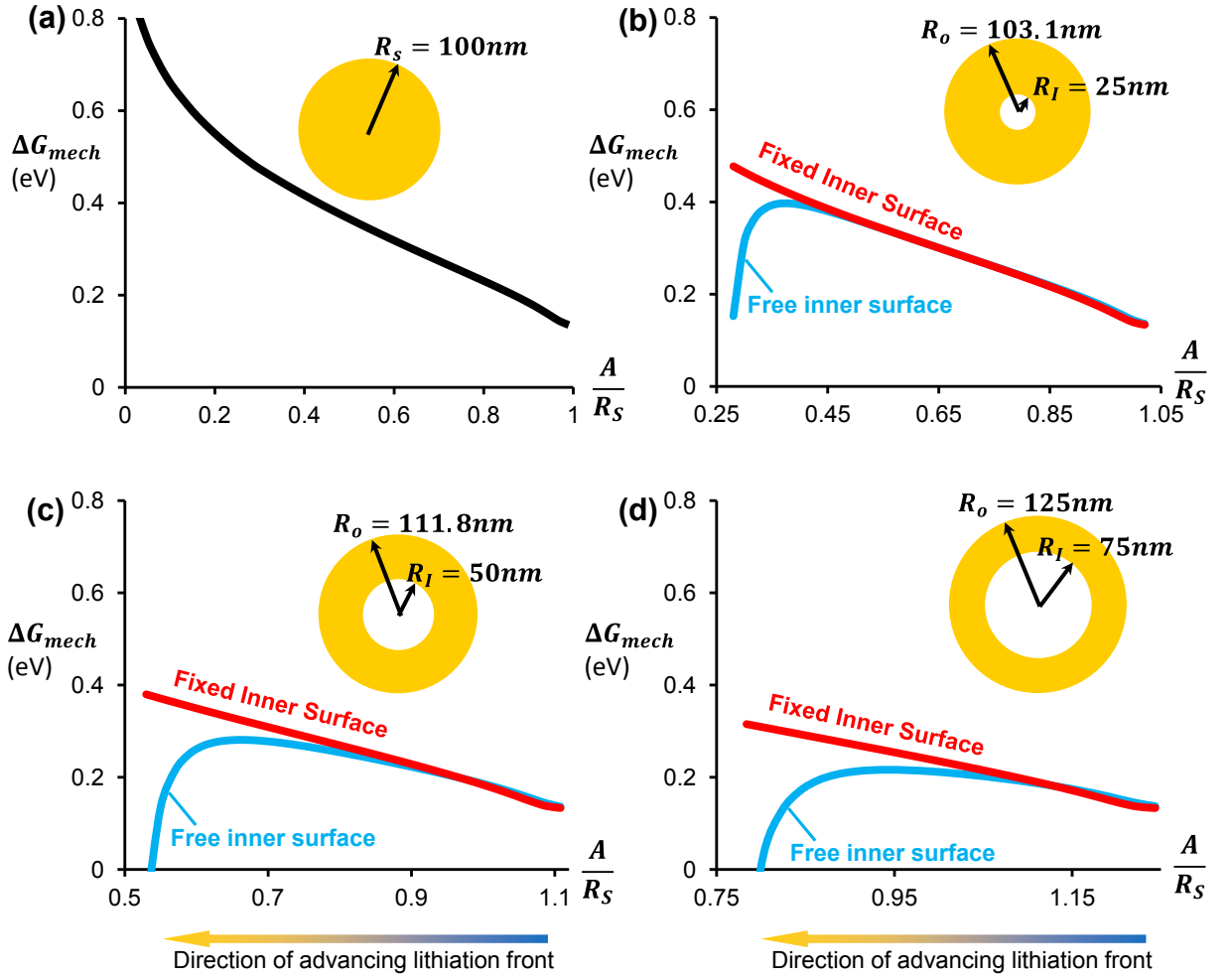


Figure 6.4. Finite element simulation results on stress-modulated driving force for lithiation as a function of the lithiation front position A/R_s , for (a) a solid silicon nanowire and (b-d) hollow silicon nanowires with normalized inner radius of (b) $R_i/R_s=0.25$, (c) $R_i/R_s=0.5$ and (d) $R_i/R_s=0.75$, respectively. Blue lines in (b-d) represent the case of a hollow nanowire with a traction-free inner surface and red lines represent the case of a hollow nanowire with a fixed inner surface.

ΔG_{stress} can also be explicitly solved using the theoretical formulation delineated above.

For example, the driving forces associated with lithiation-induced stress in a hollow silicon nanowire with traction-free inner surface and fixed inner surface can be given by

$$\Delta G_{stress}^{traction-free} = \frac{2\sigma_Y\Omega^{Si}}{x} \left[\frac{2}{3\sqrt{3}} \log\left(\frac{A}{r_o}\right) \frac{(1+\mu)A^2}{A^2-R_i^2} - \frac{\beta}{\sqrt{3}} \log\left(\frac{A}{r_o}\right) + \frac{\beta}{3} \right] \quad (6.26.1)$$

$$\text{and } \Delta G_{stress}^{fixed} = \frac{2\sigma_Y \Omega^{Si}}{x} \left[\frac{2}{3\sqrt{3}} \log\left(\frac{A}{r_o}\right) \frac{(1+\mu)A^2}{(1-2\mu)R_l^2 + A^2} - \frac{\beta}{\sqrt{3}} \log\left(\frac{A}{r_o}\right) + \frac{\beta}{3} \right], \quad (6.26.2)$$

respectively. Equations (6.26.1) and (6.26.2) are plotted in Figs. 6.5 (b-d) for the same anode structures as in Fig. 6.4. Here, we take $\beta = 4$, $x = 3.75$, $\Omega^{Si} = 2 * 10^{-29} m^3$ and $\sigma_Y = 1.5 GPa$. The prediction of the evolution of stress-modulated driving force for lithiation reaction from theoretical mechanics model shows reasonable agreement with that from finite element simulations, with a modestly higher level of ΔG_{stress} values, resulting from the slight difference in the predicted lithiation-induced stresses as explained above.

Nonetheless, both finite element simulations and theoretical mechanics model predict that a hollow silicon nanowire anode can be fully lithiated more easily than a solid one with the same volume, due to reduced resistance to reaction associated with lithiation-induced stress.

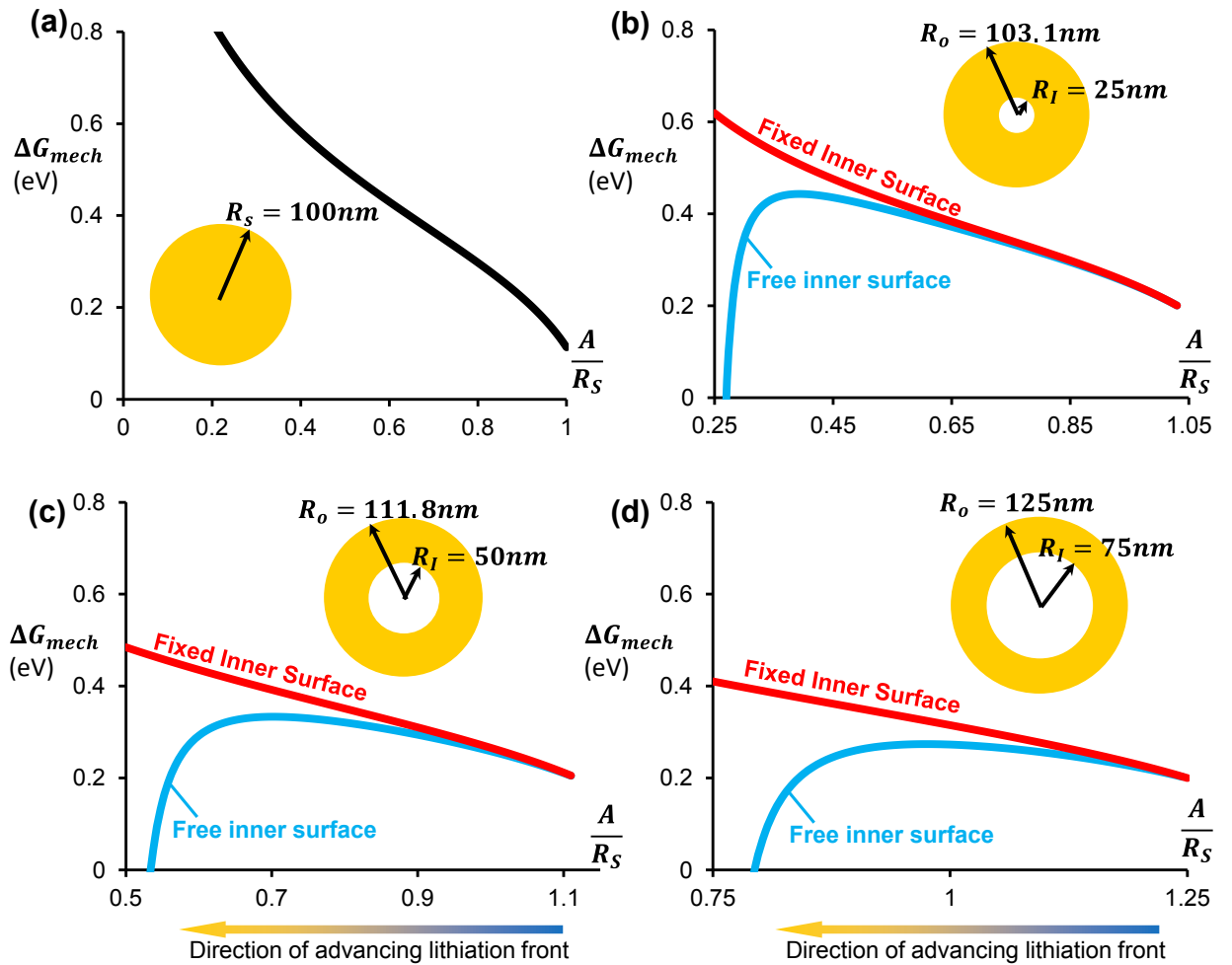


Figure 6.5. Theoretical mechanics model results on stress-modulated driving force for lithiation as a function of the lithiation front position A/R_S , for (a) a solid silicon nanowire and (b-d) hollow silicon nanowires with normalized inner radius of (b) $R_I/R_S=0.25$, (c) $R_I/R_S=0.5$ and (d) $R_I/R_S=0.75$, respectively. Blue lines in (b-d) represent the case of a hollow nanowire with a traction-free inner surface and red lines represent the case of a hollow nanowire with a fixed inner surface.

6.1.4. Summary

This paper presents a chemo-mechanical simulation and a theoretical model considering concurrent reaction and deformation to study the lithiation-induced stress in hollow silicon nanowire anode and its effect on driving force for movement of lithiation front.

We first demonstrate that surface effect is negligible in silicon nanowire anodes with diameter on the order of 100nm. The stress and deformation field in the hollow silicon nanowire is fully specified once the position of the lithiation front and the boundary condition at the inner surface is known. The inward movement of the reaction front fully evolves the stress field. The contribution of mechanical stresses to the driving force for lithiation reaction $Li + \frac{1}{x}Si = \frac{1}{x}Li_xSi$ is calculated based on the stress field at the reaction front. It is shown that a hollow silicon nanowire is easier to be fully lithiated than its solid counterpart because the stress-related energy barrier is lower in hollow nanowire. We also study the size effect on stress-modulated driving force. It is demonstrated that a hollow nanowire with larger inner radius and traction-free inner surface possess lower stress-induced reaction barrier and thus is a promising anode design. It is hoped that the results may shed lights on optimal design of hollow silicon anodes for high performance lithium-ion batteries.

6.2. Stress Generation during Two-Step Electrochemical Lithiation of Amorphous Silicon

6.2.1. Introduction

Driven by emerging applications in portable electronics and electric vehicles, there has been intense interest in recent years in developing new high-capacity anode materials for

next-generation lithium-ion batteries^{159, 209, 210}. Silicon can host a large amount of lithium atoms, making its theoretical capacity as high as ten times that of conventional graphite-based anodes. Therefore, among all candidate materials, silicon is emerging as the most promising anode material^{177, 211, 212}. However, the large volume change (~300%) during lithium insertion/extraction may fracture the active silicon anodes and solid-electrolyte interface (SEI)¹⁹⁶, resulting in irreversible capacity fading^{32, 154, 169}. Recent electrochemical studies indicate that the issue of excessive volume expansion could be especially significant in crystalline Si (c-Si) anodes. Because experimental evidences have accumulated that the lithiation of c-Si advances by the movement of an atomically-sharp reaction front, which separates a pristine c-Si phase and an amorphous $\text{Li}_{3.75}\text{Si}$ phase, i.e., the lithiation of c-Si occurs through a two-phase reaction^{199-201, 213, 214}. A large change of Li concentration across the amorphous-crystalline phase boundary results in drastically volume mismatch, causing high stress and mechanical degradation. Moreover, in situ TEM studies have also revealed that lithiation of c-Si is highly anisotropic, with predominant volume expansion along $\langle 110 \rangle$ direction but negligibly small expansion along $\langle 111 \rangle$ direction. As a result, the fracture sites of c-Si anodes are preferentially located between neighboring 110 lateral planes^{169, 208, 215}. This intriguing fracture behavior is attributed to the intensified tensile hoop stress induced by the anisotropic volume expansion during lithiation of c-Si.

To mitigate the mechanical failure of c-Si anodes during two-phase lithiation, intensive

research efforts have been focused on developing nanostructured anodes including nanowires^{32, 180, 216}, nano-sized thin film¹⁸¹, nanoporous structures^{34, 182}, nano-particles^{185, 186} and nanowalls²¹⁷. In parallel, considerable efforts have been devoted to designing anodes with amorphous counterpart of c-Si, i.e., α -Si, which was thought to be lithiated via one-phase mechanism and thus has homogeneous volume expansion²¹⁸. Actually, lithiation mechanism of amorphous Si (a-Si) remained opaque until recent real-time visualization through TEM revealed the lithiation of α -Si occurs via a two-step mechanism^{218, 219}. In the first step, the lithiation advances by a two-phase mechanism with a migrating amorphous-amorphous interface between α -Si phase and $\text{Li}_{2.5}\text{Si}$ phase until the α -Si is fully consumed¹⁸³. This process is depicted by figures 6.6a-c. Then the second step of lithiation sets in without any visible interface, resulting in the final product of $\text{Li}_{3.75}\text{Si}$ with a total volume expansion of $\sim 280\%$, as shown in schematics 1c-d. This newly-reported two-step lithiation mechanism of α -Si is important because stress evolution, fracture behavior and lithiation kinetics are strongly affected by the lithiation mechanism¹⁹¹. For example, the critical size for fracture of anodes is reported to be larger for α -Si spheres than its c-Si counterparts, which suggests mitigated stress field during lithiation of α -Si²¹⁹. Theoretical analysis has been conducted to understand the basic underlying physics of two-stage lithiation²²⁰. However, the stress field evolution during lithiation of α -Si and the stress mitigation mechanism by the two-step lithiation still remains unclear to us.

In this work, the two-step lithiation and concurrent stress evolution in solid spherical α -Si anode are investigated via a chemo-mechanical finite element model and theoretical formulation. Recently, hollow nanostructured α -Si anodes are attracting more attentions since they have more free inner space to accommodate the large lithiation-induced volume expansion^{34, 162, 204-207}. Therefore, the influence of the hollow geometry on the stress field during two-step lithiation will also be studied here. Furthermore, compared with one-step (two-phase) lithiation, we show that the two-step lithiation mechanism intrinsically mitigates the lithiation-induced stress. How does the mitigated stress field affect fracture behavior and lithiation kinetics will also be discussed.

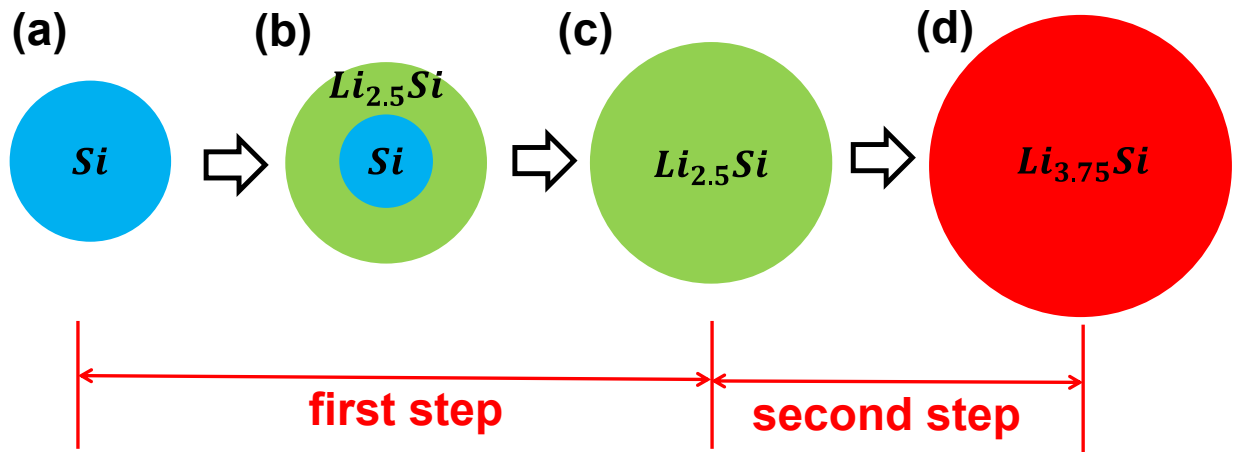


Figure 6.6. Schematic illustration of lithiation of Si NPs during the two-step lithiation. (a-c) In the first step of lithiation, the lithiation advances by a two-phase mechanism with a migrating amorphous-amorphous interface between α -Si phase and $Li_{2.5}Si$ phase. The interface exists until the α -Si phase is fully consumed, leading to a phase of $Li_{2.5}Si$. (c-d) In the second step of lithiation, the $Li_{2.5}Si$ phase is further lithiated to $Li_{3.75}Si$ phase without a visible interface.

6.2.2. FEM Model of Two-phase Lithiation

To study the stress evolution driven by the two-step lithiation of α -Si, the lithiated

amorphous Li_xSi phase is considered to be linear-elastic perfectly-plastic. The total strain rate $\dot{\epsilon}_{ij}$ of lithated silicon can be expressed as $\dot{\epsilon}_{ij} = \dot{\epsilon}_{ij}^l + \dot{\epsilon}_{ij}^e + \dot{\epsilon}_{ij}^p$. Here $\dot{\epsilon}_{ij}^l$ is the rate of the lithiation-induced volumetric strain; it is dilational and proportional to the rate of the normalized lithium concentration \dot{c} . $\dot{\epsilon}_{ij}^l = \beta \dot{c} \delta_{ij}$. Here, β is the lithiation-induced volume expansion coefficient which is analogous to thermal expansion coefficient and it is taken to be 0.6 to model the 300% volume change at full lithiation of α -Si²¹⁸. c represents the normalized lithium concentration of Li_xSi phase and is defined by $c = \frac{x}{3.75}$. δ_{ij} is the Kronecker delta. Moreover, $\dot{\epsilon}_{ij}^e$ and $\dot{\epsilon}_{ij}^p$ are the elastic strain rate and plastic strain rate. Specifically, $\dot{\epsilon}_{ij}^e = \frac{1}{E} [(1 + \nu)\dot{\sigma}_{ij} - \nu\dot{\sigma}_{kk}\delta_{ij}]$. E and ν denote the Young's Modulus and Poisson's ratio, respectively, and they are both assumed to linearly vary with normalized Li concentration c from 160 to 40 GPa and from 0.24 to 0.22¹⁷¹. The plastic strain rate $\dot{\epsilon}_{ij}^p$ is determined by classical flow rule and the yield strength is taken to be 1Gpa³⁹. The concurrent lithiation and lithiation-induced stress-strain field can be obtained by solving a boundary-value problem.

The abovementioned numerical scheme is employed to investigate the lithiation process of α -Si particle with lithium inserting through its outer surface. In order to mimic the migration of the amorphous-amorphous interface observed in the first step of lithiation, the α -Si particle is evenly divided into N (an integer) number of shells and those shells are sequentially lithiated from outer ones to inner ones. The lithiation of each shell is modeled by prescribing normalized concentration $c = 0.67$, which is specified by the

$Li_{2.5}Si$ phase. Experimental evidence on c-Si has accumulated that the reaction front is atomically sharp with thickness of ~ 1 nm. In our simulation on α -Si, the thickness of the amorphous-amorphous interface is determined by the thickness of each shell and it is set to be 2nm in our FEM modeling to make a compromise between numerical expense and simulation accuracy. In the second step of lithiation, the lithiation is considered to be one-phase with very gentle gradient of lithium concentration. In our simulation, for simplicity but without losing generality, the normalized lithium concentration c is assumed to be uniform inside the lithiated silicon particle and ramps from 0.67 to 1 during the second step of lithiation. The two-step lithiation is simulated using commercial FEM package ABAQUS 6.13.

6.2.3. Evolution of Stress Field during Two-phase Lithiation of α -Si Particle

a. Evolution of stress field in solid α -Si particle

We consider a pristine solid α -Si particle with outer radius B as the reference state. In the reference configuration, a material element of α -Si is identified by the radius R . At time t , after lithiation this material element is deformed and moved to a position with radius r in current configuration. Particularly, the outer radius of particle at time t is denoted by $b(B, t)$. The function $r(R, t)$ fully specifies the deformation field. In this work, the reference coordinate system R is used as an independent variable to describe the stress field during two-step lithiation.

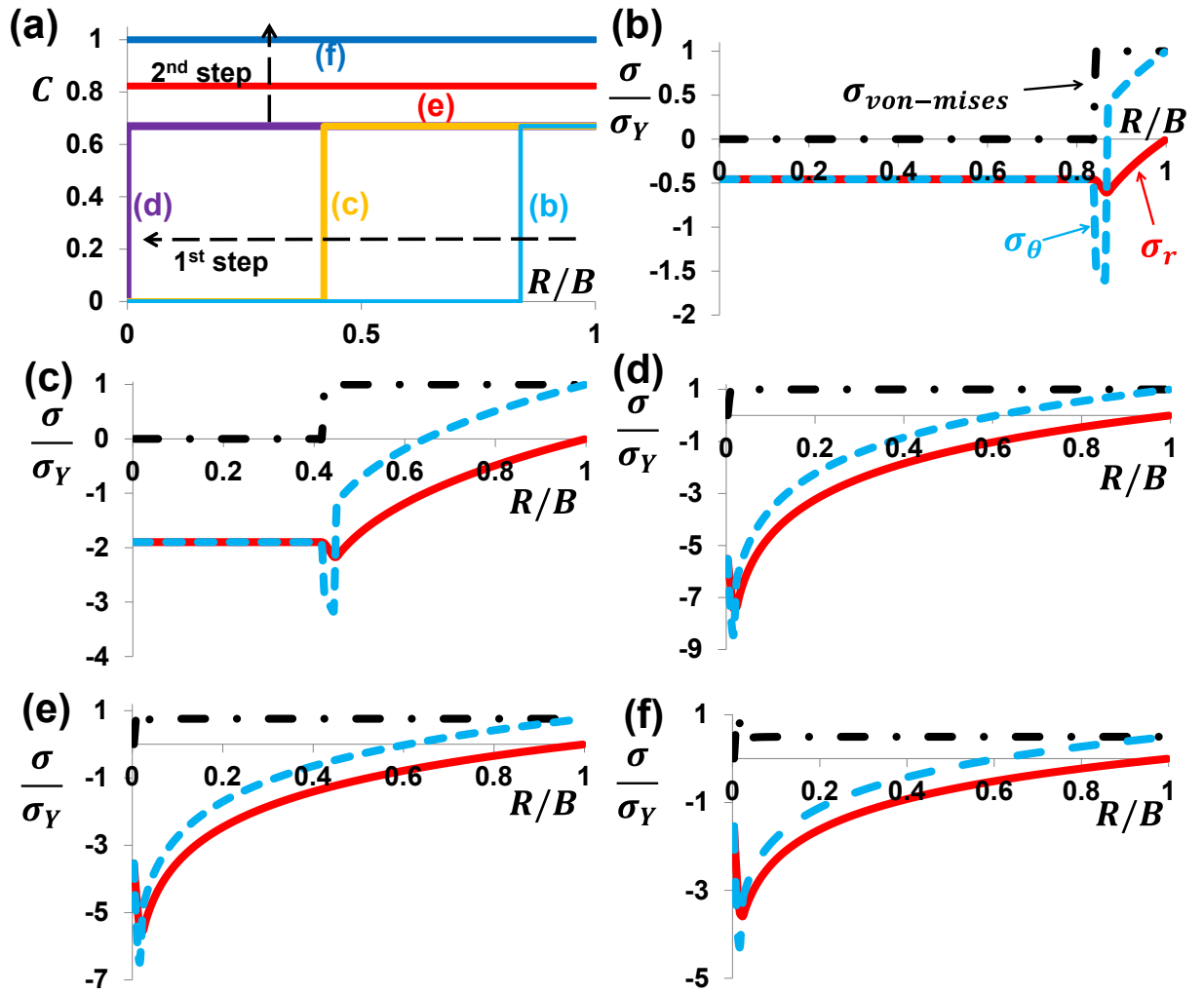


Figure 6.7. Stress evolution of α -Si particle during two-step lithiation. (a) Radial distribution of normalized lithium concentration C . The first step of lithiation advances via a two-phase mechanism, with an atomically sharp α -Si/ $\text{Li}_{2.5}\text{Si}$ interface propagating towards the center of the particle as indicated by the black arrow. In the second step of lithiation, the lithium concentration distribution within the particle is assumed to be uniform and ramps from 0.67 ($\text{Li}_{2.5}\text{Si}$) to 1 ($\text{Li}_{3.75}\text{Si}$). (b-d) stress ($\sigma_{\text{von-mises}}$, σ_r , σ_θ) distribution in the first step of lithiation. (d-f) stress distribution in the second step of lithiation.

Based on the simulation strategy, the stress distributions associated with evolving lithium concentration fields are evaluated. Figure 6.7b-f show the simulated results of stress distributions (with dot-dash line being Von-Mises stress, solid line radial stress and dash

line hoop stress) corresponding to the Li profiles in Fig. 6.7a. In the first step of lithiation as shown by figure 6.7b-d, the lithiation advances via the well-known two-phase mechanism. The amorphous-amorphous interface migrates towards the center of the anode particle, with normalized lithium concentration C changing suddenly from 0 to 0.67 across the interface. Within the interface, the core of α -Si is under hydrostatic compression. On the amorphous-amorphous interface, it is noted that highly compressive hoop stress σ_θ naturally arises owing to the geometrical constraint experienced by the material elements on the interface. In the outer $Li_{2.5}Si$ shell, the stress state is highly triaxial and inhomogeneous, causing Von-Mises stress readily reaching the yielding strength, i.e., $\sigma_{Von-Mises} = 0$. Due to the well-known “pushing-out” effect, $Li_{2.5}Si$ material elements undergo elastic unloading and the hoop stress σ_θ gradually becomes tensile in the shell and eventually reaches σ_Y at the external surface of the particle, i.e., $\sigma_\theta(B, t) = \sigma_Y$. The radial stress σ_r in the $Li_{2.5}Si$ shell is compressive, with $\sigma_r(B, t) = 0$ at the surface of the particle. The first step of lithiation ends up consuming all α -Si phase (figure 6.7d), leading to vanishing of the visible α -Si/ $Li_{2.5}Si$ interface.

Then, the second step of lithiation sets in, with uniformly-distributed Li concentration C gradually ramping from 0.67 ($Li_{2.5}Si$) to 1 ($Li_{3.75}Si$) as depicted in figure 6.7a. The most salient feature of the second step is the stress releasing experienced by the anodes particle, which is characterized by the dropping of Von-Mises stress below σ_Y . As a result, the hoop stress at the surface of the particle $\sigma_\theta(B, t)$ decreases from σ_Y (when $C = 0.67$,

figure 6.7d) to $0.76\sigma_Y$ (when $C = 0.83$, figure 6.7e) and finally to $0.49\sigma_Y$ (when $C = 1$, figure 6.7f). As widely reported, the tensile stress in the surface layer of particle could cause fracture during Li insertion. Therefore, the partial releasing of hoop stress at particle surface protects the anode particle from fracturing. The influence of two-step lithiation on the size-dependent fracture behavior of α -silicon particle will be discussed later.

To understand the origin of abovementioned stress releasing during second step of lithiaion, it is instructive to compare the two-step lithiation mechanism with another two hypothetical lithiation scenarios. Figure 6.8a summarizes the evolution of hoop stress $\sigma_\theta(B)$ as a function of state of charge (SOC) in an α -Si particle undergoing two-step lithiation. The black solid dots represent the numerical results from the FEM calculation. After lithiation starts, the first step advances by the two-phase mechanism. The lithiation front sweeps through the material elements on the particle surface (figure 6.8a(i)), creating a large dilational strain at the surface of the particle. Owing to the constraint from the inner unlithiated α -Si, local compressive stress develops at particle surface and readily reaches the yielding strength, i.e. $\sigma_\theta(B) = -\sigma_Y$. Due to the well-known “pushing-out” effect, as the amorphous-amorphous interface continues to move towards the center, the lithiation-induced swelling at the interface pushes out the material elements behind it. This action causes displacement of elements on surface in the outward radial direction and simultaneously stretches them in the hoop direction, leading to elastic

unloading, tensile elastic loading and finally plastic yielding of those elements. As a result, material elements at surface experience tensile hoop stress of σ_Y , i.e. $\sigma_\theta(B) = \sigma_Y$ as the interface moves inwards until the end of the first lithiation step ($SOC = 0.67$), corresponding to (ii) shown in figure 6.8a. After that, the second step of lithiation ($0.67 < SOC \leq 1$) sets in, causing an intriguing stress releasing mechanism: hoop stress $\sigma_\theta(B)$ linearly decreases from σ_Y to $0.49\sigma_Y$ at full lithiation ($SOC = 1$). Figure 6.8b shows the development of hoop stress $\sigma_\theta(B)$ in α -Si particles undergoing a hypothetical one-step two-phase lithiation mechanism which is similar to the first step of the two-step mechanism. As the lithiation starts, the material elements at particle surface experience compressive plastic yielding when lithiation front sweeps through the particle surface, followed by tensile plastic yielding when lithiation front further migrates towards the center. However, no stress releasing occurs in this case. The simulated color-contour plots, (ii) and (iii) in figure 6.8b, confirm that hoop stress at surface $\sigma_\theta(B)$ remains to be σ_Y till the fully charging state ($SOC = 1$). Comparison between figure 6.8(a) and 6.8(b) indicates that stress releasing is indeed due to the second step of lithiation of two-step mechanism. To test how two-step lithiation affects the stress distribution, we hypothetically assume the Young's Modulus of α -Si is insensitive to the Li concentration C and Young's Modulus is fixed to $160GPa$. The hoop stress profile is presented in figure 6.8(c). Material elements sequentially undergo compressive plastic yielding and tensile plastic yielding as illustrated by snapshots (i-iii). However, it is somewhat

unexpected to find that no stress releasing occurs in the anode particle even when the lithiation advances via two-step mechanism. This is in contrast to the case shown in figure 6.8(a), in which the stiffness of Li_xSi phase decreases with increasing Li concentration. Therefore, the direct comparison between figure 6.8(a) and 6.8(c) implies that the stiffness softening of α -Si anodes during lithiation plays a key role in the stress releasing phenomenon. A detailed explanation will be given through a theoretical formulation.

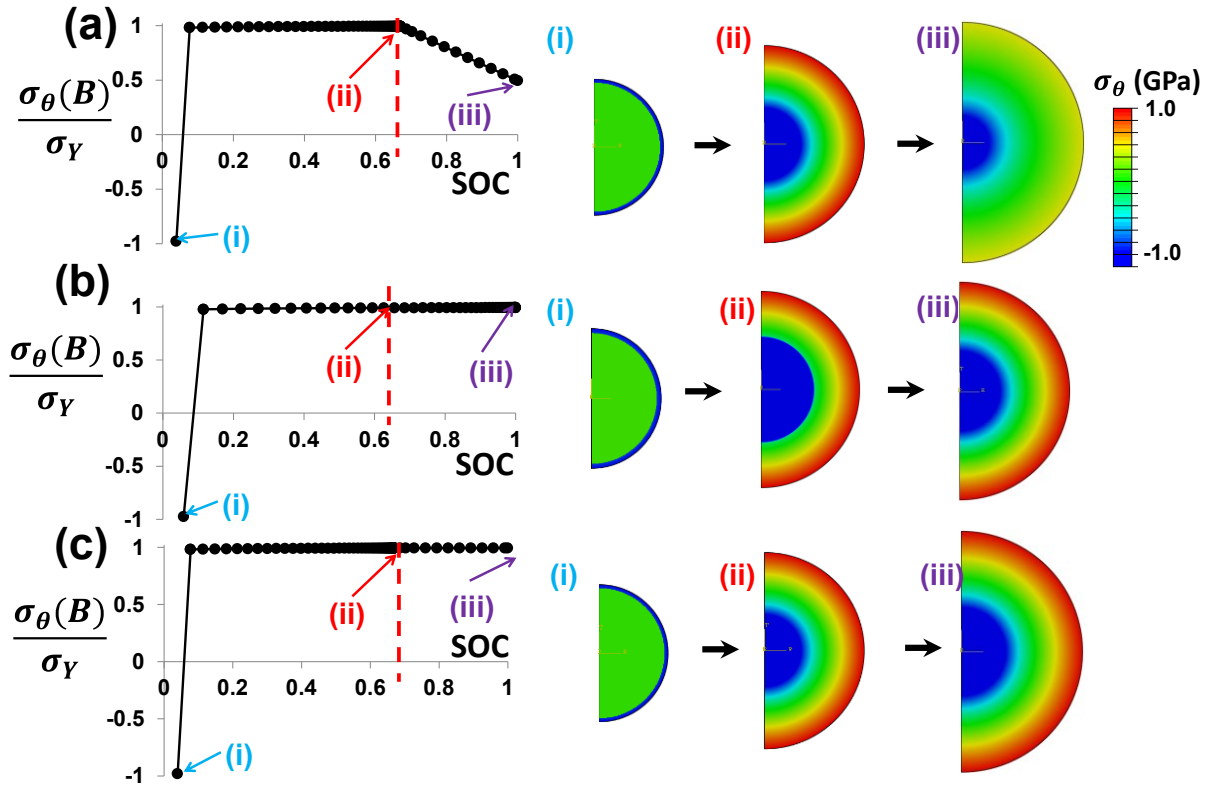


Figure 6.8. Evolution of hoop stress at the surface layer of the particle undergoing (a) two-step lithiation of α -Si. To understand the stress releasing occurring in the second step of lithiation, two control simulations with two hypothetical lithiation mechanisms are carried out: (b) one-step and two-phase lithiation; (c) two-step lithiation with concentration-independent stiffness of Li_xSi phase.

A theoretical model considering concurrent lithiation and plasticity has been established recently. According to the model, during two-phase lithiation, the radial stress and hoop stress on the reaction front are $\sigma_r = 2\sigma_Y \log\left(\frac{A}{b}\right)$, $\sigma_\theta = -\sigma_Y + 2\sigma_Y \log\left(\frac{A}{b}\right)$, with A being the position of amorphous-amorphous interface and b the current radius of the particle. At the beginning of the lithiation ($SoC \rightarrow 0$), the reaction front is right on the particle surface. By setting $A = b$, we obtain that

$$\sigma_\theta(B, 0) = -\sigma_Y \quad (6.27)$$

Subsequently, as the reaction front migrates towards the center of the particle, the material elements on the surface are pushed outward, being part of the $Li_{2.5}Si$ shell. The stress field within the lithiated shell is given by $\sigma_r = 2\sigma_Y \log\left(\frac{r}{b}\right)$, $\sigma_\theta = \sigma_Y + 2\sigma_Y \log\left(\frac{r}{b}\right)$. At the particle surface, $r = b$; therefore, hoop stress at the surface is calculated as

$$\sigma_\theta(B, SoC) = \sigma_Y, \quad (0 < SoC \leq 0.67) \quad (6.28)$$

In the second step of lithiation, owing to the uniform distribution of Li concentration C (figure 6.7a), the changing rate of the concentration \dot{C} is uniform inside the particle and thus the lithiation-induced volumetric strain rate ε_{ij}^l is also uniform. As a result, the anode particle swells homogeneously and thus freely in the second step of lithiation, without causing any further mechanical mismatch. Moreover, as aforementioned, the stiffness of Li_xSi linearly decreases from $79.6GPa$ to $40GPa$ as x increases from 2.5 to 3.75. This concentration-determined stiffness softening of Li/Si alloy as well as the

free volume expansion of anode particle leads to elastic unloading. Therefore, in the second step of lithiation ($0.67 < SOC \leq 1$) the whole anode particle behave elastically and thus the plastic strain rate $\dot{\varepsilon}_{ij}^p$ vanishes. It is also noted that the homogeneous volumetric strain rate naturally satisfies the strain compatibility and does not induce any elastic strain rate $\dot{\varepsilon}_{ij}^e$ in the second step, i.e. $\dot{\varepsilon}_{ij}^e = 0$ and $\varepsilon_{ij}^e(R, SOC) = \varepsilon_{ij}^e(R, 0.67)$ given $0.67 \leq SOC \leq 1$. The strain profile speculated above has been verified by the FEM results. According to linear elasticity, It is obtained that $\sigma_r(R, SOC) = \frac{E(Li_xSi)}{(1+\nu)(1-2\nu)} [(1-\nu)\varepsilon_r^e(R, 0.67) + 2\nu\varepsilon_\theta^e(R, 0.67)]$ and $\sigma_\theta(R, SOC) = \frac{E(Li_xSi)}{(1+\nu)(1-2\nu)} [\varepsilon_\theta^e(R, 0.67) + \nu\varepsilon_r^e(R, 0.67)]$. Here, we have $0.67 \leq SoC \leq 1$. As a result, considering the negligible change of Poission's ratio during lithiation and the fixed elastic strain fields, the hoop stress varies linearly with $E(Li_xSi)$ during the second step of lithiation. Therefore, the hoop stress at particle surface can be written as

$$\sigma_\theta(B, SOC) = \Omega(SOC) \sigma_\theta(B, 0.67), \quad (0.67 \leq SOC \leq 1) \quad (6.29)$$

where Ω is a linear dimensionless function of the stiffness of Li_xSi , defined as $\Omega(SOC) = \frac{(1-SOC)*E(Si)+SOC*E(Li_{3.75}Si)}{E(Li_{2.5}Si)}$. Therefore, based on equation (1-3), evolution of hoop stress at the particle surface is plotted in figure 6.9(a). Schematics (i-iv) are shown to illustrate the anode structure at several important snapshots. The theoretical prediction agrees with FEM results (figure 6.8a) remarkably well; only distinction is at the initial lithiation stage with $SOC < 0.1$. It is because the theoretical model neglects the elastic deformation of freshly lithiated phase right behind the reaction front, which causes the

sudden jump of $\sigma_\theta(B)$ from $-\sigma_Y$ to σ_Y when reaction front sweeps through the particle surface. Similarly, during the second step of lithiation, all stresses including components of hoop/radial stress and Von-Mises stress in the particle scale linearly with their counterparts at $SOC = 0.67$ via a scaling factor of $\Omega(SOC)$:

$$\sigma_r(R, SOC) = 2\sigma_Y \log\left(\frac{R}{B}\right) \Omega(SOC) \quad (6.30.1)$$

$$\sigma_\theta(R, SOC) = [\sigma_Y + 2\sigma_Y \log\left(\frac{R}{B}\right)] \Omega(SOC) \quad (6.30.2)$$

The stress field distributions with $SOC = 0.67$ and $SOC = 1$ are plotted in figure 6.9(b) and 6.9(c), respectively. Comparison between figure 6.9(b, c) and figure 6.8(d, f) indicates a great consistency of the stress distributions between the FEM simulation and theoretical formulation. The analytical formulation shown in this section provides a transparent mechanics foundation for a more direct understanding of stress fields associated with two-phase lithiation mechanism.

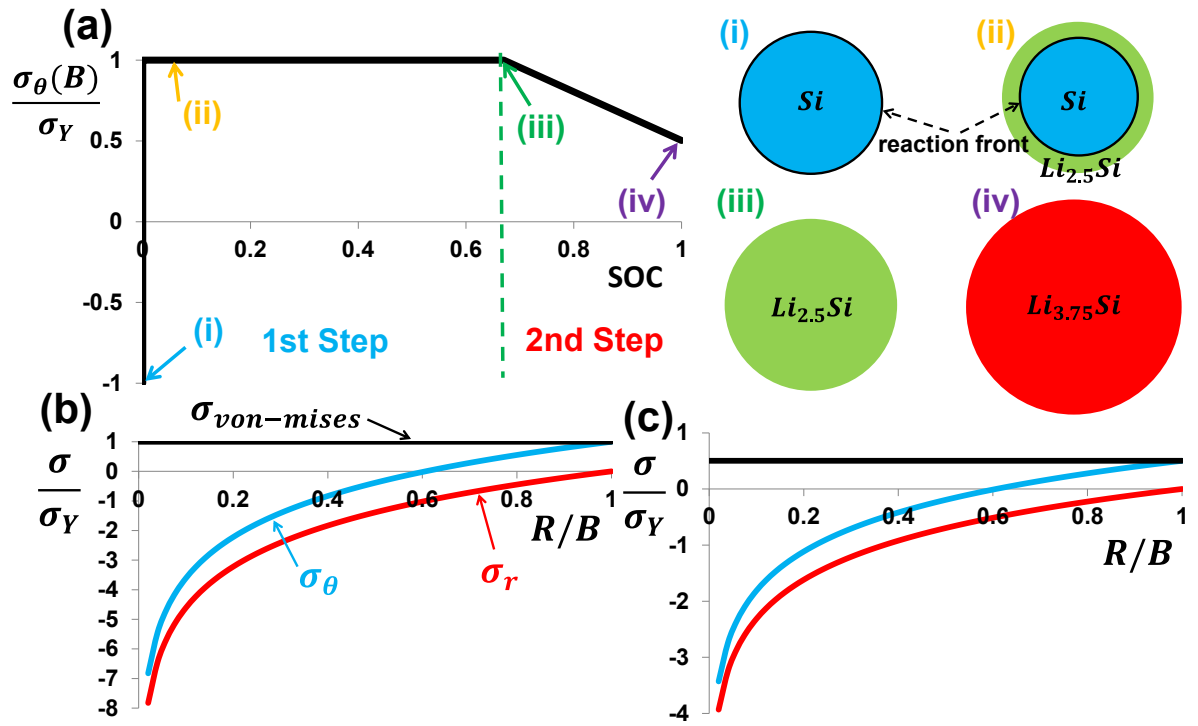


Figure 6.9. Theoretical results of an α -Si particle undergoing two-step lithiation. (a) Hoop stress evolution at the particle surface ($R = B$) as a function of state of charge (SOC). The plastic yielding during the first step and the linear decreasing of hoop stress owing to stiffness softening during the second step are captured by the theoretical model. Snapshots (i-iv) illustrate the lithiation state at various SOC. The Von-Mises stress, hoop stress and radial stress distribution in the whole particle are plotted at (b) the start of second step ($SOC = 0.67$) and (c) end of second step ($SOC = 1$)

b. Evolution of stress field in mechanical-supported hollow α -Si particle

Recently, hollow nanostructured silicon anodes are attracting more attentions because of their strong mechanical integrity and improved electric conductivity. Here, FEM-based chemo-mechanical simulations are carried out to understand the role of two-step lithiation mechanism on the mechanical response of hollow α -Si particle. We assume the hollow α -Si particle is deposited on an inner core (e.g. SiO_2) which acts as mechanical support (figure 6.10a). The hollow particle has inner radius R_I and outer radius R_o , therefore the

thickness of the hollow shell is given by $H = R_o - R_I$. We represent an element by its distance R from the center in the reference state. It is noted that the elastic stiffness of the inner core like SiO_2 is around 10 times that of the lithiated silicon. The deformation of rigid inner core is neglected. Because of the mechanical constraint imposed by the core, the inner surface of the α -Si hollow particle is constrained and cannot deform. Figure 6.10b shows the representative radial Li profiles. The corresponding stress distributions are shown in figure 6.10(c-d). Evidently, the $\text{Li}_{2.5}\text{Si}$ phase experiences plastic yielding and develops tensile hoop stress of magnitude σ_Y at the outer layer of the particle due to ‘push-out’ effect as the first-step lithiation proceeds (figure 6.10c and 6.10d). This agrees with the development of surface hoop tension in particles under one-step lithiation. However, once the reaction front hits the inner surface ($\frac{R-R_I}{H} = 0$), the second step of lithiation sets in. The inner rigid core confines the volume expansion along the outward radial direction and simultaneously compresses material elements in the particle in the hoop direction, causing elastic unloading in the outer part of the particle. As a result, the tensile hoop stress near the outer layer drops as the second-step of lithiation advances.

We plot the hoop stress evolution at the surface layer as a function of state of charge (SOC) in figure 6.11a. At $SOC = 0$, $\sigma_\theta(B)$ switches from $-\sigma_Y$ to σ_Y since the lithiation front sweeps through the particle surface. Then the surface layer remains under hoop tension σ_Y until $SOC = 0.67$, after that the hoop stress drops down as aforementioned to $0.17\sigma_Y$ at the end of lithiation. Snapshots from FEM simulation further confirm the evolution. Evidently, as shown in figure 6.11a, the hoop stress

decreases nonlinearly with state of charge at second step of lithiation. This is in contrast to the linear decrease observed in solid α -Si particle as shown in figure 6.8a. It is because that the stress releasing in this hollow anode particle is mainly attributed to the mechanical constraint from the inner rigid core, rather than the stiffness softening of lithiated silicon phase. As a comparison, assuming one-step two-phase lithiation mechanism, the hoop stress in the surface layer is plotted as a function of SOC in figure 6.11b. The curve as well as the stress contour (ii) and (iii) both reveal that hoop stress remains to be σ_Y till the end of lithiation, without stress releasing. This further shows that two-step lithiation mechanism helps to release tensile hoop stress at surface layer.

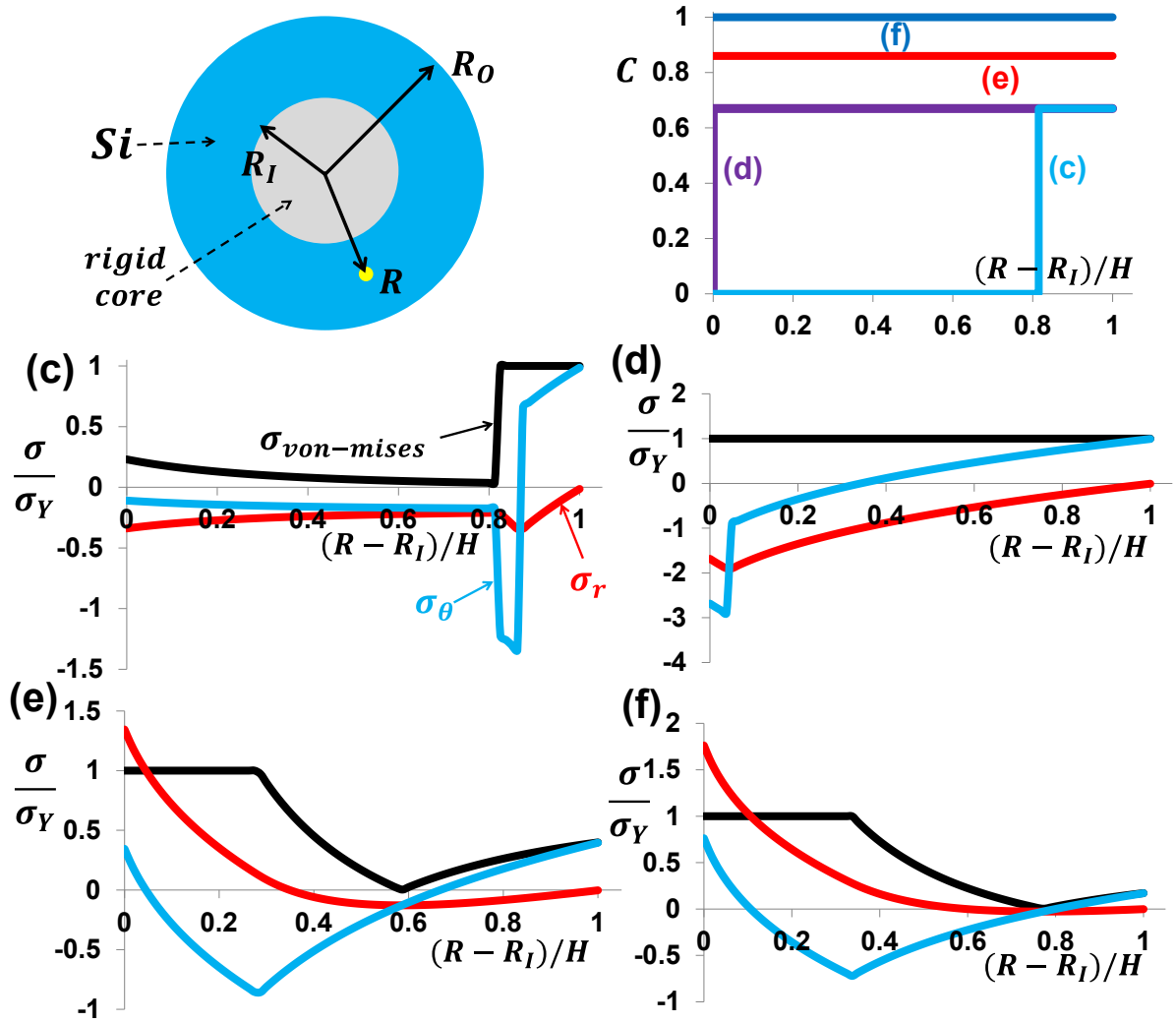


Figure 6.10. Stress evolution of hollow $\alpha\text{-Si}$ particle supported by inner rigid core during two-step lithiation. (a) Schematic of the hollow particle, with R_I being the inner radius, R_O the outer radius and R the distance from an element to the center. All dimension are defined in reference configuration (b) Representative Li profiles C along the radial direction are plotted as a function of $(R - R_I)/H$. (c-d) stress ($\sigma_{\text{von-mises}}$, σ_r , σ_θ) distribution in the first step of lithiation. (e-f) stress distribution in the second step of lithiation. Hoop stress is partially released because of the compression induced by the inner hard core.

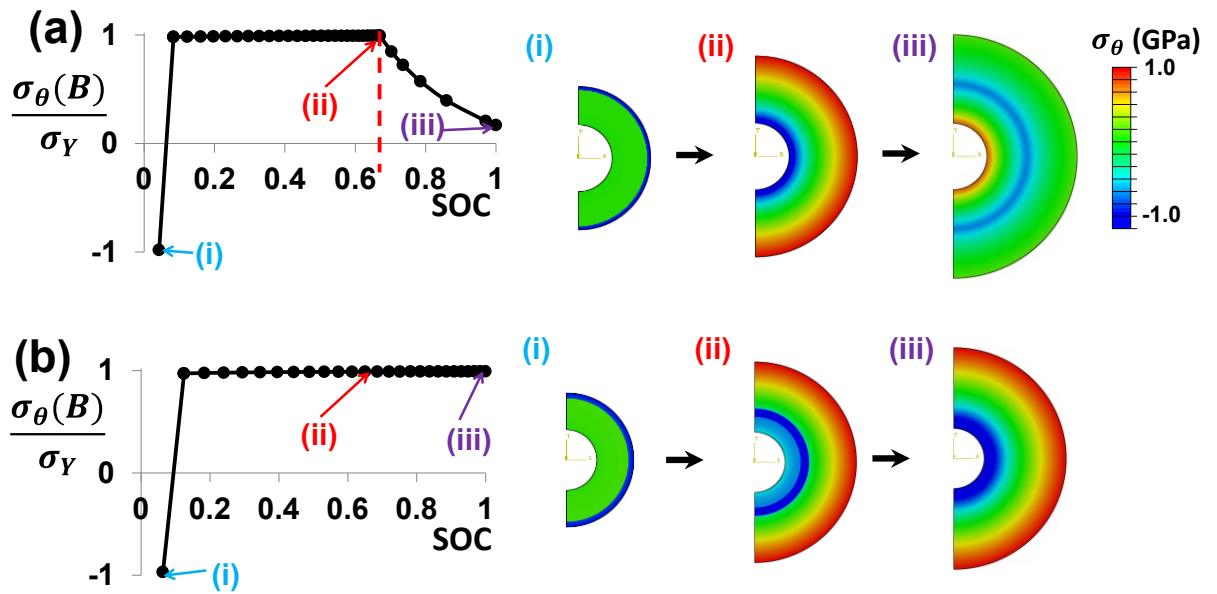


Figure 6.11. Evolution of hoop stress at the surface layer of the hollow α -Si particle undergoing (a) two-step lithiation and (b) one-step two-phase lithiation. Direct comparison reveals that second step of lithiation partially releases the high tensile stress at surface layer which is built up in the first step.

6.2.4. Effect of Two-step Mechanism on Lithiation Kinetics

Researches on lithiation kinetics have been performed on c-Si anodes. Experimental measurements of reaction velocity in solid c-silicon particles reveal that the reaction front slows down as it progresses into the solid particles¹⁹⁷. Existing theoretical studies show that lithiation-induced stress field could reversely affect the lithiation reaction²²¹. A theoretical model accounting for concurrent lithiation and plasticity was established recently¹⁹¹. Based on the model, the evolving stress field across the reaction front acts as an energy barrier and retards the velocity of the reaction front in c-Si. This stress-induced energy barrier is given as

$$\Delta G_{mech} = \frac{1}{x} [\sigma_{Si}^m \Omega_{Si} - \sigma_{Li_x Si}^m \Omega_{Li_x Si}] \quad (6.31)$$

where Ω^{Si} and $\Omega^{Li_x Si}$ represent volume of one Si atom and one $Li_x Si$ atom, respectively. And, σ_m^{Si} and $\sigma_m^{Li_x Si}$ denote the mean stress in remaining unlithiated silicon and the mean stress on the lithiation front, respectively. The definition of energy barrier implies that higher ΔG_{mech} causes slower migration of reaction front.

As aforementioned, recent experiments revealed that the lithiation of α -Si occurs via two-step mechanism and the first step of lithiation progresses by the migration of a sharp amorphous-amorphous interface, i.e., the reaction front. Interestingly, the lithiation reaction in α -Si is reported to be approximately constant and does not slow as much as in the crystalline case²¹⁹. Experimentalists attributed this to different stress evolution in α -Si during lithiation²¹⁹. However, no quantitative evidence existed to support this speculation before. Through FEM simulation, we calculated the stress fields in α -Si particle undergoing two-step lithiation. The stress profiles are plugged into (5) to evaluate the mechanical energy barrier due to stresses, where the mean stress is obtained by $\sigma_m = \frac{1}{3}(\sigma_r + 2\sigma_\theta)$ and x is 2.5 for $Li_{2.5}Si$ phase formed at reaction front. The FEM-based results are plotted as blue solid dots in figure 6.12(a) and (b) for solid and hollow α -Si particle, respectively. As comparison, mechanical energy barrier for c-Si particle under one-step two-phase lithiation is also shown in figure 6.12 (with red solid dots). Note that x is 3.75 in this case. For simplicity, we assume the lithiation of c-Si is also isotropic. In figure 6.12a, the horizontal axis is the normalized position of the

reaction front, with 1 representing reaction front at the particle surface and 0 denoting reaction front at the center. As expected, the energy barrier due to the stresses is positive and retards lithiation. The magnitude of the contribution increases as the unreacted core shrinks. It is important to note that the energy barrier ΔG_{mech} in α -Si (blue dots) is slightly lower than that in crystalline case (red dots), as shown in both figure 6.12a. The lithiation mechanism plays a key role here. $Li_{2.5}Si$ phase forms in the first step of lithiation and leads to $\sim 200\%$ volume expansion, i.e. $\Omega_{Li_{2.5}Si}/\Omega_{Si} = 3$. Compared to lithiation of c-Si with $\sim 300\%$ volume change due to formation of $Li_{3.75}Si$, the α -Si experiences less mechanical mismatch at lithiation front and thus lower energy barrier for migration of lithiation front. Theoretical shows that the mechanical energy barrier for lithiation is given by

$$\Delta G_{mech} = \frac{2\sigma_Y \Omega_{Si}}{x} \left[\left(\frac{\Omega_{Li_x Si}}{\Omega_{Si}} - 1 \right) \log \left(\frac{b}{A} \right) + \frac{\Omega_{Li_x Si}}{3\Omega_{Si}} \right] \quad (6.32)$$

where the current outer radius $b = \left(A^3 + \frac{\Omega_{Li_x Si}}{\Omega_{Si}} (B - A)^3 \right)^{\frac{1}{3}}$. x equals to 2.5 for α -Si lithiation and 3.75 for c-Si case. Note that $\Omega_{Li_{2.5}Si}/\Omega_{Si} = 3$ and $\Omega_{Li_{3.75}Si}/\Omega_{Si} = 4$. σ_Y is taken to be $1 GPa$ ³⁹ and $\Omega_{Si} = 2.9 \times 10^{-29} m^3$ ²²². The theoretical results are plotted in figure 6.12a as short dash lines and they agree with FEM results well. This further confirms that two-step lithiation of α -Si induces less energy barrier ΔG_{mech} than one-step lithiation of c-Si. From mechanics perspective, our calculation partially explains why the reaction front in α -Si does not slow as much as that in crystalline case. However,

the difference of lithiation kinetics between α -Si and c-Si may also be owing to electrochemistry, which is beyond the scope of this work.

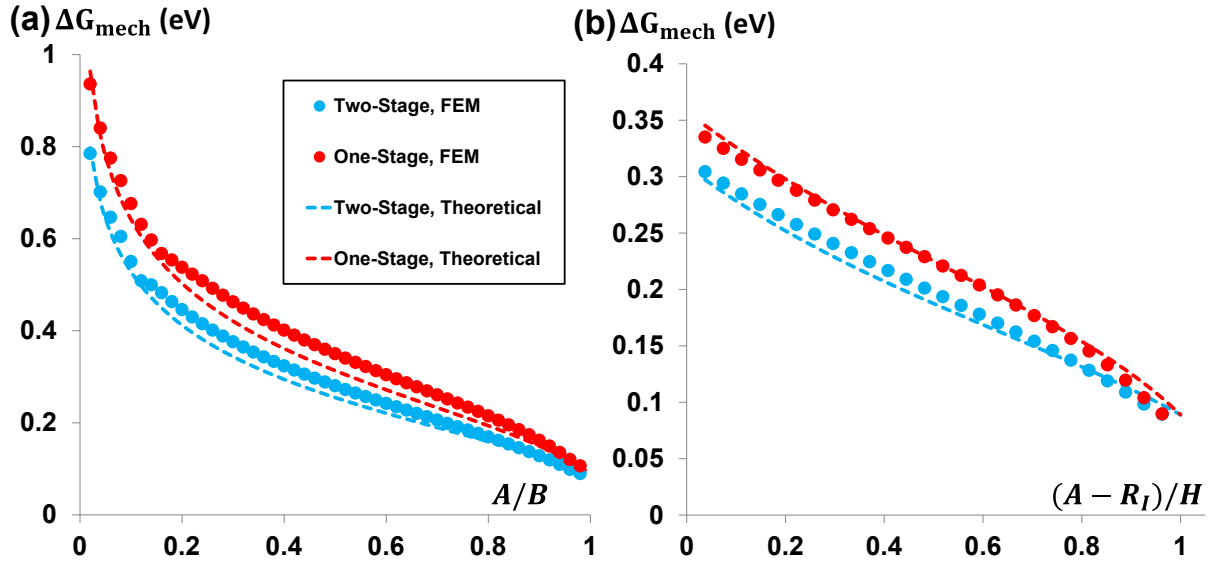


Figure 6.12. Stress-modulated energy barrier for migration of lithiation front is shown with various lithiation front position in (a) solid α -Si (blue dots) and c-Si (red dots) particles and (b) hollow ones. Theoretical results are also shown to benchmark the FEM calculations

Figure 6.12b shows ΔG_{mech} with different positions of lithiation front in hollow silicon particles (as illustrated in figure 6.9a). All conclusions about the comparison between solid α -Si and c-Si particle still hold in the hollow particle case. But it is worth nothing that the maximum ΔG_{mech} for completely lithiating a hollow α -Si particle is only about 0.3eV, less than half of that (~ 0.8 eV) for hollow c-Si particle. This suggests that hollow particles can be lithiated with lower energy expense from mechanis perspective and this might shed light on optimizing design of lithium-ion battery.

6.2.5 Reaction-induced fracture during two-phase lithiation of solid α -Si particle

We now study the reaction-induced fracture. The fracture of the α -Si particle is caused by the tensile hoop stress generated near the particle surface during the lithiation. As discussed above, in the second step of lithiation, the particle expands almost freely and the tensile hoop stress keeps decreasing because of the stiffness softening. Therefore, we assume the fracture of the particle mainly occurs in the first-step lithiation. Dimensional analysis dictates that the energy release rate during the first step should take the form $G = Z \frac{\sigma_Y^2}{E(Li_{2.5}Si)} b^{191}$, let Γ be the fracture energy of the particle. No preexisting flaws will advance if the maximum energy release rate is below the fracture energy. Thus, a critical particle size can be determined:

$$b_{cr} = \frac{E(Li_{2.5}Si)\Gamma}{Z\sigma_Y^2} \quad (6.33)$$

Under two-phase lithiation, it has been reported $Z \sim 0.91$ for a particle with a precrack of modest crack length¹⁹¹. Here, we just take $Z = 1$. Taking representative values: $\Gamma = 7J/m^2$ ²²³, $E(Li_{2.5}Si) = 79.6GPa$ and $\sigma_Y = 1GPa$ ³⁹. we find that the critical radius at the end of first-lithiation step is $b_{cr}^\alpha = 557.2nm$. The corresponding critical radius of the pristine α -silicon is thus $B_{cr}^\alpha = 386.3nm$, which agrees reasonably with the reported 435nm critical radius of amorphous silicon particle²¹⁹. Similarly, the critical radius of c-Si particle at full lithiation can be calculated by $b_{cr}^c = \frac{E(Li_{3.75}Si)\Gamma}{Z\sigma_Y^2} = 280nm$. The corresponding critical radius of pristine crystalline silicon particle is $B_{cr}^c = 176.4nm$. This estimation is much larger than the 75nm reported for c-Si particles in literature²¹⁹.

This might be due to we neglect the anisotropic lithiation nature of crystalline silicon particle.

In this section, it is demonstrated that the critical radius of pristine amorphous silicon particle B_{cr}^{α} is 386.3nm, larger than that of c-Si particle even if the anisotropic lithiation of c-Si is omitted. This suggests that the two-step lithiation mechanism of α -Si increases the critical fracture size of particles and explains the experimental observation quantitatively.

6.2.6 Summary

We have calculated the stress evolution in amorphous silicon particle undergoing two-step lithiation. The two-step lithiation causes important consequences for mechanical stress evolution during lithiation. It is demonstrated that the uniform distribution of Li during second step as well as the stiffness softening of lithiated silicon helps to release the tensile hoop stress at the surface layer of the particle. The results from FEM calculation have been verified by theoretical analysis for solid α -Si particle. We also show that the two-step lithiation mechanism plays an important role in the lithiation kinetics and fracture behavior of α -Si particle. Compared with crystalline silicon case, the movement of reaction front in α -Si particle experiences lower mechanical energy barrier; and the critical fracture size of α -Si is much higher, 386.3nm, which agrees reasonably with experimental observations.

Chapter 7. Mechanics on Tin Anodes in Sodium-Ion Batteries

7.1. Tin Anode for Sodium-Ion Batteries Using Natural Wood Fiber as a Mechanical Buffer and Electrolyte Reservoir⁵

7.1.1. Introduction

Grid scale storage is a crucial component of an energy landscape that incorporates a wide variety of renewable energy sources. Li-ion batteries and other electrochemical storage methods are considered among the most promising technologies for energy storage due to their high energy density and cyclability.²²⁴⁻²²⁶ Grid scale storage requires a low cost, safe, and environmentally benign battery system. Na is an earth abundant material and Na-ion batteries fulfill these requirements better than Li-ion batteries. Widespread implementation of Na-ion batteries is limited by several factors: (1) slow Na ion diffusion kinetics, (2) large volume changes and structural pulverization during charging/discharging, and (3) difficulty in maintaining a stable solid electrolyte interphase (SEI).⁴² These challenges are related to the large size of the Na ion (372% larger in volume than Li ion for a coordination number of four; $R_{Li}=59$ pm, $R_{Na}=99$ pm),²²⁷ which makes it impossible to simply adopt the recent knowledge and strategies developed for high performance Li-ion batteries. Several cathode materials and electrolyte systems have been studied for Na-ion batteries, including bi-layered $Na_2V_2O_5$,

⁵ *Experimental results shown in section 7.1 are obtained by Dr. Hongli Zhu and Prof. Liangbing Hu from Department of Materials Science Engineering, University of Maryland-College Park.*

$\text{P}_2\text{Na}_{0.66}\text{Fe}_{0.5}\text{Mn}_{0.5}\text{O}_2$, and fluorinated ethylene carbonate (FEC) as an electrolyte additive.^{48, 228-235} Anode materials that have been investigated include metal oxides and alloys, hard carbon, and nano-composites.^{231, 236, 237} Sn is a promising anode material because it alloys with Na at a high specific capacity of 847 mAh/g when $\text{Na}_{15}\text{Sn}_4$ is formed. Studies of Sn film and nanostructured anodes were reported; the cycle life, however, is limited to 20 cycles due to pulverization.^{55, 238, 239} The pulverization is primarily due to a 420% volume expansion associated with the formation of $\text{Na}_{15}\text{Sn}_4$.⁵⁷ Recently developed Sn nanoforests and SnO_2 @graphene nanocomposites improve cycling performance but lack the processability and cycling performance required for low cost grid scale storage.^{240, 241}

Wood naturally absorbs ions and water as part of the metabolism process. Specifically, this function is performed by wood fibers, or tracheids. The wood fibers are intrinsically soft, porous, and form into a multi-channel structure.²⁴² In this study, we develop a nature inspired low cost electrode consisting of an electrodeposited Sn film on conductive wood fiber. Conductivity is achieved by a solution-based coating of carbon nanotube (CNT) on the fiber surface. We find that the wood fiber increases the cyclability of Sn for Na-ion batteries by alleviating: 1) the capacity loss due to electrode pulverization, and 2) the poor rate performance as a result of slow ion diffusion kinetics. The stress reduction mechanism predicted by modeling the sodiation stresses throughout the Sn film on wood fiber agrees well with the experimental results. Control experiments with atomic layer deposition (ALD) confirm the role of the wood fiber as a mechanical buffer and

electrolyte reservoir for ion diffusion. The Sn anode described is ideal for grid scale storage. The materials used are earth abundant and environmentally friendly, and electrodeposition and conductive fiber substrates are scalable for large throughput manufacturing.

7.1.2. Fabrication of Tin-based Anodes and Chemo-electrical Performance of the Anodes

The hierarchical structure of wood fibers, spanning the macroscale to the nanoscale, is illustrated in Figure 7.1 (a). Wood fibers are tracheids; hollow, elongated cells that transport water and mineral salts. Pores in the fiber wall allow for intercellular fluid transportation. One tracheid is comprised of thousands of microfibrills, creating a multi-channel, mesoporous structure ideal for the absorption and transport of water and essential ions. Natural wood fibers with diameters on the order of 25 μm serve as the substrate for our Sn film. Compared to conventional rigid metallic substrates, the wood fiber is extremely soft. Initially, the fibers are coated with a thin layer (10 nm) of single walled carbon nanotubes (SWCNTs) to provide electrical conductivity. Various other conductive materials, including graphene, metal nanowires, and conductive polymers could be deposited on wood fibers with similar solution-based processes. Rich hydroxyl (-OH) groups on the cellulose surface provide strong hydrogen bonding between the fiber and conductive material. We predict that the soft substrate acts as a mechanical buffer during the sodiation/desodiation process. Figure 7.1 (b) illustrates how the wood fibers release the stresses experienced by the Sn electrode. The substrate deforms together with

the Sn film to release high stresses and prevent the delamination and pulverization characteristic of Sn anodes. Additionally, the wood fiber has a high capacity for electrolyte absorption. Liquid electrolytes penetrate the porous structure of the fiber, allowing for Na ion diffusion through the fiber cell walls in addition to diffusion at the Sn film surface, Figure 7.1 (c). This creates a dual ion transport path that effectively addresses the slow kinetics of Sn anodes for Na-ion batteries.

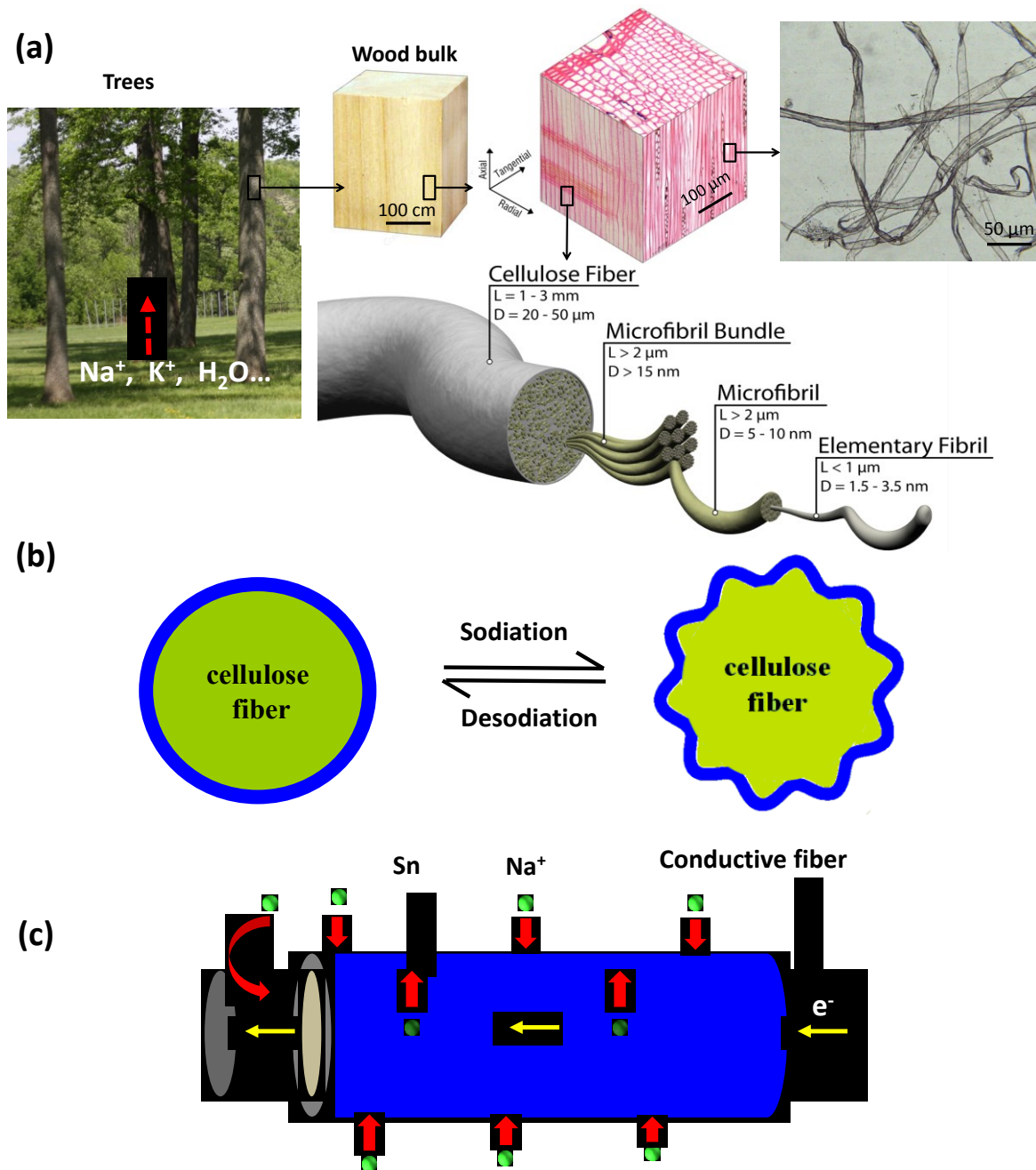


Figure 7.1. (a) Hierarchical structure of wood fiber. (b) Soft wood fiber substrates effectively release sodiation generated stresses by structural wrinkling. The thickness of Sn is 50 nm and the fiber diameter is $\sim 25 \mu\text{m}$. (c) Dual pathways for ion transport. The hierarchical and mesoporous structure of the fiber plays an important role as an electrolyte reservoir.

The effect of substrate stiffness on electrochemical performance is evaluated by comparing the cyclability of two Sn based electrodes; 50 nm Sn on wood fiber (Sn@WF)

and 50 nm Sn on Cu. The areal mass of the Sn@WF is ~ 4 times greater than that on Cu due to the three-dimensional structure of the wood fiber substrate. Each electrode is tested in a half-cell configuration with a Na metal counter electrode and 1M NaPF₆ in ethylene carbonate and diethyl carbonate (EC:DEC) electrolyte. Figure 7.2 (a) plots the voltage profiles for the Sn@WF electrode at the 1st, 2nd, 100th, and 400th cycle at a current density of 84 mA/g (C/10). Distinct plateaus at 0.18, 0.27, 0.54, and 0.75 V vs. Na/Na⁺ are observed, corresponding to the formation of Na₁₅Sn₄, Na₉Sn₄, NaSn, and NaSn₅, respectively.¹⁸ An initial discharge capacity of 339 mAh/g is achieved. After 400 cycles, the 0.18 and 0.54 V plateaus remain and the electrode maintains a capacity of 145 mAh/g. The mechanism for the loss of the other two plateaus is currently under investigation. Voltage plateaus at 0.18, 0.27, 0.54 and 0.75 V vs. Na/Na⁺ are initially observed with a capacity of 599 mAh/g. The capacity decreases to 97 mAh/g by the 10th cycle, and the voltage plateaus disappear after the 50th cycle. By the 100th cycle, the capacity decays to 22 mAh/g.

Figure 7.2 (b) plots the specific capacity vs. cycle number for Sn on three different substrates at a rate of C/10; natural wood fiber, Cu, and ALD Al₂O₃-coated wood fiber. The Sn@WF exhibits a lifetime of 400 cycles; among the longest cycling performance for Sn anodes in Na-ion batteries.^{55, 238} The capacity decayed during the cycling process, especially during the first few cycles. There are several potential explanations for this effect. Electrical contact between conductive fibers can be one possible reason. The

initial volume changes associated with sodiation rearrange the fibers in such a way as to reduce the contact resistance at the intersection of two fibers. The decay rate reduces after the first a few cycles. Another possible mechanism for the faster initial decay is Sn locally cracking in some places along Sn@WF electrode; however cracking to the extent of complete pulverization is prevented by the fiber wrinkling. The third possible mechanism for the capacity decay includes loss of electrical contact between individual fibers and at the fiber–coin cell case interface. As a comparison, the usable lifetime of the other two substrates is only 10 cycles. Sn deposited on a rigid Cu substrate cracks and delaminates after the sodiation/desodiation process as a result of a large volume expansion.

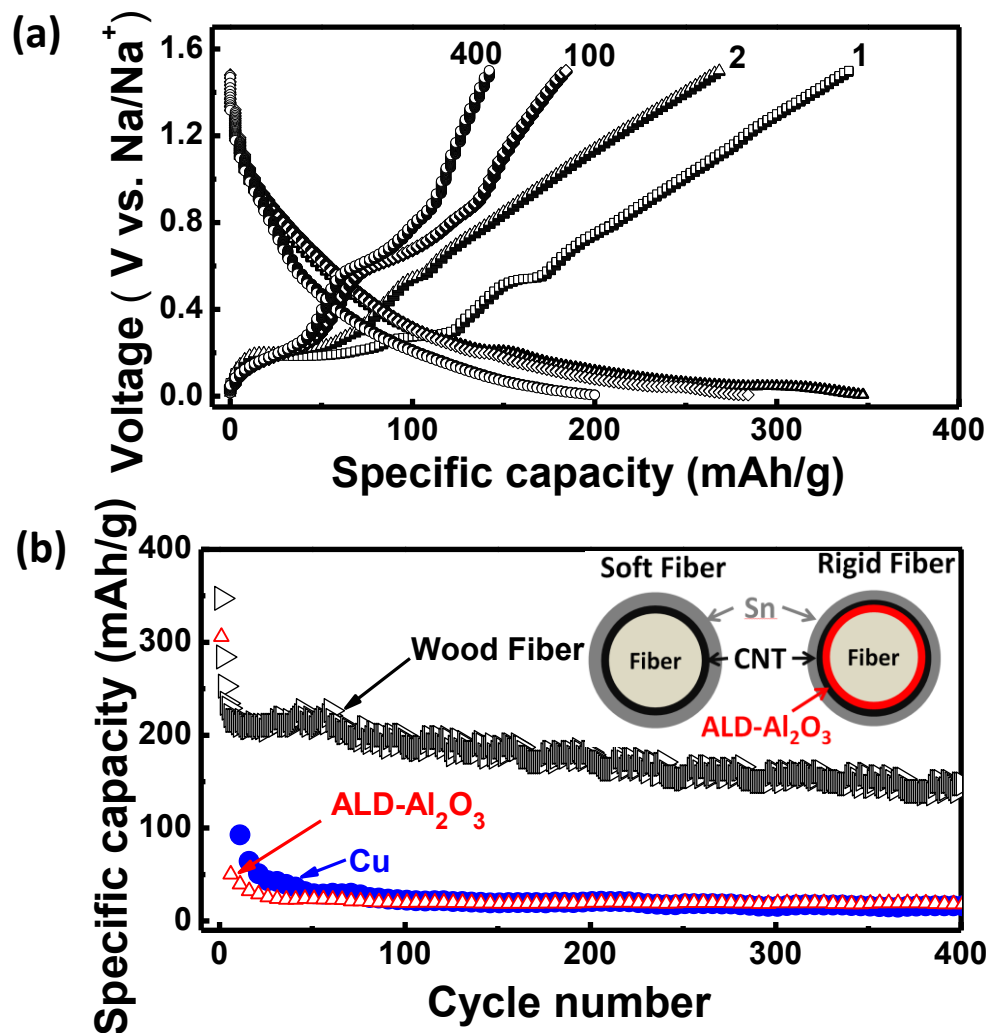


Figure 7.2. Electrochemical performance of the Sn anodes. (a) Galvanostatic charge/discharge voltage profiles of Sn@WF at the 1st, 2nd, 100th, and 400th cycle at a rate of C/10. (b) Cycling performance of Sn@WF, Al₂O₃ coated fiber, and Cu current collector at a rate of C/10. The inset illustrates the structure of the wood fiber and Al₂O₃ coated fiber.

We hypothesize that the dramatic increase in electrochemical performance is a result of the wood fiber acting as a mechanical buffer against sodiation induced stresses. It has been demonstrated that soft binders function as buffers to accommodate the mechanical stresses in batteries, effectively improving the device performance.^{226, 243} To prove this hypothesis, we intentionally introduce a stiff oxide layer between the wood fiber and

SWCNT layer, maintaining all other parameters. As illustrated in Figure 7.2 (b), a 50 nm layer of Al₂O₃ is deposited via ALD to prevent any deformation of the fiber by the Sn film. The cycling performance of this control sample is similar to that of the Sn on Cu electrode. Stiffness measures the ability of a material to resist deformation under an external force; in this case the stresses associated with the sodiation of Sn. The circumferential stiffness of wood fibers ranges from 0.7~3.0 GPa, and the stiffness of Cu and Al₂O₃ is 102 GPa and 375 GPa, respectively.^{244,245} The low stiffness of the wood fiber releases the stresses induced during the charge/discharge cycling.

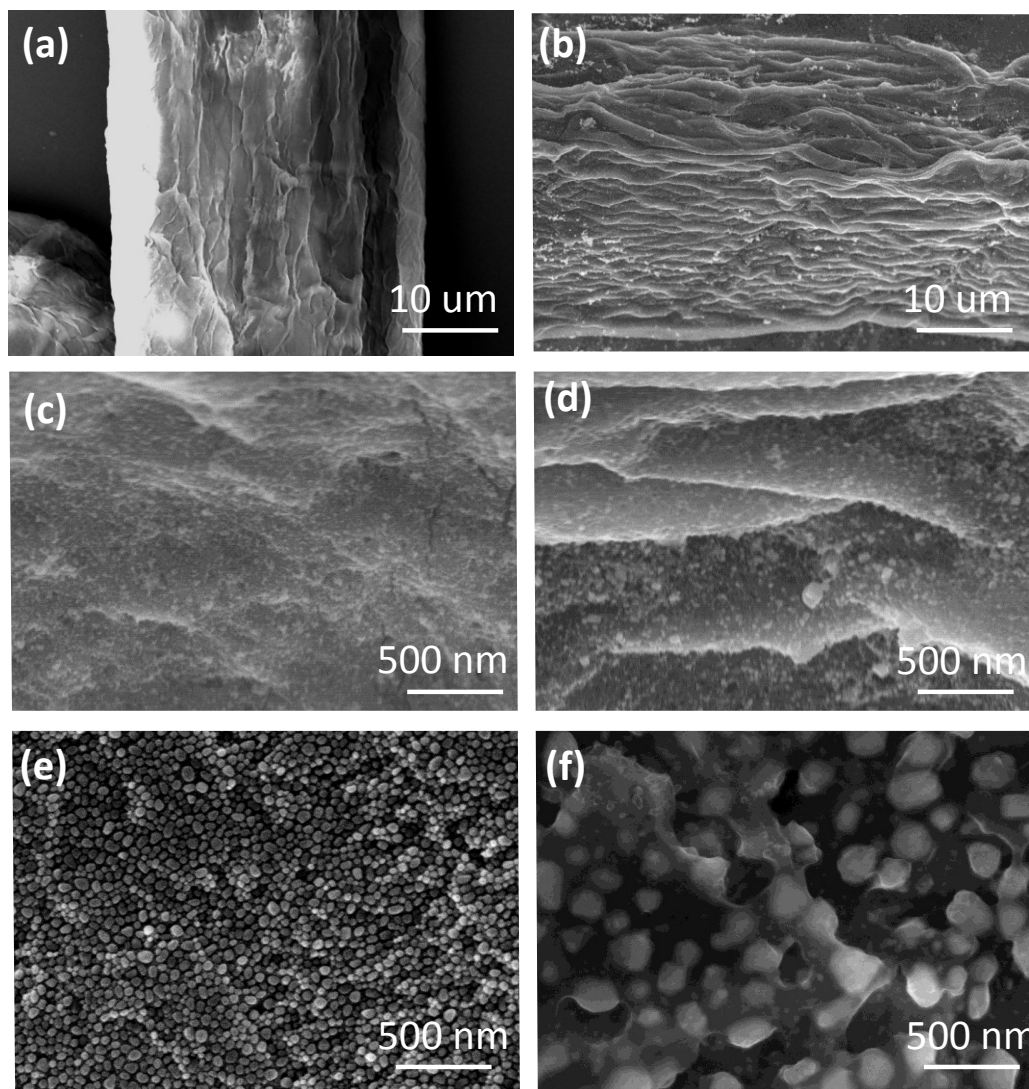


Figure 7.3. Sn@WF (a,c) before and (b,d) after 400 cycles at a rate of C/10. Sn on Cu current collector (e) before and (f) after 400 cycles. SEI formation and Sn volume expansion are clearly observed.

The morphology of the Sn@WF is characterized before and after galvanostatic cycling with a field emission scanning electronic microscope (FESEM). The cells were disassembled and washed in acetonitrile in the glove box, then vacuumed dried and transferred into SEM for characterization. Figures 7.3 (a) and (c) show that the electrodeposited Sn initially forms a continuous nanoparticle film on the conductive

wood fiber. The Sn nanoparticle thin film is in electrical contact with the SWCNTs that wrap the wood fibers. Typical sheet resistance of the conductive fiber current collector is ~ 30 Ohm/sq. After 400 cycles the cell is disassembled at the fully sodiated stage, washed with acetonitrile, and examined in the FESEM. The formation of a wrinkled structure on all wood fibers is observed in Figures 7.3 (b) and (d). The wrinkling is associated with fiber deformation, resulting in the improved cycling performance. As shown in Figure 7.3 (d), no significant SEI layer is observed on the Sn@WF, a dramatic difference to the thick SEI observed on the Sn on Cu sample, Figure 7.3 (f). The lack of continuous SEI growth confirms the unique phenomenon of the mechanical stress release by wrinkling formation. The wrinkling deformation of the Sn film reduces rupturing of the SEI and exposure of the Sn to the electrolyte. The morphology of the Sn surface does not change after cycling, indicating the robustness of the structure on the wood fiber. The wrinkled structure aligns parallel to the long fiber direction. A similar wrinkling effect has been observed in Si anodes on a PDMS (Polydimethylsiloxane) soft substrate for Li-ion batteries as a mean to effectively release stresses during cycling.²⁴⁶⁻²⁴⁸ The morphology of the Sn on Cu current collector before and after cycling is presented in Figures 7.3 (e) and (f). The Sn particles expand and agglomerate upon cycling, resulting in pulverization and delamination of the film. The Sn volume expansion ruptures the SEI layer, and continuous exposure of the Sn electrode to the electrolyte results in further electrolyte decomposition and an increase in SEI layer thickness, a critical mechanism for capacity

decay.²⁴⁹

7.1.3. Mechanics Modeling on Wrinkling-induced Stress Releasing in Cellulose-supported Tin Anodes

Continuum chemomechanical modeling is performed with ABAQUS to investigate the morphology evolution of the Sn@WF during galvanostatic charging and discharging at the C/10 rate. The modeling results clearly confirm our hypothesis that the wood fibers act as a mechanical buffer (Figure 7.4). As the system is charged, Na ions insert into the Sn and induce compressive stresses in the film. The compressive stress increases with the degree of sodiation. Given the large aspect ratio of the Sn film (50 nm over 10's of μm in circumferential length on wood fiber) and large Sn/wood fiber stiffness ratio, the initially smooth morphology of the thin Sn film becomes unstable and wrinkles when the compressive film stress is sufficiently high.

We define a normalized sodiation state (NSS), with NSS=0 being the pristine unsodiated state and NSS=1 the maximum sodiated state observed in the experiment. Simulations indicate that the Sn@WF begins to wrinkle at NSS=0.4, and wrinkling increases with further sodiation. At the fully sodiated state, the wrinkle morphology is characterized by a wavelength of ~ 450 nm and an amplitude of ~ 70 nm, in good agreement with the experimentally observed wrinkled surface features in Figure 7.3 (b). The morphology at both the fully sodiated and fully desodiated states for the first cycle was examined. Two

cells, one charged to 0.005 V vs. Na/Na⁺ and one charged to 0.005 V vs. Na/Na⁺ and then discharged to 1.5 V vs. Na/Na⁺, were disassembled in a glove box for examination at the fully sodiated and desodiated state, respectively. The sodiation-induced wrinkles are partially released after full desodiation. The mechanical modeling assumes an ideal initial Sn@WF structure with a perfectly cylindrical wood fiber and a smooth, uniformly thick Sn film. Real WFs have rough surface irregularities; we therefore do not expect a full release of the wrinkles in the Sn film to achieve a smooth surface morphology. By contrast, for a Sn film deposited on a stiff substrate (e.g., Al₂O₃ or Cu), film deformation is constrained to be rather uniform as any wrinkling deformation in the film would require distortion of the stiff substrate. As a result, Sn films on Al₂O₃ or Cu remain smooth during the sodiation process, and no wrinkling occurs. Wrinkling of the Sn@WF reduces sodiation induced deformations, effectively mitigating the associated stresses. Sn films supported by a stiff substrate must accommodate sodiation induced deformation via lattice distortion, resulting in a high film stress. Figure 7.4 (a) plot the Sn film morphology on the wood fiber and the contour of hoop stress $\sigma_{\theta\theta}$ (normal stress in the circumferential direction) in the Sn film at the fully sodiated and half sodiated states, respectively. Figure 7.4 (b) plots the hoop stress distribution through the fully sodiated Sn film thickness at three representative locations: the crest (A), midpoint (B) and trough (C) of the wrinkle. For comparison, the hoop stress distribution in a fully sodiated Sn film supported by a stiff substrate is plotted in Figure 7.4 (b). The majority of

sodiation-induced hoop stresses in the wrinkled Sn on wood fiber are significantly less than those in the smooth Sn film on a stiff substrate. The maximum hoop stress at location B is 1.7 times less than in the stiff substrate-supported Sn film.

Modeling results further reveal that wrinkling of the Sn film on a soft cellulose fiber during sodiation half-cycle not only mitigates the sodiation-induced compressive stress, but also plays a crucial role in reducing the tensile stress level in the Sn film during the desodiation half-cycle. It is this tensile stress that is the key driving force for Sn anode fracture during cycling. During discharging, Na ions are removed from the Sn@WF, smoothing out the wrinkling deformation. The Sn film recovers the rather smooth initial morphology after complete desodiation (Figure 7.4 (c)). Desodiation causes contraction of the Sn film; contraction that is constrained by the substrate. As a result, tensile hoop stresses accumulate in the Sn film during discharging. A high hoop stress could initiate and drive crack propagation through the Sn film, leading to the mechanical failure of the anode and capacity loss. In discharging the wrinkled Sn film from the fully sodiated state, smoothing of the wrinkled morphology partially accommodates the film contraction. Consequently, the resulting tensile stress after discharging is reduced. Stiff substrates (Al₂O₃ or Cu) also constrain the discharging-induced contraction in the Sn film. As shown in Figure 7.4 (c-d), the majority of tensile stresses of the Sn film supported by the wood fiber at full desodiation are effectively reduced. In comparison, high tensile stresses are apparent throughout the Sn film supported by a stiff substrate. In some locations on

the Sn film supported by the wood fiber (e.g., near the interface at A or near surface at C), the tensile stress is moderately higher than for the stiff substrate supported Sn film. The stresses are localized to an area half the thickness of the entire Sn film; the stresses in the other half of the film, however, are much less. This behavior is crucial to prevent crack propagation through the film. Cracks initiating from regions of high tensile stresses will not propagate through the entire Sn film due to an insufficient driving force in the low stress region. The overall structural integrity of the Sn film is preserved, ideal for high cycle performance. By contrast, the high tensile stresses in the Sn film supported by a stiff substrate are uniform through the entire film. Once cracks initiate, they will propagate through the film, pulverizing the Sn anode and reducing the active capacity and cycle performance.

The above chemomechanical modeling results reveal the following mechanistic understanding: a Sn@WF anode effectively releases the sodiation/desodiation-induced

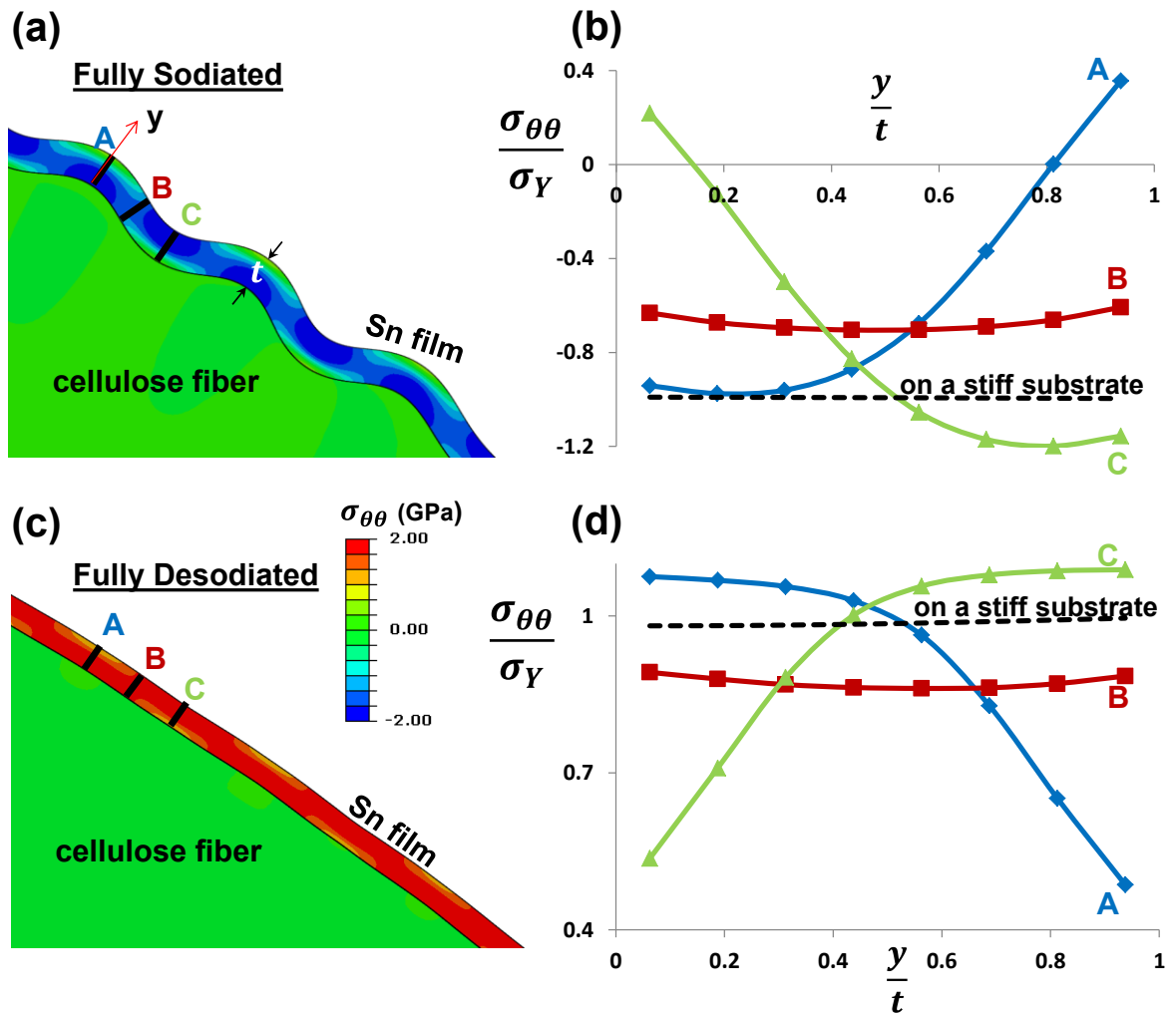


Figure 7.4. Chemomechanical modeling of the hoop stresses in Sn@WF at the fully sodiated (a) and desodiated (c) states. Color contours denote the hoop stress ($\sigma_{\theta\theta}$) level. The associated distributions of hoop stress normalized by yield stress versus location along film thickness are presented in (b) and (d). The hoop stress distributions for the Sn on a stiff substrate (Al_2O_3 or Cu) are denoted by the dashed line for comparison. The stress level comparison reveals that the wrinkling of Sn@WF effectively releases the sodiation/desodiation induced mechanical stresses.

stresses via a wrinkling deformation. In particular, the reduced tensile stress during discharging prevents pulverization of the Sn anode, resulting in the significantly enhanced cycling performance evident in Figure 7.2 (b). Chemomechanical simulations with four different initial Sn film thicknesses: $t_{\text{Sn}}=50$ nm, 100 nm, 150 nm, and 200 nm

are compared to investigate the effect of Sn mass loading on electrochemical performance. The maximum film thickness for theoretical modeling of Sn on the soft fiber is 200 nm. The stress mitigation effect of the soft wood fiber decreases as the thickness of the Sn film increases, largely due to the decreased wrinkle formation in the Sn film. These results suggest that a high mass loading may result in mechanical degradation and thus reduced electrochemical cycling performance of the Sn anode.

7.1.4. Summary

The key metrics for Na-ion batteries are low cost and material abundance, as opposed to high energy density for Li ion batteries. The target application for Na-ion batteries, therefore, is grid-scale energy storage. This removes some design constraints for materials and structures. The typical weight distribution ratio for electrode materials in batteries is as follows: active material to conductive additive to polymeric binder is 80:10:10, which provides for electrodes with high electronic conductivity, mechanical strength, and stability. Large volume changes and stresses occur in high-capacity electrode materials; a higher weight percentage of binder is therefore preferred to improve the cycling performance. These inactive materials increase the total weight and cost of the battery and introduce inhomogeneous constituents to the electrode. We utilize electrochemical deposition to prepare a binder free electrode consisting of a nanoparticle Sn thin film on a conductive wood fiber substrate/current collector. The active Sn maintains good electrical contact with the current collector, and the wood fibers provide a lightweight substrate

with excellent mechanical properties, large surface area, and a porous structure that provides effective ion and electron transport.

A mechanical wrinkling effect releases mechanical stresses associated with the large volume change. Both experimental results and chemomechanical modeling prove that the extremely soft wood fiber effectively releases the mechanical stress generated during the sodiation/desodiation process. The mechanical properties of wood fibers result in unprecedented cycling performance of Sn anodes for Na-ion batteries. The porosity of the wood fibers acts as an electrolyte reservoir, providing additional Na ion pathways to the Sn anode and improving the kinetics of Na ion transport. Blocking these pores greatly reduces electrochemical performance of these anodes. The abundance and large scale roll-to-roll processability of wood fibers make them an excellent candidate for energy storage applications where low costs are desired.

Chapter 8. Conclusions and Outlook

8.1. Summary and Concluding Remarks

This thesis studies the deformation mechanism, stress and mechanical failure of novel functional nanostructures in flexible electronics and high-performance lithium/sodium-ion batteries. We investigate both brittle fracture of ceramics active components and ductile failure of metal thin films in flexible electronics by FEM simulation and theoretical formulation. For novel anodes in high-performance batteries, we studied the swelling-induced deformation, stress generation and associated mechanical failure of the silicon/tin based anodes. We formulate a theory that couples lithiation reaction and concurrent deformation based on continuum theory. The developed theory is applied into nanowire silicon anodes to analyze the features of the stress field evolution and lithiation kinetics during charging/discharging cycle. In addition, We recognize that two-stage lithiation mechanism that happens in amorphous silicon helps release stresses and thus leads larger critical fracture size. Our theoretical and FEM result can well capture the intriguing experimental observation on amorphous silicon particle with $\sim 700\text{nm}$ critical diameter for fracture. Further, we study the deformation of cellulose-supported wood fiber by FEM simulation. Our simulation indicates wrinkling of the tin anodes during sodiation and desodiation helps releases elevated stress level. Here I briefly summarize the main conclusions in the previous chapters.

Research finding 1: Two failure mechanisms that are fatal for the barrier performance, namely, cracking of the top oxide layer and delamination along the oxide-organic interface, are shown to facilitate each other, and thus to co-evolve. The driving force for the oxide-organic delamination along the tensile direction and that for the oxide layer cracking and the concomitant oxide-organic delamination perpendicular to the tensile direction are quantitatively determined, from which an effective driving force for the oxide layer cracking is defined and shown to decrease as the oxide-organic interfacial adhesion increases. This suggests that a strong interlayer adhesion is crucial for the mechanical durability of the multilayer hybrid permeation barriers.

Research finding 2: Coherent study integrating *in situ* electro-mechanical experiments and mechanics modeling deciphers the failure mechanics of ITO thin films on polyimide substrates under tension. Our *in situ* tensile tests inside SEM reveal real time details of crack initiation and propagation, crack density evolution, and associated electrical resistance variations in thin ITO conductors on polyimide substrates. The corresponding mechanics model offers quantitative determination of critical mechanical properties (ITO cohesive toughness, fracture stress, and ITO/polyimide interfacial toughness) from the experimental data and explains the experimentally observed thickness dependence of crack density evolution in ITO conductors. While the understanding from the two dimensional model used in this paper sheds light on the governing failure mechanisms of the ITO/polymer structure (i.e., ITO channel cracking vs. ITO/polymer interfacial

delamination), further studies such as three dimensional modeling are necessary to capture the detailed interplay of these two governing failure mechanisms.

Research finding 3: Three buckling-driven failure modes in substrate-supported thin brittle films are specified, two of which eventually leads to film cracking and the third involves only buckling-driven delamination without film cracking. These three failure modes are mapped out in the parameter space of interfacial adhesion energy and initial interfacial defect size. As the substrate becomes more compliant, the failure modes leading to film cracking becomes more dominant against the delamination-only failure mode. Interestingly emerging from the results is that, a thin brittle film strongly bonded on a substrate is indeed more prone to buckling-driven cracking, a more detrimental failure mode for transparent ITO conductors widely used in displays and flexible electronics.

Research finding 4: A comprehensive investigation deciphers the quantitative correlation in two representative material structures, namely, a metal layer supported by a stiff plastic substrate, and a metal layer supported by a compliant elastomer substrate, respectively. The results dictate that a substrate can help to retard the necking band formation. In particular, it is shown that a metal layer supported by a sufficiently stiff and thick elastomer substrate is immune from necking instability. This study offers quantitative understanding of necking retardation in substrate-supported metal film under arbitrary biaxial loading.

Research finding 5: *f*-CNT@ α -Si beads-string heterostructures with chemically tailored carbon-silicon interface were synthesized based on a fundamental understanding of carbon surface chemistry and Si nucleation on covalently modified CNT surfaces. FEM studies suggest that the strong Si-C interface made possible by the carboxylic functional bands on CNTs plays key roles in enabling non-cracking *f*-CNT@ α -Si beads-string heterostructures.

Research finding 6: The stress and deformation field in the hollow silicon nanowire is fully specified once the position of the lithiation front and the boundary condition at the inner surface is known. The inward movement of the reaction front fully evolves the stress field. The contribution of mechanical stresses to the driving force for lithiation reaction $Li + \frac{1}{x}Si = \frac{1}{x}Li_xSi$ is calculated based on the stress field at the reaction front. It is shown that a hollow silicon nanowire is easier to be fully lithiated than its solid counterpart because the stress-related energy barrier is lower in hollow nanowire. It is demonstrated that a hollow nanowire with larger inner radius and traction-free inner surface possess lower stress-induced reaction barrier and thus is a promising anode design.

Research finding 7: The two-step lithiation causes important consequences for mechanical stress evolution during lithiation. It is demonstrated that the uniform distribution of Li during second step as well as the stiffness softening of lithiated silicon helps to release the tensile hoop stress at the surface layer of the particle. The results form

FEM calculation have been verified by theoretical analysis for solid α -Si particle. The two-step lithiation mechanism plays a important role in the lithiation kinetics and fracture behavior of α -Si particle. Compared with crystalline silicon case, the movement of reaction front in α -Si particle experiences lower mechanical energy barrier; and the critical fracture size of α -Si is much higher, 386.3nm, which agrees reasonably with experimental observations.

Research finding 8: A mechanical wrinkling effect releases mechanical stresses In cellulose-supported tin anodes. Both experimental results and chemomechanical modeling prove that the extremely soft wood fiber effectively releases the mechanical stress generated during the sodiation/desodiation process. The mechanical properties of wood fibers result in unprecedented cycling performance of Sn anodes for Na-ion batteries. The porosity of the wood fibers acts as an electrolyte reservoir, providing additional Na ion pathways to the Sn anode and improving the kinetics of Na ion transport. Blocking these pores greatly reduces electrochemical performance of these anodes. The abundance and large scale roll-to-roll processability of wood fibers make them an excellent candidate for energy storage applications where low costs are desired. Li-ion battery is an emerging filed that is full of challenges and opportunities.

8.2. Outlook and Future Work

A comprehensive understanding of the failure mechanism of novel functional

nanostructures is necessary for development of future stretchable electronics and high-performance batteries. In terms of basic research, flexible electronics provide excellent models to explore the large deformation and its influence on performance of electronics. High-performance lithium/sodium-ion batteries offers opportunity to investigate the interplay between mechanics and electrochemistry. Interdisciplinary research does not only help to improve the performance of Li-ion batteries, it also provides important insight into the coupling between mechanics and chemistry.

Beyond the work in this thesis, the following questions remain interesting to explore in future work.

1 Recent experimental evidence has accumulated that deformation of lithiated silicon is visco-plastic²⁵⁰. However, very little work attempts to consider the influence of viscoplasticity on stress generation and failure of silicon electrodes so far. The experimental measurement of viscoplastic properties of fully lithiated silicon has been done by experimentalists. From the theoretical perspective, we can develop a theory that incorporates viscoplasticity and the theory can help explore how stress generation is affected by the viscoplastic material nature; It would also be interesting to clarify explain why the performance of silicon anode is charging-rate dependent.

2 As discussed in Chapter 6, during lithiation process, the driving force of the lithiation reaction is $\Delta G = \Delta G_r - e\Phi + \frac{1}{x}(\sigma_m^{\text{Si}}\Omega^{\text{Si}} - \sigma_m^{\text{Li}_x\text{Si}}\Omega^{\text{Li}_x\text{Si}})$, which is affected strongly by the

stress distribution in across the lithiation front. Evidently, very little published work studied how the external loading affect the driving force. In our further researches, theory established in chapter 6 offers us effective tool to investigate the driving force of lithiation under various external loading conditions. The study will offer guidance on how to control the lithiation kinetics via external mechanics approach.

3 Recently, many existing experimental findings on sodium-ion battery emerges²⁵¹. Sodium is one of the most abundant elements on earth and thus makes sodium-ion battery a promising candidate for grid-scale energy storage. However, mechanics study on sodium-ion batteries are poorly reported. The knowledge we have of Li-ion batteries might be applied to study interesting behaviors of Na-ion batteries.

Bibliography

1. Forrest, S. R., The path to ubiquitous and low-cost organic electronic appliances on plastic. *Nature* 2004, 428, 911-918.
2. Reuss, R. H.; Chalamala, B. R.; Moussessian, A.; Kane, M. G.; Kumar, A.; Zhang, D. C.; Rogers, J. A.; Hatalis, M.; Temple, D.; Moddel, G.; Eliasson, B. J.; Estes, M. J.; Kunze, J.; Handy, E. S.; Harmon, E. S.; Salzman, D. B.; Woodall, J. M.; Alam, M. A.; Murthy, J. Y.; Jacobsen, S. C.; Olivier, M.; Markus, D.; Campbell, P. M.; Snow, E., Macroelectronics: Perspectives on technology and applications. *Proceedings of the Ieee* 2005, 93, 1239-1256.
3. Nathan, A.; Chalamala, B. R., Flexible electronics technology, part II: Materials and devices. *Proceedings of the Ieee* 2005, 93, 1391-1393.
4. Rogers, J. A.; Someya, T.; Huang, Y., Materials and Mechanics for Stretchable Electronics. *Science* 2010, 327, 1603-1607.
5. Beuth, J. L., CRACKING OF THIN BONDED FILMS IN RESIDUAL TENSION. *International Journal of Solids and Structures* 1992, 29, 1657-1675.
6. Hutchinson, J. W.; Suo, Z., MIXED-MODE CRACKING IN LAYERED MATERIALS. *Advances in Applied Mechanics, Vol 29* 1992, 29, 63-191.
7. Huang, R.; Prevost, J. H.; Huang, Z. Y.; Suo, Z., Channel-cracking of thin films with the extended finite element method. *Engineering Fracture Mechanics* 2003, 70, 2513-2526.
8. Vlassak, J. J., Channel cracking in thin films on substrates of finite thickness. *International Journal of Fracture* 2003, 119, 299-323.
9. Tsui, T. Y.; McKerrow, A. J.; Vlassak, J. J., Constraint effects on thin film channel cracking behavior. *Journal of Materials Research* 2005, 20, 2266-2273.
10. Ma, Q., A four-point bending technique for studying subcritical crack growth in thin films and at interfaces. *Journal of Materials Research* 1997, 12, 840-845.
11. Ho, S.; Suo, Z., TUNNELING CRACKS IN CONSTRAINED LAYERS. *Journal of Applied Mechanics-Transactions of the Asme* 1993, 60, 890-894.
12. Liu, X. H.; Lane, M. W.; Shaw, T. M.; Simonyi, E., Delamination in patterned films. *International Journal of Solids and Structures* 2007, 44, 1706-1718.
13. Cotterell, B.; Chen, Z., Buckling and cracking of thin films on compliant substrates under compression. *International Journal of Fracture* 2000, 104, 169-179.

14. Ambrico, J. M.; Begley, M. R., The role of initial flaw size, elastic compliance and plasticity in channel cracking of thin films. *Thin Solid Films* 2002, 419, 144-153.
15. Mei, H.; Pang, Y.; Huang, R., Influence of interfacial delamination on channel cracking of elastic thin films. *International Journal of Fracture* 2007, 148, 331-342.
16. Cordero, N.; Yoon, J.; Suo, Z., Channel cracks in a hermetic coating consisting of organic and inorganic layers. *Applied Physics Letters* 2007, 90.
17. Guo, Y.-G.; Hu, J.-S.; Wan, L.-J., Nanostructured materials for electrochemical energy conversion and storage devices. *Advanced Materials* 2008, 20, 2878-2887.
18. Peng, K.; Jie, J.; Zhang, W.; Lee, S.-T., Silicon nanowires for rechargeable lithium-ion battery anodes. *Applied Physics Letters* 2008, 93.
19. Green, M.; Fielder, E.; Scrosati, B.; Wachtler, M.; Serra Moreno, J., Structured silicon anodes for lithium battery applications. *Electrochemical and Solid State Letters* 2003, 6, A75-A79.
20. Gao, B.; Sinha, S.; Fleming, L.; Zhou, O., Alloy formation in nanostructured silicon. *Advanced Materials* 2001, 13, 816-+.
21. Baranchugov, V.; Markevich, E.; Pollak, E.; Salitra, G.; Aurbach, D., Amorphous silicon thin films as a high capacity anodes for Li-ion batteries in ionic liquid electrolytes. *Electrochemistry Communications* 2007, 9, 796-800.
22. Bang, B.; Kim, M. H.; Moon, H. S.; Lee, Y. K.; Park, J. W., Electrochemical properties of silicon deposited on patterned wafer. *Journal of Power Sources* 2006, 156, 604-609.
23. Limthongkul, P.; Jang, Y. I.; Dudney, N. J.; Chiang, Y. M., Electrochemically-driven solid-state amorphization in lithium-silicon alloys and implications for lithium storage. *Acta Materialia* 2003, 51, 1103-1113.
24. Netz, A.; Huggins, R. A.; Weppner, W., The formation and properties of amorphous silicon as negative electrode reactant in lithium systems. *Journal of Power Sources* 2003, 119, 95-100.
25. Maranchi, J. P.; Hepp, A. F.; Kumta, P. N., High capacity, reversible silicon thin-film anodes for lithium-ion batteries. *Electrochemical and Solid State Letters* 2003, 6, A198-A201.
26. Obrovac, M. N.; Krause, L. J., Reversible cycling of crystalline silicon powder. *Journal of the Electrochemical Society* 2007, 154, A103-A108.
27. Dong, H.; Ai, X. P.; Yang, H. X., Carbon/Ba-Fe-Si alloy composite as high capacity anode materials for Li-ion batteries. *Electrochemistry Communications* 2003, 5, 952-957.

28. Datta, M. K.; Kumta, P. N., Silicon and carbon based composite anodes for lithium ion batteries. *Journal of Power Sources* 2006, 158, 557-563.
29. Dong, H.; Feng, R. X.; Ai, X. P.; Cao, Y. L.; Yang, H. X., Structural and electrochemical characterization of Fe-Si/C composite anodes for Li-ion batteries synthesized by mechanical alloying. *Electrochimica Acta* 2004, 49, 5217-5222.
30. Doh, C. H.; Kalaiselvi, N.; Park, C. W.; Jin, B. S.; Moon, S. I.; Yun, M. S., Synthesis and electrochemical characterization of novel high capacity $\text{Si}_{3-x}\text{Fe}_x\text{N}_4$ anode for rechargeable lithium batteries. *Electrochemistry Communications* 2004, 6, 965-968.
31. Beaulieu, L. Y.; Hewitt, K. C.; Turner, R. L.; Bonakdarpour, A.; Abdo, A. A.; Christensen, L.; Eberman, K. W.; Krause, J. L.; Dahn, J. R., The electrochemical reaction of Li with amorphous Si-Sn alloys. *Journal of the Electrochemical Society* 2003, 150, A149-A156.
32. Chan, C. K.; Peng, H.; Liu, G.; McIlwrath, K.; Zhang, X. F.; Huggins, R. A.; Cui, Y., High-performance lithium battery anodes using silicon nanowires. *Nature Nanotechnology* 2008, 3, 31-35.
33. Cui, L.-F.; Ruffo, R.; Chan, C. K.; Peng, H.; Cui, Y., Crystalline-Amorphous Core-Shell Silicon Nanowires for High Capacity and High Current Battery Electrodes. *Nano Letters* 2009, 9, 491-495.
34. Kim, H.; Han, B.; Choo, J.; Cho, J., Three-Dimensional Porous Silicon Particles for Use in High-Performance Lithium Secondary Batteries. *Angewandte Chemie-International Edition* 2008, 47, 10151-10154.
35. Chen, X.; Gerasopoulos, K.; Guo, J.; Brown, A.; Wang, C.; Ghodssi, R.; Culver, J. N., Virus-Enabled Silicon Anode for Lithium-Ion Batteries. *Acs Nano* 2010, 4, 5366-5372.
36. Huggins, R. A.; Nix, W. D., Decrepitation Model For Capacity Loss During Cycling of Alloys in Rechargeable Electrochemical Systems. *Ionics* 2000, 6, 57-63.
37. Aifantis, K. E.; Hackney, S. A.; Dempsey, J. P., Design criteria for nanostructured Li-ion batteries. *Journal of Power Sources* 2007, 165, 874-879.
38. Bhandakkar, T. K.; Gao, H., Cohesive modeling of crack nucleation under diffusion induced stresses in a thin strip: Implications on the critical size for flaw tolerant battery electrodes. *International Journal of Solids and Structures* 2010, 47, 1424-1434.
39. Sethuraman, V. A.; Chon, M. J.; Shimshak, M.; Srinivasan, V.; Guduru, P. R., In situ measurements of stress evolution in silicon thin films during electrochemical lithiation and delithiation. *Journal of Power Sources* 2010, 195, 5062-5066.

40. Yang, Z.; Zhang, J.; Kintner-Meyer, M. C. W.; Lu, X.; Choi, D.; Lemmon, J. P.; Liu, J., Electrochemical Energy Storage for Green Grid. *Chemical Reviews* 2011, 111, 3577-3613.
41. Kovalenko, I.; Zdyrko, B.; Magasinski, A.; Hertzberg, B.; Milicev, Z.; Burtovyy, R.; Luzinov, I.; Yushin, G., A Major Constituent of Brown Algae for Use in High-Capacity Li-Ion Batteries. *Science* 2011, 334, 75-79.
42. Ong, S. P.; Chevrier, V. L.; Hautier, G.; Jain, A.; Moore, C.; Kim, S.; Ma, X.; Ceder, G., Voltage, stability and diffusion barrier differences between sodium-ion and lithium-ion intercalation materials. *Energy & Environmental Science* 2011, 4, 3680-3688.
43. Ponrouch, A.; Marchante, E.; Courty, M.; Tarascon, J.-M.; Rosa Palacin, M., In search of an optimized electrolyte for Na-ion batteries. *Energy & Environmental Science* 2012, 5, 8572-8583.
44. Komaba, S.; Ishikawa, T.; Yabuuchi, N.; Murata, W.; Ito, A.; Ohsawa, Y., Fluorinated Ethylene Carbonate as Electrolyte Additive for Rechargeable Na Batteries. *Acs Applied Materials & Interfaces* 2011, 3, 4165-4168.
45. Abouimrane, A.; Weng, W.; Eltayeb, H.; Cui, Y.; Niklas, J.; Poluektov, O.; Amine, K., Sodium insertion in carboxylate based materials and their application in 3.6 V full sodium cells. *Energy & Environmental Science* 2012, 5, 9632-9638.
46. Cao, Y.; Xiao, L.; Sushko, M. L.; Wang, W.; Schwenzer, B.; Xiao, J.; Nie, Z.; Saraf, L. V.; Yang, Z.; Liu, J., Sodium Ion Insertion in Hollow Carbon Nanowires for Battery Applications. *Nano Letters* 2012, 12, 3783-3787.
47. Kim, S.-W.; Seo, D.-H.; Ma, X.; Ceder, G.; Kang, K., Electrode Materials for Rechargeable Sodium-Ion Batteries: Potential Alternatives to Current Lithium-Ion Batteries. *Advanced Energy Materials* 2012, 2, 710-721.
48. Palomares, V.; Serras, P.; Villaluenga, I.; Hueso, K. B.; Carretero-Gonzalez, J.; Rojo, T., Na-ion batteries, recent advances and present challenges to become low cost energy storage systems. *Energy & Environmental Science* 2012, 5, 5884-5901.
49. Komaba, S.; Murata, W.; Ishikawa, T.; Yabuuchi, N.; Ozeki, T.; Nakayama, T.; Ogata, A.; Gotoh, K.; Fujiwara, K., Electrochemical Na Insertion and Solid Electrolyte Interphase for Hard-Carbon Electrodes and Application to Na-Ion Batteries. *Advanced Functional Materials* 2011, 21, 3859-3867.
50. Tepavcevic, S.; Xiong, H.; Stamenkovic, V. R.; Zuo, X.; Balasubramanian, M.; Prakapenka, V. B.; Johnson, C. S.; Rajh, T., Nanostructured Bilayered Vanadium Oxide Electrodes for Rechargeable Sodium-Ion Batteries. *Acs Nano* 2012, 6, 530-538.

51. Yabuuchi, N.; Kajiyama, M.; Iwatate, J.; Nishikawa, H.; Hitomi, S.; Okuyama, R.; Usui, R.; Yamada, Y.; Komaba, S., P2-type Na-x Fe_{1/2}Mn_{1/2} O-2 made from earth-abundant elements for rechargeable Na batteries. *Nature Materials* 2012, 11, 512-517.
52. Zhao, L.; Zhao, J.; Hu, Y.-S.; Li, H.; Zhou, Z.; Armand, M.; Chen, L., Disodium Terephthalate (Na₂C₈H₄O₄) as High Performance Anode Material for Low-Cost Room-Temperature Sodium-Ion Battery. *Advanced Energy Materials* 2012, 2, 962-965.
53. Park, Y.; Shin, D.-S.; Woo, S. H.; Choi, N. S.; Shin, K. H.; Oh, S. M.; Lee, K. T.; Hong, S. Y., Sodium Terephthalate as an Organic Anode Material for Sodium Ion Batteries. *Advanced Materials* 2012, 24, 3562-3567.
54. Xu, Y. H.; Zhu, Y. J.; Liu, Y. H.; Wang, C. S., Electrochemical Performance of Porous Carbon/Tin Composite Anodes for Sodium-Ion and Lithium-Ion Batteries. *Advanced Energy Materials* 2013, 3, 128-133.
55. Chevrier, V. L.; Ceder, G., Challenges for Na-ion Negative Electrodes. *Journal of the Electrochemical Society* 2011, 158, A1011-A1014.
56. Xiao, L.; Cao, Y.; Xiao, J.; Wang, W.; Kovarik, L.; Nie, Z.; Liu, J., High capacity, reversible alloying reactions in SnSb/C nanocomposites for Na-ion battery applications. *Chemical Communications* 2012, 48, 3321-3323.
57. Wang, J. W.; Liu, X. H.; Mao, S. X.; Huang, J. Y., Microstructural Evolution of Tin Nanoparticles during In Situ Sodium Insertion and Extraction. *Nano Letters* 2012, 12, 5897-5902.
58. Liu, Y.; Xu, Y.; Zhu, Y.; Culver, J. N.; Lundgren, C. A.; Xu, K.; Wang, C., Tin-Coated Viral Nanoforests as Sodium-Ion Battery Anodes. *Acs Nano* 2013, 7, 3627-3634.
59. Su, D.; Ahn, H.-J.; Wang, G., SnO₂@graphene nanocomposites as anode materials for Na-ion batteries with superior electrochemical performance. *Chemical Communications* 2013, 49, 3131-3133.
60. McElvain, J.; Antoniadis, H.; Hueschen, M. R.; Miller, J. N.; Roitman, D. M.; Sheats, J. R.; Moon, R. L., Formation and growth of black spots in organic light-emitting diodes. *Journal of Applied Physics* 1996, 80, 6002-6007.
61. Sutherland, D. G. J.; Carlisle, J. A.; Elliker, P.; Fox, G.; Hagler, T. W.; Jimenez, I.; Lee, H. W.; Pakbaz, K.; Terminello, L. J.; Williams, S. C.; Himpfel, F. J.; Shuh, D. K.; Tong, W. M.; Jia, J. J.; Callcott, T. A.; Ederer, D. L., Photo-oxidation of electroluminescent polymers studied by core-level photoabsorption spectroscopy. *Applied Physics Letters* 1996, 68, 2046-2048.

62. Liew, Y. F.; Aziz, H.; Hu, N. X.; Chan, H. S. O.; Xu, G.; Popovic, Z., Investigation of the sites of dark spots in organic light-emitting devices. *Applied Physics Letters* 2000, 77, 2650-2652.
63. Papadimitrakopoulos, F.; Zhang, X. M.; Higginson, K. A., Chemical and morphological stability of aluminum tris(8-hydroxyquinoline) (Alq(3)): Effects in light-emitting devices. *Ieee Journal of Selected Topics in Quantum Electronics* 1998, 4, 49-57.
64. Schaer, M.; Nuesch, F.; Berner, D.; Leo, W.; Zuppiroli, L., Water vapor and oxygen degradation mechanisms in organic light emitting diodes. *Advanced Functional Materials* 2001, 11, 116-121.
65. Lewis, J. S.; Weaver, M. S., Thin-film permeation-barrier technology for flexible organic light-emitting devices. *Ieee Journal of Selected Topics in Quantum Electronics* 2004, 10, 45-57.
66. Chwang, A. B.; Rothman, M. A.; Mao, S. Y.; Hewitt, R. H.; Weaver, M. S.; Silvernail, J. A.; Rajan, K.; Hack, M.; Brown, J. J.; Chu, X.; Moro, L.; Krajewski, T.; Rutherford, N., Thin film encapsulated flexible organic electroluminescent displays. *Applied Physics Letters* 2003, 83, 413-415.
67. Weaver, M. S.; Michalski, L. A.; Rajan, K.; Rothman, M. A.; Silvernail, J. A.; Brown, J. J.; Burrows, P. E.; Graff, G. L.; Gross, M. E.; Martin, P. M.; Hall, M.; Mast, E.; Bonham, C.; Bennett, W.; Zumhoff, M., Organic light-emitting devices with extended operating lifetimes on plastic substrates. *Applied Physics Letters* 2002, 81, 2929-2931.
68. Kim, T. W.; Yan, M.; Erlat, G.; McConnelee, P. A.; Pellow, M.; Deluca, J.; Feist, T. P.; Duggal, A. R.; Schaepkens, M., Transparent hybrid inorganic/organic barrier coatings for plastic organic light-emitting diode substrates. *Journal of Vacuum Science & Technology A* 2005, 23, 971-977.
69. Graff, G. L.; Williford, R. E.; Burrows, P. E., Mechanisms of vapor permeation through multilayer barrier films: Lag time versus equilibrium permeation. *Journal of Applied Physics* 2004, 96, 1840-1849.
70. Li, T.; Suo, Z., Ductility of thin metal films on polymer substrates modulated by interfacial adhesion. *International Journal of Solids and Structures* 2007, 44, 1696-1705.
71. Lu, N.; Wang, X.; Suo, Z.; Vlassak, J., Metal films on polymer substrates stretched beyond 50%. *Applied Physics Letters* 2007, 91.
72. Lu, N.; Wang, X.; Suo, Z.; Vlassak, J., Failure by simultaneous grain growth, strain localization, and interface debonding in metal films on polymer substrates. *Journal of Materials Research* 2009, 24, 379-385.

73. Lacour, S. P.; Jones, J.; Wagner, S.; Li, T.; Suo, Z. G., Stretchable interconnects for elastic electronic surfaces. *Proceedings of the Ieee* 2005, 93, 1459-1467.
74. Lipomi, D. J.; Bao, Z., Stretchable, elastic materials and devices for solar energy conversion. *Energy & Environmental Science* 2011, 4, 3314-3328.
75. Jia, Z.; Tucker, M. B.; Li, T., Failure mechanics of organic-inorganic multilayer permeation barriers in flexible electronics. *Composites Science and Technology* 2011, 71, 365-372.
76. Wagner, S.; Lacour, S. P.; Jones, J.; Hsu, P. H. I.; Sturm, J. C.; Li, T.; Suo, Z. G., Electronic skin: architecture and components. *Physica E-Low-Dimensional Systems & Nanostructures* 2004, 25, 326-334.
77. Someya, T.; Sekitani, T.; Iba, S.; Kato, Y.; Kawaguchi, H.; Sakurai, T., A large-area, flexible pressure sensor matrix with organic field-effect transistors for artificial skin applications. *Proceedings of the National Academy of Sciences of the United States of America* 2004, 101, 9966-9970.
78. Begley, M. R.; Scott, O. N.; Utz, M.; Bart-Smith, H., Fracture of nanoscale copper films on elastomer substrates. *Applied Physics Letters* 2009, 95.
79. Li, T.; Huang, Z. Y.; Suo, Z.; Lacour, S. P.; Wagner, S., Stretchability of thin metal films on elastomer substrates. *Applied Physics Letters* 2004, 85, 3435-3437.
80. Li, T.; Huang, Z. Y.; Xi, Z. C.; Lacour, S. P.; Wagner, S.; Suo, Z., Delocalizing strain in a thin metal film on a polymer substrate. *Mechanics of Materials* 2005, 37, 261-273.
81. Zhang, Z.; Li, T., Effects of grain boundary adhesion and grain size on ductility of thin metal films on polymer substrates. *Scripta Materialia* 2008, 59, 862-865.
82. Rochat, G.; Leterrier, Y.; Fayet, P.; Manson, J. A. E., Mechanical analysis of ultrathin oxide coatings on polymer substrates in situ in a scanning electron microscope. *Thin Solid Films* 2003, 437, 204-210.
83. Leterrier, Y.; Medico, L.; Demarco, F.; Manson, J. A. E.; Betz, U.; Escola, M. F.; Olsson, M. K.; Atamny, F., Mechanical integrity of transparent conductive oxide films for flexible polymer-based displays. *Thin Solid Films* 2004, 460, 156-166.
84. Jansson, N. E.; Leterrier, Y.; Medico, L.; Manson, J. A. E., Calculation of adhesive and cohesive fracture toughness of a thin brittle coating on a polymer substrate. *Thin Solid Films* 2006, 515, 2097-2105.
85. Cairns, D. R.; Witte, R. P.; Sparacin, D. K.; Sachsman, S. M.; Paine, D. C.; Crawford, G. P.; Newton, R. R., Strain-dependent electrical resistance of tin-doped indium oxide on polymer substrates. *Applied Physics Letters* 2000, 76, 1425-1427.

86. Sierros, K. A.; Morris, N. J.; Ramji, K.; Cairns, D. R., Stress-corrosion cracking of indium tin oxide coated polyethylene terephthalate for flexible optoelectronic devices. *Thin Solid Films* 2009, 517, 2590-2595.
87. Jansson, N. E.; Leterrier, Y.; Manson, J. A. E., Modeling of multiple cracking and decohesion of a thin film on a polymer substrate. *Engineering Fracture Mechanics* 2006, 73, 2614-2626.
88. Leterrier, Y., Durability of nanosized oxygen-barrier coatings on polymers - Internal stresses. *Progress in Materials Science* 2003, 48, 1-55.
89. Nix, W. D., MECHANICAL-PROPERTIES OF THIN-FILMS. *Metallurgical Transactions a-Physical Metallurgy and Materials Science* 1989, 20, 2217-2245.
90. Peng, C.; Jia, Z.; Bianculli, D.; Li, T.; Lou, J., In situ electro-mechanical experiments and mechanics modeling of tensile cracking in indium tin oxide thin films on polyimide substrates. *Journal of Applied Physics* 2011, 109.
91. Bowden, N.; Brittain, S.; Evans, A. G.; Hutchinson, J. W.; Whitesides, G. M., Spontaneous formation of ordered structures in thin films of metals supported on an elastomeric polymer. *Nature* 1998, 393, 146-149.
92. Huang, Z. Y.; Hong, W.; Suo, Z., Nonlinear analyses of wrinkles in a film bonded to a compliant substrate. *Journal of the Mechanics and Physics of Solids* 2005, 53, 2101-2118.
93. Huang, R., Kinetic wrinkling of an elastic film on a viscoelastic substrate. *Journal of the Mechanics and Physics of Solids* 2005, 53, 63-89.
94. Khang, D. Y.; Jiang, H. Q.; Huang, Y.; Rogers, J. A., A stretchable form of single-crystal silicon for high-performance electronics on rubber substrates. *Science* 2006, 311, 208-212.
95. Hutchinson, J. W.; Thouless, M. D.; Liniger, E. G., GROWTH AND CONFIGURATIONAL STABILITY OF CIRCULAR, BUCKLING-DRIVEN FILM DELAMINATIONS. *Acta Metallurgica Et Materialia* 1992, 40, 295-308.
96. Thouless, M. D.; Hutchinson, J. W.; Liniger, E. G., PLANE-STRAIN, BUCKLING-DRIVEN DELAMINATION OF THIN-FILMS - MODEL EXPERIMENTS AND MODE-II FRACTURE. *Acta Metallurgica Et Materialia* 1992, 40, 2639-2649.
97. Yu, H. H.; He, M. Y.; Hutchinson, J. W., Edge effects in thin film delamination. *Acta Materialia* 2001, 49, 93-107.
98. Yu, H. H.; Hutchinson, J. W., Influence of substrate compliance on buckling delamination of thin films. *International Journal of Fracture* 2002, 113, 39-55.

99. Cordill, M. J.; Bahr, D. F.; Moody, N. R.; Gerberich, W. W., Adhesion measurements using telephone cord buckles. *Materials Science and Engineering a-Structural Materials Properties Microstructure and Processing* 2007, 443, 150-155.
100. Mei, H.; Huang, R.; Chung, J. Y.; Stafford, C. M.; Yu, H.-H., Buckling modes of elastic thin films on elastic substrates. *Applied Physics Letters* 2007, 90.
101. Thouless, M. D., COMBINED BUCKLING AND CRACKING OF FILMS. *Journal of the American Ceramic Society* 1993, 76, 2936-2938.
102. Faulhaber, S.; Mercer, C.; Moon, M. W.; Hutchinson, J. W.; Evans, A. G., Buckling delamination in compressed multilayers on curved substrates with accompanying ridge cracks. *Journal of the Mechanics and Physics of Solids* 2006, 54, 1004-1028.
103. Wagner, S.; Lacour, S.; Jones, J.; Hsu, P.; Sturm, J.; Li, T.; Suo, Z., Electronic skin: architecture and components. *Physica E - Low-Dimensional Systems & Nanostructures* 2004, 25, 326-334.
104. Li, T.; Huang, Z.; Suo, Z.; Lacour, S.; Wagner, S., Stretchability of thin metal films on elastomer substrates. *Applied Physics Letters* 2004, 85, 3435-3437.
105. Lacour, S. P.; Jones, J.; Wagner, S.; Li, T.; Suo, Z., Stretchable interconnects for elastic electronic surfaces. *Proceedings of the IEEE* 2005, 93, 1459-1467.
106. Li, T.; Suo, Z.; Lacour, S.; Wagner, S., Compliant thin film patterns of stiff materials as platforms for stretchable electronics. *Journal of Materials Research* 2005, 20, 3274-3277.
107. Lacour, S. P.; Chan, D.; Wagner, S.; Li, T.; Suo, Z., Mechanisms of reversible stretchability of thin metal films on elastomeric substrates. *Applied Physics Letters* 2006, 88, 204103.
108. Lu, N. S.; Wang, X.; Suo, Z. G.; Vlassak, J., Metal films on polymer substrates stretched beyond 50%. *Applied Physics Letters* 2007, 91.
109. Cotton, D. P. J.; Graz, I. M.; Lacour, S. P., A Multifunctional Capacitive Sensor for Stretchable Electronic Skins. *Ieee Sensors Journal* 2009, 9, 2008-2009.
110. Lu, N. S.; Suo, Z. G.; Vlassak, J. J., The effect of film thickness on the failure strain of polymer-supported metal films. *Acta Materialia* 2010, 58, 1679-1687.
111. Cordill, M. J.; Taylor, A.; Schalko, J.; Dehm, G., Fracture and Delamination of Chromium Thin Films on Polymer Substrates. *Metallurgical and Materials Transactions a-Physical Metallurgy and Materials Science* 2010, 41A, 870-875.

112. Xu, W.; Lu, T. J.; Wang, F., Effects of interfacial properties on the ductility of polymer-supported metal films for flexible electronics. *International Journal of Solids and Structures* 2010, 47, 1830-1837.
113. Graudejus, O.; Jia, Z.; Li, T.; Wagner, S., Size-dependent rupture strain of elastically stretchable metal conductors. *Scripta Materialia* 2012, 66, 919-922.
114. Considere, A., **Memoire sur l'emploi du fer et de l'acier dans les constructions**. *Annales des Ponts et Chaussées* 1885, 9, 574-775.
115. Xue, Z. Y.; Hutchinson, J. W., Neck retardation and enhanced energy absorption in metal-elastomer bilayers. *Mechanics of Materials* 2007, 39, 473-487.
116. Li, T.; Suo, Z., Deformability of thin metal films on elastomer substrates. *International Journal of Solids and Structures* 2006, 43, 2351-2363.
117. Li, T.; Huang, Z.; Xi, Z.; Lacour, S.; Wagner, S.; Suo, Z., Delocalizing strain in a thin metal film on a polymer substrate. *Mechanics of Materials* 2005, 37, 261-273.
118. PASHLEY, D., A STUDY OF THE DEFORMATION AND FRACTURE OF SINGLE-CRYSTAL GOLD FILMS OF HIGH STRENGTH INSIDE AN ELECTRON MICROSCOPE. *PROCEEDINGS OF THE ROYAL SOCIETY OF LONDON SERIES A-MATHEMATICAL AND PHYSICAL SCIENCES* 1960, 255, 218-&.
119. Keller, R. R.; Phelps, J. M.; Read, D. T., Tensile and fracture behavior of free-standing copper films. *Materials Science and Engineering a-Structural Materials Properties Microstructure and Processing* 1996, 214.
120. Huang, H. B.; Spaepen, F., Tensile testing of free-standing Cu, Ag and Al thin films and Ag/Cu multilayers. *Acta Materialia* 2000, 48, 3261-3269.
121. Xiang, Y.; Chen, X.; Vlassak, J. J., Plane-strain bulge test for thin films. *Journal of Materials Research* 2005, 20, 2360-2370.
122. Nicola, L.; Xiang, Y.; Vlassak, J. J.; Van der Giessen, E.; Needleman, A., Plastic deformation of freestanding thin films: Experiments and modeling. *Journal of the Mechanics and Physics of Solids* 2006, 54, 2089-2110.
123. Espinosa, H. D.; Prorok, B. C.; Fischer, M., A methodology for determining mechanical properties of freestanding thin films and MEMS materials. *Journal of the Mechanics and Physics of Solids* 2003, 51.
124. Chiu, S. L.; Leu, J.; Ho, P. S., Fracture of metal-polymer line structures. 1. Semiflexible polyimide. *Journal of Applied Physics* 1994, 76, 5136-5142.
125. Macionczyk, F.; Bruckner, W., Tensile testing of AlCu thin films on polyimide foils. *Journal of Applied Physics* 1999, 86, 4922-4929.

126. Hommel, M.; Kraft, O., Deformation behavior of thin copper films on deformable substrates. *Acta Materialia* 2001, 49, 3935-3947.
127. Alaca, B. E.; Saif, M. T. A.; Sehitoglu, H., On the interface debond at the edge of a thin film on a thick substrate. *Acta Materialia* 2002, 50, 1197-1209.
128. Yu, D. Y. W.; Spaepen, F., The yield strength of thin copper films on Kapton. *Journal of Applied Physics* 2004, 95, 2991-2997.
129. Xiang, Y.; Li, T.; Suo, Z.; Vlassak, J., High ductility of a metal film adherent on a polymer substrate. *Applied Physics Letters* 2005, 87, 161910.
130. Niu, R. M.; Liu, G.; Wang, C.; Zhang, G.; Ding, X. D.; Sun, J., Thickness dependent critical strain in submicron Cu films adherent to polymer substrate. *Applied Physics Letters* 2007, 90.
131. Xue, Z.; Vaziri, A.; Hutchinson, J. W., Material aspects of dynamic neck retardation. *Journal of the Mechanics and Physics of Solids* 2008, 56, 93-113.
132. Shenoy, V. B.; Freund, L. B., Necking bifurcations during high strain rate extension. *Journal of the Mechanics and Physics of Solids* 1999, 47, 2209-2233.
133. Sorensen, N. J.; Freund, L. B., Unstable neck formation in a ductile ring subjected to impulsive radial loading. *International Journal of Solids and Structures* 2000, 37, 2265-2283.
134. Guduru, P. R.; Freund, L. B., The dynamics of multiple neck formation and fragmentation in high rate extension of ductile materials. *International Journal of Solids and Structures* 2002, 39, 5615-5632.
135. Mercier, S.; Molinari, A., Predictions of bifurcation and instabilities during dynamic extension. *International Journal of Solids and Structures* 2003, 40, 1995-2016.
136. Mercier, S.; Granier, N.; Molinari, A.; Llorca, F.; Buy, F., Multiple necking during the dynamic expansion of hemispherical metallic shells, from experiments to modelling. *Journal of the Mechanics and Physics of Solids* 2010, 58, 955-982.
137. Zhang, H.; Ravi-Chandar, K., On the dynamics of necking and fragmentation - I. Real-time and post-mortem observations in Al6061-O. *International Journal of Fracture* 2006, 142, 183-217.
138. Xue, Z. Y.; Hutchinson, J. W., Neck development in metal/elastomer bilayers under dynamic stretchings. *International Journal of Solids and Structures* 2008, 45, 3769-3778.

139. Zhang, H.; Liechti, K. M.; Ravi-Chandar, K., On the dynamics of localization and fragmentation-III. Effect of cladding with a polymer. *International Journal of Fracture* 2009, 155, 101-118.
140. Morales, S. A.; Albrecht, A. B.; Zhang, H.; Liechti, K. M.; Ravi-Chandar, K., On the dynamics of localization and fragmentation: V. Response of polymer coated Al 6061-O tubes. *International Journal of Fracture* 2011, 172, 161-185.
141. Amini, M. R.; Isaacs, J.; Nemat-Nasser, S., Investigation of effect of polyurea on response of steel plates to impulsive loads in direct pressure-pulse experiments. *Mechanics of Materials* 2010, 42, 628-639.
142. Amini, M.; Nemat-Nasser, S., Micromechanisms of ductile fracturing of DH-36 steel plates under impulsive loads and influence of polyurea reinforcing. *International Journal of Fracture* 2010, 162, 205-217.
143. Hill, R., CONSTITUTIVE INEQUALITIES FOR ISOTROPIC ELASTIC SOLIDS UNDER FINITE STRAIN. *Proceedings of the Royal Society of London Series a-Mathematical and Physical Sciences* 1970, 314, 457-&.
144. Hutchinson, J. W.; Neale, K. W., Sheet necking-II. Time-independent behavior. In *Mechanics of Sheet Metal Forming*, Wang, D. P. K. a. N.-M., Ed. Plenum Publishing Corporation: 1980; pp 127-153.
145. Marciniak, Z.; Kuczynski, K.; Pokora, T., INFLUENCE OF PLASTIC PROPERTIES OF A MATERIAL ON FORMING LIMIT DIAGRAM FOR SHEET-METAL IN TENSION. *International Journal of Mechanical Sciences* 1973, 15, 789-&.
146. Barlat, F., CRYSTALLOGRAPHIC TEXTURE, ANISOTROPIC YIELD SURFACES AND FORMING LIMITS OF SHEET METALS. *Materials Science and Engineering* 1987, 91, 55-72.
147. Zhao, L.; Sowerby, R.; Sklad, M. P., A theoretical and experimental investigation of limit strains in sheet metal forming. *International Journal of Mechanical Sciences* 1996, 38, 1307-1317.
148. Kuroda, M.; Tvergaard, V., Forming limit diagrams for anisotropic metal sheets with different yield criteria. *International Journal of Solids and Structures* 2000, 37, 5037-5059.
149. Stoughton, T. B., A general forming limit criterion for sheet metal forming. *International Journal of Mechanical Sciences* 2000, 42, 1-27.

150. Hashiguchi, K.; Protasov, A., Localized necking analysis by the subloading surface model with tangential-strain rate and anisotropy. *International Journal of Plasticity* 2004, 20, 1909-1930.
151. Zhang, L.; Wang, J., Modeling the localized necking in anisotropic sheet metals. *International Journal of Plasticity* 2012, 39, 103-118.
152. Wu, H.; Chan, G.; Choi, J. W.; Ryu, I.; Yao, Y.; McDowell, M. T.; Lee, S. W.; Jackson, A.; Yang, Y.; Hu, L.; Cui, Y., Stable Cycling of Double-Walled Silicon Nanotube Battery Anodes Through Solid-Electrolyte Interphase Control. *Nat. Nanotechnol.* 2012, 7, 309-314.
153. Hu, L. B.; Wu, H.; Gao, Y. F.; Cao, A. Y.; Li, H. B.; McDough, J.; Xie, X.; Zhou, M.; Cui, Y., Silicon-Carbon Nanotube Coaxial Sponge as Li-Ion Anodes with High Areal Capacity. *Adv. Energy Mater.* 2011, 1, 523-527.
154. Liu, X. H.; Zhong, L.; Huang, S.; Mao, S. X.; Zhu, T.; Huang, J. Y., Size-Dependent Fracture of Silicon Nanoparticles during Lithiation. *ACS Nano* 2012, 6, 1522-1531.
155. Bridel, J. S.; Azais, T.; Morcrette, M.; Tarascon, J. M.; Larcher, D., Key Parameters Governing the Reversibility of Si/Carbon/CMC Electrodes for Li-Ion Batteries. *Chem. Mater.* 2010, 22, 1229-1241.
156. Liu, X. H.; Zheng, H.; Zhong, L.; Huan, S.; Karki, K.; Zhang, L. Q.; Liu, Y.; Kushima, A.; Liang, W. T.; Wang, J. W.; Cho, J.-H.; Epstein, E.; Dayeh, S. A.; Picraux, S. T.; Zhu, T.; Li, J.; Sullivan, J. P.; Cumings, J.; Wang, C.; Mao, S. X.; Ye, Z. Z.; Zhang, S.; Huang, J. Y., Anisotropic Swelling and Fracture of Silicon Nanowires during Lithiation. *Nano Lett.* 2011, 11, 3312-3318.
157. Goldman, J. L.; Long, B. R.; Gewirth, A. A.; Nuzzo, R. G., Strain Anisotropies and Self-Limiting Capacities in Single-Crystalline 3D Silicon Microstructures: Models for High Energy Density Lithium-Ion Battery Anodes. *Adv. Funct. Mater.* 2011, 21, 2412-2422.
158. Yang, H.; Huang, S.; Huang, X.; Fan, F.; Liang, W.; Liu, X. H.; Chen, L.-Q.; Huang, J. Y.; Li, J.; Zhu, T.; Zhang, S., Orientation-Dependent Interfacial Mobility Governs the Anisotropic Swelling in Lithiated Silicon Nanowires. *Nano Lett.* 2012, 12, 1953-1958.
159. Armand, M.; Tarascon, J. M., Building better batteries. *Nature* 2008, 451, 652-657.
160. Kang, B.; Ceder, G., Battery materials for ultrafast charging and discharging. *Nature* 2009, 458, 190-193.

161. Ji, X.; Lee, K. T.; Nazar, L. F., A highly ordered nanostructured carbon-sulphur cathode for lithium-sulphur batteries. *Nature Materials* 2009, 8, 500-506.
162. Magasinski, A.; Dixon, P.; Hertzberg, B.; Kvit, A.; Ayala, J.; Yushin, G., High-performance lithium-ion anodes using a hierarchical bottom-up approach. *Nature Materials* 2010, 9, 353-358.
163. Kim, H.; Cho, J., Superior Lithium Electroactive Mesoporous Si@Carbon Core-Shell Nanowires for Lithium Battery Anode Material. *Nano Letters* 2008, 8, 3688-3691.
164. Cui, L.-F.; Yang, Y.; Hsu, C.-M.; Cui, Y., Carbon-Silicon Core-Shell Nanowires as High Capacity Electrode for Lithium Ion Batteries. *Nano Letters* 2009, 9, 3370-3374.
165. Hwang, T. H.; Lee, Y. M.; Kong, B.-S.; Seo, J.-S.; Choi, J. W., Electrospun Core-Shell Fibers for Robust Silicon Nanoparticle-Based Lithium Ion Battery Anodes. *Nano Letters* 2012, 12, 802-807.
166. Yao, Y.; Huo, K.; Hu, L.; Liu, N.; Ha, J. J.; McDowell, M. T.; Chu, P. K.; Cui, Y., Highly Conductive, Mechanically Robust, and Electrochemically Inactive TiC/C Nanofiber Scaffold for High-Performance Silicon Anode Batteries. *Acs Nano* 2011, 5, 8346-8351.
167. Chan, C. K.; Ruffo, R.; Hong, S. S.; Huggins, R. A.; Cui, Y., Structural and electrochemical study of the reaction of lithium with silicon nanowires. *Journal of Power Sources* 2009, 189, 34-39.
168. Wang, C.-M.; Li, X.; Wang, Z.; Xu, W.; Liu, J.; Gao, F.; Kovarik, L.; Zhang, J.-G.; Howe, J.; Burton, D. J.; Liu, Z.; Xiao, X.; Thevuthasan, S.; Baer, D. R., In Situ TEM Investigation of Congruent Phase Transition and Structural Evolution of Nanostructured Silicon/Carbon Anode for Lithium Ion Batteries. *Nano Letters* 2012, 12, 1624-1632.
169. Liu, X. H.; Zheng, H.; Zhong, L.; Huan, S.; Karki, K.; Zhang, L. Q.; Liu, Y.; Kushima, A.; Liang, W. T.; Wang, J. W.; Cho, J.-H.; Epstein, E.; Dayeh, S. A.; Picraux, S. T.; Zhu, T.; Li, J.; Sullivan, J. P.; Cumings, J.; Wang, C.; Mao, S. X.; Ye, Z. Z.; Zhang, S.; Huang, J. Y., Anisotropic Swelling and Fracture of Silicon Nanowires during Lithiation. *Nano Letters* 2011, 11, 3312-3318.
170. Ryu, I.; Choi, J. W.; Cui, Y.; Nix, W. D., Size-dependent fracture of Si nanowire battery anodes. *Journal of the Mechanics and Physics of Solids* 2011, 59, 1717-1730.
171. Yang, H.; Huang, S.; Huang, X.; Fan, F.; Liang, W.; Liu, X. H.; Chen, L.-Q.; Huang, J. Y.; Li, J.; Zhu, T.; Zhang, S., Orientation-Dependent Interfacial Mobility Governs the Anisotropic Swelling in Lithiated Silicon Nanowires. *Nano Letters* 2012, 12, 1953-1958.

172. Wu, H.; Zheng, G.; Liu, N.; Carney, T. J.; Yang, Y.; Cui, Y., Engineering Empty Space between Si Nanoparticles for Lithium-Ion Battery Anodes. *Nano Letters* 2012, 12, 904-909.
173. Guo, L. J., Nanoimprint lithography: Methods and material requirements. *Advanced Materials* 2007, 19, 495-513.
174. Notten, P. H. L.; Roozeboom, F.; Niessen, R. A. H.; Baggetto, L., 3-D integrated all-solid-state rechargeable batteries. *Advanced Materials* 2007, 19, 4564-4567.
175. Kim, D. K.; Muralidharan, P.; Lee, H. W.; Ruffo, R.; Yang, Y.; Chan, C. K.; Peng, H.; Huggins, R. A.; Cui, Y., Spinel LiMn₂O₄ Nanorods as Lithium Ion Battery Cathodes. *Nano Letters* 2008, 8, 3948-3952.
176. Marom, R.; Amalraj, S. F.; Leifer, N.; Jacob, D.; Aurbach, D., A review of advanced and practical lithium battery materials. *Journal of Materials Chemistry* 2011, 21, 9938-9954.
177. Obrovac, M. N.; Christensen, L., Structural changes in silicon anodes during lithium insertion/extraction. *Electrochemical and Solid State Letters* 2004, 7, A93-A96.
178. Obrovac, M. N.; Christensen, L.; Le, D. B.; Dahnb, J. R., Alloy design for lithium-ion battery anodes. *Journal of the Electrochemical Society* 2007, 154, A849-A855.
179. Kasavajjula, U.; Wang, C.; Appleby, A. J., Nano- and bulk-silicon-based insertion anodes for lithium-ion secondary cells. *Journal of Power Sources* 2007, 163, 1003-1039.
180. Karki, K.; Epstein, E.; Cho, J.-H.; Jia, Z.; Li, T.; Picraux, S. T.; Wang, C.; Cumings, J., Lithium-Assisted Electrochemical Welding in Silicon Nanowire Battery Electrodes. *Nano Letters* 2012, 12, 1392-1397.
181. Takamura, T.; Ohara, S.; Uehara, M.; Suzuki, J.; Sekine, K., A vacuum deposited Si film having a Li extraction capacity over 2000 mAh/g with a long cycle life. *Journal of Power Sources* 2004, 129, 96-100.
182. Baggetto, L.; Danilov, D.; Notten, P. H. L., Honeycomb-Structured Silicon: Remarkable Morphological Changes Induced by Electrochemical (De)Lithiation. *Advanced Materials* 2011, 23, 1563-1566.
183. Sun, C.-F.; Karki, K.; Jia, Z.; Liao, H.; Zhang, Y.; Li, T.; Qi, Y.; Cumings, J.; Rubloff, G. W.; Wang, Y., A Beaded-String Silicon Anode. *Acs Nano* 2013, 7, 2717-2724.

184. Wan, J.; Kaplan, A. F.; Zheng, J.; Han, X.; Chen, Y.; Weadock, N. J.; Faenza, N.; Lacey, S.; Li, T.; Guo, J.; Hu, L., Two dimensional silicon nanowalls for lithium ion batteries. *Journal of Materials Chemistry A* 2014, 2, 6051-6057.
185. Haftbaradaran, H.; Xiao, X.; Verbrugge, M. W.; Gao, H., Method to deduce the critical size for interfacial delamination of patterned electrode structures and application to lithiation of thin-film silicon islands. *Journal of Power Sources* 2012, 206, 357-366.
186. Soni, S. K.; Sheldon, B. W.; Xiao, X.; Verbrugge, M. W.; Ahn, D.; Haftbaradaran, H.; Gao, H., Stress Mitigation during the Lithiation of Patterned Amorphous Si Islands. *Journal of the Electrochemical Society* 2012, 159, A38-A43.
187. Sethuraman, V.; Srinivasan, V.; Bower, A.; Guduru, P., In Situ Measurements of Stress-Potential Coupling in Lithiated Silicon. *Journal of the Electrochemical Society* 2010, 157, A1253-A1261.
188. Sethuraman, V.; Van Winkle, N.; Abraham, D.; Bower, A.; Guduru, P., Real-time stress measurements in lithium-ion battery negative-electrodes. *Journal of Power Sources* 2012, 206, 334-342.
189. Sethuraman, V.; Nguyen, A.; Chon, M.; Nadimpalli, S.; Wang, H.; Abraham, D.; Bower, A.; Shenoy, V.; Guduru, P., Stress Evolution in Composite Silicon Electrodes during Lithiation/Delithiation. *Journal of the Electrochemical Society* 2013, 160, A739-A746.
190. Hu, Y.; Zhao, X.; Suo, Z., Averting cracks caused by insertion reaction in lithium-ion batteries. *Journal of Materials Research* 2010, 25, 1007-1010.
191. Zhao, K.; Pharr, M.; Wan, Q.; Wang, W. L.; Kaxiras, E.; Vlassak, J. J.; Suo, Z., Concurrent Reaction and Plasticity during Initial Lithiation of Crystalline Silicon in Lithium-Ion Batteries. *Journal of the Electrochemical Society* 2012, 159, A238-A243.
192. Huang, S.; Fan, F.; Li, J.; Zhang, S.; Zhu, T., Stress generation during lithiation of high-capacity electrode particles in lithium ion batteries. *Acta Materialia* 2013, 61, 4354-4364.
193. Bower, A.; Guduru, P.; Sethuraman, V., A finite strain model of stress, diffusion, plastic flow, and electrochemical reactions in a lithium-ion half-cell. *Journal of the Mechanics and Physics of Solids* 2011, 59, 804-828.
194. Christensen, J.; Newman, J., Stress generation and fracture in lithium insertion materials. *Journal of Solid State Electrochemistry* 2006, 10, 293-319.
195. Gao, Y. F.; Zhou, M., Coupled mechano-diffusional driving forces for fracture in electrode materials. *Journal of Power Sources* 2013, 230, 176-193.

196. Zhao, K.; Pharr, M.; Hartle, L.; Vlassak, J. J.; Suo, Z., Fracture and debonding in lithium-ion batteries with electrodes of hollow core-shell nanostructures. *Journal of Power Sources* 2012, 218, 6-14.
197. McDowell, M.; Ryu, I.; Lee, S.; Wang, C.; Nix, W.; Cui, Y., Studying the Kinetics of Crystalline Silicon Nanoparticle Lithiation with In Situ Transmission Electron Microscopy. *Advanced Materials* 2012, 24, 6034-+.
198. Liu, X.; Fan, F.; Yang, H.; Zhang, S.; Huang, J.; Zhu, T., Self-Limiting Lithiation in Silicon Nanowires. *Acs Nano* 2013, 7, 1495-1503.
199. Liu, X.; Wang, J.; Huang, S.; Fan, F.; Huang, X.; Liu, Y.; Krylyuk, S.; Yoo, J.; Dayeh, S.; Davydov, A.; Mao, S.; Picraux, S.; Zhang, S.; Li, J.; Zhu, T.; Huang, J., In situ atomic-scale imaging of electrochemical lithiation in silicon. *Nature Nanotechnology* 2012, 7, 749-756.
200. Key, B.; Bhattacharyya, R.; Morcrette, M.; Seznec, V.; Tarascon, J.; Grey, C., Real-Time NMR Investigations of Structural Changes in Silicon Electrodes for Lithium-Ion Batteries. *Journal of the American Chemical Society* 2009, 131, 9239-9249.
201. Key, B.; Morcrette, M.; Tarascon, J.; Grey, C., Pair Distribution Function Analysis and Solid State NMR Studies of Silicon Electrodes for Lithium Ion Batteries: Understanding the (De)lithiation Mechanisms. *Journal of the American Chemical Society* 2011, 133, 503-512.
202. Gao, Y.-F.; Zhou, M., Strong dependency of lithium diffusion on mechanical constraints in high-capacity Li-ion battery electrodes. *Acta Mechanica Sinica* 2012, 28, 1068-1077.
203. Gao, Y. F.; Zhou, M., Strong stress-enhanced diffusion in amorphous lithium alloy nanowire electrodes. *Journal of Applied Physics* 2011, 109.
204. Yao, Y.; McDowell, M. T.; Ryu, I.; Wu, H.; Liu, N.; Hu, L.; Nix, W. D.; Cui, Y., Interconnected Silicon Hollow Nanospheres for Lithium-Ion Battery Anodes with Long Cycle Life. *Nano Letters* 2011, 11, 2949-2954.
205. Liu, N.; Wu, H.; McDowell, M. T.; Yao, Y.; Wang, C.; Cui, Y., A Yolk-Shell Design for Stabilized and Scalable Li-Ion Battery Alloy Anodes. *Nano Letters* 2012, 12, 3315-3321.
206. Yan, N.; Wang, F.; Zhong, H.; Li, Y.; Wang, Y.; Hu, L.; Chen, Q., Hollow Porous SiO₂ Nanocubes Towards High-performance Anodes for Lithium-ion Batteries. *Scientific Reports* 2013, 3.

207. Chen, D.; Mei, X.; Ji, G.; Lu, M.; Xie, J.; Lu, J.; Lee, J. Y., Reversible Lithium-Ion Storage in Silver-Treated Nanoscale Hollow Porous Silicon Particles. *Angewandte Chemie-International Edition* 2012, 51, 2409-2413.
208. Lee, S. W.; McDowell, M. T.; Berla, L. A.; Nix, W. D.; Cui, Y., Fracture of crystalline silicon nanopillars during electrochemical lithium insertion. *Proceedings of the National Academy of Sciences of the United States of America* 2012, 109, 4080-4085.
209. Tarascon, J. M.; Armand, M., Issues and challenges facing rechargeable lithium batteries. *Nature* 2001, 414, 359-367.
210. Yang, Y.; McDowell, M. T.; Jackson, A.; Cha, J. J.; Hong, S. S.; Cui, Y., New Nanostructured Li₂S/Silicon Rechargeable Battery with High Specific Energy. *Nano Letters* 2010, 10, 1486-1491.
211. Li, J.; Dahn, J. R., An in situ X-ray diffraction study of the reaction of Li with crystalline Si. *Journal of the Electrochemical Society* 2007, 154, A156-A161.
212. Wu, H.; Cui, Y., Designing nanostructured Si anodes for high energy lithium ion batteries. *Nano Today* 2012, 7, 414-429.
213. Goldman, J. L.; Long, B. R.; Gewirth, A. A.; Nuzzo, R. G., Strain Anisotropies and Self-Limiting Capacities in Single-Crystalline 3D Silicon Microstructures: Models for High Energy Density Lithium-Ion Battery Anodes. *Advanced Functional Materials* 2011, 21, 2412-2422.
214. Lee, S. W.; McDowell, M. T.; Choi, J. W.; Cui, Y., Anomalous Shape Changes of Silicon Nanopillars by Electrochemical Lithiation. *Nano Letters* 2011, 11, 3034-3039.
215. Pharr, M.; Zhao, K.; Wang, X.; Suo, Z.; Vlassak, J. J., Kinetics of Initial Lithiation of Crystalline Silicon Electrodes of Lithium-Ion Batteries. *Nano Letters* 2012, 12, 5039-5047.
216. Bogart, T. D.; Oka, D.; Lu, X.; Gu, M.; Wang, C.; Korgel, B. A., Lithium Ion Battery Performance of Silicon Nanowires with Carbon Skin. *Acs Nano* 2014, 8, 915-922.
217. Wan, J.; Kaplan, A. F.; Jia, Z.; Han, X.; Chen, Y.; Weadock, N. J.; Faenza, N.; Lacey, S.; Li, T.; Guo, J.; Hu, L., two dimensional silicon nanowalls for lithium ion batteries. *Journal of Materials Chemistry A*, 2014; Vol. 2, pp 6051-6057.
218. Wang, J. W.; He, Y.; Fan, F.; Liu, X. H.; Xia, S.; Liu, Y.; Harris, C. T.; Li, H.; Huang, J. Y.; Mao, S. X.; Zhu, T., Two-Phase Electrochemical Lithiation in Amorphous Silicon. *Nano Letters* 2013, 13, 709-715.
219. McDowell, M. T.; Lee, S. W.; Harris, J. T.; Korgel, B. A.; Wang, C.; Nix, W. D.; Cui, Y., In Situ TEM of Two-Phase Lithiation of Amorphous Silicon Nanospheres. *Nano Letters* 2013, 13, 758-764.

220. Cui, Z.; Gao, F.; Qu, J., Two-phase versus two-stage versus multi-phase lithiation kinetics in silicon. *Applied Physics Letters* 2013, 103.
221. Grantab, R.; Shenoy, V. B., Pressure-Gradient Dependent Diffusion and Crack Propagation in Lithiated Silicon Nanowires. *Journal of the Electrochemical Society* 2012, 159, A584-A591.
222. Zhao, K.; Wang, W. L.; Gregoire, J.; Pharr, M.; Suo, Z.; Vlassak, J. J.; Kaxiras, E., Lithium-Assisted Plastic Deformation of Silicon Electrodes in Lithium-Ion Batteries: A First-Principles Theoretical Study. *Nano Letters* 2011, 11, 2962-2967.
223. Pharr, M.; Suo, Z.; Vlassak, J. J., Measurements of the Fracture Energy of Lithiated Silicon Electrodes of Li-Ion Batteries. *Nano Letters* 2013, 13, 5570-5577.
224. Yang, Z. G.; Zhang, J. L.; Kintner-Meyer, M. C. W.; Lu, X. C.; Choi, D. W.; Lemmon, J. P.; Liu, J., Electrochemical Energy Storage for Green Grid. *Chemical Reviews* 2011, 111, 3577-3613.
225. Chan, C. K.; Peng, H. L.; Liu, G.; McIlwrath, K.; Zhang, X. F.; Huggins, R. A.; Cui, Y., High-performance lithium battery anodes using silicon nanowires. *Nature Nanotechnology* 2008, 3, 31-35.
226. Kovalenko, I.; Zdyrko, B.; Magasinski, A.; Hertzberg, B.; Milicev, Z.; Burtovyy, R.; Luzinov, I.; Yushin, G., A Major Constituent of Brown Algae for Use in High-Capacity Li-Ion Batteries. *Science* 2011, 333, 75-79.
227. Dean, J. A., *Lange's Handbook of Chemistry (15th Edition)*. 15 ed.; McGraw-Hill, 1999.
228. Ponrouch, A.; Marchante, E.; Courty, M.; Tarascon, J.-M.; Rosa Palacin, M., In search of an optimized electrolyte for Na-ion batteries. *Energy & Environmental Science* 2012, 5.
229. Komaba, S.; Ishikawa, T.; Yabuuchi, N.; Murata, W.; Ito, A.; Ohsawa, Y., Fluorinated Ethylene Carbonate as Electrolyte Additive for Rechargeable Na Batteries. *Acs Applied Materials & Interfaces* 2011, 3.
230. Abouimrane, A.; Weng, W.; Eltayeb, H.; Cui, Y. J.; Niklas, J.; Poluektov, O.; Amine, K., Sodium insertion in carboxylate based materials and their application in 3.6 V full sodium cells. *Energy & Environmental Science* 2012, 5, 9632-9638.
231. Cao, Y.; Xiao, L.; Sushko, M. L.; Wang, W.; Schwenzer, B.; Xiao, J.; Nie, Z.; Saraf, L. V.; Yang, Z.; Liu, J., Sodium Ion Insertion in Hollow Carbon Nanowires for Battery Applications. *Nano Letters* 2012, 12.

232. Kim, S.-W.; Seo, D.-H.; Ma, X.; Ceder, G.; Kang, K., Electrode Materials for Rechargeable Sodium-Ion Batteries: Potential Alternatives to Current Lithium-Ion Batteries. *Advanced Energy Materials* 2012, 2.
233. Komaba, S.; Murata, W.; Ishikawa, T.; Yabuuchi, N.; Ozeki, T.; Nakayama, T.; Ogata, A.; Gotoh, K.; Fujiwara, K., Electrochemical Na Insertion and Solid Electrolyte Interphase for Hard-Carbon Electrodes and Application to Na-Ion Batteries. *Advanced Functional Materials* 2011, 21.
234. Tepavcevic, S.; Xiong, H.; Stamenkovic, V. R.; Zuo, X.; Balasubramanian, M.; Prakapenka, V. B.; Johnson, C. S.; Rajh, T., Nanostructured Bilayered Vanadium Oxide Electrodes for Rechargeable Sodium-Ion Batteries. *Acs Nano* 2012, 6.
235. Yabuuchi, N.; Kajiyama, M.; Iwatate, J.; Nishikawa, H.; Hitomi, S.; Okuyama, R.; Usui, R.; Yamada, Y.; Komaba, S., P2-type $\text{Na}_x[\text{Fe}_{1/2}\text{Mn}_{1/2}]\text{O}_2$ made from earth-abundant elements for rechargeable Na batteries. *Nat Mater* 2012, 11, 512-517.
236. Zhao, L.; Zhao, J. M.; Hu, Y. S.; Li, H.; Zhou, Z. B.; Armand, M.; Chen, L. Q., Disodium Terephthalate ($\text{Na}_2\text{C}_8\text{H}_4\text{O}_4$) as High Performance Anode Material for Low-Cost Room-Temperature Sodium-Ion Battery. *Advanced Energy Materials* 2012, 2, 962-965.
237. Park, Y.; Shin, D.-S.; Woo, S. H.; Choi, N. S.; Shin, K. H.; Oh, S. M.; Lee, K. T.; Hong, S. Y., Sodium Terephthalate as an Organic Anode Material for Sodium Ion Batteries. *Advanced Materials* 2012, 24.
238. Xu, Y.; Zhu, Y.; Liu, Y.; Wang, C., Electrochemical Performance of Porous Carbon/Tin Composite Anodes for Sodium-Ion and Lithium-Ion Batteries. *Advanced Energy Materials* 2012, n/a-n/a.
239. Xiao, L.; Cao, Y.; Xiao, J.; Wang, W.; Kovarik, L.; Nie, Z.; Liu, J., High capacity, reversible alloying reactions in SnSb/C nanocomposites for Na-ion battery applications. *Chemical Communications* 2012, 48.
240. Liu, Y.; Xu, Y.; Zhu, Y.; Culver, J. N.; Lundgren, C. A.; Xu, K.; Wang, C., Tin Coated Viral-Nanoforests as Sodium-Ion Battery Anodes. *ACS Nano* 2013.
241. Su, D.; Ahn, H.-J.; Wang, G., SnO₂@graphene nanocomposites as anode materials for Na-ion batteries with superior electrochemical performance. *Chemical Communications* 2013.
242. Hon, D. N.-S.; Shiraishi, N., *Wood and Cellulosic Chemistry*. Second ed.; CRC Press: 2000.

243. Komaba, S.; Matsuura, Y.; Ishikawa, T.; Yabuuchi, N.; Murata, W.; Kuze, S., Redox reaction of Sn-polyacrylate electrodes in aprotic Na cell. *Electrochemistry Communications* 2012, 21, 65-68.
244. Cichocki, F. R.; Thomason, J. L., Thermoelastic anisotropy of a natural fiber. *Composites Science and Technology* 2002, 62.
245. Tomioka, Y.; Yuki, N., Bend stiffness of copper and copper alloy foils. *Journal of Materials Processing Technology* 2004, 146.
246. Iwamura, S.; Nishihara, H.; Kyotani, T., Fast and reversible lithium storage in a wrinkled structure formed from Si nanoparticles during lithiation/delithiation cycling. *Journal of Power Sources* 2013, 222, 400-409.
247. Bhandakkar, T. K.; Johnson, H. T., Diffusion induced stresses in buckling battery electrodes. *Journal of the Mechanics and Physics of Solids* 2012, 60, 1103-1121.
248. Yu, C. J.; Li, X.; Ma, T.; Rong, J. P.; Zhang, R. J.; Shaffer, J.; An, Y. H.; Liu, Q.; Wei, B. Q.; Jiang, H. Q., Silicon Thin Films as Anodes for High-Performance Lithium-Ion Batteries with Effective Stress Relaxation. *Advanced Energy Materials* 2012, 2, 68-73.
249. Wu, H.; Chan, G.; Choi, J. W.; Ryu, I.; Yao, Y.; McDowell, M. T.; Lee, S. W.; Jackson, A.; Yang, Y.; Hu, L.; Cui, Y., Stable cycling of double-walled silicon nanotube battery anodes through solid-electrolyte interphase control. *Nat Nano* 2012, 7, 310-315.
250. Boles, S. T.; Thompson, C. V.; Kraft, O.; Moenig, R., In situ tensile and creep testing of lithiated silicon nanowires. *Applied Physics Letters* 2013, 103.
251. Zhu, H.; Jia, Z.; Chen, Y.; Weadock, N.; Wan, J.; Vaaland, O.; Han, X.; Li, T.; Hu, L., Tin Anode for Sodium-Ion Batteries Using Natural Wood Fiber as a Mechanical Buffer and Electrolyte Reservoir. *Nano Letters* 2013, 13, 3093-3100.